Max-Planck-Institut
für Meteorologie

REPORT No. 93

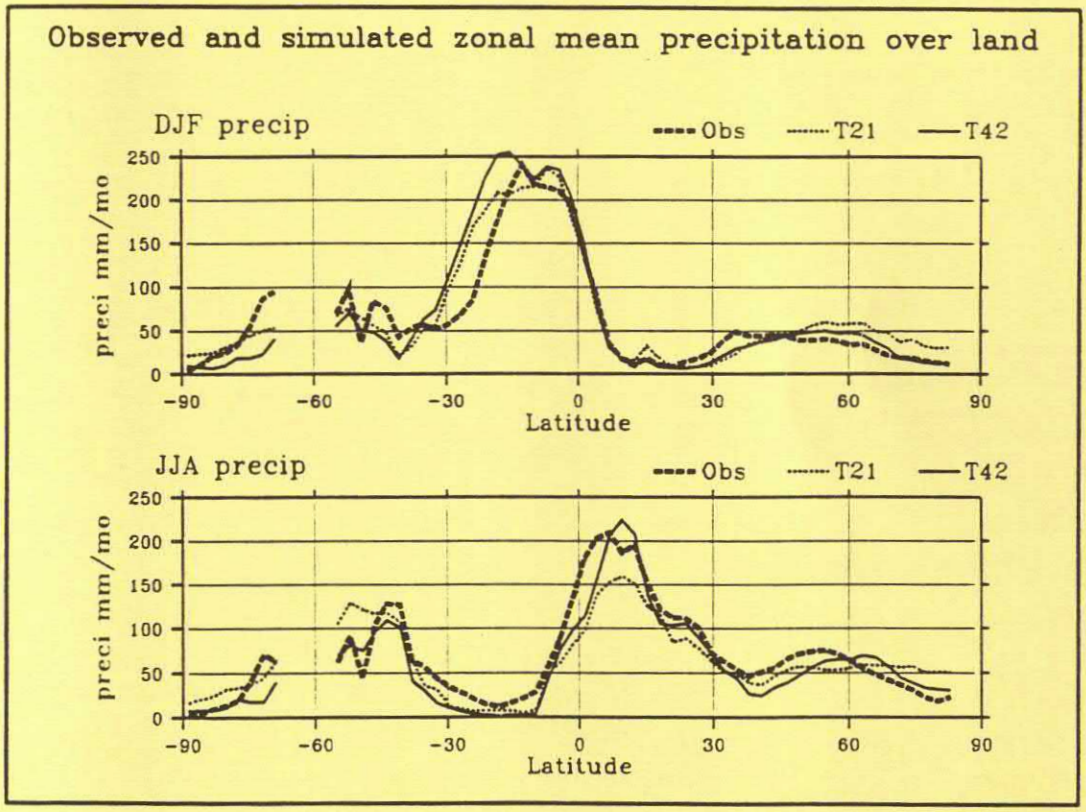

SIMULATION OF THE PRESENT-DAY CLIMATE WITH THE ECHAM MODEL: IMPACT OF MODEL PHYSICS AND RESOLUTION

by

E. ROECKNER • K. ARPE • L. BENGTSSON • S. BRINKOP
L. DÜMENIL • M. ESCH • E. KIRK • F. LUNKEIT • M. PONATER
B. ROCKEL • R. SAUSEN • U. SCHLESE • S. SCHUBERT • M. WINDELBAND

HAMBURG, OCTOBER 1992

AUTHORS:

Erich Roeckner
Klaus Arpe
Lennart Bengtsson
Lydia Dümenil
Monika Esch

Max-Planck-Institut
für Meteorologie

Edilbert Kirk
Frank Lunkeit
Silke Schubert
Martin Windelband

Universität Hamburg
Meteorologisches Institut
Bundesstraße 55
D-2000 Hamburg 13
FRG

Ulrich Schlese

Deutsches Klimarechenzentrum (DKRZ)
Bundesstraße 55
D-2000 Hamburg 13
FRG

Sabine Brinkop
Michael Ponater
Robert Sausen

Deutsche Forschungsanstalt
für Luft- und Raumfahrt (DLR)
Institut für Physik der Atmosphäre
D-8031 Oberpfaffenhofen
FRG

Burkhardt Rockel

GKSS Forschungszentrum Geesthacht
Institut für Physik
Postfach 11 60
D-2054 Geesthacht
FRG

MAX-PLANCK-INSTITUT
FÜR METEOROLOGIE
BUNDESSTRASSE 55
D-2000 HAMBURG 13
F.R. GERMANY

Tel.: +49 (40) 4 11 73-0
Telex: 211092 mpime d
Telemail: MPI.METEOROLOGY
Telefax: +49 (40) 4 11 73-298

REPb 93

Simulation of the present-day climate with the ECHAM model: Impact of model physics and resolution

E.Roeckner[1], K.Arpe[1], L.Bengtsson[1], S.Brinkop[4], L.Dümenil[1], M.Esch[1], E.Kirk[2], F.Lunkeit[2], M.Ponater[4], B.Rockel[5], R.Sausen[4], U.Schlese[3], S.Schubert[2] and M.Windelband[2]

[1] Max-Planck-Institut für Meteorologie, Hamburg

[2] Meteorologisches Institut der Universität, Hamburg

[3] Deutsches Klimarechenzentum (DKRZ), Hamburg

[4] Deutsche Forschungsanstalt für Luft- und Raumfahrt (DLR), Institut für Physik der Atmosphäre, Oberpfaffenhofen

[5] Institut für Physik am GKSS Forschungszentrum Geesthacht

Abstract

A detailed description of the third-generation atmospheric general circulation model ECHAM is presented. The climatology of ECHAM3, as simulated at low and high resolution (T21 and T42, respectively), is compared with ECMWF analyses (1981-1990) and also with the climatology of two earlier low resolution versions ECHAM1 and ECHAM2.

At low resolution, the impact of the improved model physics is evident primarily in the simulated time-mean state which is more successfully reproduced by the more recent model versions, particularly by ECHAM3. The impact of increased horizontal resolution can be identified not only by a generally improved time-mean circulation, particularly in the Southern Hemisphere, but most significantly by the increased level of high-frequency variability. In the low-frequency range, however, the impact of increased horizontal resolution is modest, and all models fail to reproduce the observed level of low-frequency intraseasonal variability.

ISSN 0937–1060

1. INTRODUCTION

General circulation models of the atmosphere and ocean are designed to derive the climate from first physical principles such as the conservation laws of angular momentum, energy and mass. The solution of the governing equations can, however, only be obtained by approximate methods which require a discretization of the space-time continuum. In addition to the truncation of the continuous spectrum, the basic error sources are generated by inaccuracies of the numerical solution method and, furthermore, by the need to consider the statistical effect of the unresolved scales on the resolved scales of the model, generally referred to as the parameterization problem.

During the past decades, considerable success has been achieved to improve both, numerical weather prediction (NWP) models and general circulation models (GCMs), by increasing the spatial resolution (parallel to the increase of computer power), by improving the numerical solution techniques, and by refining the parameterization schemes.

There is no doubt that increasing the spatial resolution reduces the forecast errors of NWP models (Simmons et al., 1989). On the other hand, there is no clear evidence that the climate simulated by GCMs will significantly improve with increasing resolution (Boer and Lazare, 1988; Boer et al., 1991; Boville, 1991). On the basis of a model intercomparison study which was undertaken to document the skill of GCMs to reproduce the modern climate, Boer et al. (1991) concluded that the models are more sensitive to changes of the parameterization schemes than to changes of the horizontal resolution.

The objectives of the present study are similar to those of Boer et al. (1991). However, instead of comparing a diversity of models with different resolution, different numerics and different physical parameterizations, we use only one model which allows us to isolate the relative importance of the processes under consideration in a more systematic manner. Furthermore, we will not only compare the simulated and observed time mean climates but also the respective intraseasonal fluctuations.

The model used in this study is the so-called ECHAM model (Roeckner et al., 1989) which evolved from the numerical weather prediction model developed at the European Centre for Medium Range Weather Forecasts (ECMWF). An old version of the ECMWF model (the so-called cycle 17 version, operational in 1985, in the following referred to as "ECHAM0") has been extensively used for climate studies at the Max-Planck-Institute for Meteorology and the University of Hamburg (Fischer, 1987, v.Storch, 1988; Fischer, 1989; Barnett et al., 1989; Latif et al., 1990; Metz and Lu, 1990; Ponater et al., 1990; Robertson and Metz, 1990; Barnett et al., 1991). In these studies, a number of model weaknesses have been identified as, for example, a cold bias in the tropical troposphere of more than 5K and a warm bias over the polar regions. The reduction of the meridional temperature gradient caused a weakening of the mean zonal flow. In particular, the near-surface flow on the Southern Hemisphere was severely underestimated. The intraseasonal variability was significantly smaller than observed, particularly in the low frequency range, but also at higher frequencies in the storm strack region of the North Atlantic, and the circulation

over Antarctica showed a pathological behaviour. Moreover, part of the model physics was constrained to present-day climate conditions, such as the transfer of heat and water within the soil or the parameterization of CO_2 absorption, so that climate change experiments could not be conducted.

In the second generation model (ECHAM1 and ECHAM2), several parameterization schemes were either replaced (radiation, cloud formation, land surface processes, horizontal diffusion) or additionally implemented (gravity wave drag in ECHAM1), and minor changes were introduced in the numerics (formulation of the pressure gradient term) and in the vertical transport schemes (convection, turbulent diffusion). The ECHAM1 model, coupled to an oceanic GCM, has been predominantly used to study the climatic impact of increasing levels of greenhouse gases in the atmosphere (Cubasch et al., 1992) or soot emission from burning oil wells in Kuwait (Bakan et al., 1991). The ECHAM2 model differs from ECHAM1 basically with respect to a weaker orographic forcing (no gravity wave drag and use of a grid-mean orography instead of an envelope orography)

The third generation model (ECHAM3) which was released in 1991, employs a comprehensive mass flux scheme for cumulus convection (Tiedtke, 1989), instead of the Kuo scheme in the former models, and the effect of clouds on the turbulent mixing in the boundary layer is taken into account.

All of these models use a comparatively high vertical resolution (19 layers, except for ECHAM0 which has only 16). The horizontal resolution is typical of GCMs that have been used so far for long term climate simulations, namely triangular truncation at zonal wavenumber 21 (T21), corresponding to a Gaussian transform grid of approximately 5.6°. The more recent model version (ECHAM3) has been designed primarily for higher resolution such as T42, for example.

All of these models have been integrated in the so-called uncoupled control mode by specifying the sea surface temperatures (SSTs) and sea ice limits according to the observed climatological seasonal cycle so that interannual fluctuations of SST and sea ice have been artificially suppressed. The simulated time is 10-20 years, and the model climates are compared with ECMWF analyses for the time period of 1981-1990.

The sections 2 and 3 provide a fairly detailed description of the dynamics and physics used in ECHAM3. For more information and for technical details, we refer to the model documentation (DKRZ-Report No. 6). Section 4 contains a list of the various model versions that have been used for performing long term control experiments. The sensitivity of the ECHAM model to changes of physical parameterizations and to doubling the horizontal resolution is discussed in section 5, and a summary (section 6) concludes this report.

2. MODEL DYNAMICS

2.1 GOVERNING EQUATIONS AND SOLUTION METHOD

Like the ECMWF numerical weather prediction model, the climate model ECHAM is based on the primitive equations. Prognostic variables are the vorticity ζ and the divergence D, the temperature T, the specific humidity q_v and the logarithm of the surface pressure ln p_s. In addition to the prognostic variables of the ECMWF model, the cloud water mixing ratio q_w (liquid and ice) is also a prognostic variable in ECHAM. Basic equations are the vorticity and the divergence equations,

$$\frac{\partial \xi}{\partial t} = \frac{1}{a(1-\mu^2)}\frac{\partial}{\partial \lambda}(F_V + P_V) - \frac{1}{a}\frac{\partial}{\partial \mu}(F_U + P_U) + K_\xi \tag{2.1.1}$$

$$\frac{\partial D}{\partial t} = \frac{1}{a(1-\mu^2)}\frac{\partial}{\partial \lambda}(F_U + P_U) + \frac{1}{a}\frac{\partial}{\partial \mu}(F_V + P_V) - \nabla^2(\phi + E) + K_D \tag{2.1.2}$$

where

$$F_U = (f+\xi)V - \dot{\eta}\frac{\partial U}{\partial \eta} - \frac{R_d T_v}{a}\frac{\partial}{\partial \lambda} lnp \tag{2.1.3}$$

and

$$F_V = -(f+\xi)U - \dot{\eta}\frac{\partial V}{\partial \eta} - \frac{R_d T_v}{a}(1-\mu^2)\frac{\partial}{\partial \mu} lnp \tag{2.1.4}$$

The remaining equations are the hydrostatic approximation,

$$\frac{\partial \phi}{\partial \eta} = -\frac{R_d T_v}{p}\frac{\partial p}{\partial \eta} \tag{2.1.5}$$

the thermodynamic equation,

$$\frac{\partial T}{\partial t} = -\frac{U}{a(1-\mu^2)}\frac{\partial T}{\partial \lambda} - \frac{V}{a}\frac{\partial T}{\partial \mu} - \dot{\eta}\frac{\partial T}{\partial \eta} + \frac{\kappa T_v \omega}{\left(1 + \left(\frac{c_{pv}}{c_{pd}} - 1\right)q_v\right)p} + P_T + K_T \tag{2.1.6}$$

the continuity equation,

$$\frac{\partial}{\partial t} lnp_s = -\frac{1}{p_s}\int_0^1 \nabla \cdot (v_h \frac{\partial p}{\partial \eta})\, d\eta \tag{2.1.7}$$

the equation for the water vapour mixing ratio

$$\frac{\partial q_v}{\partial t} = -\frac{U}{a(1-\mu^2)}\frac{\partial q_v}{\partial \lambda} - \frac{V}{a}\frac{\partial q_v}{\partial \mu} - \dot{\eta}\frac{\partial q_v}{\partial \eta} + P_{q_v} + K_{q_v} \tag{2.1.8}$$

and finally the equation for the cloud water mixing ratio, $q_w = q_e + q_i$, where q_e is the liquid fraction and q_i is the solid fraction,

$$\frac{\partial q_w}{\partial t} = -\frac{U}{a(1-\mu^2)}\frac{\partial q_w}{\partial \lambda} - \frac{V}{a}\frac{\partial q_w}{\partial \mu} - \dot{\eta}\frac{\partial q_w}{\partial \eta} + P_{q_w} + K_{q_w} \tag{2.1.9}$$

In these equations t is the time, a the radius ot the earth, λ the longitude and $\mu = \sin\varphi$ is the sine of latitude φ. η is the vertical coordinate, which increases monotonically from 0 at the top of the atmosphere to 1 at the bottom of the atmosphere. η will be specified below. f is the Coriolis parameter, R_d the gas constant for dry air. $T_v = T(1 + (R_v/R_d - 1)q_v)$ is the virtual temperature, R_v the gas constant for water vapour. $\phi = gz$ is the geopotential height. $U = u\cos\varphi$, $V = v\cos\varphi$, where u and v indicate the horizontal velocity components in zonal and meridional direction, respectively. $\underset{\sim}{v}_h = (u, v)$ is the horizontal wind vector. $E = (u^2 + v^2)/2(1-\mu^2)$ is the kinetic energy per unit mass. $\kappa = R_d/c_{pd}$, where c_{pd} and c_{pv} is the specific heat at constant pressure of dry air and water vapour, respectively. P_x represents the rate of change of variable x due to parameterized physical processes such as radiation, convection, vertical turbulent mixing, gravity wave drag and phase transition. K_x denotes the influence of unresolved horizontal scales on variable x. The treatment of K_x differs from that of P_x in that it does not involve a physical model of sub-grid scale processes, but rather a numerically convenient form of scale selective diffusion with coefficients determined empirically to ensure a realistic behaviour of the resolved scales (cf, section 2.2).

The pressure coordinate vertical velocity ω is given by

$$\omega = \underset{\sim}{v}_h \nabla p - \int_0^\eta \nabla \cdot (\underset{\sim}{v}_h \frac{\partial p}{\partial \eta})\, d\eta \tag{2.1.10}$$

The horizontal velocity components can be expressed in terms of the stream function ψ and the velocity potential χ:

$$U = \frac{1}{a}\{-(1-\mu^2)\frac{\partial \psi}{\partial \mu} + \frac{\partial \chi}{\partial \lambda}\} \tag{2.1.11}$$

$$V = \frac{1}{a}\{(1-\mu^2)\frac{\partial \chi}{\partial \mu} + \frac{\partial \psi}{\partial \lambda}\} \tag{2.1.12}$$

Vorticity and divergence are then given by

$$\zeta = \nabla^2 \psi \tag{2.1.13}$$

$$D = \nabla^2 \chi \tag{2.1.14}$$

Vertical discretization

Vertically, the model is discretized using 19 levels in a hybrid σ–p-coordinate system. The vertical coordinate η makes a smooth transition from σ-coordinates at the surface to p-coordinates at the top of the atmosphere.

Table 1: Vertical-coordinate parameters of the 19-layer ECHAM model and typical pressures at model levels assuming: P_S = 1013.25 hPa.

k	$A_{k+1/2}\,(Pa)$	$B_{k+1/2}$	$P_{k+1/2}$ [hPa] half levels	P_k [hPa] full levels
0	0.000000	0.0000000000	0	
1	2000.000000	0.0000000000	20	10
2	4000.000000	0.0000000000	40	30
3	6046.110595	0.0003389933	61	51
4	8267.927560	0.0033571866	86	74
5	10609.513232	0.0130700434	119	103
6	12851.100169	0.0340771467	163	141
7	14698.498086	0.0706498323	219	191
8	15861.125180	0.1259166826	286	253
9	16116.236610	0.2011954093	365	326
10	15356.924115	0.2955196487	453	409
11	13621.460403	0.4054091989	545	499
12	11101.561987	0.5249322235	643	594
13	8127.144155	0.6461079479	736	690
14	5125.141747	0.7596983769	821	779
15	2549.969411	0.8564375573	893	857
16	783.195032	0.9287469142	949	921
17	0.000000	0.9729851852	986	968
18	0.000000	0.9922814815	1005	996
19	0.000000	1.0000000000	1013	1009

The prognostic variables ζ, D, T, q_v and q_w are defined at $K = 19$ levels (Table 1). The pressure is defined on the interfaces between the layers (half levels) and is given by

$$p_{k+1/2} = A_{k+1/2} + p_s B_{k+1/2} \qquad (2.1.15)$$

for $k = 0, 1, 2, \ldots K$. The constants $A_{k+1/2}$ and $B_{k+1/2}$ define the vertical coordinates. $A_{k+1/2}$ deter-

mines the contribution of the p-coordinate, $B_{k+1/2}$ the contribution of the σ-coordinate. The values used in ECHAM are given in Table 1 and the vertical distribution of variables is illustrated in Figure 1.

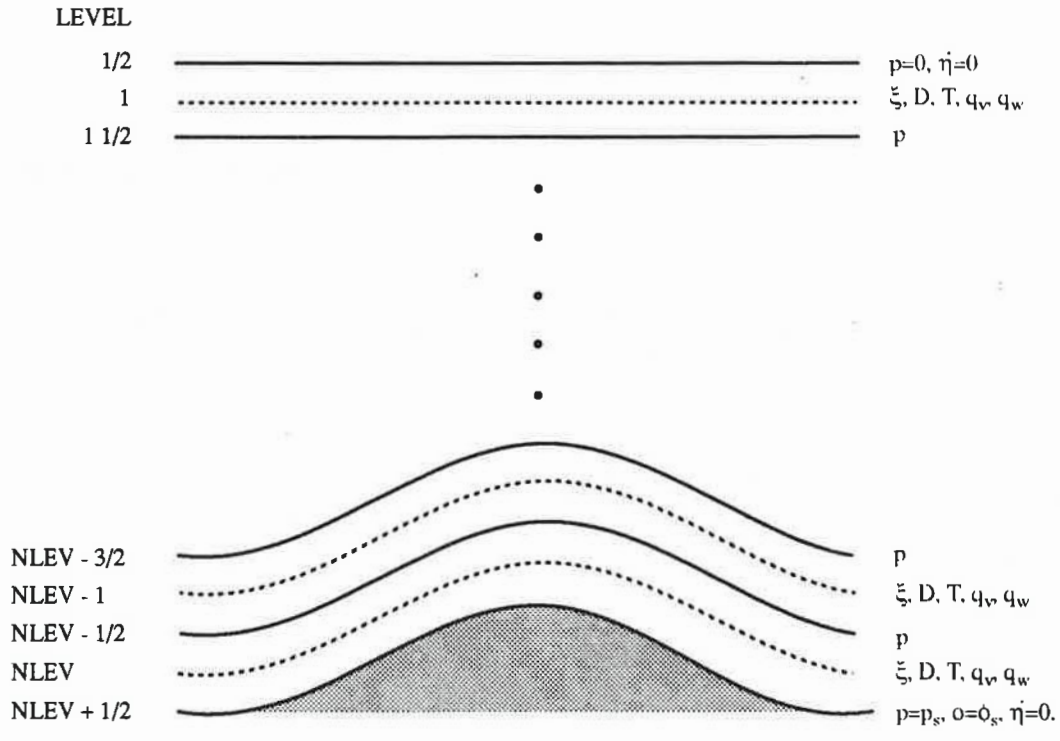

Figure 1 Vertical distribution of variables

The pressure at full levels is defined as

$$p_k = \frac{1}{2}(p_{k+1/2} + p_{k-1/2}) \tag{2.1.16}$$

and η at half levels is given by

$$\eta_{k+1/2} = \frac{A_{k+1/2}}{p_0} + B_{k+1/2} \tag{2.1.17}$$

where p_0 is a reference sea-level pressure of 1013.25 hPa.

Vertical derivatives are approximated by second order finite differences. Provided that all P_x and K_x are zero, energy and mass is conserved.

Horizontal discretization

Horizontally, the model equations are solved using the spectral method. All variables are represented by triangular truncated series of spherical harmonics, i.e. for any variable x we have

$$X(\lambda, \mu, \eta, t) = \sum_{n=0}^{N} \sum_{m=-n}^{n} X_{n,m}(\eta, t) P_n^m(\mu) e^{im\lambda} \tag{2.1.18}$$

For $n = 0, 1, 2, \ldots$, and $m = -n, -n+1, -n+2, \ldots, n$, the $P_n^m(\mu)$ are the associated Legendre polynomials of the first kind,

$$P_n^m(\mu) = \sqrt{(2n+1)\frac{(n-m)!}{(n+m)!}} \frac{1}{2^n n!} (1-\mu^2)^{m/2} \frac{d^{(n+m)}}{d\mu^{(n+m)}} (\mu^2-1), \quad (m \geq 0) \tag{2.1.19}$$

and

$$P_n^{-m}(\mu) = P_n^m(\mu) \qquad (m < 0) \tag{2.1.20}$$

The normalization of $P_n^m(\mu)$ is such that

$$\frac{1}{2} \int_{-1}^{1} P_n^m(\mu) P_{n'}^m(\mu) d\mu = \delta_{nn'} \tag{2.1.21}$$

where $\delta_{nn'}$ is the Kronecker delta.

While horizontal derivatives on a sphere are calculated in the spectral domain rather efficiently, if the spectral method is used, the calculation of non-linear terms is rather complicated as it involves convolutions. That is even more the case for certain terms in the parameterization of physical processes. Thus, the transform method (Eliasen et al., 1970; Orszag, 1970) is applied. At each time step the variables are transformed to an almost regular latitude-longitude grid ($\Delta\varphi \approx \Delta\lambda \approx 5.6°$ for T21, $\approx 2.8°$ for T42). In the meridional direction the gridpoints are 32 and 64 Gaussian latitudes, i.e. the zeros of the Legendre polynomials $P_{32}(\mu)$ and $P_{64}(\mu)$, respectively. In the zonal direction 64, and 128, resp., equidistant longitudes are used.

Non-linear terms are calculated in the physical domain on the Gaussian grid. Then the spectral tendencies are calculated by an inverse transformation into the spectral domain. Here, a semi-implicit time stepping scheme with a time step of 40 minutes (T21) and 24 minutes (T42), resp., is applied. In order to avoid a decoupling of the two time levels of the time stepping scheme, the prognostic variables are smoothed by a weak time filter (Asselin, 1972).

In versions 2 and 3 of ECHAM a mean orography is used: the orographic height of each grid point is calculated as the spatial mean of the real orography of the grid box under consideration. The resulting height distribution is spectrally truncated at T21 (T42) in order to form the model orography, which explicitly enters the basic equations via the geopotential height of surface, and implicitly in several phy-

sical parameterizations. In ECHAM1, however, an envelope orography is applied, which is defined as the sum of the mean orography plus the sub-grid scale standard deviation. The land-sea distribution is shown in Figure 2 together with the mean orography for T21 resolution (upper panel) and for T42 resolution (lower panel).

Figure 2 Land-sea mask and spectrally adapted mean orography at T21 (upper panel) and T42 (lower panel) horizontal resolution. Contour spacing is .5, 1., 2., 3... km.

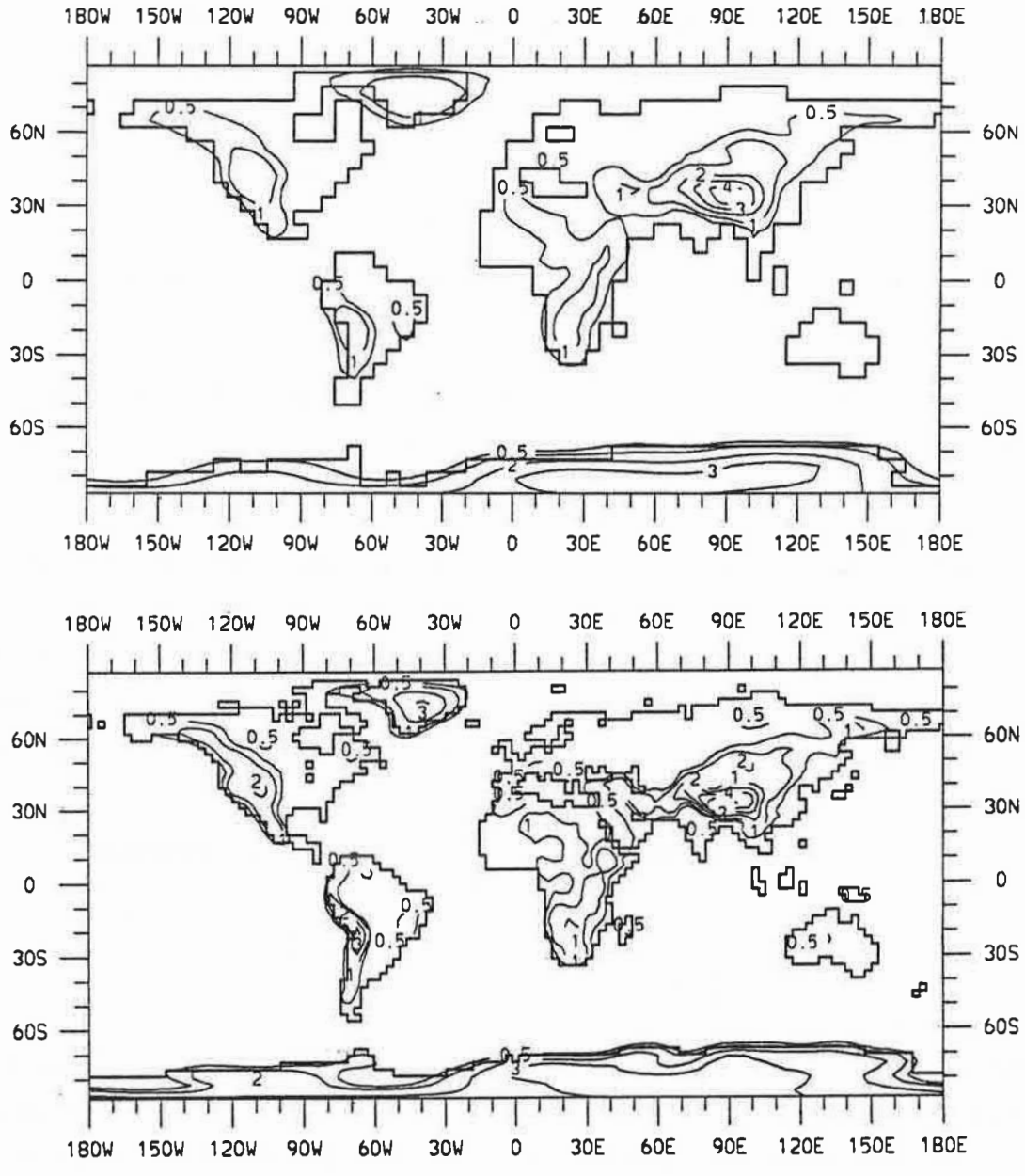

2.2 HORIZONTAL DIFFUSION

While the original ECMWF model uses a ∇^4 horizontal diffusion, ECHAM uses a diffusion parameterization based on the ideas of Laursen and Eliasen (1989). The contribution to the spectral tendency of any prognostic variable X is

$$-k_X \, L_n \, X_n^m \tag{2.2.1}$$

With this term, calculated at the new time $t + \Delta t$, the diffusive contribution to the semi-implicit time stepping scheme is

$$X_n^m(t+\Delta t) \; = \; X_n^m(t-\Delta t) \cdot \{1 + 2\Delta t \; k_X \; L_n\}^{-1} \tag{2.2.2}$$

L_n is chosen such that large scales are not damped, while short waves can be damped selectively,

$$L_n \; = \; \begin{cases} (n - n_*)^{\alpha} & \text{for} \quad (n > n_*) \\ 0 & \text{for} \quad (n \le n_*) \end{cases} \tag{2.2.3}$$

with $\alpha = 2$ for T21, and $\alpha = 4$ for T42 truncation. For both resolutions, we chose a cut-off wave number $n_* = 15$, i.e. only modes with $n \ge 16$ are damped.

The diffusion coefficient k_X varies for different variables and levels. While the lower levels (6 to 19) use the same k_X, the upper levels are stronger damped,

$$k_X(l) \; = \; k_X \cdot fac(l) \tag{2.2.4}$$

where l denotes the vertical level. For $fac = 1$ and T21 resolution (ECHAM2, ECHAM3) the damping time $1/(k_X \cdot L_n)$ of the shortest scale is 1.12 days for the vorticity, 0.22 days for the divergence and 5.59 days for temperature, humidity and cloud water, respectively. For T42 resolution the respective times are 0.30, 0.06 and 0.76 days. Table 2 shows the amplification factor for the six uppermost levels and Figure 3 shows the damping times of the vorticity due to the horizontal diffusion as a function of the total wave number n and level l.

Table 2: Amplification factor of the horizontal diffusion

l	1	2	3	4	5	6
fac	16	16	8	4	2	1

A modified diffusion scheme is used for the temperature to avoid unrealistic warming of mountain tops and excessive summer precipitation associated with substantial mixing in the vicinity of steep mountain slopes. Only the deviation of the temperature field from the ICAO standard atmosphere is inserted into the diffusion procedure.

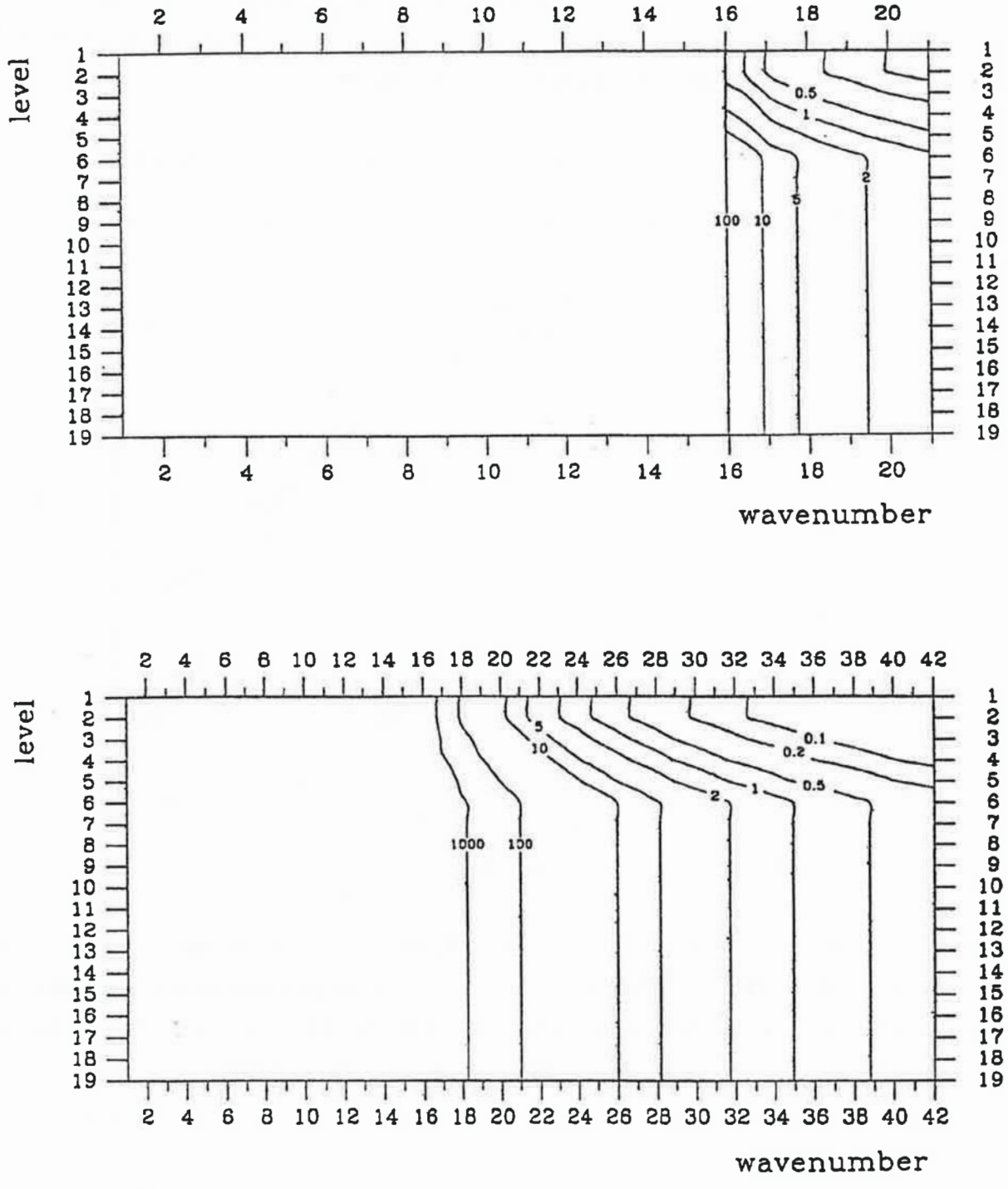

Figure 3 Damping times for the vorticity due to horizontal diffusion for T21 (upper panel) and T42 (lower panel) horizontal resolution. Contours for 0.1, 0.2, 0.5, 1, 2, 5, 10, 100, 1000 days.

The diffusion coefficients were chosen such that the slope of the spectral kinetic energy is close to observations (see Figure 4). Moreover, as a result of the new diffusion scheme together with a time step of 40 (24) minutes for T21 (T42) resolution, the need for additional damping to avoid violation of the CFL-criterion is considerably reduced as compared to the ECMWF model.

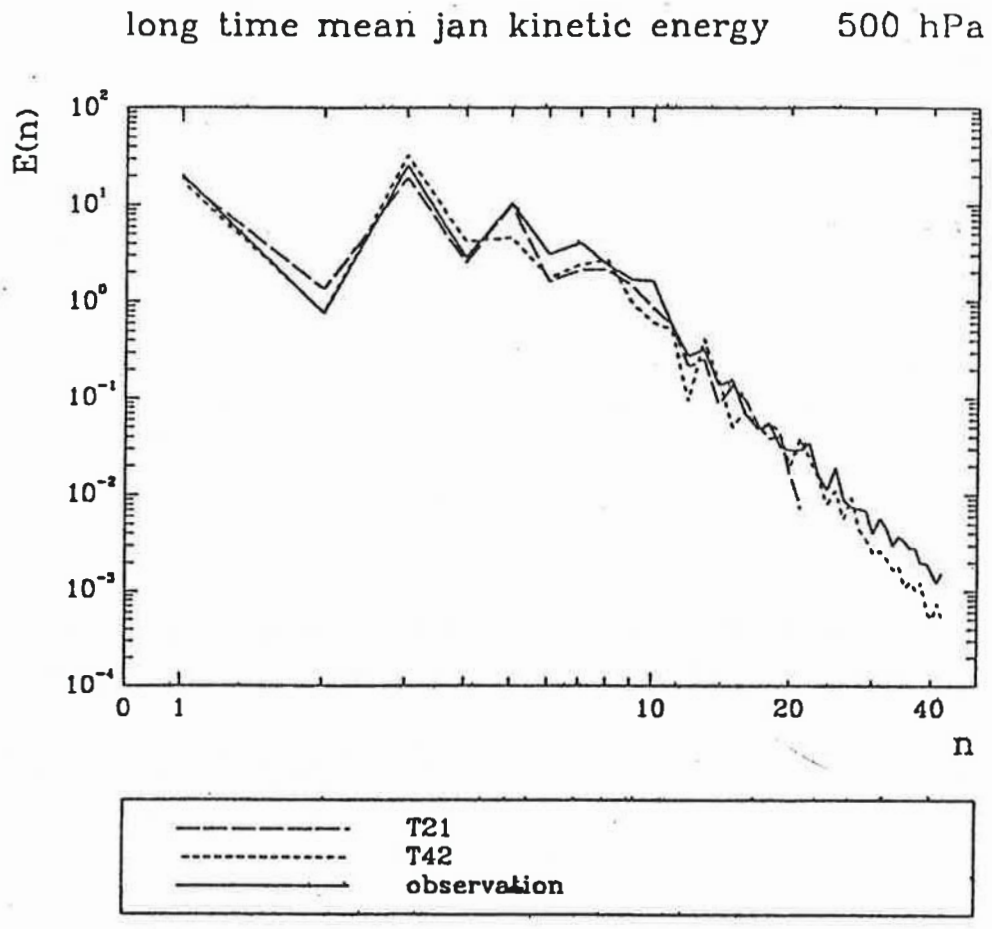

Figure 4 Mean kinetic energy spectra at 500 hPa during January for observations (ECMWF, mean of 1980 - 1989), for ECHAM2/T21 (mean of a 20 year control run with prescribed climatological sea surface temperature) and for ECHAM3/T42 (mean of a 10 year simulation with the observed sea surface temperatures of the years 1979 - 1988).

3. MODEL PHYSICS

The model physics is formulated in a simplified parametric form, either because the respective process cannot be resolved explicitly (e.g., turbulent transfer, cumulus convection or cloud microphysics), or because a more accurate treatment would exceed the computer resources presently available (e.g., the computation of radiative transfer).

The radiation scheme (section 3.1) uses a broad-band formulation of the radiative transfer equations with six spectral intervals in the terrestrial infrared and four intervals in the solar part of the spectrum (Hense et al., 1982; Rockel et al., 1991). Gaseous absorption due to water vapour, carbon dioxide and ozone is taken into account as well as scattering and absorption due to aerosols and clouds. The cloud optical properties are parameterized in terms of the cloud water content which is a prognostic variable of the model.

The vertical turbulent transfer of momentum, heat, water vapour and cloud water (section 3.2) is based upon the Monin-Obukhov similarity theory for the surface layer and the eddy diffusivity approach above the surface layer (Louis, 1979). The drag and heat transfer coefficients depend on roughness length and Richardson number, and the eddy diffusion coefficients depend on wind shear, mixing length and Richardson number which has been reformulated in terms of cloud-conservative variables (Brinkop, 1991, 1992)

The effect of orographically excited gravity waves on the momentum budget (section 3.3) is parameterized on the basis of linear theory and dimensional considerations (Palmer et al., 1986; Miller et al., 1989). The vertical structure of the momentum flux induced by gravity waves in stably stratified flow over irregular terrain is calculated from a local Richardson number which describes the onset of turbulence due to convective instability and the breakdown approaching a critical level.

The cumulus convection scheme (section 3.4) comprises the effect of deep, shallow and mid-level convection on the budget of heat, water vapour and momentum (Tiedtke, 1989). Cumulus clouds are represented by a bulk model including the effect of entrainment and detrainment on the updraft and downdraft convective mass fluxes. Mixing due to stratocumulus convection is parameterized as a vertical diffusion process (Tiedtke et al., 1988) with eddy diffusion coefficients depending on the cloud water content, cloud fraction and relative humidity jump at cloud top.

The prediction of stratiform clouds (section 3.5) is based upon the cloud water equation (cf., section 2.1) including sources and sinks due to condensation/evaporation and precipitation formation by coalescence of cloud droplets and sedimentation of ice crystals (Sundqvist, 1978; Roeckner et al., 1991). Sub-grid scale condensation and cloud formation is taken into account by specifying appropriate thresholds of relative humidity depending on height and static stability.

The soil model (section 3.6) comprises the budgets of heat and water in the soil, the snow pack over land and the heat budget of permanent land ice and sea ice (Dümenil and Todini, 1992). The heat transfer equation is solved in a five-layer model assuming vanishing heat flux at the bottom. Vegetation effects such as interception of rain and snow in the canopy and stomatal control of evapotranspiration are para-

meterized in a highly idealized way (Blondin, 1989). The runoff scheme is based on catchment considerations and takes into account sub-grid scale variations of field capacity over inhomogeneous terrain.

3.1 RADIATION

The radiative transfer model is based on a two-stream approximation described by Kerschgens et al. (1978) and Zdunkowski et al. (1980). From the radiative transfer equations for the solar part of the spectrum, eqs. (3.1.1) and (3.1.2), and for the terrestrial part, eqs. (3.1.3) and (3.1.4), Hense et al. (1982) derived a broad-band formulation with spectral intervals listed in Table 3.

$$\frac{\partial}{\partial\delta}M^{+} = [1-\tilde{\omega}(1-\beta)]\frac{M^{+}}{\bar{\mu}} - \tilde{\omega}\beta\frac{M^{-}}{\delta} - \beta_0\tilde{\omega}S_0 e^{-\delta/\mu_0} \tag{3.1.1}$$

$$\frac{\partial}{\partial\delta}M^{-} = \tilde{\omega}\beta\frac{M^{+}}{\delta} - [1-\tilde{\omega}(1-\beta)]\frac{M^{-}}{\bar{\mu}} + (1-\beta_0)\tilde{\omega}S_0 e^{-\delta/\mu_0} \tag{3.1.2}$$

$$\frac{d}{d\delta}M^{+} = \frac{1}{\bar{\mu}}(M^{+}-B) \tag{3.1.3}$$

$$\frac{d}{d\delta}M^{-} = \frac{1}{\bar{\mu}}(M^{-}-B) \tag{3.1.4}$$

where M^{+} and M^{-} are the upward and downward flux densities, δ is the optical depth, $\tilde{\omega}$ is the single scattering albedo, β and β_0 are the backscattering parameters for diffuse and direct radiation respectively, $1/\bar{\mu}$ is the diffusivity factor (2 for solar and 1.66 for terrestrial radiation), S_0 is the solar irradiance, μ_0 is the cosine of the solar zenith angle, and B is the Planck function.

Table 3 Spectral intervals and absorbers of the radiative transfer model

Terrestrial		Solar	
Spectral Interval(μm)	Absorber	Spectral Interval(μm)	Absorber
3.96 - 7.98	H_2O	0.215 - 0.685	O_3
7.98 - 8.89	H_2O, dimer	0.685 - 0.891	H_2O
8.89 - 10.15	O_3, dimer	0.891 - 1.273	H_2O
10.15 - 11.76	H_2O, dimer	1.273 - 3.580	H_2O, CO_2
11.76 - 20.10	H_2O, CO_2		
20.10 - 100.	H_2O		

The parameterization of the optical parameters in a cloud-free atmosphere is taken from Hense et al. (1982) for the solar spectrum and from Eickerling (1989) for the terrestrial spectrum. In the terrestrial part scattering is neglected.

Terrestrial radiation

The optical depth δ is defined as

$$\delta = \exp \sum_{j=0}^{n} a_j (\log u_i)^j \tag{3.1.5}$$

with the effective absorber mass u_i of the ith component,

$$u_i = \rho_i \left(\frac{p}{p_0}\right)^{\alpha_p} \left(\frac{T_0}{T}\right)^{\alpha_T} d \tag{3.1.6}$$

where a_j, α_p, α_T are coefficients derived by inverting the results of an "exact" reference radiation model, ρ_i, p and T denote concentration of the ith component, pressure and temperature, respectively, averaged over an atmospheric layer with geometrical thickness d, p_0 and T_0 are reference values set to 1013 hPa and 273.15 ^{o} K, respectively.

With these definitions and assuming that the Planck function is a linear function of δ, the radiative transfer equations can be solved as described by Hense et al. (1982).

Solar radiation

For the transfer of solar radiation, absorption (subscript a) and multiple scattering (subscript s) are taken into account. The relevant parameters are the optical thickness δ, the single scattering albedo $\tilde{\omega}$ and the backscattering coefficients β, β_0. The backscattering coefficients β and β_0 are derived from theory (Kerschgens et al., 1978). Scattering and absorption coefficients of stratospheric, urban and maritime aerosols are taken from a data set provided by Shettle and Fenn (1975). Multiplication by d gives the appropriate optical thicknesses $\delta_a^{aerosol}$, $\delta_s^{aerosol}$.

The optical thickness δ_a^{gas} for gas absorption is a function of the effective absorber amount and is defined similarly to the terrestrial radiation (see above). The optical thickness δ_s^{gas} for Rayleigh scattering of gas molecules is given by

$$\delta_s^{gas} = \bar{N} \cdot A_R \cdot d \tag{3.1.7}$$

where $\bar{N}$ is the mean number density and A_R is the scattering cross-section of molecules.

For diffuse radiation, the optical thickness δ^{dif} is calculated from

$$\delta^{dif} = a_a (\delta_a^{gas} + \delta_a^{aerosol})^{b_a} + a_s (\delta_s^{gas} + \delta_s^{aerosol})^{b_s} \tag{3.1.8}$$

where a_a, b_a, a_s and b_s are coefficients derived by inverting results of an "exact" reference model.

The single scattering albedo is defined as

$$\tilde{\omega} = 1 - \frac{\delta_a^{dif}}{\delta_s^{dif}} \tag{3.1.9}$$

For direct radiation, the optical thickness δ^{dir} at a level k is calculated by adding the optical thicknesses above this level

$$\delta^{dir} = \sum_{j=1}^{k} (\delta_{a_j}^{gas} + \delta_{a_j}^{aerosol} + \delta_{s_j}^{gas} + \delta_{s_j}^{aerosol}) \tag{3.1.10}$$

where δ_a^{gas} depends on the zenith angle θ. δ_a^{gas} is parameterized for $\theta = 35^{\circ}$ and $\theta = 75^{\circ}$ only. Optical thicknesses for other zenith angles are calculated by linear interpolation.

Cloud optical properties

The emissivity ε of clouds in the terrestrial region is described by

$$\varepsilon = 1 - e^{-\left[\frac{k \cdot m \cdot d}{\bar{\mu}}\right]} \tag{3.1.11}$$

where $k = 0.084\ m^2 g^{-1}$ is the mass absorption coefficient (Stephens, 1978), d is the geometrical cloud thickness and m is the water or ice content in gm^{-3}.

Optical thickness δ, single scattering albedo $\tilde{\omega}$, and back-scattering coefficient β are the optical parameters considered in transfer of solar radiation. For both cloud phases, the parameterization of Stephens (1978) is adopted:

$$\log(\delta) = \begin{cases} 0.2633 + 1.7095 \cdot ln[\log(m \cdot d)] & (\lambda < 0.685\ \mu m) \\ 0.3492 + 1.6518 \cdot ln[\log(m \cdot d)] & \text{otherwise} \end{cases} \tag{3.1.12}$$

Single scattering albedo and back-scattering coefficients are taken from Kerschgens et al. (1978).

Surface albedo

Over snow-free land areas an annual mean background albedo is specified from satellite data (Geleyn and Preuss, 1983). According to more recent analyses (e.g., Dorman and Sellers, 1989) the satellite-based estimates are too low in the tropics and at middle latitudes (North America, Eurasia). This bias has been removed by applying an empirical correction in those areas where the satellite data suggests values of less than 15 %. The minimum values thus obtained are around 12 % for tropical rain forests.

In snow-covered areas the surface albedo is modified according to

$$\alpha_{Surf} = \alpha_{Sb} + (\alpha_S - \alpha_{Sb}) \cdot \frac{Sn}{Sn + Sn^*} \tag{3.1.13}$$

where α_S is the snow albedo (see below), α_{Sb} is the background albedo, Sn is the simulated snow depth (in water equivalent) and $Sn^* = 0.01$ m is a critical snow depth. For $Sn \gg Sn^*$ the surface albedo

approaches the albedo of snow.

The albedo of snow and ice surfaces (α_S) is a function of surface type (t_S), surface temperature (T_S) and fractional forest area (a_f) over land. For $T_S \geq T_m = 273.15$ K (i.e., for melting of snow or ice), α_S is fixed at a relatively small value, $\alpha_S = \alpha_{Smin}(t_S, a_f)$, whereas α_S is larger, $\alpha_S = \alpha_{Smax}(t_S, a_f)$, for cold surfaces ($T_S \leq T_0 = 263.15$ K) according to Robock (1980). Over land, the respective snow albedos are assumed to depend on the fractional forest area ($0 \leq a_f \leq 1$) according to

$$\begin{aligned} \alpha_{Smin}(a_f) &= a_f \cdot \alpha_{Smin}(a_f = 1) + (1 - a_f) \cdot \alpha_{Smin}(a_f = 0) \\ \alpha_{Smax}(a_f) &= a_f \cdot \alpha_{Smax}(a_f = 1) + (1 - a_f) \cdot \alpha_{Smax}(a_f = 0) \end{aligned} \tag{3.1.14}$$

In the temperature range $T_0 < T_S < T_m$, $\alpha_S = \alpha_S(T_S, t_S, a_f)$ is obtained by linear interpolation

$$\alpha_S = \alpha_{Smax} - (\alpha_{Smax} - \alpha_{Smin}) \cdot \frac{T_S - T_0}{T_m - T_0} \tag{3.1.15}$$

with α_{Smax} and α_{Smin} as specified in Table 4 according to the estimate of Robock (1980) for sea ice and snow (without the solar zenith angle correction, however) and according to Kukla and Robinson (1980) for land ice.

Over sea, the albedo is constant (0.065) for diffuse radiation but depends on the solar zenith angle θ for the direct beam

$$\alpha_{S0} = \frac{0.05}{\cos\theta + 0.15} \tag{3.1.16}$$

with the limitation $\alpha_{S0} \leq 0.15$.

Table 4 Minimum and maximum surface albedos (Robock, 1980; Kukla and Robinson, 1980) referring to the temperature ranges $T_S \geq T_m = 273.15$ K and $T_S \leq T_0 = 263.15$ K respectively. The fractional forest area (a_f) is taken from a data set compiled by Matthews (1983).

surface type		α_{Smin}	α_{Smax}
sea ice		0.5	0.75
land ice		0.6	0.8
snow on land	for $a_f = 0$	0.4	0.8
	for $a_f = 1$	0.3	0.4

3.2 VERTICAL DIFFUSION

Basic equations

The parameterization scheme represents the turbulent exchanges of heat, momentum, moisture and cloud water at the surface and the turbulent transports of the same quantities in the lowest levels of the model. The top of the turbulent layer is computed using a combination of convective and dynamic criteria. Above this boundary layer the scheme only operates when the air is statically unstable. The equation for the vertical diffusion of any conservative quantity X is:

$$\frac{\partial X}{\partial t} = \frac{1}{\rho}\frac{\partial}{\partial z}(\rho K_X \frac{\partial X}{\partial z}) = \frac{1}{\rho}\frac{\partial J_X}{\partial z} \tag{3.2.1}$$

K_X is the exchange coefficient and J_X (positive downwards) is the vertical turbulent flux of X. The following boundary conditions have been assumed:

$$K_X \frac{\partial X}{\partial z} = 0 \qquad \text{for} \quad p = p_T \tag{3.2.2.a}$$

and

$$K_X \frac{\partial X}{\partial z} \rightarrow C_X |\underline{v}_h(z)| (X(z) - X_S) \quad \text{for} \quad (z \rightarrow 0) \tag{3.2.2.b}$$

where p_T is the pressure at the top of the boundary layer and $\underline{v}_h = (u, v)$ is the horizontal windvector. The definition of the drag coefficient C_X depends on the height z above the ground at which $\underline{v}_h$ and X are taken (the natural choice is the model's lowest level) and on the stability of the layer. X_S represents a value of X at the surface.

X may be identified with each of the five variables u, v, q_v, q_w and s (dry static energy). s is defined as:

$$s = C_{pd}(1 + (C_{pv}/C_{pd} - 1)\, q_v) \cdot T + g \cdot z = C_p \cdot T + \phi \tag{3.2.3}$$

The coefficients K_X and C_X are assumed to be the same for u, v, q_v, q_w and s. Using m and h as subscripts for momentum and heat, the problem is reduced to the determination of K_m and K_h (at all atmospheric layers) and C_m and C_h at the surface. This has to be done solely from atmospheric values (at $t - \Delta t$) of u, v, T, q_v, q_w and from the surface conditions.

Surface fluxes

The surface fluxes for momentum, dry static energy and cloud water are parameterized as follows:

$$
\begin{aligned}
J_u &= \rho \cdot C_m \cdot |\underline{v}_h| \cdot u \\
J_v &= \rho \cdot C_m \cdot |\underline{v}_h| \cdot v \\
J_s &= \rho \cdot C_h \cdot |\underline{v}_h| \cdot (s - s_S) \\
J_{q_w} &= \rho \cdot C_h \cdot |\underline{v}_h| \cdot (q_w - q_{wS})
\end{aligned}
\tag{3.2.4}
$$

where C_m is the drag coefficient, C_h the transfer coefficient for heat and $|\underline{v}_h|$ the absolute value of the horizontal velocity. C_m, C_h and $|\underline{v}_h|$ apply to the lowest model level at $t - \Delta t$. u, v and s are the velocity components and the dry static energy to be computed implicitly for the lowest model level. s_S is the dry static energy at the surface at $t - \Delta t$, and q_{wS} is the cloud water content at the surface (set to zero).

The moisture flux is evaluated distinguishing sea and land. Over sea

$$
J_{q_v} = \rho \cdot C_h \cdot |\underline{v}_h| \cdot \{ q_v - q_s(T_S, p_S) \}
\tag{3.2.5}
$$

where q_s is the saturation specific humidity at surface temperature T_S and pressure p_S.

Over land, each grid square is divided into 4 fractions:

1. fraction C_{Sn} covered with snow
2. fraction $(1 - C_{Sn}) \cdot C_l$ covered with water in skin reservoir
3. fraction $(1 - C_{Sn}) \cdot (1 - C_l) \cdot (1 - C_v)$ covered with bare soil
4. fraction $(1 - C_{Sn}) \cdot (1 - C_l) \cdot C_v$ covered with vegetation

The snow cover fraction C_{Sn} depends on the snow cover Sn :

$$
C_{Sn} = min\,(1, \frac{Sn}{Sn_{cr}})
\tag{3.2.6}
$$

where Sn_{cr} is the critical snow cover (= 0.015 m equivalent water depth).

The wet skin fraction C_l is derived from the skin reservoir water content:

$$
C_l = min\left(1, \frac{W_l}{W_{lmx}}\right)
\tag{3.2.7}
$$

with

$$
W_{lmx} = W_{lmax}\,[\,(1 - C_v) + C_v \cdot L_t]
\tag{3.2.8}
$$

W_l is the prognostic variable for the skin reservoir content, W_{lmx} is the maximum skin reservoir content, C_v is the vegetation ratio, L_t is the leaf area index, and W_{lmax} is the maximum amount of water that can be held on one layer of leaf or bare ground. It is taken to be $2. \cdot 10^{-4}$ m.

The grid fraction C_v occupied by vegetation is equal to the climatological field C_{vcl} except in dry conditions when the vegetation is reduced according to the following empirical expression:

$$C_v = min\left(C_{vcl}, C_{vcl} \cdot \frac{W_S}{0.4 \cdot W_{Smax}}\right) \tag{3.2.9}$$

The quantity W_S represents the total amount of water available in the root zone and W_{Smax} is the field capacity (0.2 m).

Evaporation from snow and the skin reservoir is at the potential rate

$$J_{q_v}(i),\ (ii)\ = \rho \cdot C_h \cdot |\underline{v}_h| \cdot \{q_v - q_s(T_S, p_S)\} \tag{3.2.10}$$

For the evaporation from bare soil (no water in skin reservoir) it is assumed that the relative humidity h at the surface is related to the water content W_S of the soil layer:

$$J_{q_v}(iii)\ = \rho \cdot C_h \cdot |\underline{v}_h| \cdot \{q_v - h \cdot q_s(T_S, p_S) \tag{3.2.11}$$

$$h = max\left[0.5 \cdot \left(1 - \cos\frac{\pi \cdot W_S}{W_{Smax}}\right), min\left(1, \frac{q_v}{q_s(T_S, p_S)}\right)\right. \tag{3.2.12}$$

The evaporation from dry (no water in skin reservoir) vegetated areas is proportional to the evaporation efficiency E:

$$J_{q_v}(iv)\ = \rho \cdot C_h \cdot |\underline{v}_h| \cdot E \cdot \{q_v - q_s(T_S, p_S)\} \tag{3.2.13}$$

Based on Sellers et al. (1986), E is expressed as:

$$E = \left[1 + \frac{C_h \cdot |\underline{v}_h| \cdot R_{co}(PAR)}{F(W_S)}\right]^{-1} \tag{3.2.14}$$

where $R_{co}/F(W_S)$ is the stomatal resistance of the canopy, with a minimum value R_{co} dependent on the **P**hotosynthetically **A**ctive **R**adiation (PAR), and an empirical function of the available water in the root zone $F(W_S)$.

$$\frac{1}{R_{co}} = \frac{1}{k \cdot c}\left[\frac{b}{d \cdot PAR} \cdot ln\left(\frac{d \cdot e^{k \cdot L_t} + 1}{d + 1}\right) - ln\left(\frac{d + e^{k \cdot L_t}}{d + 1}\right)\right. \tag{3.2.15}$$

where

$$d = \frac{a + b \cdot c}{c \cdot PAR},\ k = 0.9,\ L_t = 4,\ a = 5000\ Jm^{-3},\ b = 10\ Wm^{-2},\ c = 100\ sm^{-1}$$

and PAR is 55 % of the net short wave radiation at the surface. In case of dew deposition ($q_v > q_s$) we set

$$E = h = 1 \tag{3.2.16}$$

The water stress factor $F(W_S)$ is

$$F(W_S) = \begin{cases} 1 & \text{if} \quad (W_S \geq W_{cr}) \\ \dfrac{W_S - W_{pwp}}{W_{cr} - W_{pwp}} & \text{if} \quad (W_{pwp} < W_S < W_{cr}) \\ 0 & \text{if} \quad (W_S \leq W_{pwp}) \end{cases} \tag{3.2.17}$$

W_{cr} is a critical value taken as 50% of the field capacity W_{Smax}, while W_{pwp} is the permanent wilting point taken as 20% of W_{Smax}.

The total evaporation in a grid square combines the four fractions:

$$\begin{aligned} J_{q_v} = \rho \cdot C_h \cdot |\underline{v}_h| \cdot [& \{C_{Sn} + (1 - C_{Sn}) \cdot C_l\} \cdot \{q_v - q_s\} \\ & + (1 - C_{Sn}) \cdot (1 - C_l) \cdot (1 - C_v) \cdot \{q_v - h \cdot q_s\} \\ & + (1 - C_{Sn}) \cdot (1 - C_l) \cdot C_v \cdot E \cdot \{q_v - q_s\} \ ] \end{aligned} \tag{3.2.18}$$

Definition of the drag coefficients

The method has been described by Louis (1979) and updated subsequently in Louis et al. (1982). Only the main points are mentioned here.

Starting from the Monin-Obukhov similarity theory (using dry air for simplicity), the gradients of wind (u) and internal energy ($s = c_p \cdot T + g \cdot z$) are assumed to be universal functions of a stability parameter.

$$\frac{k\ z}{u_*} \cdot \frac{\partial u}{\partial z} = \phi_m(z/L) \tag{3.2.19.a}$$

$$\frac{k\ z}{s_*} \cdot \frac{\partial s}{\partial z} = \phi_h(z/L) \tag{3.2.19.b}$$

The stability parameter L is the Obukhov length:

$$L = \frac{s \cdot u_*^2}{k \cdot g \cdot s_*} \tag{3.2.20.a}$$

where k is von Karman's constant and u_* and s_* are scaling parameters derived from the fluxes:

$$\rho \cdot u_*^2 = (J_u)_{z \to 0} = \rho \cdot C_m \cdot |u|^2 \tag{3.2.20.b}$$

$$\rho \cdot u_* \cdot s_* = (J_s)_{z \to 0} = \rho \cdot C_h \cdot |u| \cdot (s - s_S) \tag{3.2.20.c}$$

Equations (3.2.19.a) and (3.2.19.b) can be integrated over the lowest model layer, and L eliminated using (3.2.20.a) in order to derive C_m and C_h. However, such expression cannot be obtained analytically because of the complicated form of ϕ_m and ϕ_h. C_m and C_h are approximated by following analy-

tical expressions (Louis, 1979):

$$C_m = \left(\frac{k}{ln\ (z/z_0)}\right)^2 \cdot f_m(Ri, z/z_0) \tag{3.2.21.a}$$

and

$$C_h = \left(\frac{k}{ln\ (z/z_0)}\right)^2 \cdot f_h(Ri, z/z_0) \tag{3.2.21.b}$$

here the Richardson number Ri is defined as:

$$Ri = \frac{g \cdot \Delta z \cdot \Delta s}{C_p \cdot T \cdot |\Delta u|^2} \tag{3.2.22}$$

The empirical functions f_m and f_h must have the correct behaviour near neutrality and in the asymptotic cases of high stability or instability.

a) Near neutrality one obtains $Ri \to 0, z/L \to 0, \phi_m = 1 + b_m \cdot z/L$ and $\phi_h = 1 + b_h \cdot z/L$.

We obtain then

$$\begin{aligned} f_m &\cong 1 - 2 \cdot b_m \cdot Ri \\ f_h &\cong 1 - (b_m + b_h) \cdot Ri \end{aligned} \tag{3.2.23}$$

Furthermore , there is some evidence (Pandolfo ,1967), that $Ri \sim z/L$ which implies $b_h = 2 \cdot b_m$. Thus we have

$$f_m = 1 - 2 \cdot b \cdot Ri \quad \text{and} \quad f_h = 1 - 3 \cdot b \cdot Ri \tag{3.2.24}$$

In ECHAM b = 5.

b) In highly unstable cases only the problem of f_h in the case of vanishing u (free convection case) has been considered. To have a non-zero heat flux, u must vanish from $(u \cdot f_h)$ for large negative $(s - s_s)$ (that is for high negative value of Ri). So f_h must behave like $\sqrt{-Ri}$.

The analytical expression chosen for the whole unstable case $(Ri < 0)$ is:

$$f_h = 1 - \frac{3 \cdot b \cdot Ri}{1 + C_h(z/z_0) \cdot \sqrt{-Ri}} \tag{3.2.25}$$

For this free convection case one can write an equation for a new similarity theory, independent of J_u,

$$\frac{z}{s_*} \cdot \frac{\partial s}{\partial z} = C \tag{3.2.26}$$

with

$$s_* = \frac{(J_s/\rho)^{2-1/3}}{(g \cdot z)/s}$$

Using Eq. (3.2.21) for the limit $Ri \to \infty$,

$$C_h(z/z_0) = C \cdot 3 \cdot b \left[\frac{k}{ln(z/z_0)}\right]^2 [(z/z_0)^{1/3} - 1]^{3/2} \tag{3.2.27}$$

One can furthermore replace $[(z/z_0)^{1/3} - 1]^{3/2}$ by $\sqrt{(z/z_0)}$ if z is much greater than z_0, so that

$$C_h(z/z_0) = C \cdot 3 \cdot b \left[\frac{k}{ln(z/z_0)}\right]^2 \sqrt{(z/z_0)} \tag{3.2.28}$$

In order to avoid numerical problems for high z_0 values that might suppress z one replaces (z/z_0) by $(z/z_0) + 1$ in (3.2.21) and (3.2.27), (3.2.28).

In ECHAM $C = 5$.

In the highly unstable case f_m is not very important since there is little wind shear on which to act. Therefore a similar expression to (3.2.21) has been chosen with the same denominator to save computing time

$$f_m = 1 - \frac{2 \cdot b \cdot Ri}{1 + 3 \cdot b \cdot C \left[\frac{k}{ln(z/z_0 + 1)}\right]^2 \sqrt{(z/z_0 + 1)\,(-Ri)}} \tag{3.2.29}$$

c) Finally in the highly stable case we follow Ellison (1957) by combining two equations

$$\phi_m^4 - \frac{z}{L}\phi_m^3 - 1 = 0 \quad \text{KEYPS equation} \tag{3.2.30}$$

and

$$\frac{\phi_m}{\phi_h} = \frac{1 - (\frac{z}{L})/\phi_m/R_{crit}}{(1 - [(\frac{z}{L})/\phi_m])^2} \tag{3.2.31}$$

The flux Richardson number $Ri_f = \frac{z}{L}/\phi_m$ has its critical value R_{crit} for $(Ri \to \infty)$.

For $\frac{z}{L} \to +\infty$ this gives

$$f_m \sim 1/(\sqrt{\mathrm{Ri}}) \text{ and } f_h \sim 1/(Ri^{3/2}) \tag{3.2.32}$$

For lack of better information and to minimise the computing time for the whole stable range $(Ri > 0)$ the following expressions have been chosen

$$f_m = \frac{1}{1 + (2 \cdot b \cdot Ri) / (\sqrt{1 + d \cdot Ri})} \tag{3.2.33}$$

$$f_h = \frac{1}{1 + (3 \cdot b \cdot Ri) \cdot (\sqrt{1 + d \cdot Ri})} \tag{3.2.34}$$

d is related to the critical flux Richardson number R_{crit} by

$$R_{crit} = \frac{2}{3 \cdot d} \tag{3.2.35}$$

In ECHAM $d = 5$.

Definition of the exchange coefficients

The logical extension of the similarity theory for surface fluxes to the atmosphere is the mixing length approach.

$$K_m = l_m^2 \cdot \left| \frac{\partial \underline{v}_h}{\partial z} \right| \cdot f_m(Ri) \tag{3.2.36}$$

$$K_h = l_h^2 \cdot \left| \frac{\partial \underline{v}_h}{\partial z} \right| \cdot f_h(Ri) \tag{3.2.37}$$

The functional dependencies of f_m and f_h on Ri are the same as for C_m and C_h except that the term

$$\left[\frac{k}{ln(z/z_0)} \right]^2 \left[(z/z_0)^{1/3} - 1 \right]^{3/2}$$

in (3.2.27) is replaced by its equivalent

$$\frac{l^2}{(\Delta z)^{3/2} \cdot z^{1/2}} \left[\left(\frac{z + \Delta z}{z} \right)^{1/3} - 1 \right]^{3/2} \tag{3.2.38}$$

The intensity of the vertical diffusion in the atmosphere is dependent on the choice of l_h and l_m. Here, the solution of Blackadar (1962) is used, that goes smoothly from the asymptotic value $k \cdot z$ for $z \to 0$ to a constant value in the high atmosphere:

$$\frac{1}{l_m} = \frac{1}{k \cdot z} + \frac{1}{\lambda_m}, \quad \frac{1}{l_h} = \frac{1}{k \cdot z} + \frac{1}{\lambda_h} \tag{3.2.39}$$

One also has to have a relationship between λ_m, λ_h and d so that the critical flux Richardson number in the atmosphere is 1 (e.g. a balance between shear generation and buoyancy destruction).

$$R_{crit}(z \to \infty) = \frac{2}{3d} \cdot \left(\frac{\lambda_h}{\lambda_m} \right) = 1 \tag{3.2.40}$$

gives $\lambda_h = \lambda_m \sqrt{(3 \cdot d)/2}$.

In ECHAM $\lambda_m = 160$ m.

Moisture and cloud effects

In the ECMWF model and also in ECHAM1 and ECHAM2, moisture effects on stability have been included by replacing the temperature T in the definition in the Richardson number (3.2.22) by the virtual temperature T_v since it is T_v that determines the buoyancy in moist (but cloud-free) air. In ECHAM cloud effects are considered by reformulating the Richardson number to include the impact of cloud processes on the buoyancy term (Brinkop, 1992). This so-called moist Richardson number can be written according to

$$Ri_m = \frac{g}{\Theta_v} \cdot \frac{A \cdot \Delta\Theta_l + \Theta \cdot B \cdot \Delta q_t}{(\Delta u)^2 + (\Delta v)^2} \cdot \Delta z \tag{3.2.41}$$

where $q_t = q_l + q_i + q_v$ is the total water content, Θ_v is the virtual potential temperature, $\Theta_l = \Theta - (\Theta \cdot L \cdot q_l / T \cdot C_{pd})$ is the liquid water potential temperature which is a conservative quantity in the absence of freezing, precipitation and radiative effects (Betts, 1973), and Θ is the potential temperature.

The parameters A and B are defined as follows:

Unsaturated case

$$A_{unsat} = 1 + 0.61 \cdot q_t \tag{3.2.42}$$

$$B_{unsat} = 0.61 \tag{3.2.43}$$

Saturated case

$$A_{sat} = 1 + 0.61 \cdot q_t - \frac{0.622 \cdot \frac{L}{R_d \cdot T} \cdot q_s}{1 + 0.622 \cdot \frac{L^2}{R_d \cdot C_{pd} \cdot T^2}} \cdot \left(\frac{L}{C_{pd} \cdot T} (1 + 0.61 \cdot q_t) \right) \tag{3.2.44}$$

$$B_{sat} = \frac{L}{C_{pd} \cdot T} - 1 \tag{3.2.45}$$

The coefficients A and B in (3.2.41) are assumed to depend linearly on cloud cover b:

$$A = b \cdot A_{sat} + (1 - b) \cdot A_{unsat} \tag{3.2.46}$$

$$B = b \cdot B_{sat} + (1 - b) \cdot B_{unsat} \tag{3.2.47}$$

In the clear-sky case ($b = 0$ and $q_t = q_v$) Ri_m as defined by (3.2.41) is identical to the more familiar form used in the ECMWF model, for example.

Definition of the top of the boundary layer

Two levels are computed.

a) First level above the dynamical height (Ekman layer height).

$$h_{dyn} = 0.5 \cdot (u_*/f)$$

Equatorwards of 20 ° f is set to $5 \cdot 10^{-5} s^{-1}$.

b) A dry convective level, h_{cnv}, is defined as the lowest level for which the static stability s exceeds the respective value in the lowest model level.

The top of the planetary boundary layer is then given by

$$h_{pbl} = max\,(h_{dyn}, h_{cnv}) \tag{3.2.48}$$

The above formulation takes into account early morning cases (where the dry convective boundary layer starts to develop), where considering $h_{cnv} = h_{dyn}$ would give too strong a vertical constraint for the turbulent diffusion. p_t is then calculated as the pressure of the first model level above h_{pbl}.

Roughness length

Over land the roughness length z_0 is geographically prescribed. Over ice-free sea z_0 is calculated from the Charnock (1955) formula:

$$z_0 = C_{char} \cdot \frac{u_*^2}{g} \tag{3.2.49}$$

with a minimum value for z_0 of $1.5 \cdot 10^{-5} m$. In ECHAM the Charnock constant C_{char} is set to 0.018 for T21 resolution and to 0.032 for higher resolutions. Over sea ice a constant value of $z_0 = 0.001$ m is used.

In unstable conditions over sea an empirical interpolation for heat and moisture is used between the free convection limit and the neutral approximation (Miller et al., 1992):

$$C_h = C_{mn} \cdot (1 + C_R^{\gamma})^{1/\gamma} \tag{3.2.50}$$

where

$$C_R = \frac{0.0016 \cdot (\Delta\Theta_v)^{1/3}}{C_{mn} \cdot |v_h|}$$

$$C_{mn} = \left(\frac{k}{ln\,(z/z_0)}\right)^2$$

and $\gamma = 1.25$.

In stable situations the same formulation is used as over land, with z_0 according to (3.2.49).

Vertical diffusion at higher levels

Above the planetary boundary layer the vertical diffusion scheme only operates when the air is statically unstable.

3.3 GRAVITY WAVE DRAG

The parameterization scheme represents the momentum transports due to sub-grid scale gravity waves excited by stably stratified flow over irregular terrain (Miller et al., 1989). The scheme is a modified form of that proposed by Boer et al. (1984) and by Palmer et al. (1986) in which a low-level wave stress is defined together with criteria for the reduction in stress with height as the vertically propagating waves are absorbed and/or reflected.

The influence of these wave stresses in regions of wave momentum flux divergence is as follows:

$$\left(\frac{\partial \underset{\sim}{v}_h}{\partial t}\right)_{\text{gravity waves}} = -g\left(\frac{\partial \underset{\sim}{\tau}}{\partial p}\right)_{\text{gravity waves}}$$

where $\underset{\sim}{v}_h$ is the horizontal wind vector, and $\underset{\sim}{\tau}$ is the wave stress.

The formulation of the scheme consists of two parts

(i) The parametric form for $\underset{\sim}{\tau}(x, y, t)$

(ii) The modelling of the dynamical processes which determine the vertical distribution.

(i) The following quantities are defined for use in the scheme:

$\underset{\sim}{V}_L$ is the wind vector for a suitably defined low-level flow and ρ_L, N_L are the low-level density and the Brunt-Väisälä frequency respectively. The function $f_1(\underset{\sim}{x})$ describes the orographic forcing of gravity waves and in the scheme described here $f_1(\underset{\sim}{x})$ is prescribed to be a directionally dependent sub-grid scale orographic variance computed from the US Navy dataset containing mean orographic heights for (1/6 ^{o} lat * 1/6 ^{o} lon) areas. Fr is a form of Froude number for the low-level flow defined as

$$Fr = \frac{N_L \sqrt{f_1(\underset{\sim}{x})}}{|\underset{\sim}{V}_L|}$$

where $\underset{\sim}{V}_L$ represents a low-level wind vector averaged over the lowest three levels of the model.

$f_2(\underset{\sim}{x})$ is an orographic anisotropy function measuring the two-dimensionality of the sub-grid scale orography

$$f_2(\underset{\sim}{x}) = 1 - e^{(1-\alpha)}, \text{ and } \alpha = max(\alpha_1, \alpha_2) \qquad (3.3.1)$$

where α_1 and α_2 are computed from the sub-grid scale variances of the four directional components (N/S, E/W, NE/SW, NW/SE)

$$\alpha_1^2 = max\left(\frac{var(N/S)}{var(E/W)}, \frac{var(E/W)}{var(N/S)}\right)$$
$$\alpha_2^2 = max\left(\frac{var(NE/SW)}{var(NW/SE)}, \frac{var(NW/SE)}{var(NE/SW)}\right) \qquad (3.3.2)$$

z_c is the atmospheric depth corresponding to three-quarters of a hydrostatic vertical gravity wavelength and is computed by the solution of the equation

$$\int_0^{z_c} \frac{N(z)}{U(z)} dz = \frac{3\pi}{2} \qquad (3.3.3)$$

The scheme can then be written as $\underset{\sim}{\tau}_{gw}(p) = \underset{\sim}{\tau}_w(p) + \underset{\sim}{\tau}_{Fr}(p)$.

The first term $\underset{\sim}{\tau}_w(p)$ describes a part of the low-level drag and the upper part, dependent on the pressure p

$$\underset{\sim}{\tau}_w(p) = \begin{cases} \underset{\sim}{\tau}_w(p_S) \cdot (1-\beta) \cdot \dfrac{p-p'}{p_S-p'} & \text{for} \quad (p \geq p') \\ \beta \cdot \underset{\sim}{\tau}_w(p_S) \cdot f(p) & \text{for} \quad (p < p') \end{cases} \qquad (3.3.4)$$

where $f(p)$ describes the vertical stress profile, computed as shown in (ii) below.

The choice of p' determines the depth for this part of the low-level drag and is currently chosen as $p' = 0.8 \cdot p_S$, and β controls the ratio of low to high-level drag (currently equal to 0.3).

$\underset{\sim}{\tau}_w(p_S)$ is determined by

$$\underset{\sim}{\tau}_w(p_S) = K \cdot \underset{\sim}{V}_L \cdot N_L \cdot var^* \quad , \text{ where } var^* = min\left(var, (Fr_c \cdot \underset{\sim}{V}_L / N_L)^2\right)$$

and Fr_c is the critical value for the low-level Froude number (currently equal to 2).

Analytical results of an isolated bell-shaped mountain give a value for $K = \pi/(16 \cdot a)$ where a is the mountain half-width. Hence $K \sim 2.5 \cdot 10^{-5} m^{-1}$ for typical sub-grid scale orography.

The second term $\underset{\sim}{\tau}_{Fr}(p)$ describes the additional drag which occurs when the low-level flow is supercritical and the dynamical mechanism of resonant trapping of waves occurs leading to high-drag situations (see, for example, Peltier and Clark, 1986). It takes the form

$$\underset{\sim}{\tau}_{Fr}(p) = \underset{\sim}{\tau}_{Fr}(p_S) \cdot \frac{p-p_{z_c}}{p_S-p_{z_c}} \quad \text{if} \quad (Fr > Fr_c) \qquad (3.3.5)$$

where

$$\underset{\sim}{\tau}_{Fr}(p_S) = \begin{cases} K_L \cdot \rho \cdot \dfrac{\underset{\sim}{V}_L^3}{N_L} \cdot (Fr - Fr_c)^2 \cdot f_2(\underset{\sim}{x}) & \text{if} \quad (Fr > Fr_c) \\ 0 & \text{otherwise} \end{cases}$$

p_{z_c} is the pressure corresponding to the height z_c and K_L is currently 4 K. Typical values of z_c are around 3 to 5 km but much larger values do occur.

(ii) The vertical structure of $\underset{\sim}{\tau}_{gw}$ is calculated by constructing a local wave Richardson number which attempts to describe the onset of turbulence due to the gravity waves becoming convectively unstable or encountering critical layers.

This wave Richardson number can be written in the form $\tilde{R} = \bar{R} \cdot (1-\alpha) / (1+\alpha \cdot \bar{R}^{1/2})^2$ where $\bar{R}$ is the Richardson number of the basic flow. The parameter $\alpha = N \cdot \delta z / u$ is a form of inverse Froude number in which $|\delta z|$ represents the amplitude of the wave and u is the wind speed resolved in the direction of $\underset{\sim}{\tau}_{gw}$.

By requiring that $\tilde{R}$ never falls below a critical value $\tilde{R}_{crit}$ (currently equal to 0.25), values of wave stress are defined progressively from the surface upwards.

3.4 CUMULUS CONVECTION

Cumulus convection is parameterized by a mass flux scheme which is described in detail (including numerical aspects) in Tiedtke (1989). The scheme considers penetrative convection, shallow convection and mid-level convection. Clouds are represented by a bulk model and include updraft and downdraft mass fluxes. Momentum transport by convective circulations is also included following the proposal by Schneider and Lindzen (1976).

Large-scale budget equations

The contributions from cumulus convection to the large-scale budget equations of heat, moisture and momentum are:

$$\begin{aligned}
\left(\frac{\partial \bar{s}}{\partial t}\right)_{cu} &= -\frac{1}{\bar{\rho}}\frac{\partial}{\partial z}\left[M_u s_u + M_d s_d - (M_u + M_d)\,\bar{s}\right] \\
&\quad + L\,(c_u - e_d - \tilde{e}_l - \tilde{e}_p) - (L_s - L_v)\,m \\
\left(\frac{\partial \bar{q}_v}{\partial t}\right)_{cu} &= -\frac{1}{\bar{\rho}}\frac{\partial}{\partial z}\left[M_u q_u + M_d q_d - (M_u + M_d)\,\bar{q}_v\right] \\
&\quad + (c_u - e_d - \tilde{e}_l - \tilde{e}_p) \qquad (3.4.1) \\
\left(\frac{\partial \bar{u}}{\partial t}\right)_{cu} &= -\frac{1}{\bar{\rho}}\frac{\partial}{\partial z}\left[M_u u_u + M_d u_d - (M_u + M_d)\,\bar{u}\right] \\
\left(\frac{\partial \bar{v}}{\partial t}\right)_{cu} &= -\frac{1}{\bar{\rho}}\frac{\partial}{\partial z}\left[M_u v_u + M_d v_d - (M_u + M_d)\,\bar{v}\right]
\end{aligned}$$

where M_u, M_d, c_u and e_d are the net contributions from all clouds to the upward mass flux, downward mass flux, condensation/sublimation and evaporation respectively, and s_u, s_d, q_u, q_d, u_u, u_d, v_u and v_d are the weighted averages of s, q_v, u and v from all updrafts and downdrafts. Here $\tilde{e}_l$ is the evaporation of cloud water that has been detrained into the environment, $\tilde{e}_p$ is the evaporation of precipitation in the unsaturated subcloud layer and m is the melting of snow. In addition to (3.4.1) we consider the equations for precipitation

$$\begin{aligned} P^w(z) &= \int (G_P^w - e_d^w - \tilde{e}_P^w + m)\,\bar{\rho}dz \\ P^l(z) &= \int (G_P^l - e_d^l - \tilde{e}_P^l + m)\,\bar{\rho}dz \end{aligned} \tag{3.4.2}$$

where $P^w(z)$, $P^l(z)$ are the fluxes of rain water and snow at height z and G_P^w and G_P^l are the conversion rates from cloud ice and cloud water into precipitation, respectively.

Cloud model equations

The updraft of the cloud ensemble is assumed to be in a steady state. Then the bulk equations for mass, heat, moisture, cloud water content and momentum are

$$\begin{aligned} \frac{\partial M_u}{\partial z} &= E_u - D_u \\ \frac{\partial}{\partial z}(M_u s_u) &= E_u \bar{s} - D_u s_u + L\bar{\rho}c_u \\ \frac{\partial}{\partial z}(M_u q_u) &= E_u \bar{q}_v - D_u q_u - \bar{\rho}c_u \\ \frac{\partial}{\partial z}(M_u l) &= D_u l + \bar{\rho}c_u - \bar{\rho}G_P \\ \frac{\partial}{\partial z}(M_u u_u) &= E_u \bar{u} - D_u u_u \\ \frac{\partial}{\partial z}(M_u v_u) &= E_u \bar{v} - D_u v_u \end{aligned} \tag{3.4.3}$$

where E and D are the rates of mass entrainment and detrainment per unit length, l is the cloud water content (water/ice) and c_u is the net condensation/sublimation in the updrafts.

Cloud air is assumed to be saturated and cloud processes are crudely represented. Freezing and melting processes are not considered and the conversion from cloud droplets to rain/snow is assumed to be proportional to the cloud water content as

$$\bar{\rho}G_P = K(z) \cdot l \cdot M_u$$

where $K(z)$ is an empirical function that varies with height. This simple parameterization yields rather reasonable vertical distributions of the generation of raindrops (Yanai et al., 1973). Here K is assumed to be zero near cloud base and constant at higher levels

$$K(z) = \begin{cases} 0, & \text{if } (z \le Z_B + \Delta z) \\ 2 \cdot 10^{-3} m^{-1}, & \text{if } (z > Z_B + \Delta z) \end{cases} \tag{3.4.4}$$

where Δz is 1500 m over sea and 3000 m over land. The choice of $K = 0$ at lower levels ensures that shallow cumuli do not produce precipitation, noting that a sizeable portion of the liquid water content in nonprecipitating cumuli is of precipitation-sized drops.

We further note that the cloud water detrained into the environmental air is assumed to evaporate there instantaneously. Then

$$\bar{e}_l = \frac{1}{\bar{\rho}} \cdot D_u \cdot l \tag{3.4.5}$$

The vertical integration of (3.4.3) requires the knowledge of cloud base mass flux and mass entrainment and detrainment. Cloud-base mass flux is determined for the various types of convection from the parameterization assumptions discussed below. Entrainment of mass into convective plumes is assumed to occur through turbulent exchange of mass through the cloud edges and through organized inflow associated with large-scale convergence, detrainment through turbulent exchange and as organized outflow at the top:

$$E_u = E_u^{(1)} + E_u^{(2)}, \qquad D_u = D_u^{(1)} + D_u^{(2)} \tag{3.4.6}$$

Turbulent entrainment and detrainment are parameterized as

$$E_u^{(1)} = \varepsilon_u M_u, \qquad D_u^{(1)} = \delta_u M_u \tag{3.4.7}$$

where the fractional entrainment/detrainment rates depend inversely on cloud radii (Simpson and Wiggert, 1969; Simpson, 1971):

$$\varepsilon_u = \frac{0.2}{R_u}, \qquad \delta_u = \frac{0.2}{R_u} \tag{3.4.8}$$

By assuming typical cloud sizes for the various types of convection, average values of entrainment/ detrainment rates are defined. In the presence of synoptic scale flow convergence, large clouds which contribute most to the convective heating and moistening are assumed to exist and consequently small values for entrainment/detrainment rates are imposed whereas in the absence of flow convergence clouds of smaller sizes with larger entrainment rates prevail. In order to keep the scheme simple we use fixed values of turbulent entrainment/detrainment rates for each of the various types of convection:

$$\varepsilon_u = \delta_u = \begin{cases} 1 \times 10^{-4} m^{-1} & \text{for penetrative and midlevel convection in the presence of large-scale flow convergence} \\ 3 \times 10^{-4} m^{-1} & \text{for shallow convection in suppressed conditions} \end{cases} \tag{3.4.9}$$

For penetrative convection and midlevel convection we deliberately impose a very small value typical

for tropical deep convective clouds (Simpson, 1971) so as not to inhibit the penetration of clouds to large heights. For shallow convection we use a value typical for the larger trade wind cumuli (Nitta, 1975), noting that small clouds with much larger entrainment/detrainment rates which detrain immediately above cloud base are not represented in our parameterization.

The parameterization of organized entrainment and detrainment is discussed below.

Below cloud base, the net convective fluxes of heat and moisture due to updraft and compensating subsidence in the environment are assumed to decrease linearly from their values at cloud base towards zero at the surface so as not to alter the vertical structure of the subcloud layer and in particular its well-mixed character.

Downdrafts are considered to be associated with convective precipitation from the updrafts and originate from cloud air influenced by the injection of environmental air. Following Fritsch and Chappell (1980) and Foster (1958), the Level of Free Sinking (LFS) is assumed to be the highest model level where a mixture of equal parts of cloud air and saturated environmental air at wet-bulb temperature becomes negatively buoyant with respect to the environmental air. The downward mass flux is assumed to be directly proportional to the upward mass flux. Following Johnson (1976, 1980) the mass flux at the LFS is specified from the updraft mass flux at cloud base as

$$(M_d)_{LFS} = \gamma (M_u)_{base} \quad \text{with} \quad \gamma = -0.3 \tag{3.4.10}$$

The coefficient γ is a disposable parameter.

The vertical distribution of the downdraft mass flux, dry static energy and moisture below the LFS is determined by the equations for mass, dry static energy and moisture content as

$$\begin{aligned}
-\frac{\partial M_d}{\partial z} &= E_d - D_d \\
-\frac{\partial}{\partial z}(M_d s_d) &= E_d \bar{s} - D_d s_d + L\bar{\rho} e_d \\
-\frac{\partial}{\partial z}(M_d q_d) &= E_d \bar{q}_v - D_d q_d + \bar{\rho} e_d \\
-\frac{\partial}{\partial z}(M_d u_d) &= E_d \bar{u} - D_d u_d \\
-\frac{\partial}{\partial z}(M_d v_d) &= E_d \bar{v} - D_d v_d
\end{aligned} \tag{3.4.11}$$

We note that cumulus downdrafts can be viewed as the reverse of updrafts. Entrainment and detrainment in downdrafts are highly uncertain as relevant data are not available. Numerical experiments show, however, that the results are rather insensitive to changes in the entrainment and detrainment rates. We use

$$\varepsilon_d = \delta_d = 2 \times 10^{-4} m^{-1} \tag{3.4.12}$$

This gives a mass flux which is independent of height and which effectively detrains into the environment in the subcloud layer. We also note that e_d is the evaporation of convective rain to maintain a saturated descent and that the moistening and cooling of the environmental air injected at LFS is also due to evaporating rain. As the downdrafts are determined from the updrafts the remaining parameterization task is to specify the updraft. This is done by means of closures defined below for the various types of convection.

a. Penetrative convection

Many diagnostic studies show that penetrative convection predominantly occurs in disturbed situations and strongly depends on low-level synoptic scale convergence. Various parameterization schemes are based on this relationship one way or another. Here, we apply a moisture convergence hypothesis: Following Kuo (1965, 1974) and Lindzen (1981), we postulate that when there is a deep layer of conditional instability and large-scale moisture convergence, cumulus clouds exist that entrain environmental air through their base and through their sides directly proportional to the supply of moisture and detrain cloud air at higher levels.

The injection of mass into the clouds through their base is determined by imposing a moisture balance for the subcloud layer such that the moisture content is maintained in the presence of large-scale transports, turbulent transports and convective transports. This balance may be written as

$$[M_u(q_u-\bar{q}_v)+M_d(q_d-\bar{q}_v)]_B = \int_o^B \left[\bar{v}_h\cdot\nabla\bar{q}_v+\bar{w}\frac{\partial\bar{q}_v}{\partial z}+\frac{1}{\bar{\rho}}\frac{\partial(\bar{\rho}\overline{w'q'_v})_{tu}}{\partial z}\right]\rho dz \qquad (3.4.13)$$

where B denotes the cloud base height defined as the condensation level for surface air. The vertical distribution of the updraft mass flux above cloud base is determined using similar arguments as for the subcloud layer, that is, we postulate that there is organized entrainment which is directly proportional to the large-scale moisture convergence as

$$E_u^{(2)} = -\frac{\bar{\rho}}{\bar{q}_v}\left[\bar{v}_h\cdot\nabla\bar{q}_v+\bar{w}\frac{\partial\bar{q}_v}{\partial z}\right] \qquad (3.4.14)$$

Organized entrainment is only considered in the lower part of the cloud layer where large-scale convergence is encountered, that is, below the level of strongest vertical ascent. The idea to link the cloud mass flux directly to the large-scale moisture convergence has first been advocated by Lindzen (1981) who indicated that it may provide vertical profiles of mass flux and convective heating in good agreement with observations. The assumption (3.4.14) ensures that the vertical distribution of the convective mass flux follows that of the large-scale ascent which is partly supported by diagnostic studies for tropical convection (e.g. Cheng et al., 1980; Johnson, 1980). Equation (3.4.14) forms, together with the assumption (3.4.13) for the cloud base mass flux, the basic closure and as such is crucial for the performance of the parameterization of penetrative convection. The verification of the scheme during long periods of tropi-

cal convection confirms that the closure provides realistic profiles of convective mass fluxes and convective heating (see Tiedtke, 1989).

In addition to organized entrainment we consider turbulent entrainment and detrainment by equations (3.4.7) and (3.4.8).

Cumulus clouds detrain effectively at levels near to their zero-buoyancy level by means of organized outflow. Therefore, the vertical distribution of the total detrainment from all clouds depends on the spectral cloud distribution. Since spectral cloud distribution is not available, however. organized outflow is assumed to occur only in the model layer which contains the zero-buoyancy level of the deepest clouds. Our detrainment assumption implies an unimodal cloud distribution with large detrainment from the deepest clouds and little detrainment from shallow clouds and medium deep clouds.

The effect from shallow cumuli in the presence of penetrative convection has been neglected because their parameterization is still an unsolved problem. This is because the role of shallow cumuli in connection with penetrative convection is not well understood, particularly when cumulus downdraft occur simultaneously as these compete with shallow convection having similar effects on the environment as shallow cumuli (Johnson, 1976). The results obtained with this scheme indicate, however, that neglecting the contributions from shallow cumuli when penetrative convection is encountered does not introduce large errors in the convective heating and drying.

b. Shallow convection

Here we consider cumulus convection, which predominantly occurs in undisturbed flow, that is in the absence of large-scale convergent flow. Typical examples are trade wind cumuli under a subsidence inversion, convection occurring in the ridge region of tropical easterly waves and daytime convection over land. This type of convection seems to be effectively controlled by subcloud layer turbulence. In fact, most of the diagnostic studies carried out for tradewind cumuli show that the net upward moisture flux at cloud base level is nearly equal to the turbulent moisture flux at the surface (Le Mone and Pennell, 1976). As this implies a quasi-steady moisture balance, we shall apply the same moisture budget equation (3.4.13) as for penetrative convection. The difference, however, is that the moisture supply to cumulus clouds is now largely through surface evaporation as the contributions from large-scale convergence are either small or even negative, such as in the undisturbed trades where dry air is transported downward to lower levels.

Under typical tradewind conditions the vertical distribution of the total convective fluxes above cloud base is dominated by two types of clouds: very small cumuli, which in large numbers detrain immediately above cloud base, and deeper clouds, which detrain just beneath and above the trade inversion. The intrusion of cumulus clouds into the stable layer above the inversion is through overshooting of cumuli above their level of zero-buoyancy (Nitta, 1975). Because of the coarse resolution employed in large-scale models, where the vertical gridlength is typically 50 to 100 hPa, it is difficult to represent these two types. The scheme presented here ignores the effects of very small cumuli

but tentatively accounts for the effects of overshooting cumuli, as we assume that a given fraction of the cloud ensemble penetrates into the inversion layer and detrains there into the environment. Thus, cloud air shall only partly detrain into the environment within the model layer that contains the zero-buoyancy level; the remaining fraction shall intrude into the next layer above and detrain there:

$$D_u^{(2)} = \frac{(1-\beta)\,(M_u)_{k+1/2}}{\Delta z} \qquad \text{for top layer } k$$
$$D_u^{(2)} = \frac{\beta\,(M_u)_{k+1/2}}{\Delta z} \qquad \text{for layer } k-1 \tag{3.4.15}$$

where β is a tunable parameter (currently 0.15)

Although this parameterization is very crude, it clearly reproduces more realistic trade inversions than when the effect from overshooting cumuli is ignored ($\beta = 0$), as then the inversion becomes too strong in the simulation and the cloud layer below the inversion too moist (see Tiedtke, 1989).

c. Midlevel convection

Midlevel convection, that is, convective cells which have their origin not in the boundary layer but start at levels above the boundary layer, often occur at rainbands at warm fronts and in the warm sector of tropical cyclones (Browning et al., 1973; Houze et al., 1976; Herzegh and Hobbs, 1980). These cells are probably formed by the lifting of low level air until it becomes saturated (Wexler and Atlas, 1959) and the primary moisture source for the clouds is from low-level large-scale convergence (Houze et al., 1976). Often a low-level temperature inversion exists that inhibits convection from starting freely from the surface; therefore convection seems to be initiated by lifting low-level air dynamically to the level of free convection. This occurs often in connection with mesoscale circulations which might be related to conditionally symmetric instability (Bennetts and Hoskins, 1979; Bennets and Sharp, 1982) or a wave-CISK mechanism (Emanuel, 1982).

Although it is not clear how significant the organization of convection in mesoscale rainbands is for the large-scale flow a parameterization should ideally account for both convective and mesoscale circulations. Such a parameterization, however, is presently not available and we must therefore rely on simplified schemes. Here we use a parameterization which in a simple way considers the finding of the diagnostic studies mentioned above. We assume that convection is activated when there is a large-scale ascent at lower levels, the environmental air is sufficiently moist, i.e., of relative humidity in excess of 90 %, and convectively unstable layer exists above. The free convection level is determined by lifting a parcel of environmental temperature and moisture content

$$T_u = \bar{T}\,, \qquad q_u = \bar{q}_v \tag{3.4.16}$$

adiabatically, allowing for condensational heating, and then checking for buoyancy. The upward mass flux is set equal to the vertical mass transport by the large-scale flow at that level:

$$(M_u)_B = \bar{\rho}_B \bar{w}_B \tag{3.4.17}$$

which ensures that the amount of moisture which is vertically advected through cloud base by the large-scale ascent is fully available for the generation of convective cells.

In addition to the injection of mass through cloud base, we assume again that cloud air is produced by moisture convergence above cloud base through lateral entrainment in the same way as for penetrative convection given by equation (3.4.14).

Evaporation of rain and melting of snow

Melting of snow is parameterized as stratiform precipitation (see section 3.5)

The evaporation of convective rain is parameterized following a proposal of Kessler (1969), where the evaporation is assumed to be proportional to the saturation deficit $q_s - q_v$ and to be dependent on the density of rain $M_R\,(g/m^3)$

$$E = \alpha_1 \cdot (q_s - q_v) \cdot M_R^{13/20} \tag{3.4.18}$$

where α_1 is a constant being zero for $q_v > q_s$.

As the density of rain M_R is not given by the model it is convenient to express it in terms of the rain intensity R [g / (m^2 sec)] as

$$R = M_R\,(V_0 + w) \cong M_R \cdot V_0 \tag{3.4.19}$$

where V_0 is the mean fall speed of rain drops which again is parameterized following Kessler (1969).

$$V_0 = \frac{\alpha_2 \cdot M_R^{1/8}}{\sqrt{p/p_s}} \tag{3.4.20}$$

Thus we have

$$E = \alpha_1 \cdot (q_s - q_v) \left[\left(\frac{\sqrt{p/p_s}}{\alpha_2} \cdot R \right)^{13/20} \right]^{8/9} \tag{3.4.21}$$

Since the convective rain takes place only over a fraction C_c of the grid area the evaporation rate at level k becomes

$$E = C_c \cdot \alpha_1 \cdot (q_s - q_v) \left[\left(\frac{\sqrt{p/p_S}}{\alpha_2} \cdot \frac{R}{C_c} \right) \right]^{\alpha_3} \tag{3.4.22}$$

where the constants have the following values (Kessler, 1969)

$$\alpha_1 = 5.44 \cdot 10^{-4}, \quad \alpha_2 = 5.09 \cdot 10^{-3}, \quad \alpha_3 = 0.5777$$

In order to save computing time (with $\alpha_3 = 1/2$) we use slightly different values

$$\alpha_1 = 6.94 \cdot 10^{-4}, \quad \alpha_2 = 7.35 \cdot 10^{-3}, \quad \alpha_3 = 0.5$$

In view of the uncertainty of the fractional area of precipitating clouds a constant value of

$$C_c = 0.05$$

is assumed.

The evaporation rate is calculated implicitly in the model by means of

$$2g \frac{\partial}{\partial p} R^{1/2} = -A \tag{3.4.23}$$

which follows from

$$E = A \cdot R^{1/2} \qquad A = \alpha_1 (q_s - q_v) \left(\frac{\sqrt{p/p_S}}{\alpha_2} \cdot \frac{1}{C_c} \right)^{1/2} \tag{3.4.24}$$

and

$$E = \frac{1}{\rho} \cdot \frac{\partial R}{\partial z} = -g \cdot \frac{\partial R}{\partial p} \tag{3.4.25}$$

Stratocumulus

Stratocumulus convection is parameterized by means of a vertical diffusion scheme (Tiedtke et al., 1988). It is only applied in the boundary layer where it provides a net upward transport of moisture and cloud water to avoid the generation of saturated layers within a convective boundary layer.

The net effect of stratocumulus convection is given by the turbulent fluxes of heat, moisture and cloud water, which are parameterized on the basis of the eddy diffusion theory (cf., section 3.2):

$$\left(\frac{\partial s}{\partial t}\right)_{Sc} = \frac{1}{\rho} \cdot \frac{\partial}{\partial z} \left(\rho \cdot K \cdot \frac{\partial s}{\partial z}\right) \tag{3.4.26}$$

$$\left(\frac{\partial q_v}{\partial t}\right)_{Sc} = \frac{1}{\rho} \cdot \frac{\partial}{\partial z} \left(\rho \cdot K \cdot \frac{\partial q_v}{\partial z}\right) \tag{3.4.27}$$

$$\left(\frac{\partial q_w}{\partial t}\right)_{Sc} = \frac{1}{\rho} \cdot \frac{\partial}{\partial z} \left(\rho \cdot K \cdot \frac{\partial q_w}{\partial z}\right) \tag{3.4.28}$$

Equations (3.4.26), (3.4.27) and (3.4.28) are only applied below 900 hPa and when neither the criterion for deep convection nor for shallow convection is fulfilled. Cloud base is the condensation level for surface air. Then (3.4.26), (3.4.27) and (3.4.28) are applied considering the fluxes through cloud base and cloud top using the following parameterization of the eddy diffusion coefficient.

$$K\,[m^2/s] = \begin{cases} K_{max} \cdot min\left(b \cdot \dfrac{q_w}{q_{wr}}, 1\right) & \text{cloud layers and cloud base} \\ K_{max} \cdot b \cdot \delta r & \text{cloud top entrainment} \\ 0 & \text{elsewhere} \end{cases}$$

where b is cloud cover (cf., equation (3.5.6)), q_{wr} is a cloud water threshold (currently $3 \cdot 10^{-5}$), δr is the relative humidity jump at cloud top and K_{max} is a specified upper limit of K (currently $10\ m^2/s$).

3.5 STRATIFORM CLOUDS

The equations relevant for the discussion of the stratiform cloud scheme are the budget equations for the mass mixing ratio of water vapour (q_v) and cloud water ($q_w = q_l + q_i$), respectively, where q_l is the liquid fraction and q_i is the solid fraction. For convenience, the governing equations are given in a compact form according to

$$\frac{\partial q_v}{\partial t} = R(q_v) - C + E \tag{3.5.1}$$

$$\frac{\partial q_w}{\partial t} = R(q_w) + C - P \tag{3.5.2}$$

where $R(q_v)$ and $R(q_w)$ denote the sum over all advective and sub-grid scale transports of q_v and q_w, respectively. The cloud microphysical terms are the condensation of water vapour ($C > 0$), the evaporation of cloud water $C < 0$, the formation of precipitation by coalescence of cloud droplets and sedimentation of ice crystals ($P > 0$), and the evaporation of precipitation in unsaturated air ($E > 0$).

Sub-grid scale cloud formation

Since real clouds are often smaller than the size of a grid box, sub-grid scale cloud formation is taken into account. The formalism has been developed by Sundquist (1978). Assuming that a fractional horizontal area (b) of a grid box is covered by clouds while the remaining part ($1 - b$) is cloud-free, the equations (3.5.1) and (3.5.2) are modified according to

$$\frac{\partial q_v}{\partial t} = R(q_v) - b \cdot C_c - (1-b) \cdot C_o + (1-b) \cdot E_o \tag{3.5.3}$$

$$\frac{\partial q_w}{\partial t} = R(q_w) + b \cdot C_c + (1-b) \cdot C_o - b \cdot P_c \tag{3.5.4}$$

where the subscript (c) denotes the respective process in the cloudy part and the subscript (o) the process in the cloud-free part of the grid box. The transport terms are assumed to be identical in both parts as well as temperature and wind. Evaporation of precipitation is not allowed in the cloudy part, i.e. $E_c = 0$, and there is no precipitation formation outside the cloud, i.e. $P_o = 0$. The significance of C_o,

which is formally retained in eqs. (3.5.3) and (3.5.4) will be discussed below. In the cloudy part, saturation with respect to the grid averaged temperature T is assumed, $q_c = q_s(T)$, while the cloud-free part is unsaturated by definition, i.e. $q_o < q_s(T)$. Hence, fractional cloud cover (b) and grid-mean water vapour mixing ratio (q_v) are related according to

$$q_v = b \cdot q_s + (1-b) \cdot q_o \tag{3.5.5}$$

or, in terms of the relative humidity $(r = q_v/q_s)$ and solving for (b)

$$b = \frac{r - r_o}{1 - r_o} \tag{3.5.6}$$

for $r > r_o$ and $b = 0$ otherwise. The relative humidity in the cloud-free part (r_o) has to be specified or parameterized. The choice of r_o should depend on factors such as grid resolution and sub-grid scale variance of vertical velocity (Sasamori, 1975). Presently, we specify r_o as a function of height and stability only: In stable stratification, r_o decreases linearly from the surface layer ($r_o = 0.99$) to the top of the PBL ($r_o = 0.85$) above which r_o remains constant. If penetrative convection occurs, r_o decreases further to a minimum value of 0.5 near the tropopause , as suggested by Xu and Krüger (1991) who showed in a modelling study of a cumulus ensemble that convectively driven stratiform clouds such as cirrus anvils may form already in a relatively dry environment.

Condensation and evaporation

Condensational growth of cloud droplets is assumed if the grid-mean relative humidity r exceeds the threshold r_o. Oppositely, an existing cloud will be diluted by evaporation if $r < r_o$. In the case of cloud formation by moisture convergence or adiabatic cooling, for example, any supersaturation in the cloudy part of the grid box will result in a condensational growth of cloud droplets.

A basic problem is to specify the partitioning of the net moisture convergence between the b-part and the $(1-b)$ -part of the grid box.

According to the definition (3.5.5), $\overline{\frac{\partial q_v}{\partial t}}$ may be decomposed into three parts,

$$\overline{\frac{\partial q_v}{\partial t}} = b \cdot \overline{\frac{\partial q_s}{\partial t}} + (1-b) \cdot \overline{\frac{\partial q_o}{\partial t}} + (q_s - q_o) \cdot \overline{\frac{\partial b}{\partial t}} \tag{3.5.7}$$

which represent the changes of q_s, q_o and b due to temperature changes and moisture convergence. Inserting (3.5.7) into (3.5.3) and separating the b-terms, provides the condensation (evaporation) rate C_c as a function of moisture convergence (divergence) and adiabatic cooling (heating),

$$b \cdot \overline{\frac{\partial q_s}{\partial t}} = b \cdot R(q_v) - b \cdot C_c \tag{3.5.8}$$

According to (3.5.8), the b-fraction of the moisture convergence will be used for condensation while the remaining part, $(1-b) \cdot R(q_v)$, increases the relative humidity in the cloud-free part. The

condensation rate is calculated from the moisture convergence into pre-existing clouds only.

Furthermore, we assume that there is always an abundance of cloud condensation nuclei and ice nuclei so that condensational growth is allowed to start as soon as the 100 % relative humidity threshold in the b-part of the grid box is exceeded. The saturation water vapour pressure is calculated from Tetens formula (Lowe, 1977) with suitable coefficients for the liquid phase and ice phase, respectively.

It remains to calculate the cloud water evaporation rate (C_o) in the cloud-free part of the grid box. Cloud water outside the b-part may be generated by advective or diffusive transports across the boundaries of the grid box while internal mixing by molecular or turbulent diffusion is neglected. Moreover, numerical effects do contribute also as, for example, the representation of cloud water by spherical harmonics in the host model. In these cases we assume that cloud water in the $(1-b)$-part will be evaporated instantaneously,

$$R(q_w) + C_o = 0 \tag{3.5.9}$$

Note that all numerical effects are included in the transport term $R(q_w)$ which may also become negative. In this case, C_o is positive and actually represents a condensation rate.

Precipitation formation

Analogous to equation (3.5.5), the grid-mean cloud water mixing ratio is given by

$$q_w = b \cdot q_c \tag{3.5.10}$$

assuming that all of the cloud water is confined to the cloudy part of the grid box which implies that the in-cloud mixing ratio is defined as $q_c = q_w / b$.

The mechanism of precipitation formation depends crucially on the cloud water phase. Since we apply only one budget equation (3.5.4) for the cloud water mixing ratio, the liquid and ice phases are diagnosed as a function of temperature T according to

$$q_c = q_{cl} + q_{ci} = q_c \cdot f_l(T) + q_c \cdot f_i(T) \tag{3.5.11}$$

with $f_l + f_i = 1$. The fractions f_l and f_i have been obtained from a wealth of aircraft measurements, as compiled by Matveev (1984), by applying an exponential fit to these data (Rockel et al., 1991),

$$f_l(T) = 0.0059 + 0.9941 \cdot e^{-[0.003102\,(T-273.15)^2]} \tag{3.5.12}$$

The growth of cloud droplets to precipitating rain drops by autoconversion is parameterized in a convenient exponential form (Sundquist, 1978). In addition, the collision of cloud droplets with larger rain drops is taken into account (Smith, 1990) so that the total coalescence rate is given by

$$P_{cl} = q_{cl}\left[C_{r1}\left[1 - e^{-(q_{cl}/q_{cr})^2}\right] + C_{r2}\langle P\rangle\right] \tag{3.5.13}$$

where $\langle P\rangle$ is the rain flux density (stratiform and convective) at the top of the respective cloud layer and

C_{r1}, C_{r2} and q_{cr} are microphysical constants which determine the efficiency of rain formation and, thus, the cloud lifetime (in ECHAM3/T42 $C_{r1} = 10^{-4} s^{-1}$, $C_{r2} = 1\ m^2 kg^{-1}$ and $q_{cr} = 3 \cdot 10^{-4}$).

Ice crystals settle at a rate which depends on the form and size of the crystals. Both parameters are not available in the model. However, according to an observational study by Heymsfield (1977), the terminal velocity of the crystals can be parameterized in terms of the ice water mixing ratio which is a model variable,

$$V_t = \alpha \cdot (\rho_a q_{ci})^{\beta} \tag{3.5.14}$$

where ρ_a is the air density, and the constants α and β are obtained from a best fit to the data with a slight adjustment (tuning) in the respective model version (in ECHAM3/T42, $\alpha = 1.77$ and $\beta = 0.16$). The loss of ice crystals due to sedimentation is given by the divergence of the ice flux density,

$$P_{ci} = g \frac{\partial}{\partial p}(V_t \rho_a q_{ci}) \tag{3.5.15}$$

where p is the pressure and g is the acceleration of gravity. The total rate of precipitation formation is given by

$$P_c = P_{cl} + P_{ci} \tag{3.5.16}$$

A crucial assumption in the parameterization (3.5.13) - (3.5.16) is that the precipitation formation in a mixed phase, i.e. in a temperature range between about 0 ^{o} C and -40 ^{o} C, can be treated independently for the ice phase and the liquid phase, respectively. A proper treatment of the interaction between both phases, such as the rapid condensational growth of ice crystals at the expense of cloud droplets (Bergeron-Findeisen process), will require a more elaborate scheme which should be based on the budget equations for each phase.

Evaporation of precipitation and melting of snow

Precipitation falling into the cloud-free part of a grid box is exposed to evaporation which is parameterized in terms of the saturation deficit according to

$$E_o = -\frac{1}{\Delta t} \cdot \frac{\gamma \cdot (q_o - q_s)}{1 + \dfrac{L \cdot dq_s/dT}{C_{pd} \cdot (1 + (\delta - 1) q_v)}} \tag{3.5.17}$$

where γ is a tunable parameter (currently $\gamma = 0.1$) and $\delta = C_{pv}/C_{pd}$. The evaporation rate in a layer with thickness Δp is limited, however, by the precipitation flux density at the top of the layer, where $\langle\ \rangle$ denotes a vertical integral of the respective quantity,

$$\langle E_o (p + \Delta p) \rangle \leq \langle P (p) \rangle \tag{3.5.18}$$

with

$$\langle P(p) \rangle = \frac{1}{g} \int_o^p [b\ P_c - (1-b)\, E_o]\, dp' \tag{3.5.19}$$

and

$$\langle E_o(p+\Delta p) \rangle = \frac{1}{g} \int_p^{(p+\Delta p)} E_o\ dp' \tag{3.5.20}$$

Melting of snow is parameterized considering observational data summarized by Mason (1971). Melting occurs in a thin layer of a few 100 m below the freezing level. We therefore assume that the snow can melt in each layer whenever the temperature exceeds 2 ^{o} C. The melting is limited not only by the snow amount but also by keeping the included cooling of the layer such that the temperature of the layer after melting is not less than the 2 ^{o} C threshold.

3.6 SOIL PROCESSES

The surface parameterization scheme comprises the evolution of a temperature profile in the soil, the soil hydrology and the snow pack over land.

Soil temperature

The soil is divided into five layers according to Table 5. The thicknesses of the individual soil layers increase with depth.

Table 5 Thickness of individual soil layers

Layer	1	2	3	4	5
Thickness [m]	0.065	0.254	0.913	2.902	5.700

This is an extension of the scheme of Warrilow et al. (1986) to five layers. At the lowest layer boundary a zero heat flux condition is prescribed in order to ensure that no artificial heat sources and sinks may affect the energy balance of the earth-atmosphere system. The heat conduction equation follows from

$$\begin{aligned} \frac{\partial T_1}{\partial t} &= \frac{F_S}{\rho_g C_g \Delta z_1} + \frac{2\kappa (T_2 - T_1)}{\Delta z_1 (\Delta z_1 + \Delta z_2)} && \text{(layer 1)} \\ \frac{\partial T_i}{\partial t} &= -\frac{2\kappa (T_i - T_{i-1})}{\Delta z_i (\Delta z_{i-1} + \Delta z_i)} + \frac{2\kappa (T_{i+1} - T_i)}{\Delta z_i (\Delta z_i + \Delta z_{i+1})} && \text{(layers 2 to 5)} \end{aligned} \tag{3.6.1}$$

with

κ	heat diffusivity in the soil	$7.5 \cdot 10^{-7}$ m^{2}s^{-1}
$\rho_g \cdot C_g$	heat capacity of the soil per unit volume or	$2.4 \cdot 10^6$ J m^{-3} K^{-1}
	heat capacity of land ice per unit volume	$2.09 \cdot 10^6$ J m^{-3} K^{-1}
F_S	sum of the radiative and turbulent fluxes at the surface if there is no snow; heat flux from the snow to the deep soil if the snow depth exceeds 0.025 m.	

Snow pack temperature

The scheme accounts for the three different conditions at the surface boundary in the presence of a snow pack over land:

1) In the case of permanent ice cover at a grid cell, the soil heat equation Eq.(3.6.1) is solved assuming the characteristics of ice. These areas are defined by the glacier mask.
2) For a snow pack of less than 0.025 m water equivalent (3.6.1) is solved assuming the characteristics of the bare soil.
3) For snow depths deeper than 0.025 m, an extra heat conduction equation (Bauer et al., 1986) evolves according to

$$\frac{\partial}{\partial t} T_{Sn} = \frac{F_S}{\rho_{Sn} \cdot C_{Sn} \cdot Sn} \tag{3.6.2}$$

with

T_{Sn}	temperature in the middle of the snow pack	
F_S	sum of the radiative and turbulent fluxes at the surface	
$\rho_{Sn} C_{Sn}$	heat capacity of the snow per unit volume	$0.6345 \cdot 10^6$ J m^{-3} K^{-1}
	computed using a density of snow ρ_{Sn} of	300 kg m^{-3}
Sn	depth of the snow pack	

Snow melt

The temperature T_{Sn} is used to define a temperature T_S at the top of the snow pack by extrapolation. T_S serves as an interface to the atmosphere. This temperature may not exceed the snow melt temperature T_{melt}. If sufficient energy is available to raise the temperature T_{Sn} above T_{melt}, this energy is used to warm the soil underneath. Only if both T_1 and T_{Sn} reach the value of T_{melt}, further energy input will be used to melt the snow. Snow that is less deep than 0.025 m may melt if T_1 equals T_{melt}.

Sea-ice temperature

The ice-surface temperature T_{ice} is calculated from the energy balance at the ice surface. To avoid problems due to a large time step it is assumed that T_{ice} represents the uppermost 10 cm of the ice sheet. The energy balance equation for this layer can be written as

$$C_{pi}\left(\frac{dT_{ice}}{dt}\right) = F_{atm} + F_{oce} \tag{3.6.3}$$

where C_{pi} is the heat capacity of a 10 cm ice layer. F_{atm} is the atmospheric heat flux consisting of the solar and thermal radiation and the sensible and latent heat flux. The oceanic heat flux F_{oce} is parameterized as

$$F_{oce} = \frac{\alpha}{h_{ice}} \cdot (T_{oce} - T_{ice}) \tag{3.6.4}$$

where α is a heat transfer coefficient (2 W/mK), h_{ice} is the ice thickness and T_{oce} is the temperature of the underlying ocean.

To solve equation (3.6.3) the atmospheric heat flux is linearised with respect to the surface temperature at the previous time step T_S^{old}

$$F_{atm}(T_{ice}) = F_{atm}(T_S^{old}) + \frac{\partial}{\partial T}F_{atm}(T_{ice} - T_S^{old}) \tag{3.6.5}$$

This leads to a linear equation for the new ice-surface temperature T_S^{new}

$$T_S^{new} = \frac{F_{atm} - \frac{\partial}{\partial T}F_{atm}T_S^{old} + \frac{\alpha}{h_{ice}} \cdot T_{oce} + \frac{C_{pi}}{\Delta t} \cdot T_{ice}^{old}}{\frac{C_{pi}}{\Delta t} + \frac{\alpha}{h_{ice}} - \frac{\partial F_{atm}}{\partial T}} \tag{3.6.6}$$

Soil hydrology

The parameterisation of soil hydrology comprises three budget equations for

i. snow amount Sn (m water equivalent) accumulated at the surface,

ii. water amount W_l intercepted by the vegetation during rain or snow melt episodes (the so-called skin reservoir),

iii. soil water amount W_s.

The water equivalent of the snow layer is computed over land and glacier areas from

$$\frac{\partial}{\partial t}Sn = \frac{J_{q_{Sn}} + P_{Sn} - M_{Sn}}{\rho_w} \tag{3.6.7}$$

with

$J_{q_{Sn}}$	evaporation rate per unit area over the snow pack
P_{Sn}	snow fall rate per unit area
M_{Sn}	snow melt rate per unit area
ρ_w	density of water

Rain water and melting snow on the leaves is intercepted by the vegetation until its water holding

capacity W_{lmx} (cf. equation (3.2.8)) is exceeded. The corresponding budget equation is given by

$$\frac{\partial W_l}{\partial t} = \frac{J_{q_{vi}} + C_{ip} \cdot C_v \cdot (C_a \cdot P_R + M_{Sn})}{\rho_w} \tag{3.6.8}$$

with

$J_{q_{vi}}$	evaporation rate from the skin reservoir
P_R	rainfall rate per unit area
C_v	fraction of the grid box covered with vegetation (cf., (3.2.9))
C_{ip}	coefficient of efficiency of rain and snow melt interception (currently 50 %)
C_a	fractional area wetted by rain during a time step (currently 100 % for large-scale rain and 50 % for convective rain

The amount of rain and snow melt which does not enter the skin reservoir is used to calculate the amount of soil infiltration and surface runoff. The soil water reservoir evolves according to

$$\frac{\partial W_s}{\partial t} = \frac{J_{q_v} - J_{q_{vi}} + P_R - P_{Ri} + M_{Sn} - M_{Sni} - R_R - R_D}{\rho_w} \tag{3.6.9}$$

with

J_{q_v}	grid-mean evaporation rate per unit area according to (3.2.18)
P_{Ri}	rainfall rate per unit area intercepted by the skin reservoir
M_{Sni}	snow melt rate per unit area intercepted by the skin reservoir
R_R	surface runoff rate per unit area from precipitaton events and snow melt
R_D	runoff rate per unit area from drainage processes

The computation of R_D and R_R follows the scheme by Dümenil and Todini (1992) which is based on catchment considerations. The scheme accounts for the heterogeneity of a grid area by assuming that the total field capacity W_{Smax} for the grid area results from the integral of the local field capacities which are distributed over the grid area in a non-linear way. The resulting fractional saturated area s/S is a function of the degree of the grid-mean relative soil wetness W_S/W_{Smax} and a structure parameter b that defines the sub-grid scale characteristics of the basin or grid box:

$$\frac{s}{S} = 1 - \left(1 - \frac{W_S}{W_{Smax}}\right)^b \tag{3.6.10}$$

Equation (3.6.10) defines a fractional saturated area s/S of a grid box where runoff would occur for a certain rainfall (or snow melt) event, while in the area $1 - (s/S)$ the rainfall would infiltrate (cf., Figure 5). The surface runoff rate R_R is computed from the area integral of rain and snow melt that arrives in the saturated part s/S of the grid area. The amount of surface runoff resulting from a rainfall (or snow melt) event during a time interval Δt (e.g. the model time step) is computed from

$$\frac{1}{\rho_w}\int_{t_0}^{t_0+\Delta t} R_R dt = Q - (W_{Smax} - W_S) + W_{Smax}\cdot\left(1 - \frac{W_S}{W_{Smax}}\right)^{\frac{1}{1+b}} - \frac{Q}{(1+b)\cdot W_{Smax}^{1+b}} \qquad (3.6.11)$$

if $[...] > 0$ or

$$\frac{1}{\rho_w}\int_{t_0}^{t_0+\Delta t} R_R dt = Q - (W_{Smax} - W_S) \qquad (3.6.12)$$

if $[...] \leq 0$ and $Q + W_S > W_{Smax}$

where

$$Q = \int_{t_0}^{t_0+\Delta t} \frac{(P_R - P_{Ri} + M_{Sn} - M_{Sni})}{\rho_w} dt \qquad (3.6.13)$$

is the total water available for infiltration and runoff after possible interception in the skin reservoir (cf., equation (3.6.8)).

Equation (3.6.12) represents the well-known "bucket model" (Manabe, 1969) where runoff is computed if the precipitation event would cause an oversaturation of the whole grid box (i.e., $W_S + Q > W_{Smax}$). Note also, that the scheme (3.6.11) converges to the bucket model for $b \rightarrow 0$.

In the ECHAM model, the structure parameter b is parameterized in terms of the sub-grid scale height distribution which is taken as a measure of the typical steepness of the terrain in the respective grid box:

$$b = max\left[\frac{\sigma_h - \sigma_o}{\sigma_h + \sigma_{max}};0.01\right] \qquad (3.6.14)$$

where σ_h is the standard deviation of the terrain height and σ_o and σ_{max} are prescribed minimum and maximum values of σ_h depending on the model resolution (currently, σ_o = 100 m and σ_{max} = 1000 (1500) m for T21 (T42) resolution).

According to the runoff parameterization (3.6.11) - (3.6.14), surface runoff is extremely efficient in steep terrain (b approaching 0.5 for $\sigma_h \rightarrow \sigma_{max}$) while most of the precipitation is allowed to infiltrate the soil if the terrain is relatively flat ($b \rightarrow 0.01$).

The infiltration rate per unit area I_R is defined as

$$\frac{1}{\rho_w}\int_{t_0}^{t_0+\Delta t} I_R dt = Q - \frac{1}{\rho_w}\int_{t_0}^{t_0+\Delta t} R_R dt \qquad (3.6.15)$$

For frozen soil, however, we assume zero infiltration so that the surface runoff results as

$$\frac{1}{\rho_w} \int_{t_0}^{t_0+\Delta t} R_R dt = Q \tag{3.6.16}$$

Runoff due to drainage processes occurs independently of the water input Q if the soil wetness is between 5 % and 90 % of the field capacity (slow drainage) or larger than 90 % (fast drainage):

$$\frac{R_D}{\rho_w} = \begin{cases} d_{min} \cdot \dfrac{W_S}{W_{Smax}} \text{ if } (W_{Smin} < W_S < W_{dr}) \\ d_{min} \cdot \dfrac{W_S}{W_{Smax}} + (d_{max} - d_{min}) \left(\dfrac{W_S - W_{dr}}{W_{Smax} - W_{dr}} \right)^d \text{ if } (W_S \geq W_{dr}) \end{cases} \tag{3.6.17}$$

with

$$d_{min} = 2.8 \cdot 10^{-10} \text{ m/s}, \; d_{max} = 2.8 \cdot 10^{-8} \text{ m/s}, \; d = 1.5, \; W_{Smin} = 0.05 \cdot W_{Smax},$$
$$W_{dr} = 0.9 \cdot W_{Smax}$$

The amount of evaporation is computed from the atmospheric demand but is limited by the soil moisture availability over bare soil and due to vegetation.

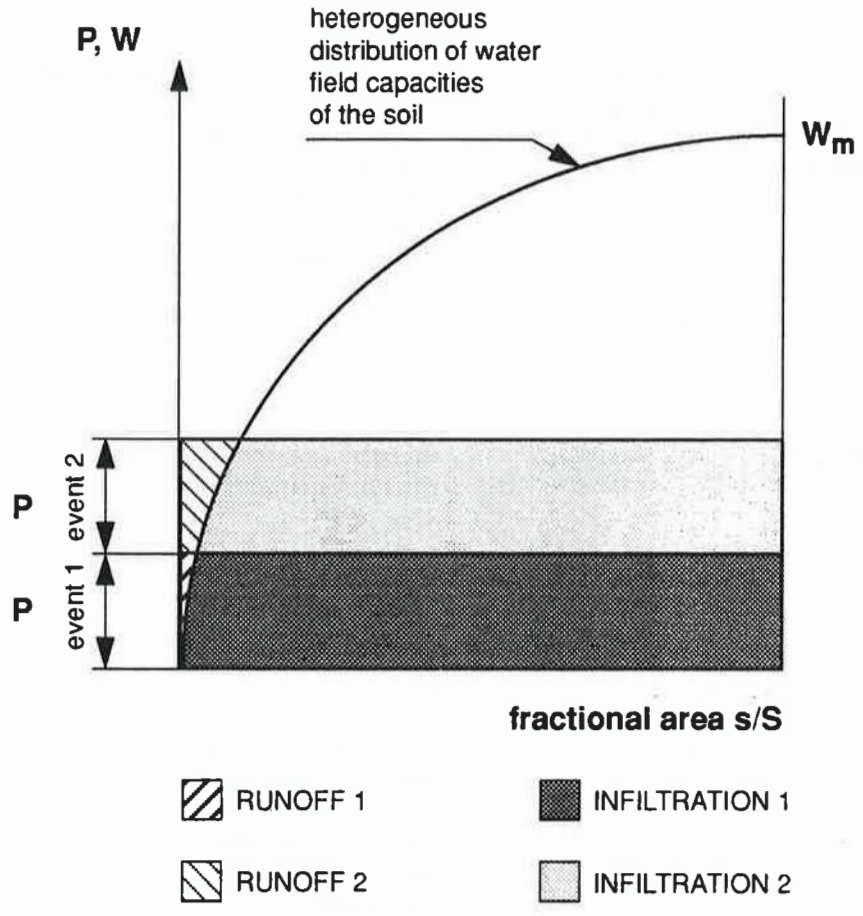

Figure 5 Surface runoff and infiltration from precipitation events.

4. MODELS AND EXPERIMENTS

A survey of the various model versions used in the present intercomparison study is presented in Table 6. It also provides information on the design of the model experiments. In each climate simulation a climatological annual cycle of sea surface temperature (SST) is prescribed as boundary forcing while interannual SST variability has been neglected. It is important to note, however, that the SST data sets used in the various model simulations differ with respect to both, analysis technique and time period.

All models have been initialized with the same set of atmospheric data (ECMWF analysis for January 1, 1983), and they need a spin-up time of at least one year in order to settle to their own climate, respectively.

Most of the observational data used for model validation are based on ECMWF analyses for a ten-year period (i.e., June 1981 to February 1991). However, all zonal means and the eddy statistics (section 5.2) have been computed for a shorter period (i.e., June 1982 to February 1989).

Table 6: ECHAM model versions and model experiments
(* denotes the same formulation as in the previous version)

	ECHAM0 (=ECMWF, cycle 17)	ECHAM1	ECHAM2	ECHAM3
Dynamics/numerics	Spectral (Baede et al., 1979)	*, but revised formulation of the pressure gradient term (Simmons and Chen, 1991)	*	*
Resolution	T21L16	T21L19	*	T42L19 and (T21L19)
Timestep (min)	45	40	*	24 (40)
Horizontal diffusion	Linear, 4th order	enhanced scale selectivity (Laursen and Eliasen, 1989)	*	*
Radiation	Geleyn and Hollingsworth (1979)	Hense et al. (1982) and Rockel et al. (1991)	*	*
diurnal cycle **annual cycle**	no yes	yes *	* *	* *
Vertical diffusion	Louis (1979)	*, but low wind correction by imposing a minimum wind speed for the exchange of heat and moisture in unstable conditions	*	*, but low wind correction according to Miller et al. (1992). The Ri number is revised to include "moist" (cloud) effects

Gravity wave drag	no	Palmer et al. (1986)	no	Miller et al. (1989); no GWD at T21 resolution.
Convection	Kuo (1974), no shallow convection	*, but with shallow convection (Tiedtke et al., 1988)	*	Tiedtke (1989) for deep, midlevel and shallow convection. Stratocumulus convection according to Tiedtke et al. (1988).
Stratiform cloud	Diagnostic scheme (Geleyn, 1981)	Prognostic scheme (Roeckner and Schlese, 1985)	*	Prognostic scheme (Roeckner et al., 1991)
Soil processes	Three-layer model for heat and soil moisture with climatologically specified deep soil temperature and moisture; no vegetation effects; sea ice temperature is climatologically prescribed.	Five-layer model for heat transfer; refined bucket model for soil moisture (Dümenil and Todini, 1992); vegetation effects included (Blondin, 1989).	*	*, but sea ice temperature is calculated from the net heat fluxes including conductive heat transfer through ice.
Orography	Average over grid area ("mean").	Enhanced ("envelope")	mean	*
Sea surface temperature and sea ice extent	Alexander and Mobley (1976)	* for sea ice, but Reynolds (1988) for SST.	*	AMIP-SST and sea-ice dataset
Simulated years in "control mode" (annual cycle of SST and sea ice climatologically specified; no interannual variations).	10	23	23	30 (10 for T21)
Averaging period (simulated years)	2-10	4-23	4-23	11-20; 21-30 (2-10 for T21)
Write-up interval (hours)	24	12	12	12

Table 6 (cont.)

5. MODEL CLIMATOLOGY

In this section we compare the time-mean climate state, its intraseasonal variations and stationary eddy variances and fluxes as simulated by different versions of the ECHAM model. Most of the discussions will concentrate on the zonal averages of basic climate variables such as temperature, wind, pressure and precipitation. We refer, however, also to the respective geographical distributions which are summarized in Appendix A. The results of the T21 model simulations (ECHAM1, ECHAM2 and ECHAM3) are presented for the time period indicated in Table 6 (section 4), whereas the results of the ECHAM3/T42 simulation are shown separately for the first 10 years and for the second 10 years of the total simulation period of 20 years in order to demonstrate the stability of the statistics presented in this report.

5.1 TIME-MEAN CLIMATE

Temperature

One of the most apparent deficiencies of the ECHAM0 model is a cold tropospheric bias of approximately 3K globally with peak values of 7- 8K in the tropical upper troposphere (Dümenil and Schlese, 1987). This error is caused primarily by a lack of latent heat exchange between the ocean surface and the atmosphere, predominantly at low latitudes. Another contributing factor is the excessive radiative cooling caused mainly by tropical cirrus cloud being optically too thin (Roeckner et al., 1989).

In the more recent model versions (ECHAM1 to ECHAM3), the temperature errors are significantly reduced, as apparent from Figs. 6 and 7, where the zonal mean errors (with respect to ECMWF analyses) are shown for northern winter (DJF) and northern summer (JJA), respectively. The most striking model error is the cold bias in the polar upper troposphere and lower stratosphere which prevails nearly independent of season, hemisphere or model physics and horizontal resolution. This common GCM deficiency (e.g. Boer et al., 1991) is possibly caused by an insufficient vertical resolution of the stratosphere. The warm bias in the upper tropical troposphere which is typical of all models shown in Figs. 6 and 7, but less common in other GCMs (Boer et al., 1991), is very likely related to deficiencies of the radiative transfer scheme (cf. section 3.1). As compared to "exact" line-by-line radiative transfer models, the present scheme systematically underestimates the (clear-sky) longwave cooling in the upper troposphere, while the longwave cooling in the lower layers is slightly too strong, particularly in the tropics (not shown). This feature is consistent with the vertical structure of the temperature error as shown in Figs. 6 and 7.

All model versions perform reasonably well in the middle and lower troposphere, but the ECHAM3 errors (at both resolutions) are slightly smaller in the low-latitude boundary layer. This is apparent particularly in the Figs. A1 and A2 (Appendix A) which show the respective geographical distributions of the temperature errors at 850 hPa for both seasons. Additional test simulations (not shown) with individual processes switched on and off have indicated that the error reduction is caused primarily (70%) by

the new mass-flux convection scheme in ECHAM3 (cf. section 3.4), while the remaining 30% is due to the introduction of a "moist" Richardson number (cf. section 3.2) which allows for more efficient turbulent mixing within a cloud-topped planetary boundary layer.

At 850 hPa (Figs. A1, A2), all model versions have a cold bias over the polar regions in both hemispheres and, to a lesser extent, over the low-latitude oceans as well (see discussion above), and these biases occur nearly independent of season. The cold polar bias which is also evident in the zonal means (Figs. 6, 7) can be related to a lack of water vapour in these regions due to the use of the spectral transform method which tends to produce spurious condensation ("spectral rain"), particularly in mountainous areas such as Antarctica or Greenland.

As noted above, the ECHAM3 errors over the low-latitude oceans are significantly reduced as a result of the enhanced physics. The impact of the increased resolution can be seen particularly in the oceanic storm track region in the Southern Hemisphere (SH) between about 40°S and 70°S where the warm bias of the T21 versions (Figs. A1 and A2, d- f) is larger than in both samples of the T42 simulation (Figs. A1 and A2, b,c).

In ECHAM3, the most persistent error patterns appear over the subtropical oceans in the high pressure cells off the west coasts of North America, South America, Africa and Australia, where the simulated temperatures are 2-4K lower than observed. Excessive cloud radiative cooling can be excluded because the quasi-permanent stratiform cloud decks in these areas are significantly underestimated in all model versions (not shown). Since the thermal balance in these areas is achieved essentially by longwave radiative cooling and adiabatic warming in sinking air (Boville, 1985), a combination of dynamical and radiative factors may play a role.

The temperature errors over land are much more seasonally dependent and also model dependent. Furthermore, the error patterns over land are less spatially coherent than over the oceans, and in many cases the temperature errors may be related to the inadequate representation of surface inhomogeneities such as orography, surface roughness, surface albedo etc.. Small shifts in the circulation patterns do contribute also as, for example, in Northern Hemisphere (NH) winter over North America and Europe where the warm bias of the ECHAM3/T42 model (Figs. A1b,c) can be related to anomalous warm air advection by a low-level flow which is too zonal over North America and too strong with an anomalous southerly component over Europe (cf. Figs. A7,A11). During NH summer, the largest error of the T42 simulation (Figs. A2b,c) is found over the low-latitude continents of the Northern Hemisphere with spatially coherent error patterns of more than +2K and peak values of about +6K over the central part of the United States. The reason for this model deficiency is not known. The temperature error is, however, consistent with anomalously small precipitation in those areas (Figs. A20a-c) and is also consistent with reduced cloudiness and soil moisture (not shown).

The temperature distribution of the stratosphere evolves quite differently from that of the troposphere,

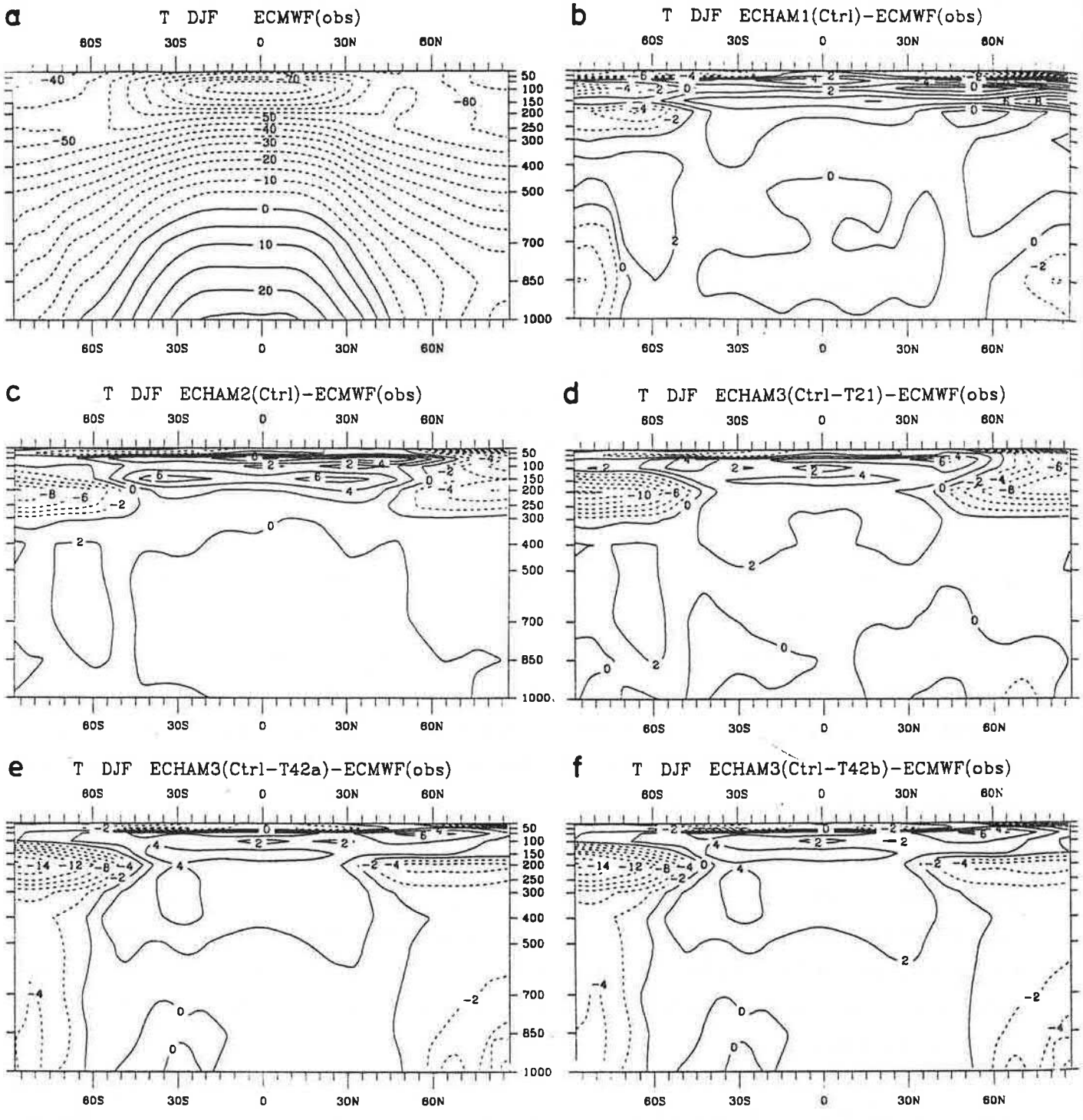

Figure 6 Latitude-pressure distributions of (a) zonal mean temperature (°C) for the DJF season according to ECMWF analyses and (b-f) simulation errors of different versions of the ECHAM model. The lower panel (e,f) shows two 10-year samples of the same model (ECHAM3/T42).

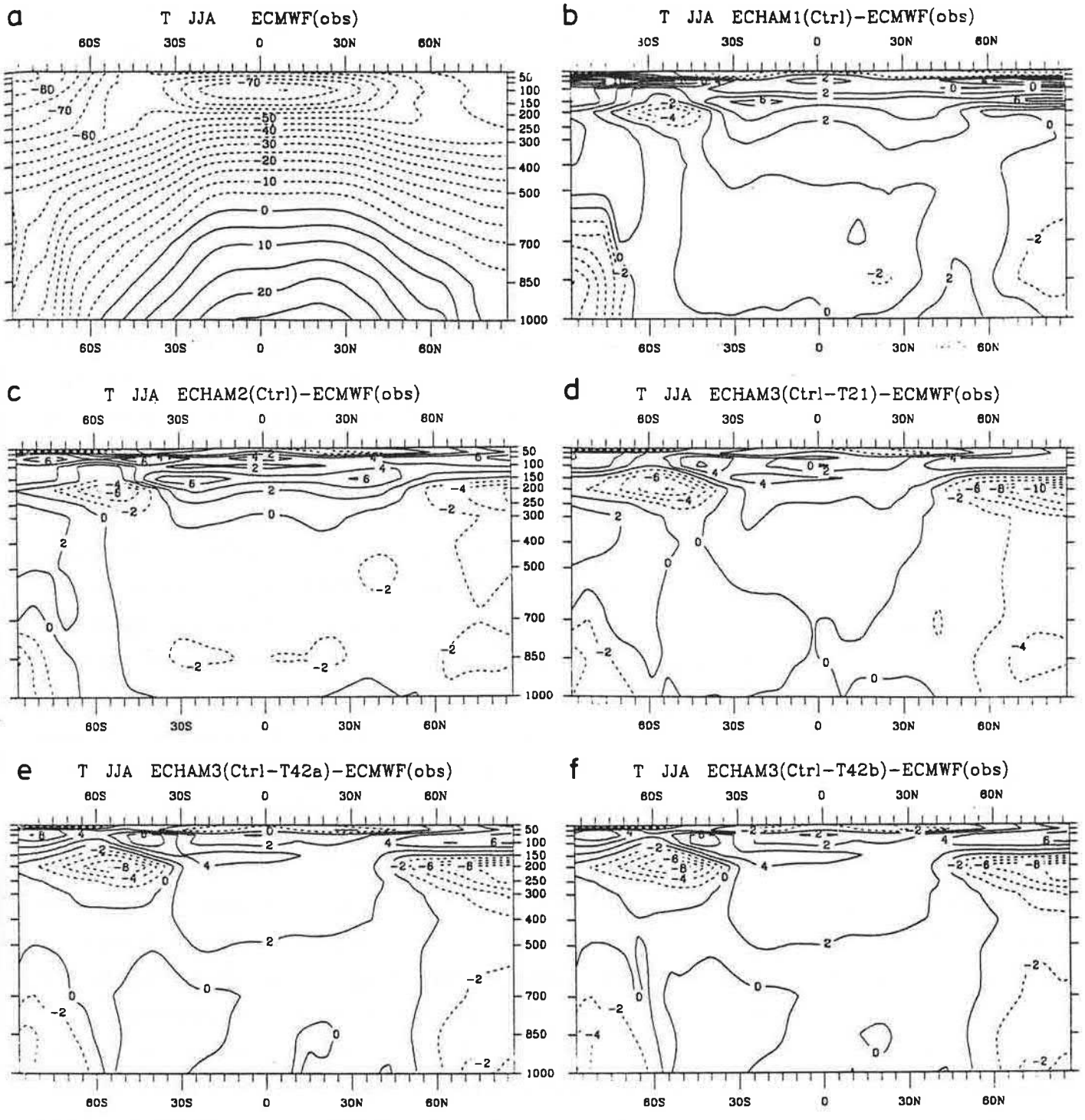

Figure 7 As in Fig. 6 except for the JJA season.

and the essential processes are the absorption of solar radiation by ozone, the emission and absorption of longwave radiation, and dynamical processes including internal dissipation by breaking gravity waves, for example. As an example of the skill of the models to simulate the lower stratosphere, we show the temperature distributions at the 50 hPa level which corresponds to a height of approximately 20 km. During NH winter (Fig. A3), vertically propagating planetary waves excited by orography and land-sea contrast are responsible for a distortion of the cold polar vortex by a seasonal-mean stationary wave disturbance over the North Pacific. This observed feature (Fig. A3a) is simulated by all models, except for ECHAM1 (Fig. A3b) where the temperature gradients are significantly reduced and the resulting flow is much too weak (not shown). Oppositely, in ECHAM2 (Fig. A3c) and ECHAM3/T21 (Fig. A3d) the meridional temperature gradient is overestimated by nearly a factor of two, whereas the ECHAM3/T42 model (Figs. A3e,f) simulates the correct pattern and amplitude as well. The temperature distributions simulated by the models are consistent with the modeling of the polar night jet which is too strong in the T21 versions of ECHAM2 and ECHAM3 but correctly reproduced at T42 resolution (cf. Fig. 8).

Although the 50 hPa errors in the T42 model are considerably smaller than in all of the T21 versions, the resolution plays probably only an indirect role. The large difference between ECHAM1 (which includes the parameterization of the gravity wave drag) and ECHAM2 and ECHAM3/T21 (which do not) indicates that internal dissipation via its influence on the momentum budget and meridional heat transfer is of major importance. Consequently, the improved simulation of the T42 model can most likely be attributed to the inclusion of a well-tuned gravity drag scheme (cf., Table 6), whereas in ECHAM1 the effect of the gravity wave drag is obviously too strong. In conclusion, even low resolution models seem to need an appropriate stratospheric drag for realistically maintaining the momentum budget (McFarlane, 1987). The stratospheric temperature distribution may be used as a criterion for tuning the scheme.

During the NH summer, the meridional temperature gradient is reversed (Fig. A4), and the resulting stratospheric easterlies are much less distorted than the westerly flow in winter. The temperature distribution is reasonably well simulated by all of the models. The meridional temperature gradient, however, is generally too large, nearly independent of model physics and horizontal resolution. This is true, to some extent, during the SH summer (Fig. A5) as well so that additional processes which are identical in all model versions such as the parameterization of radiative transfer or inadequate dynamics resulting from insufficient vertical resolution, for example, have to be invoked to explain the errors. During SH winter (Fig. A6), the meridional temperature gradient at mid-latitudes is slightly too weak, except in the T42 model. However, the cold core over Central Antarctica with observed temperatures less than -85°C is too warm by 5-10° in all of the model simulations.

Wind

The observed and simulated zonal mean zonal wind distributions are shown in Fig. 8 and Fig. 9 for the months of DJF and JJA, respectively. The impact of an (overestimated) gravity wave drag (GWD) in a low-resolution model is apparent from Fig. 8b which shows the zonal wind as simulated by the ECHAM1 model. The polar night jet is only weakly indicated (cf. discussion above and Fig. A3b), but the NH subtropical jet core is well simulated both in strength and position. The NH westerlies, however, are too weak polewards of about 40°N. In the Southern Hemisphere, the westerlies are generally too weak which is a common feature of low-resolution GCMs (Boer et al., 1991). In ECHAM2 (Fig. 8c) and in ECHAM3/T21 (Fig. 8d) the band of NH westerlies is extended further polewards (which is realistic) but also further equatorwards at higher levels (which is unrealistic). Since both model versions have been run without a GWD parameterization, the polar night jet is overestimated (cf. discussion above and Fig. A3c,d). In ECHAM3/T21, the SH subtropical jet is stronger and more realistic than in ECHAM1 and ECHAM2. The most realistic mean zonal wind distribution during DJF is simulated by the T42 model (Fig. 8e,f) in both hemispheres and in the troposphere and stratosphere as well. Nevertheless, the model simulation is not perfect, and the zonal wind errors are by and large consistent with the temperature errors via the thermal wind relation (Fig. 6e,f): The subtropical jets are slightly too strong in both hemispheres, and there is also a slight poleward shift of the jet cores, in particular in the Southern Hemisphere, as opposed to the T21 models which tend to shift the SH subtropical jet equatorwards.

During JJA (Fig. 9), the differences between ECHAM1 and ECHAM2 are smaller because the GWD effect on the circulation is small in summer, and the GWD is also much smaller in the Southern Hemisphere than in the Northern Hemisphere during the respective winter season. The enhanced physics in ECHAM3 produces stronger westerlies in both hemispheres and weaker easterlies in the tropical upper troposphere and lower stratosphere, nearly independent of resolution. The impact of increased resolution is, however, evident in the Southern Hemisphere where only the T42 model is able to reproduce the observed double jet structure. As compared to the ECMWF analyses, the subtropical jets are too strong in the Southern Hemisphere, particularly in the ECHAM3 simulations, and this feature is consistent with the temperature errors at these levels (cf. Fig. 7).

In Figs. 10 and 11 the mean meridional wind distributions during DJF and JJA, respectively, are presented for the ECMWF analyses (upper left) and for the various model simulations. The three-cell structure of the mean meridional circulation and its seasonal variation is simulated with some skill by all of the models, and the differences between the models are smaller than those evident in the simulation of the mean zonal flow. In the lower branch of the Hadley cell the simulated inflow is generally larger than in the ECMWF analyses, while the opposite holds for the upper branch. The simulated height of the upper tropospheric outflow region is systematically too low.

The wind systems at the 850 hPa level (Figs. A7 and A8) are generally well simulated. In particular the T42 model is able to capture the strength and position of the observed pattern with remarkable skill (Figs.

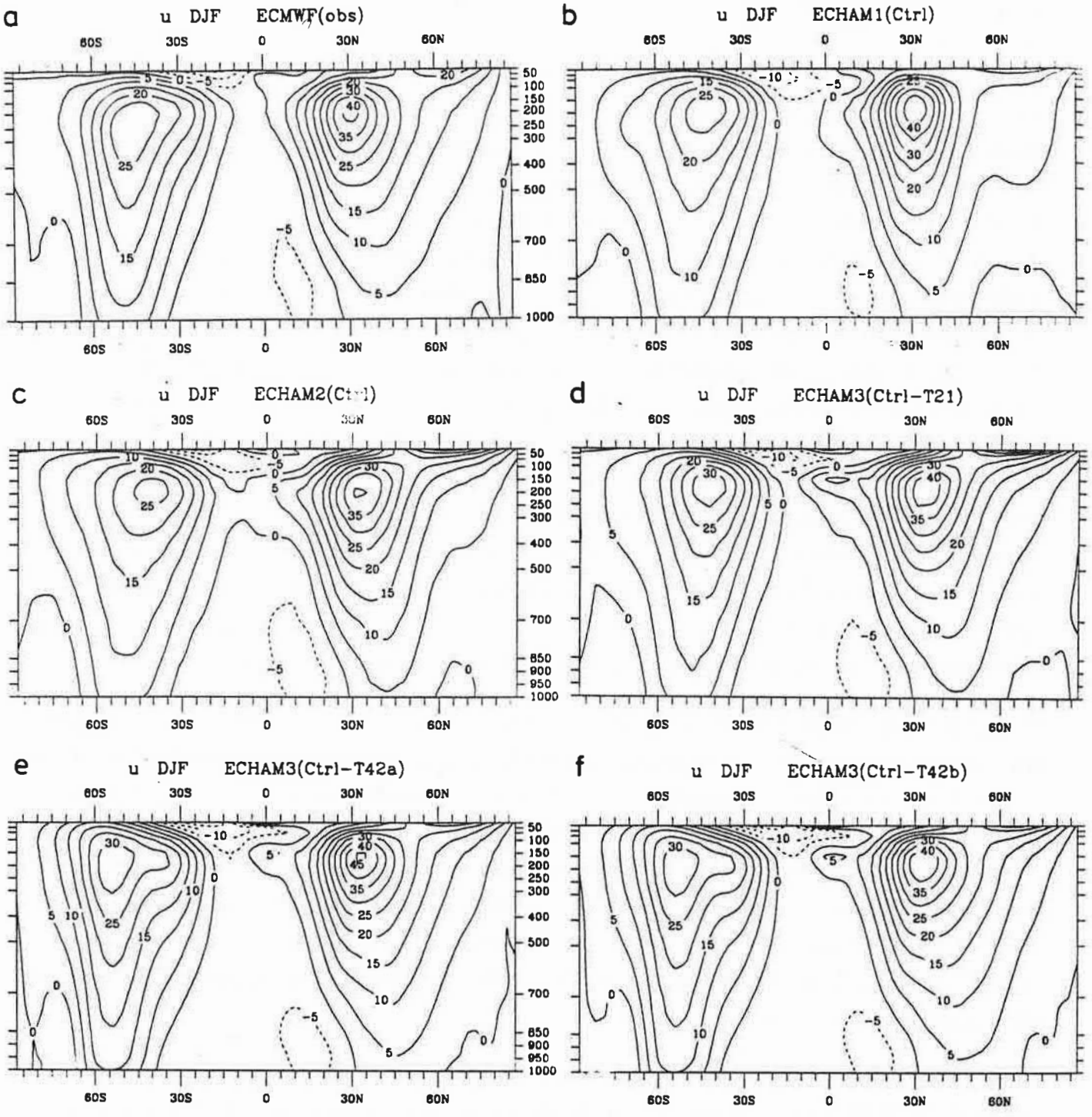

Figure 8 Latitude-pressure distributions of zonal mean zonal wind (m/s) for the DJF season according to (a) ECMWF analyses and (b-f) ECHAM model simulations.

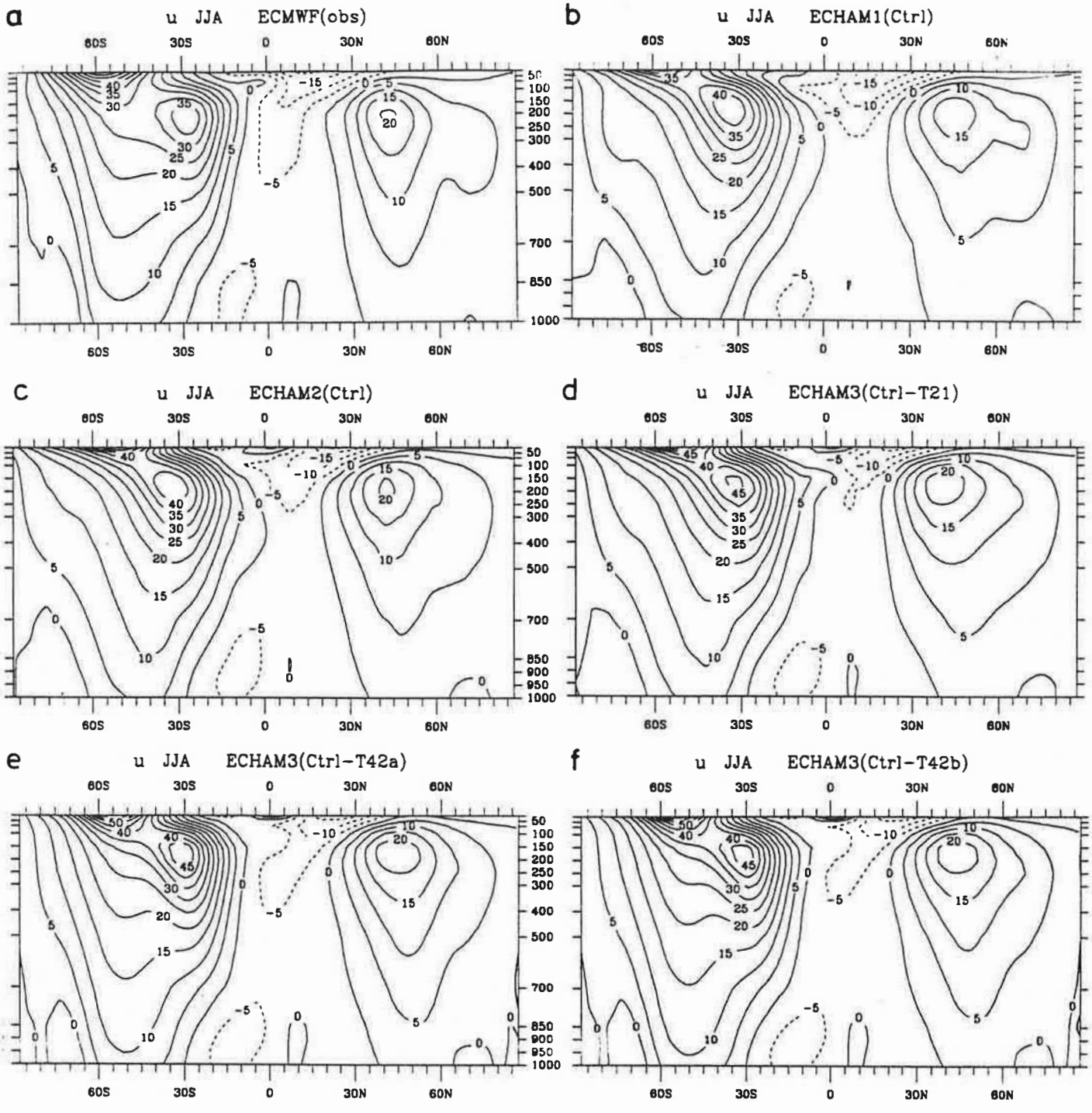

Figure 9 As in Fig. 8 except for the JJA season.

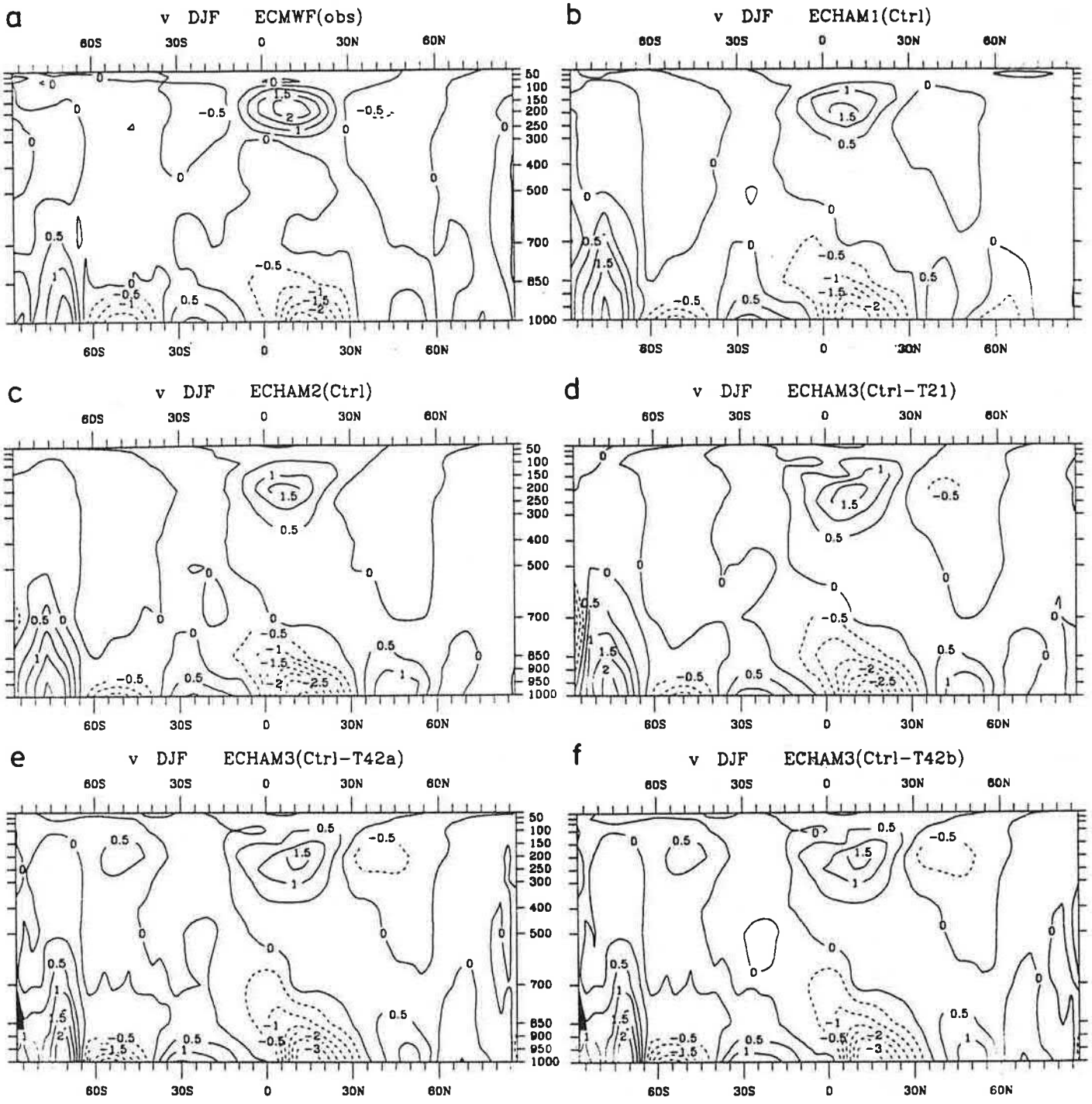

Figure 10 Latitude-pressure distributions of zonal mean meridional wind (m/s) for the DJF season according to (a) ECMWF analyses and (b-f) ECHAM model simulations.

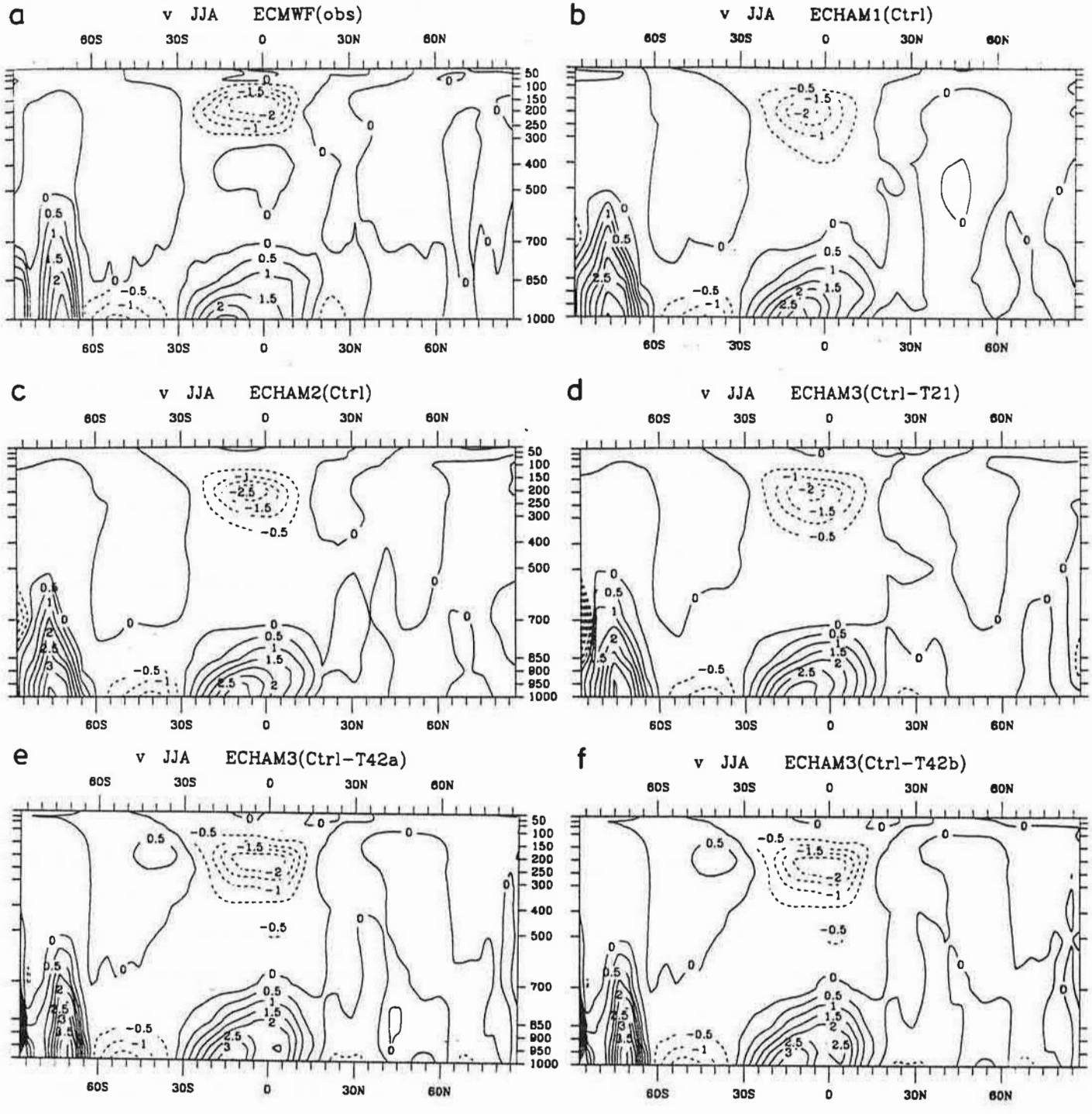

Figure 11 As in Fig. 10 except for the JJA season.

A7b,c and A8b,c). In DJF the tropical easterlies are slightly larger than observed. whereas in JJA the southwest monsoon over the Arabian Sea is too weak. In the T21 models, the mid-latitude westerlies in the Southern Hemisphere are weaker than observed in both seasons (Figs. A7d-f and A8d-f), and the westerly wind maximum over Eurasia is shifted to the south in winter (Fig. A7d-f). In ECHAM1, the flow over the North Atlantic is much too weak in winter (Fig. A7d).

At 200 hPa, the mid-latitude westerlies simulated by the T42 model are too strong in both hemispheres and and in both seasons (Figs. A9b,c and A10b,c), as discussed already above (cf. Figs. 8 and 9), whereas the positions of the jet maxima are well captured. The tropical easterlies are slightly too strong in the T42 model during DJF, whereas the tropical easterly jet during JJA over the Indian Ocean is weaker than observed. The anticyclonic flow off the west coast of Central America during JJA (Fig. A10b,c) and its cyclonic counterpart at 850 hPa (Fig. A8b,c) are much stronger than observed. The DJF flow at 200 hPa simulated by the T21 models ECHAM2 and ECHAM3 (Figs. A9e,f) is fairly realistic. The westerly bias is slightly reduced as compared to the T42 model, in particular in ECHAM2. In ECHAM1, the mid-latitude flow during NH winter is generally too zonal (Fig. A9d), and the jet axis over the east coast of the United States does not show the observed southwest-northeast orientation. During JJA, the biggest impact of increased resolution is found in the Southern Hemisphere where the observed southward extension of the jet in the Indian Ocean sector is only reproduced at T42 resolution (cf. Fig. 9). The impact of changed physics (essentially convection) is particularly evident in the tropics where the easterly jet over the Indian Ocean is significantly reduced in ECHAM3 as compared to ECHAM1 and ECHAM2.

Surface pressure

The zonally averaged surface pressure (reduced to mean sea level height) is shown in Fig. 12 for DJF (upper pair) and for JJA (lower pair). There is generally good agreement between the simulated and observed distributions but a few exceptions are noteworthy. During DJF, the ECHAM1 model simulates excessively high pressure over the Arctic (Fig. 12b) which can be explained by the use of a gravity wave drag parameterization being not properly adjusted for that particular model. Furthermore, all T21 model versions underestimate the meridional pressure gradient in the "roaring fourties" of the Southern Hemisphere (Figs. 12b and 12d): The subtropical highs are slightly too weak whereas the Antarctic trough is not deep enough. In this respect, the T42 model performs better, particularly during JJA (Fig. 12c), and this seems to be typical of modern GCMs (Boer et al., 1991). During DJF (Fig. 12a), however, the T42 model overestimates the SH meridional pressure gradient, and there is also a southward shift by approximately 5° of the respective pressure patterns. In all ECHAM simulations the equatorial trough is slightly too deep.

In Fig. 13 and 14 we compare the interannual variability of DJF and JJA means of surface pressure for the ECHAM3 model simulations at T21 and T42 resolution and for the observations, respectively. The

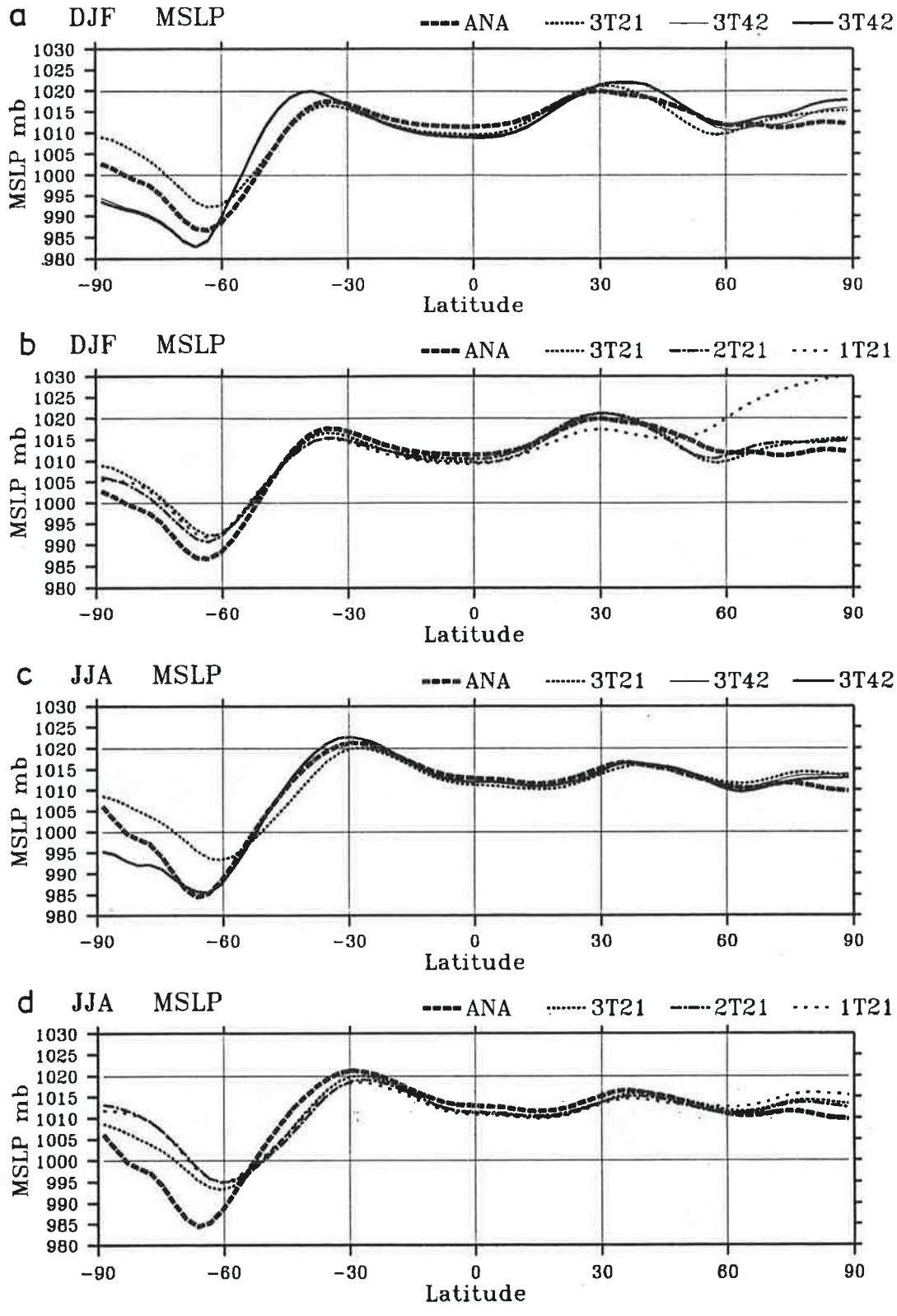

Figure 12 Zonal means of mean sea level pressure (MSLP) for the DJF season (a,b) and for the JJA season (c,d). ANA denotes ECMWF analyses, and nTxx denotes ECHAMn at Txx horizontal resolution. 3T42 refers to two 10-year samples simulated with the same model (ECHAM3/T42).

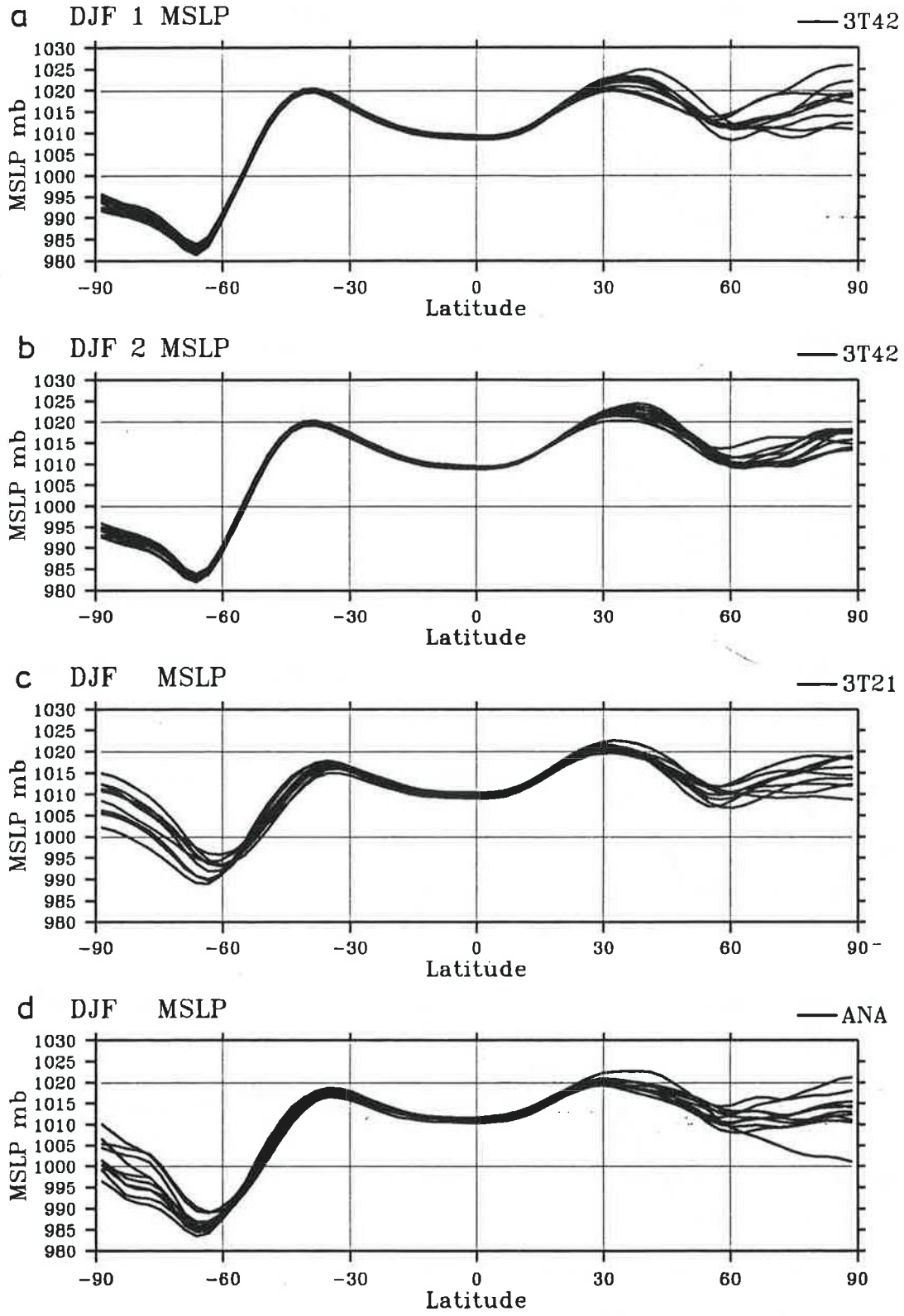

Figure 13 Interannual variations of zonal mean simulated (a-c) and observed (d) mean sea level pressure for the DJF season (10 seasonal samples in each panel).

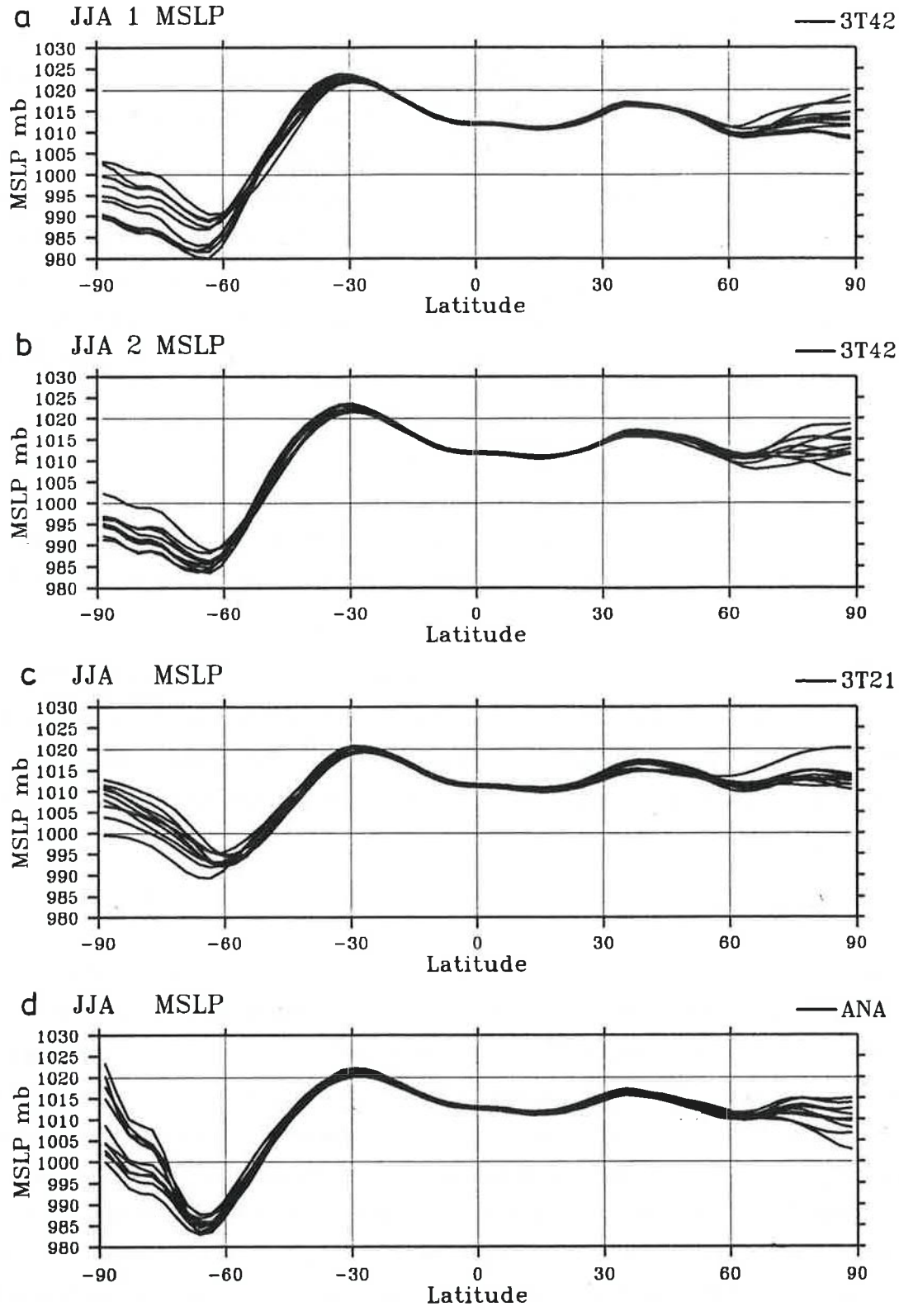

Figure 14 As in Fig. 13 except for the JJA season.

observed large variability at high latitudes is well captured by the models although interannual variations of surface boundary conditions (SST and sea ice) are suppressed. During DJF, there is less variability in the Southern Hemisphere at T42 resolution, particularly over Antarctica (Fig. 13a,b). However, the surface pressure south of 70°S should generally be viewed with caution because significant uncertainties may be introduced by the reduction to mean sea level.

The geographical distributions of the simulated and observed surface pressures are shown in Figs. A11-A14, separately for the Northern and Southern Hemisphere, during DJF and JJA, respectively. During NH winter (Fig. A11), all T21 models simulate a relatively deep and extensive Aleutian low. The Icelandic low, however, is nearly absent in ECHAM1, it is too weak in ECHAM2, but it is reasonably well simulated in ECHAM3, both in strength and position. In the T42 model (lower pair of figures) the strength and position of both systems are reasonably well captured. The Aleutian low is shifted, however, slightly to the east (Fig. A11f) and both systems are confined to a smaller area (with respect to observations) due to the northward extension of the subtropical highs which are also stronger than observed over South Europe and in the North Pacific.

During NH summer (Fig. A12), all models are able to reproduce the observed pressure configuration with high pressure over the oceans and low pressure over land. In the T42 model the oceanic highs are more intense and also more realistic than in the T21 models. Over land, however, the pressure is slightly too low, in particular over the western part of the United States where the surface pressure is about 5 hPa lower than observed.

The advantages of the T42 model are evident in the Southern Hemisphere, both during DJF (Fig. A13) and during JJA (Fig. A14), whereas the impact of the different model physics in the T21 models is less obvious. In general, all T21 models significantly underestimate the meridional pressure gradients, whereas the T42 model slightly overestimates the subtropical highs and the Antarctic trough in DJF (Fig. A13; see also Fig. 12a).

Geopotential height (500 hPa)

The geographical distributions of the observed and simulated geopotential height at 500 hPa are shown in Figs. A15-A18. During NH winter (Fig. A15), all models are able to capture the basic features such as the troughs over the eastern parts of Asia and North America and the ridges over the west coasts of North America and Europe. A number of details, however, are simulated less satisfactorily. The largest errors are simulated by the ECHAM1 model (Fig. A15b) showing a much too pronounced stationary wave amplitude, a shift of the European ridge-trough system to the west and a general weakening of the geostrophic wind. Again, these errors are due to an excessive gravity wave drag in the ECHAM1 model. The T21 models which do not employ a GWD parameterization perform much better, and apart from a slightly underestimated American ridge-trough system the simulated geopotential height distribution is close to the observed (Figs. A15c,d). The T42 model, on the other hand, seems to perform slightly worse

(Figs. A15e,f). In particular, the American ridge is only weakly indicated and the American trough is shifted to the east.

Altough the basic error patterns mentioned above occur in both 10-year samples of the T42 model, there is a surprisingly large interdecadal variability, in particular over the North Atlantic and Europe, which can also be identified in the two samples of the surface pressure distribution (cf. Figs. A11e,f) showing a significantly enhanced southwesterly (geostrophic) flow over the Atlantic during the second decade. Interdecadal variability is poorly understood, and the observed deepening of the Icelandic low during the past 40 years (e.g. Wigley and Santer, 1990) is sometimes taken as an indication of enhanced greenhouse forcing or explained by long-term variations of the ocean-atmosphere system. However, the results presented above suggest that internal atmospheric dynamics may contribute as well.

The JJA circulation in the Northern Hemisphere (Fig. A16) is much more zonally symmetric than in winter, and the differences between the models themselves and between the models and the observations are relatively small. By and large, the observed patterns are slightly better reproduced by the T42 model (Figs. A16e,f).

In the Southern Hemisphere, the summer circulation is too strong in the T42 model (Fig. A17e,f) while it is too weak in the T21 models. The winter circulation, on the other hand, is simulated accurately by the T42 model (Figs. A18e,f) while it is too weak again at T21 resolution, particularly in ECHAM1 (Fig. A18b) and ECHAM2 (Fig. A18c).

Precipitation

Precipitation is one of the most important climate parameters, since it does not only affect the water budget of the soil but it indicates also the areas where the atmospheric circulation is influenced by the release of latent heat. Unfortunately, the distribution of precipitation on Earth is not well known, and there are huge data gaps particularly over the oceans. Consequently, any comparison of observed and simulated precipitation pattern should be viewed with caution. As an indication of the uncertainties of present-day precipitation climatologies, we compare two distributions which are often used in model validation studies. Figure 15 shows a comparison for the months DJF of the well-known climatology compiled by Jaeger (1976) and a more recent one prepared by Legates and Willmot (1990). While the climatologies agree reasonably well over land, there are big discrepancies over the oceans. Over the North Atlantic and North Pacific, for example, the new climatology suggests significantly larger values and over the tropical Pacific as well.

During JJA (Fig. 16), the new climatology has smaller values over the mid-latitude oceans but there is again more precipitation in general over the tropical oceans. In some areas, for example in the ITCZ over the Pacific, the new values are more than twice as large as those suggested by Jaeger (1976).

In Figure 17 we compare the simulated and observed (both climatologies) zonally averaged precipitation

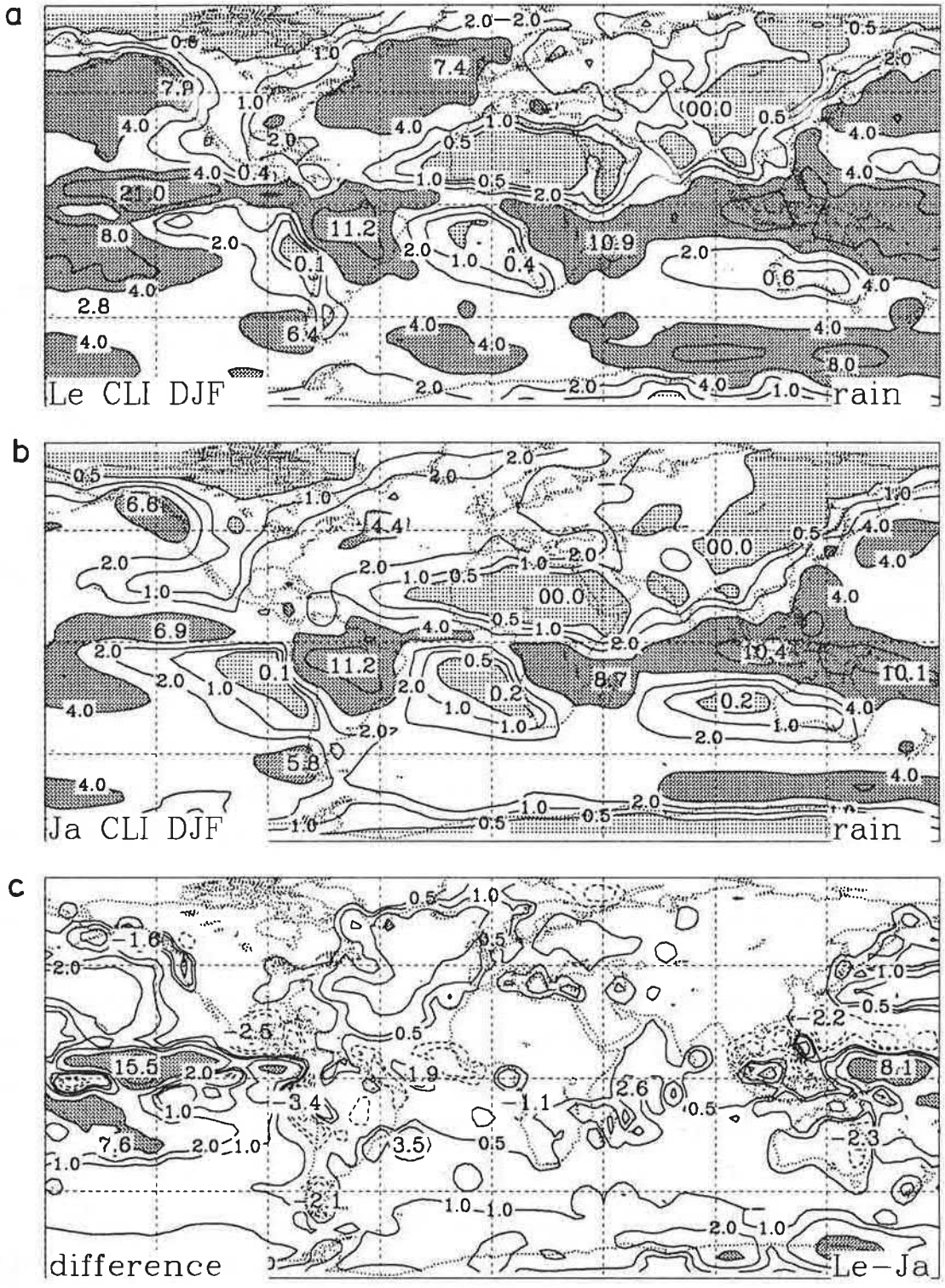

Figure 15 Comparison of precipitation climatologies (mm/d) for the DJF season according to (a) Legates and Willmott (1990) and (b) Jaeger (1976). The lower panel shows the difference (a) - (b). Contour spacing: .5, 1., 2., 4., 8., ...mm/d.

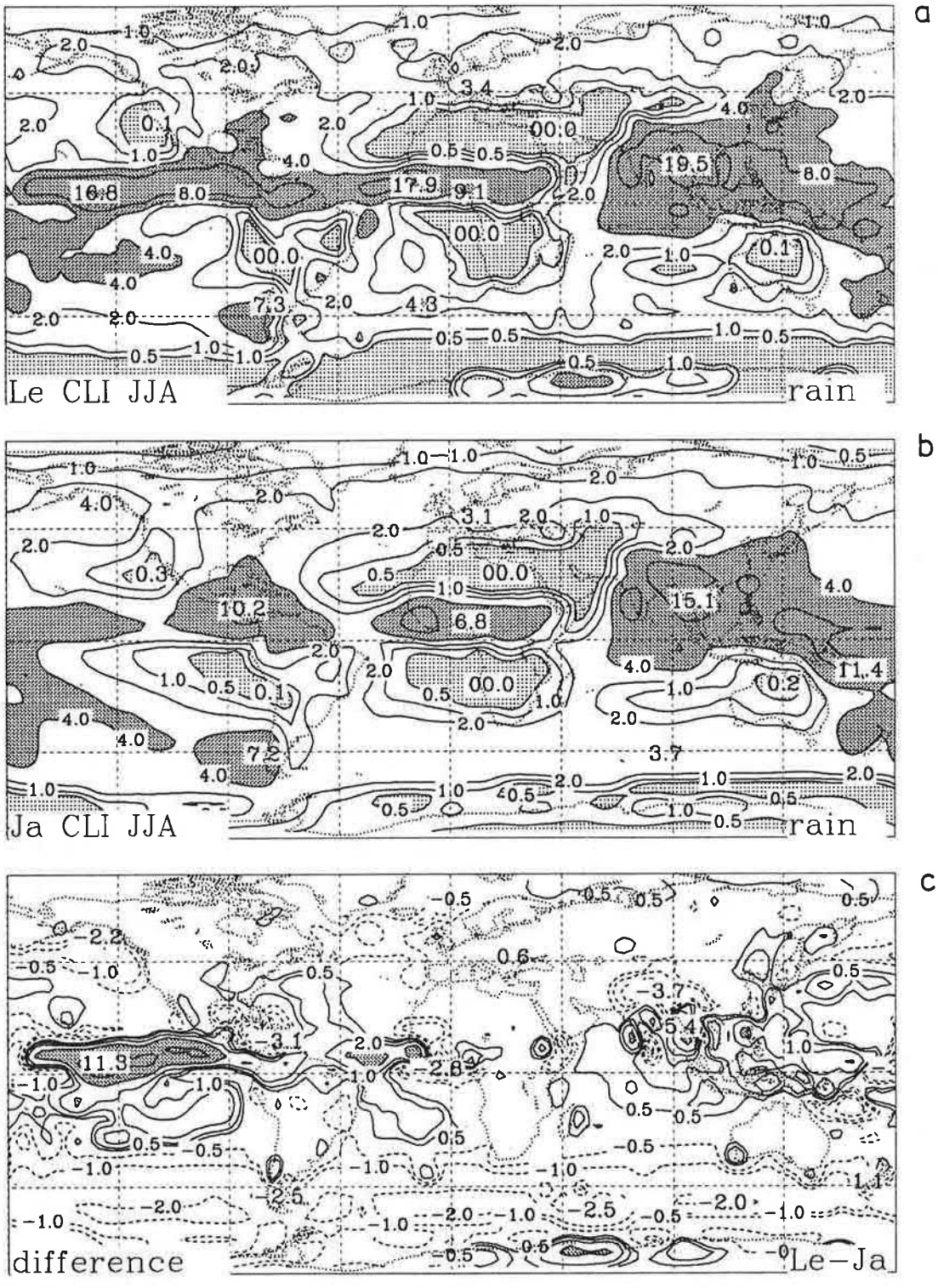

Figure 16 As in Fig. 15 except for the JJA season.

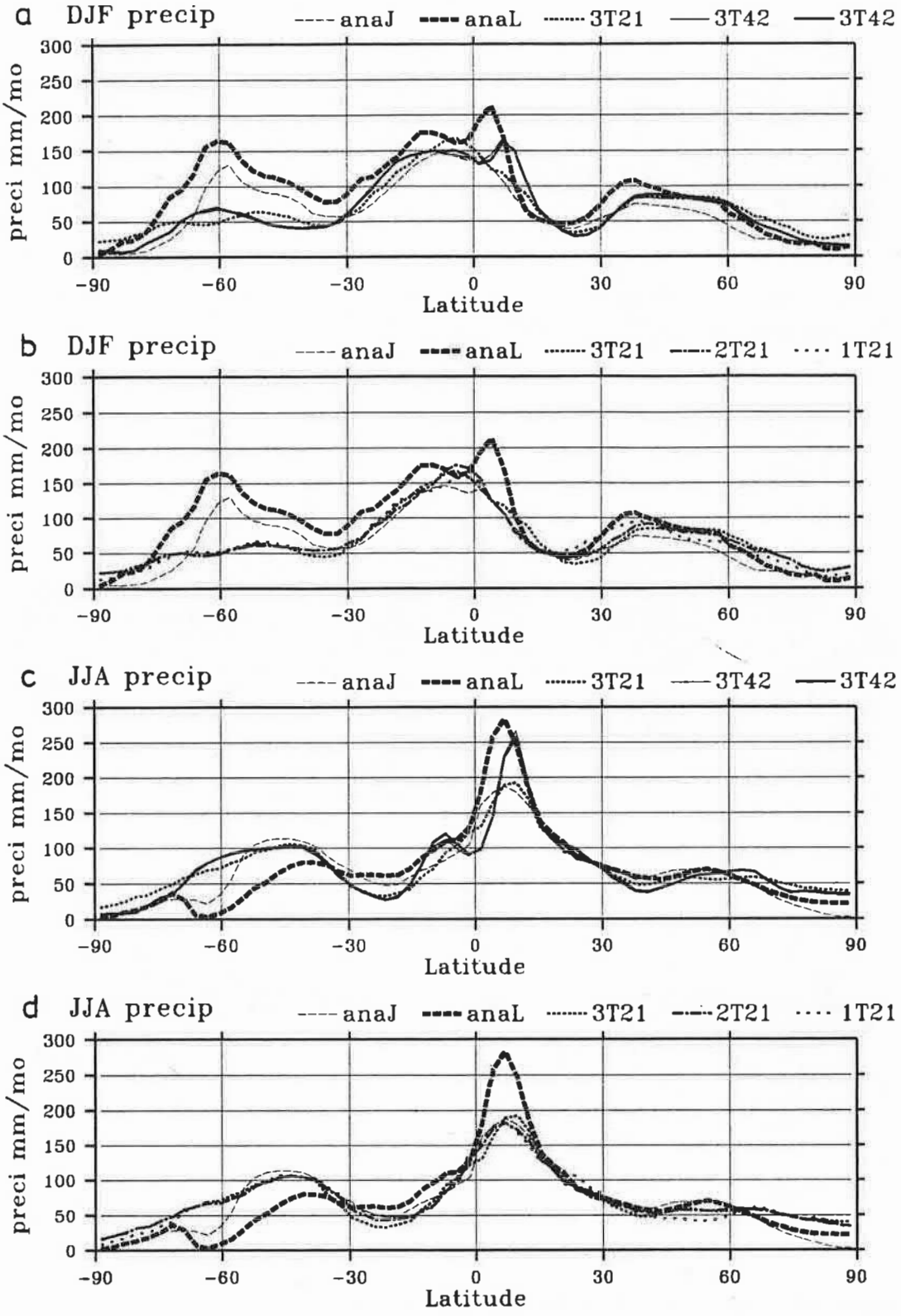

Figure 17 Zonal means of analysed and simulated precipitation for the DJF season (a,b) and for the JJA season (c,d). anaJ and anaL refer to the precipitation climatologies of Jaeger (1976) and Legates and Willmott (1990), respectively. For model notations see Fig. 12.

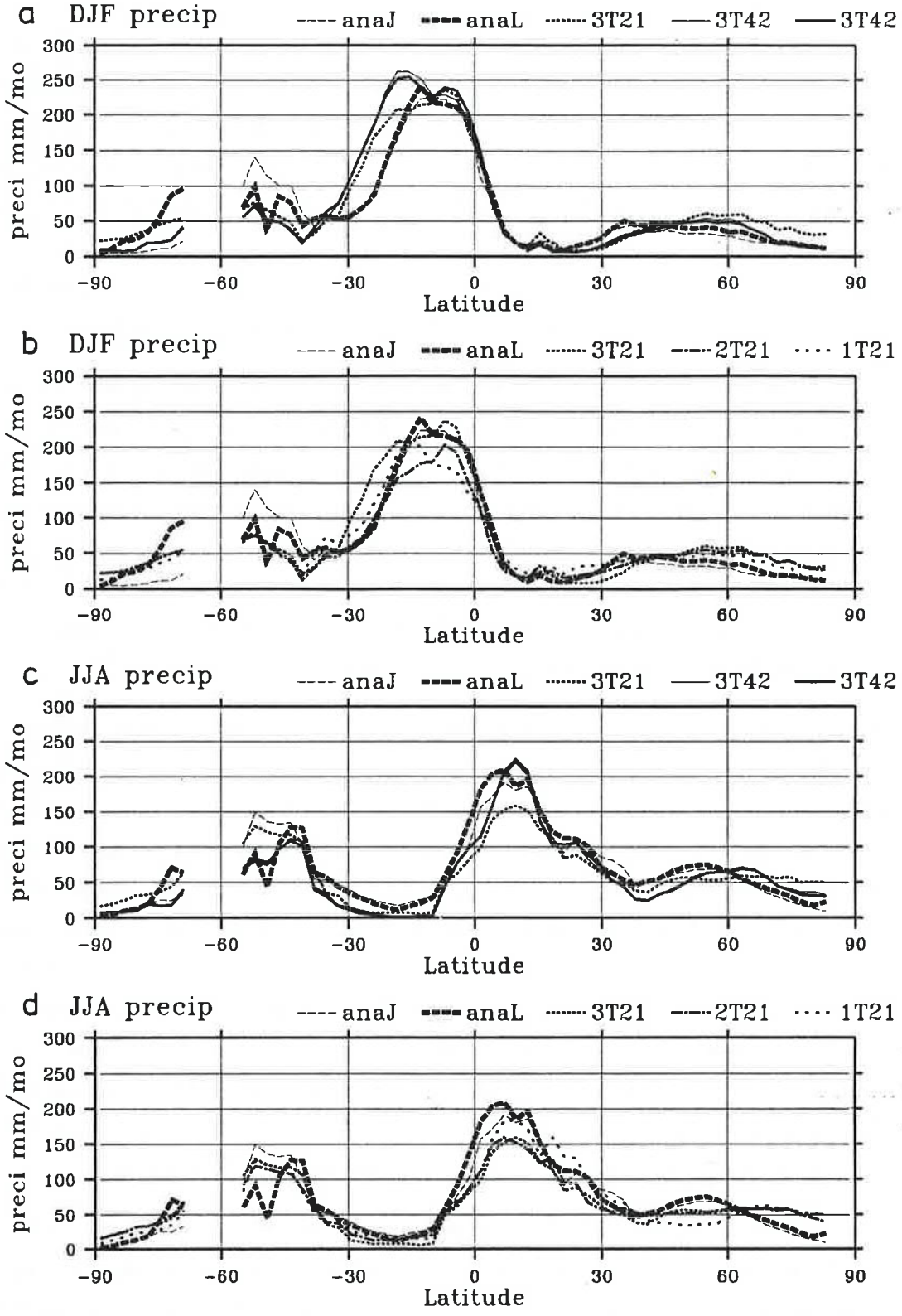

Figure 18 As in Fig. 17 except for the zonal mean precipitation over land.

rates for DJF (upper pair of figures) and for JJA (lower pair). The impact of increased horizontal resolution is shown in Figs. 17a and 17c, respectively, while the impact of different model physics is shown in Figs. 17b and 17d, respectively. Generally, the differences between ECHAM3/T21 and ECHAM3/T42 simulations are larger than those for ECHAM1,2,3 at T21 resolution. During DJF, the T42 model is able to resolve the double maximum in the tropics (slightly displaced to the north, however), which is indicated in the Legates-climatology but not in the Jaeger-climatology (Fig. 17a). The equatorial minimum simulated by the T42 model in JJA (Fig. 17c) is not found in any of the climatologies. The tropical maximum in JJA is more pronounced in the T42 simulation, but the observations provide little guidance because they differ as much as the models do. The observed peak values near 60°S during DJF are not reproduced by any of the models, and this is typical of other GCMs as well (Boer et al., 1991). However, the reliability of the analyses at these latitudes is very low due to a lack of measurements. In the polar regions, an impact of the modified model physics is hardly detectable, whereas the T42 model simulates much lower values which agree favourably with the Legates-climatology in particular.

Over land (Fig. 18) the zonally averaged observed climatologies agree reasonably well, except over the southern tip of South America and in the coastal regions of Antarctica (cf. Figs. 15 and 16). There is also better agreement between the observations and the model results, and apart from a few problem areas the models perform reasonably well. Exceptions are the significantly overestimated precipitation in ECHAM3, particularly at T42 resolution, between about 10°S and 30°S during DJF (Fig. 18a). Moreover, there is generally less than observed precipitation in the subtropics. During JJA, ECHAM3 at both resolutions produces hardly any precipitation near 20°S. In the tropics and at high latitudes, there is a favourable impact of the increased horizontal resolution, however.

The observed (Legates) and simulated global distributions of the precipition rates are shown in Figs. A19 and A20 for DJF and JJA, respectively. There is generally good agreement between the observed and simulated (T42) patterns during DJF in the NH storm track regions (Fig. A19a-c), while the precipitation rates are somewhat smaller in these regions for the T21 models (Figs. A19d-f). Except for a few problem areas, the structure of the tropical precipitation belt is well captured by all of the models while the DJF precipitation maximum over the mid-latitude oceans in the Southern Hemisphere is not reproduced by any of the models (see discussion above). In ECHAM3, in particular in its T42 version, there are a few areas which deserve attention. In DJF there is clearly too much precipitation over South Africa and Australia, and the dry regions with precipitation rates of less than 0.5 mm/day are more extended than the Legates analysis suggests. Both types of errors are less pronounced in ECHAM1 and ECHAM2, if present at all. These models, on the other hand, underestimate the precipitation in those areas of the tropics where the observed values are high (ITCZ, SPCZ, South America, West Pacific).

During JJA (Fig. A20), the ECHAM3/T42 model produces too much precipitation off the west coast of Central America, and this error is consistent with an anomalous circulation pattern showing low-level convergence and high-level divergence (cf. Figs. A8a-c and A10a-c). Moreover, similar to DJF, there is

less precipitation than observed in the "dry" zones, in particular over North and South America and also in the dry regions in the lee of the Himalaya. In the Asian monsoon area, the ECHAM3/T42 model tends to produce too much precipitation over the ocean and not enough over land as, for example, over India. Although less obvious, there is also a lack of precipition over Europe, and in this area the model is not able to reproduce the correct annual cycle with more precipitation in summer than in winter. Most of these model errors can also be identified in ECHAM1 and ECHAM2 as, for example, the lack of summer precipitation over Europe which is even more pronounced in these models. On the other hand, the T21 models generate more precipitation over India, but the observed small-scale structure of the monsoon precipitation is better reproduced at higher resolution. Similar conclusions are found by Sperber and Palmer (1992) who investigated the resolution dependence of the Indian monsoon simulation using the ECMWF model.

5.2 TRANSIENT FLUCTUATIONS AND STATIONARY EDDIES

The analysis of the transient and stationary variances and covariances follows the standard procedure. The stationary eddies are defined as departures from the respective zonal means, averaged over season (here: DJF). The stationary variances and covariances are calculated from the individual seasonal mean stationary eddies and then averaged over the respective seasonal samples.

Transient eddies are defined as the departure of a 12-hourly value (sampling interval of the simulations) of the respective variable from its seasonal mean. The transient variances and covariances are calculated for both, unfiltered and filtered time series, of the respective season. For time filtering we use the method of Blackmon (1976) in order to separate high-frequency fluctuations associated with traveling cyclones, for example, and low-frequency fluctuations which characterize processes like mature and decaying cyclones, blocking highs or regime transitions. The frequency response of the filter is the same as used by Blackmon (1976). The so-called band-pass filter emphasizes periods between about 2.5 and 6 days, whereas the low-pass filter emphasizes periods between 10 and 90 days with the seasonal cycle removed (Ponater et al., 1990).

The results are presented analogously to the respective time-mean variables (section 5.1) in the form of zonally averaged cross sections. Additionally, a selection of maps is presented in Appendix A in order to discuss the regional distribution of the eddy statistics during winter (DJF) in the Northern Hemisphere (Figs. A21-A44). Results are presented for the following statistics: Root-mean-square deviation of temperature and geopotential height, kinetic energy, northward transport of westerly momentum and sensible heat. For each variable, we show the respective unfiltered, band-pass filtered, low-pass filtered and stationary eddy statistics.

Temperature fluctuations

The zonally averaged transient temperature fluctuations (RMS) for DJF are shown in Figs. 19-21 for the

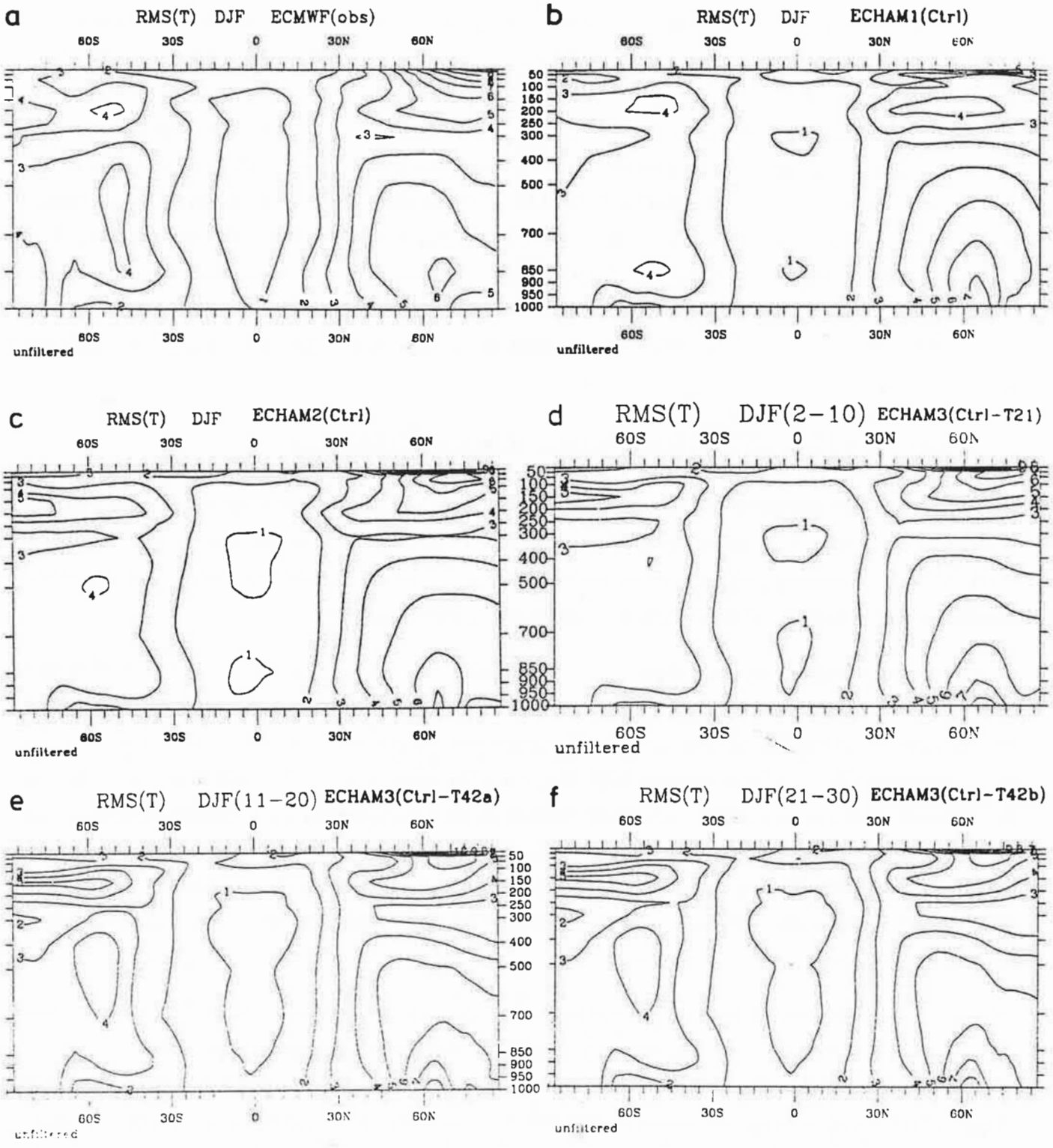

Figure 19 Latitude-pressure distributions of zonal mean standard deviation of temperature (K) due to transient eddies computed from the unfiltered time series for the DJF season. (a) ECMWF analyses, (b-f) model simulations. The lower panel (e,f) shows two 10-year samples of ECHAM3/T42.

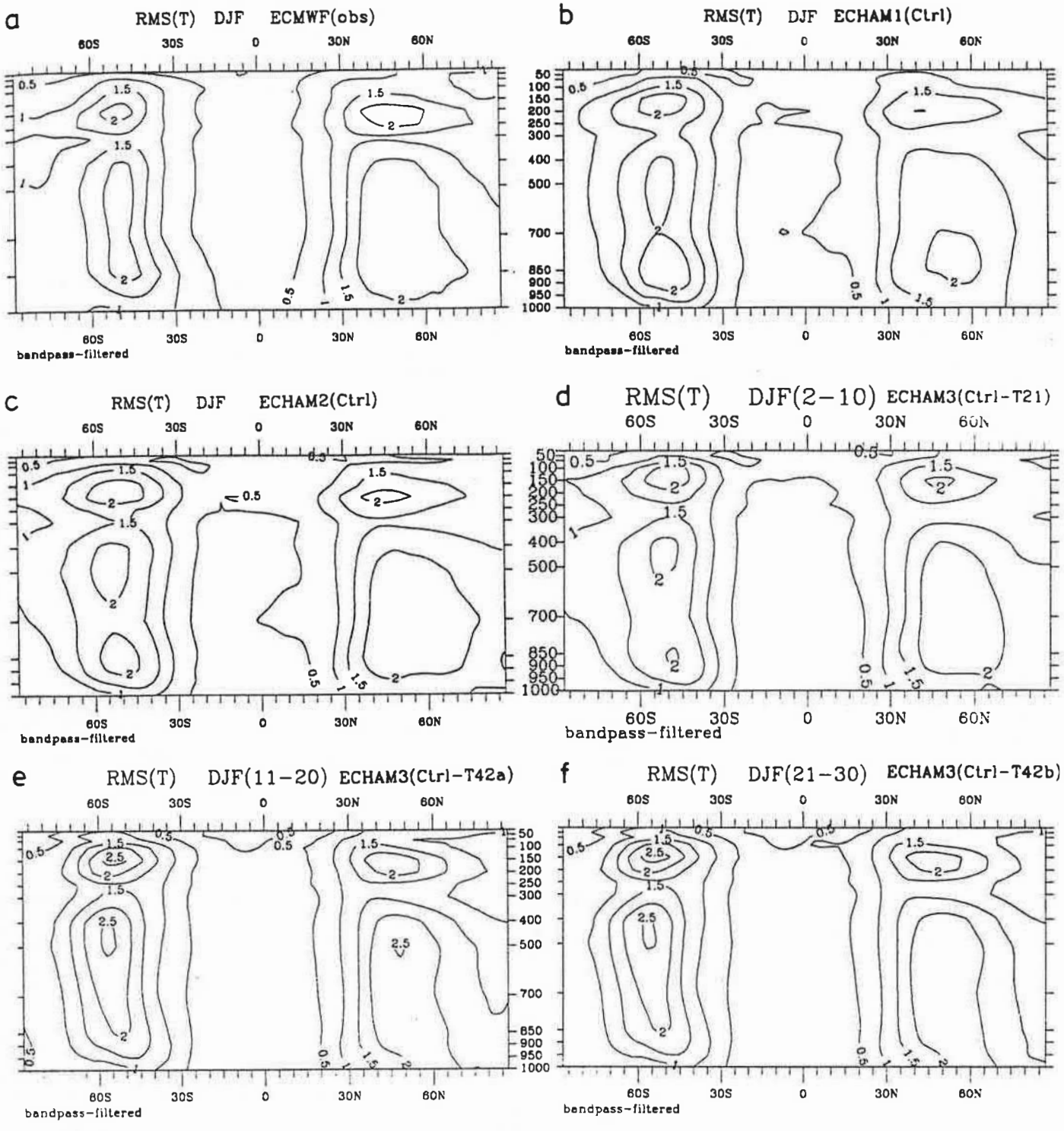

Figure 20 As in Fig. 19 except for the band-pass filtered frequency range.

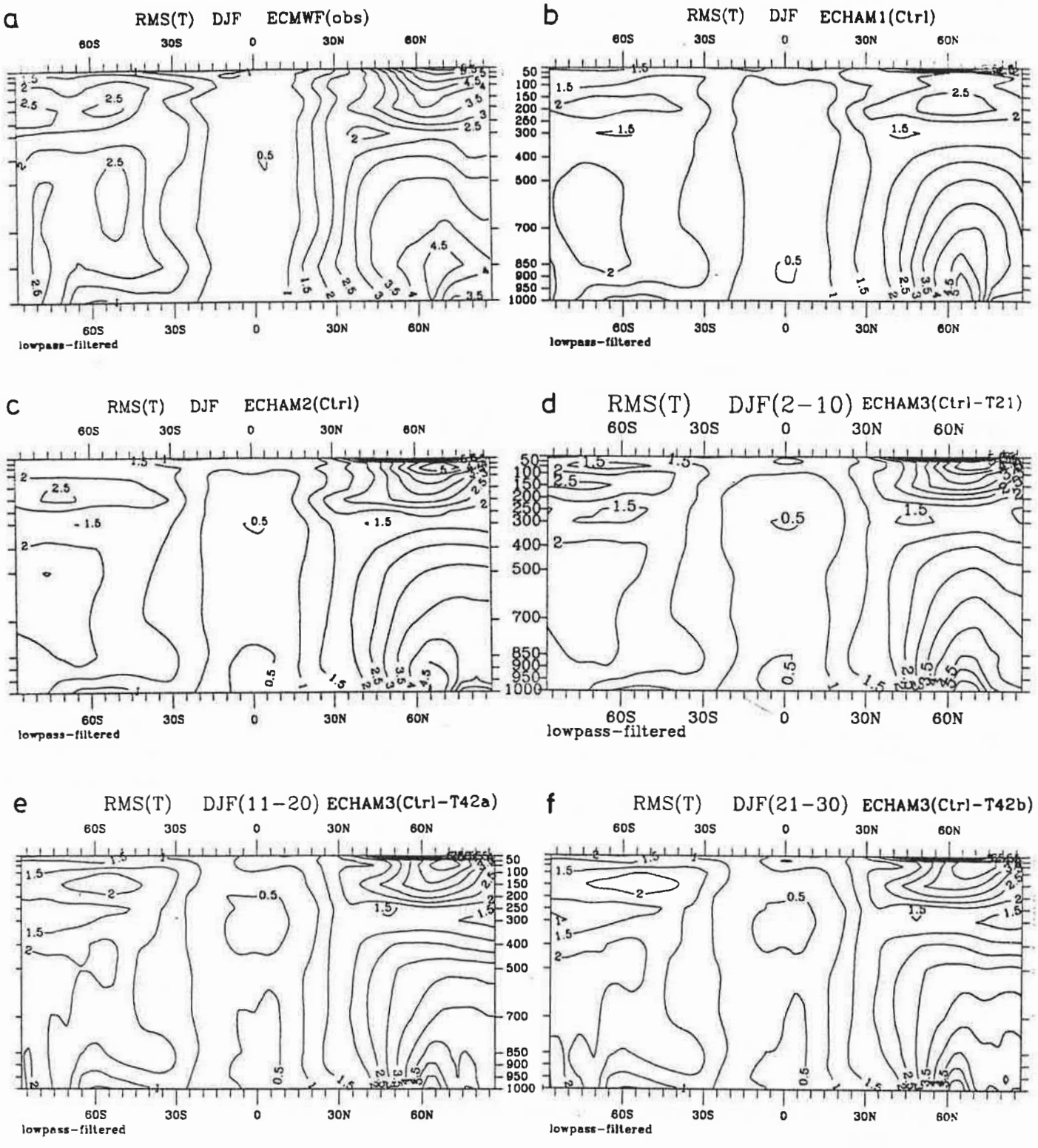

Figure 21 As in Fig. 19 except for the low-pass filtered frequency range.

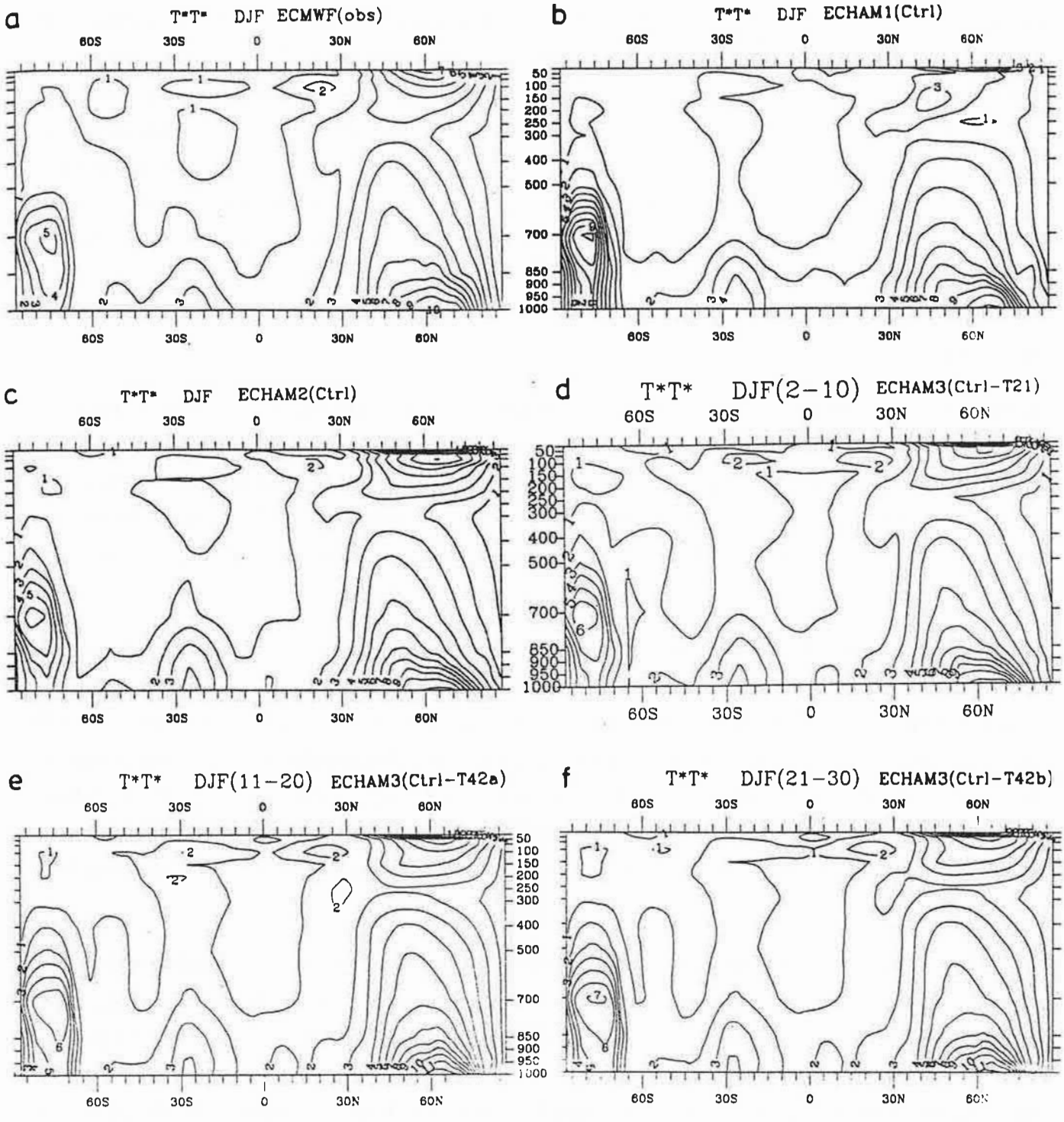

Figure 22 As in Fig. 19 except for the standard deviation of temperature due to stationary eddies.

unfiltered data (Fig. 19), for the band-pass filtered data (Fig. 20) and for the low-pass filtered data (Fig. 21). In addition, the respective stationary eddy variances are shown in Fig. 22. All models are able to capture the observed pattern of the unfiltered and band-pass filtered RMS-values with reasonable skill, but the T42 model performs somewhat better in the tropics and in the Southern Hemisphere. In ECHAM1 (upper right panel), the band-pass filtered RMS-values are somewhat too small in the Northern Hemisphere. The low-frequency variability (Fig. 21) is also reasonably well simulated by all models in the Northern Hemisphere (except for a lack of stratospheric variance in ECHAM1), but the simulated tropospheric values are lower than observed in the Southern Hemisphere. The low-frequency variability in the tropics is also too small in all models, partly to be attributed to missing interannual SST fluctuations.

In the Northern Hemisphere, the stationary eddy variance (Fig. 22), generated by orography and land-sea contrast, has local maxima close to the surface and in the stratosphere, similar to the transient eddy variance. In the Southern Hemisphere (summer!), the pattern is quite different with peak values over Antarctica and a secondary maximum generated by the Andes mountains near 30°S. Except for the lack of stationary eddy variance of ECHAM1 in the stratosphere, there is no evidence of a significant model dependence, and the models agree favourably with observations also.

Maps of the transient temperature fluctuations for the Northern Hemisphere winter at 850 hPa and 500 hPa, respectively, are shown in Figs. A21-A26. There is generally good agreement between the model results and the observations. In particular, the regional separation of the band-pass fluctuations at 850 hPa, with large values generated by developing baroclinic wave disturbances over the western parts of the mid-latitude oceans (Fig. A22), and peak values of low-frequency variability over the Rocky Mountains (Fig. A23), is well simulated by all models. The relatively weak band-pass filtered eddy activity in the ECHAM1 model (Fig. A22b) is consistent with the poorly developed Icelandic low in that model (cf. Fig. A11b).

At 500 hPa (Figs. A24-A26), the impact of increased resolution is evident for the simulation of the band-pass RMS-values (Fig. A25). Especially over the Atlantic Ocean, the T42 model simulates larger and also more realistic values. Again, ECHAM1 shows the poorest simulation (Fig. A25b) while ECHAM3/T21 (Fig. A25d) is slightly more realistic than ECHAM2 (Fig. A25c) over the Atlantic Ocean whereas the maximum variance in the Pacific is shifted too far to the east. A similar tendency can also be seen in the T42 model (Figs. A25e,f). All models slightly underestimate the low-pass RMS-values over North America (Fig. A26). The observed low-pass maximum of 4K over Scandinavia is indicated only during the first decade of the T42 simulation (Fig. A26e).

Geopotential height fluctuations

The differences between the model simulations on the one side, and between the model simulations and the observations on the other side, are slightly more pronounced in the geopotential height fluctuations

than in the temperature fluctuations.The poorest simulation is provided by ECHAM1 with significantly too small values in both hemispheres (Figs. 23-26). While ECHAM3/T21 is slightly more realistic than ECHAM2, there is a major improvement with increased resolution in the band-pass range (Figs. 24e,f) where the T42 simulation is close to the observations.The impact of increased horizontal resolution on the simulation of the low-frequency variability (which is too small in all model versions) is insignificant, however. There is also little evidence of a resolution effect on the simulation of the stationary eddies (Fig. 26) but there is a substantial difference between the T21 model simulations, and the largest and also most realistic values are simulated by ECHAM3.

On the regional scale (Figs. A27-A32), the observed separation of the areas with large band-pass filtered variance at 1000 and 500 hPa, respectively (Figs. A28,A31), and those with large low-pass filtered variances (Figs. A29,A32) is well simulated by all models. The impact of increased resolution is apparent in the band-pass range, where the ECHAM3/T42 model simulates larger and generally more realistic values than its T21 counterpart. There is, however, little if any improvement in the low-frequency range at 1000 hPa (Fig. A29), while at 500 hPa the T42 simulation is more realistic, particularly over Scandinavia (Fig. A32). The observed level of low-frequency variability is reached, however, by none of the models.

Kinetic energy

In Figs. 27-30 we compare the observed (upper left) and simulated zonal mean transient and stationary kinetic energies. It is evident that all T21 versions are not able to reproduce the observed level of transient kinetic energy (Fig. 27b-d) whereas the T42 model (Figs. 27e,f) simulates the peak values and also the distribution with remarkable skill, except for a poleward displacement of the SH maximum. Furthermore, the maxima in both hemispheres are displaced upwards to a level of about 250 hPa while the ECMWF analyses suggest a height of approximately 300 hPa. The impact of the horizontal resolution on the simulation of transient kinetic energy is, however, strongly model dependent. In a study using the Canadian Climate Center (CCC) model, Boer and Lazare (1988) found only a weak resolution dependence between T20 and T40, while Boville (1991) found a systematic increase with resolution (T21, T31, T42, T63) of the transient kinetic energy in the CCM1 model of the National Center for Atmospheric Research (NCAR). Both GCMs suffered, however, from a general lack of transient kinetic energy, and the peak values simulated by CCM/T40 and CCM1/T63 were comparable to those of ECHAM3/T21, for example.

The impact of resolution in the ECHAM model is particularly evident in the band-pass range (Fig. 28) whereas the differences in the low-frequency range (Fig. 29) and for the stationary eddies (Fig. 30) are less obvious. There is, however, a marked impact of model physics on the simulation of the stationary kinetic energy with peak values nearly twice as large in ECHAM3/T21 (Fig. 30d) as compared to those of ECHAM1 or ECHAM2 (Figs. 30b,c).

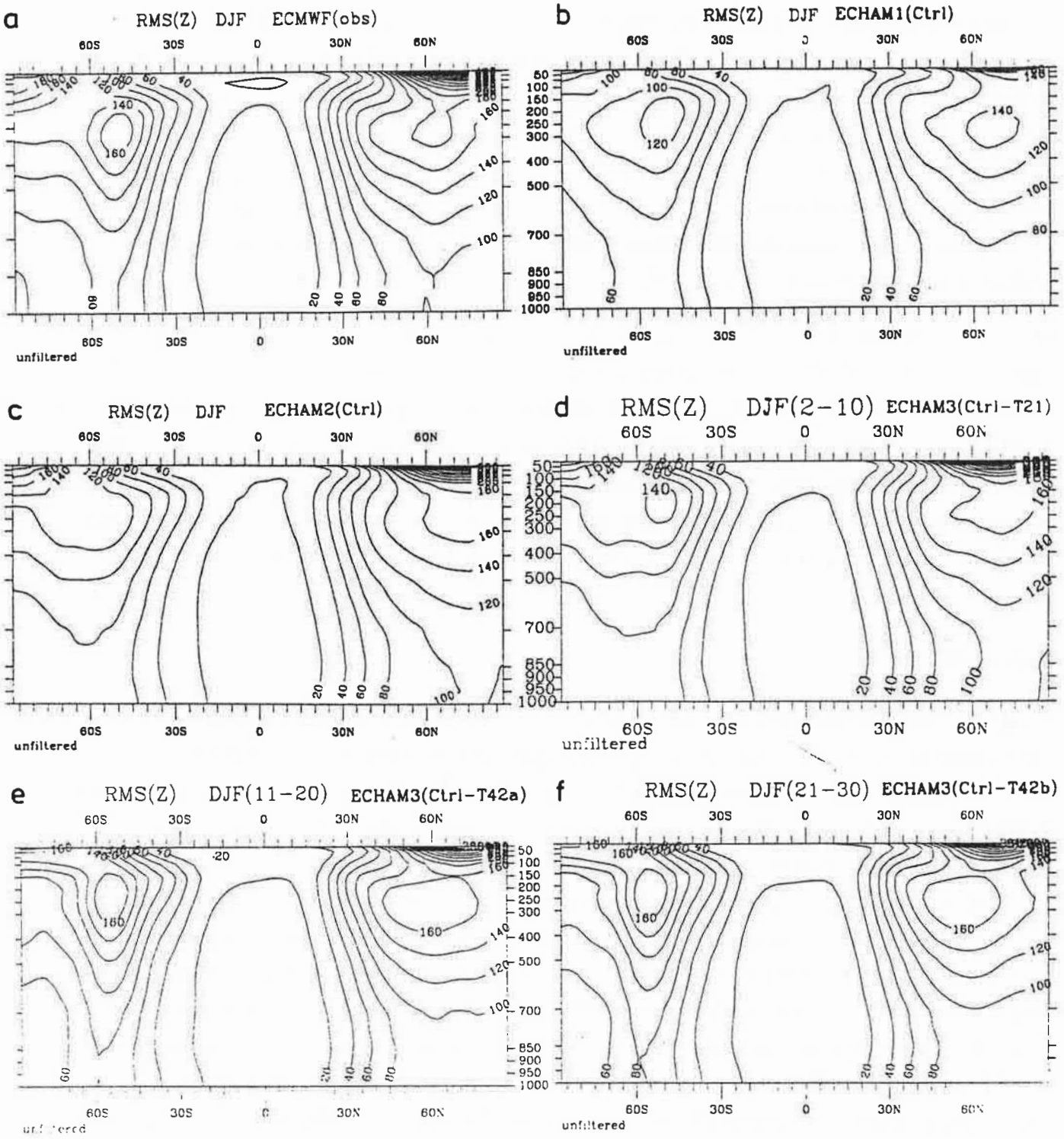

Figure 23 Latitude-pressure distributions of zonal mean standard deviation of geopotential height (m) due to transient eddies computed from the unfiltered time series for the DJF season. a) ECMWF analyses, (b-f) model simulations. The lower panel (e,f) shows two 10-year samples of ECHAM3/T42.

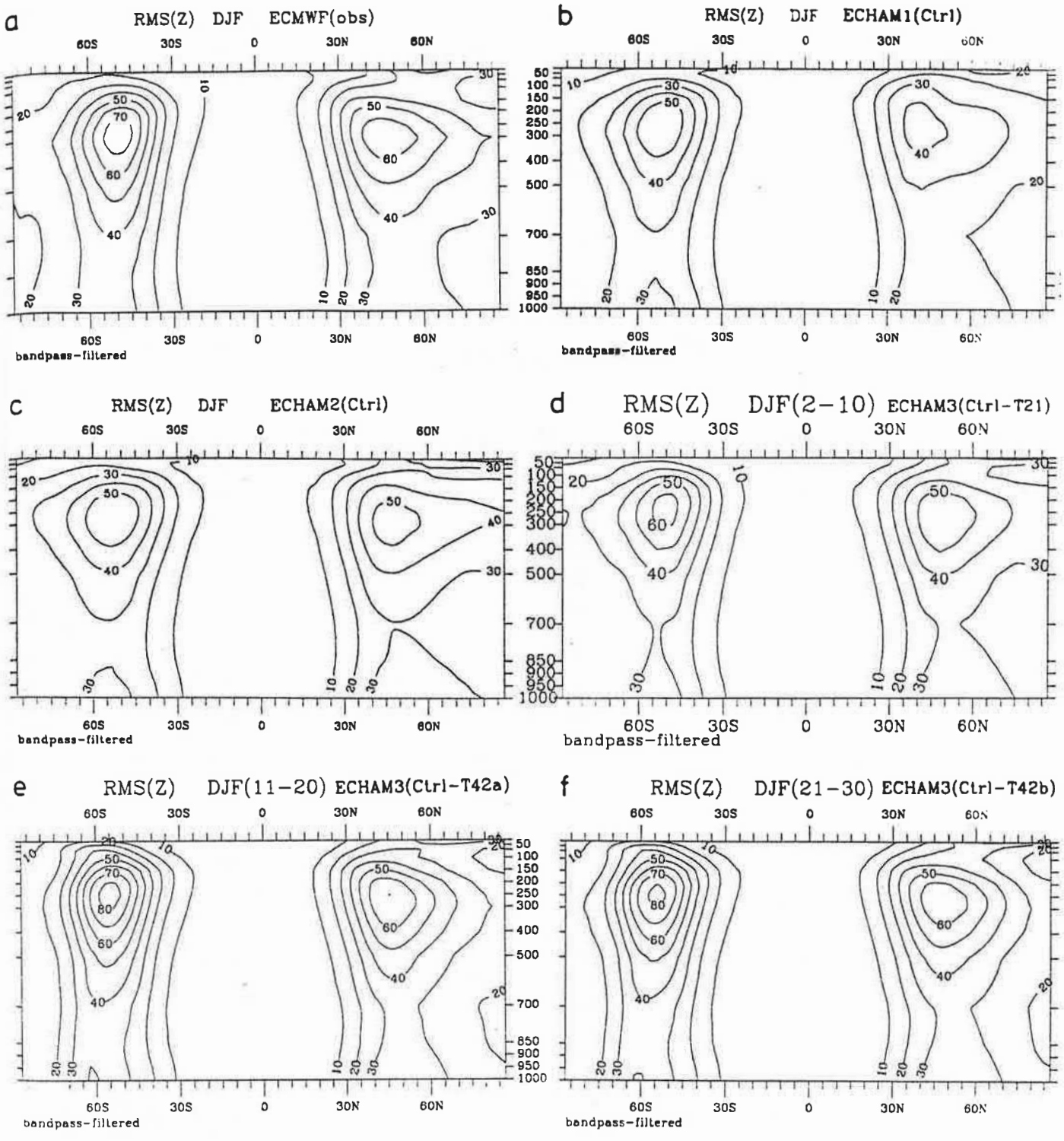

Figure 24 As in Fig. 23 except for the band-pass filtered frequency range.

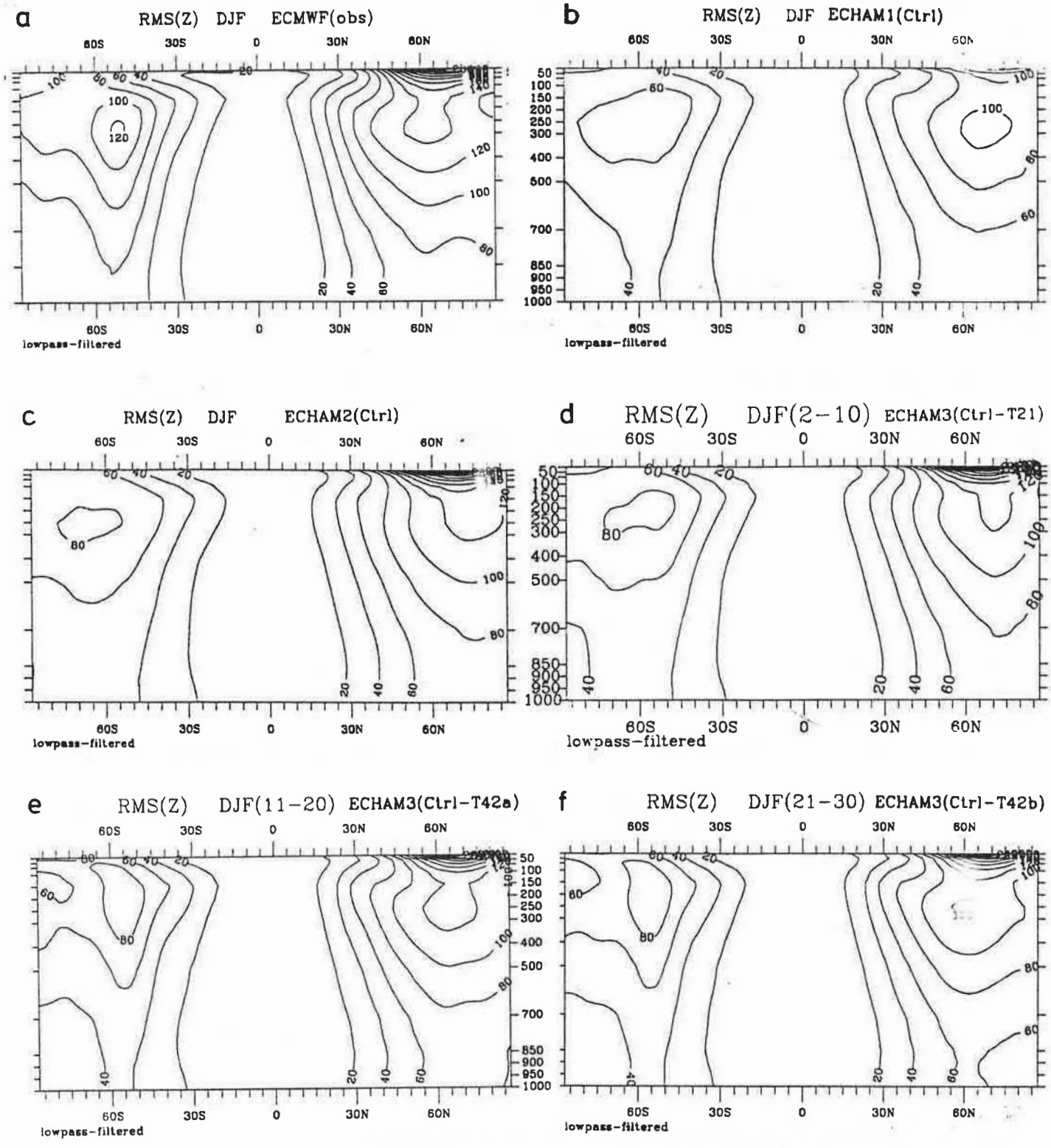

Figure 25 As in Fig. 23 except for the low-pass filtered frequency range.

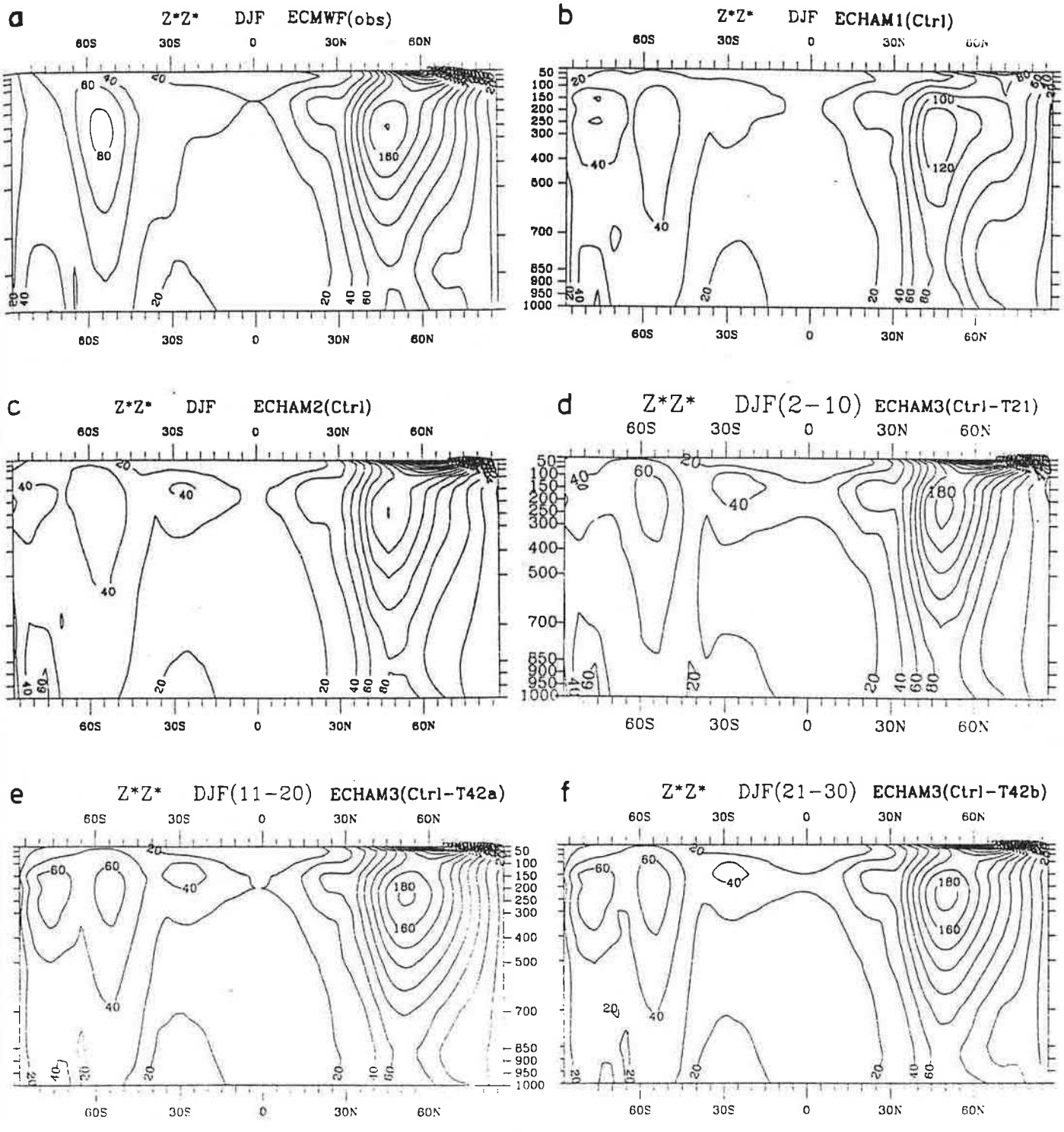

Figure 26 As in Fig. 23 except for the standard deviation of geopotential height due to stationary eddies.

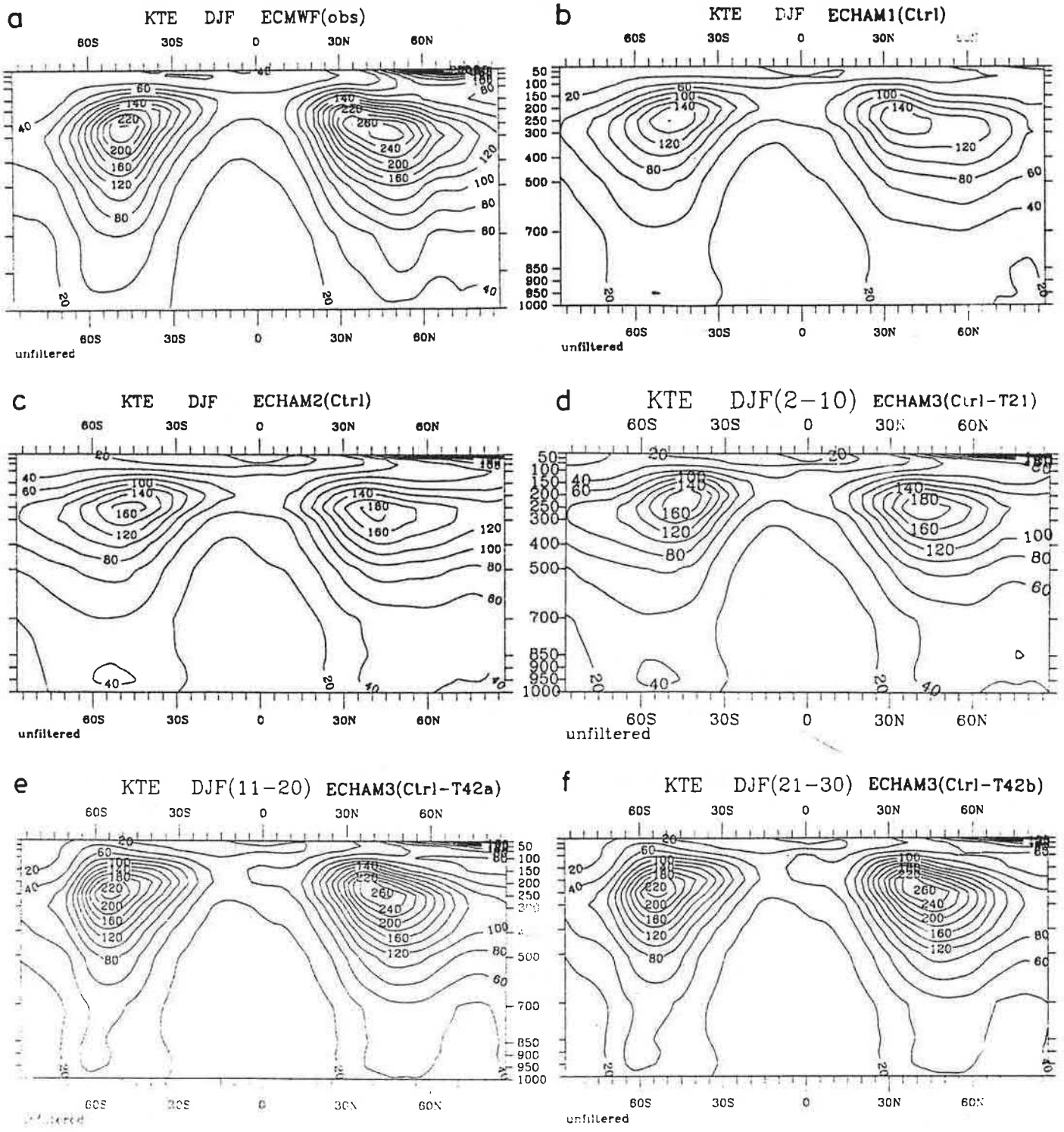

Figure 27 Latitude-pressure distributions of zonal mean transient eddy kinetic energy (m^2/s^2) computed from the unfiltered time series for the DJF season. a) ECMWF analyses, (b-f) model simulations. The lower panel (e,f) shows two 10-year samples of ECHAM3/T42.

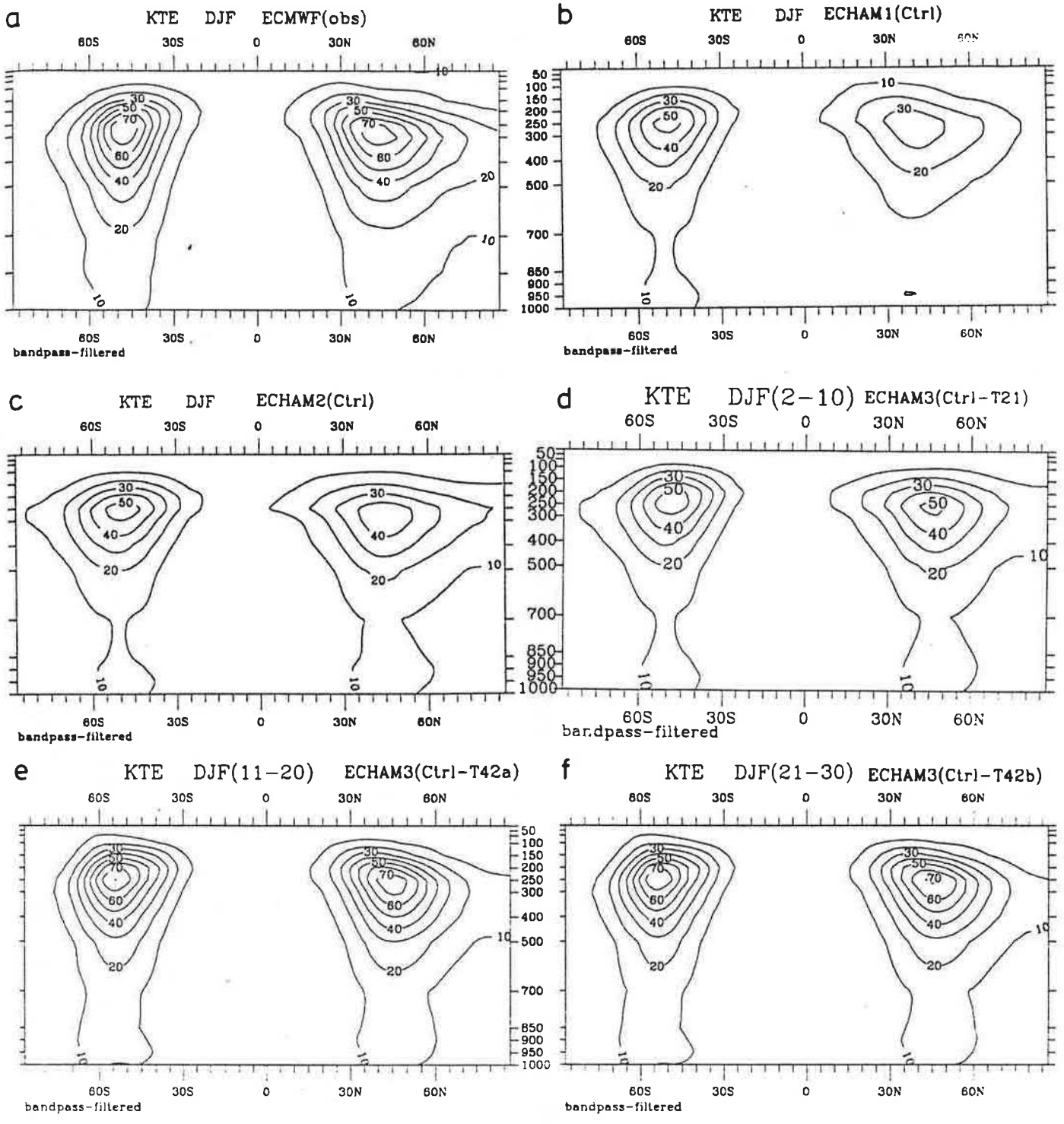

Figure 28 As in Fig. 27 except for the band-pass filtered frequency range.

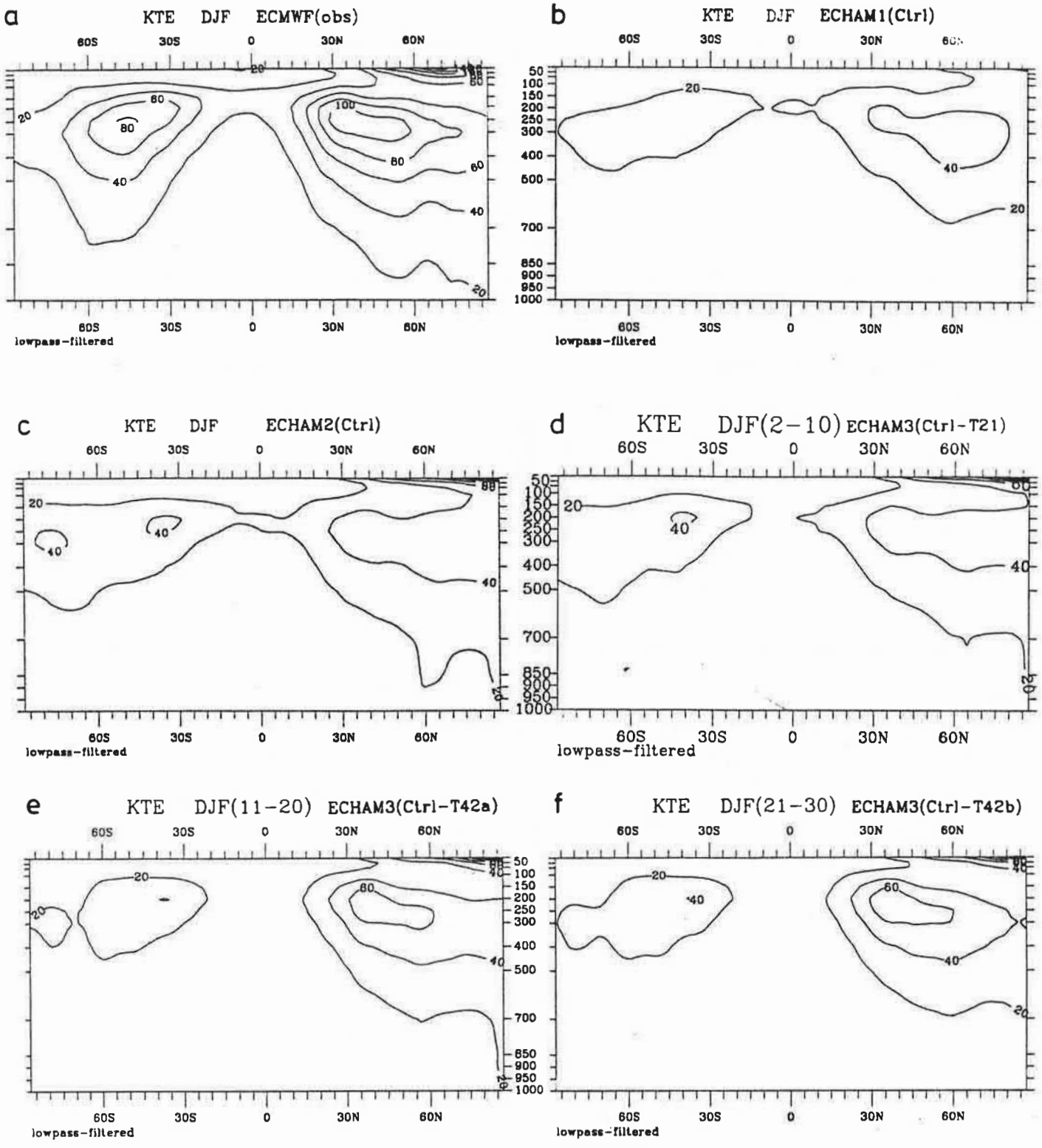

Figure 29 As in Fig. 27 except for the low-pass filtered frequency range.

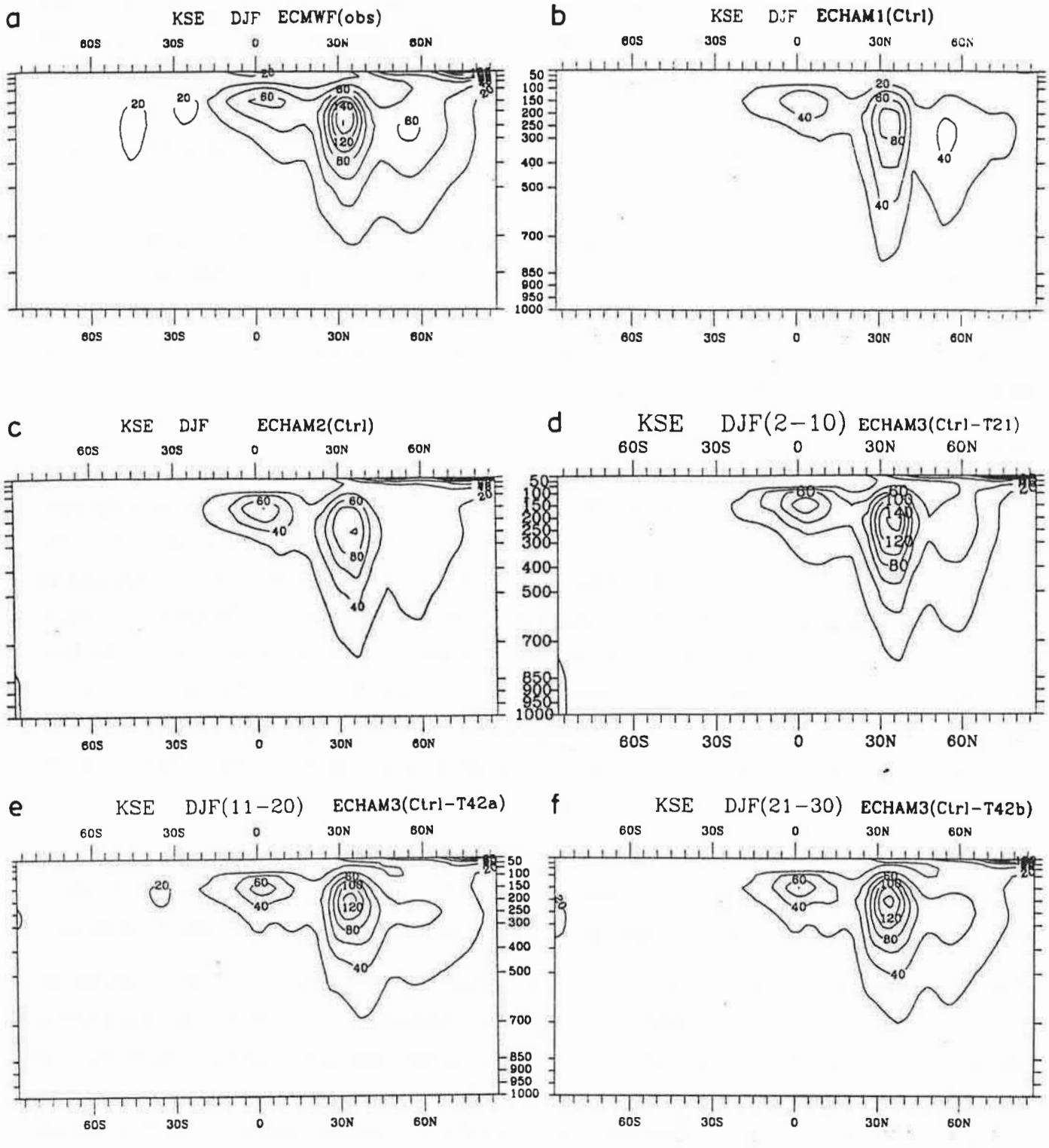

Figure 30 As in Fig. 27 except for the stationary eddy kinetic energy.

All of the differences discussed above are evident on the regional scale as well (Figs. A33-A35). The unfiltered transient eddy kinetic energy at 300 hPa (Fig. A33) is significantly higher at T42 resolution than at T21 resolution and also more realistic although the simulated values are systematically smaller than the observations suggest (Fig. A33a). As discussed above, this deficit does not indicate a general underestimation of the transient kinetic energy in the T42 model but rather an upward displacement of the level where the peak values are simulated (cf. Figs. 27a and 27e,f).

The impact of increased resolution is significant in the band-pass range (Fig. A34) while the impact of changed physics is noticeable only between ECHAM1 and ECHAM2 in the North Atlantic area. In the low-frequency range (Fig. A35), all models fail to simulate the observed values. Nevertheless, the simulations seem to gradually approach the observations with more elaborate physics (ECHAM1 to ECHAM3) and with higher resolution as well.

Momentum fluxes

One of the most serious deficiencies of the ECHAM0/T21 model is a drastic underestimation of the meridional fluxes of westerly momentum by transient eddies (Ponater et al., 1990). To some extent, this shortcoming is also apparent in the more recent low-resolution ECHAM versions (Figs. 31-33) although the simulations are much more realistic in the Southern Hemisphere as compared to ECHAM0. In the band-pass range, there is also a gradual improvement from ECHAM1 to ECHAM3, particularly in the Northern Hemisphere (Figs. 32b-d). The most dramatic change is caused, however, by the increased horizontal resolution in the T42 model with nearly a doubling of the band-pass filtered westerly momentum fluxes in both hemispheres. In fact, the simulated values are generally larger than the ECMWF analyses suggest.

The impact of increased resolution can also be seen in the low-pass range (Fig. 33) where the T42 model simulates significantly larger momentum fluxes than the T21 models but still underestimates the observed fluxes by typically 30%. In this frequency range the impact of changed physics is hardly detectable.

The stationary eddy momentum fluxes (Fig. 34) are negligible in the Southern Hemisphere (during the summer months!), but they have a distinct maximum of northward transport in the Northern Hemisphere (during winter!) associated with a southwest-northeast tilt of the stationary troughs and ridges between about 15°N and 55°N (cf., the time-mean 500 hPa height distribution shown in Fig. A15). The southward transport of westerly momentum, on the other hand, indicates a northwest-southeast tilt of the respective trough and ridge axes which is unrealistically strong in the ECHAM1 model (cf. Fig. A15b) but not strong enough in the other model versions. Apart from the deficient ECHAM1 simulation, the model simulations are fairly realistic, and there is less model dependence than for the transient momentum fluxes.

Maps of the transient eddy momentum fluxes at 300 hPa (Figs. A36-A38) indicate that, apart from the

ECHAM1 model, all models are able to reproduce the observed large-scale pattern of the unfiltered fluxes (Fig. A36), such as the large poleward transports of westerly momentum over North America, North Africa and East Asia, and the southward transports to the north of about 50°N with peak values over the East Pacific and over the North Atlantic. Over North America and over the East Pacific, all models overestimate the northward transport of westerly momentum, particularly at T42 resolution. The observed large poleward fluxes over the Central Pacific are not reproduced by any of the models.

In the band-pass range (Fig. A37), the largest model errors are found over the Pacific and over North America. The ECMWF analyses show a distinct dipole pattern over the Central Pacific and a clear separation of this pattern from an area with large northward transport of westerly momentum over North America (Fig. A37a). In the models, however, except for ECHAM2 and ECHAM3/T42 during the first decade (Figs. A37c,e), the Pacific dipole is but weakly developed and the maximum over North America is too pronounced in the T42 simulation. In ECHAM1 (Fig. A37b), the areas with large southward transport are too extended while the northward transport is much too weak. In the Atlantic-European area, the most realistic simulation is provided by the T42 model which is able to reproduce the characteristic southwest-northeast orientation of the dipole pattern with remarkable skill (Figs. A37e,f). The increased convergence of the momentum flux over Scandinavia and England during the second decade of the T42 simulation is consistent with the deepening of the Icelandic low and with the enhanced flow in the whole troposphere over that area (cf. Figs. A7b,c; A9b,c; A11e,f; A15e,f).

The notorious underestimation of the low-frequency variability in all ECHAM simulations is also apparent in the respective momentum fluxes, particularly in the low-resolution models (Fig. A38).

Heat fluxes

The zonal mean meridional heat fluxes by transient and stationary eddies (Figs. 35-38) are well reproduced by the models. The largest model errors are found in the upper troposphere, particularly in the T42 simulation, where the simulated heat fluxes are significantly too large, consistent with the overestimated meridional temperature gradient at these levels (cf. Fig. 6).

In the band-pass range (Fig. 36), all models perform reasonably well in the lower troposphere (except for ECHAM1 in the Northern Hemisphere), while the upper tropospheric meridional heat fluxes are again too large in the T42 model. The deficit of low-frequency variance is less obvious for the heat fluxes (Fig. 37), and the model dependence of the simulated heat fluxes is not very pronounced. This applies also to the simulated stationary eddy heat fluxes which are reasonably well simulated by all of the models, except for ECHAM1 in the stratosphere (Fig. 38) where the simulated values are much too small.

The maps of the meridional heat fluxes by transient eddies at 850 hPa (Figs. A39-A41) show a distinct regional separation of the band-pass filtered fluxes with peak values generated by developing baroclinic

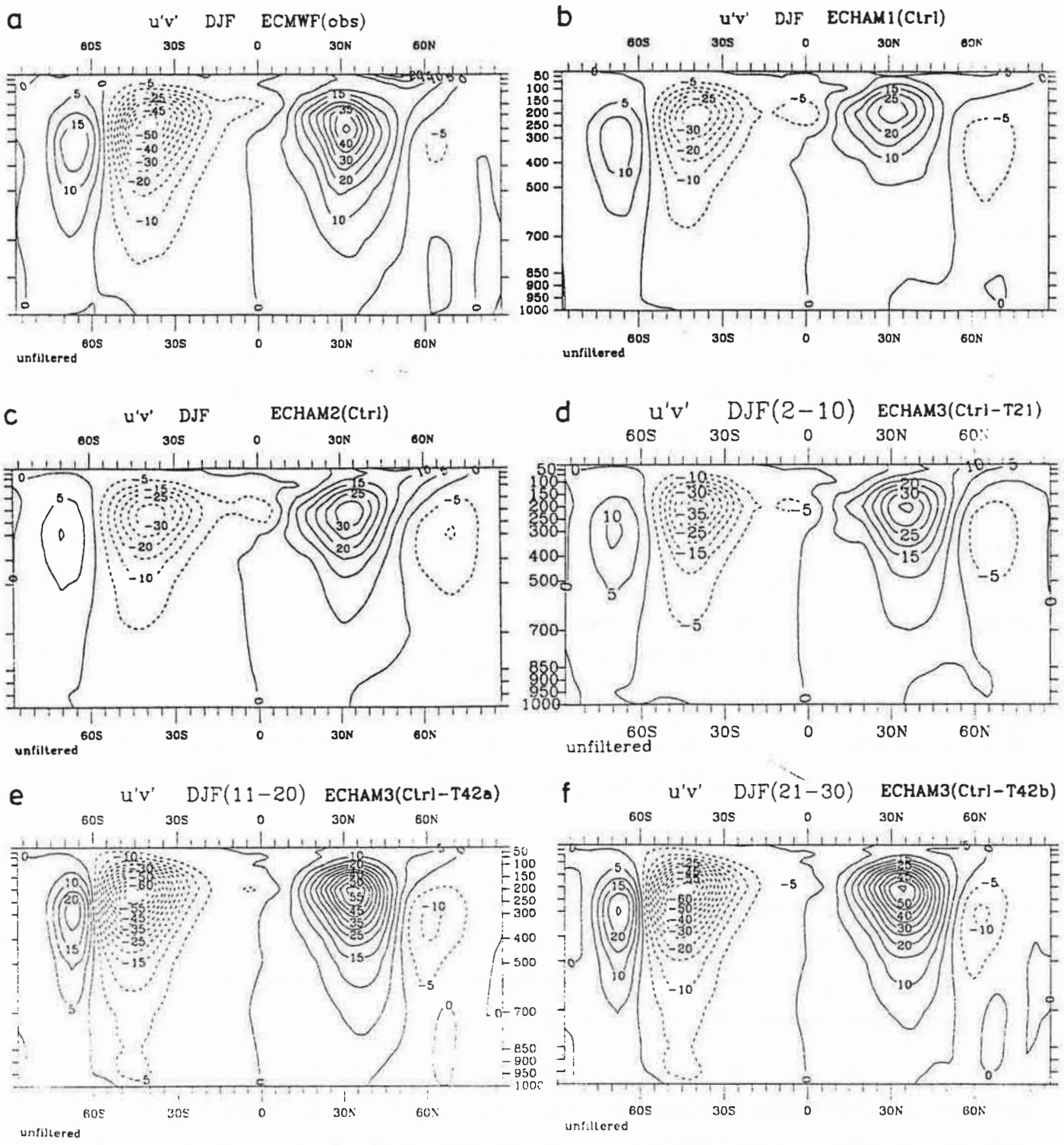

Figure 31 Latitude-pressure distributions of the zonal mean northward transport of westerly momentum by transient eddies (m^2/s^2) computed from the unfiltered time series for the DJF season. a) ECMWF analyses, (b-f) model simulations. The lower panel (e,f) shows two 10-year samples of ECHAM3/T42.

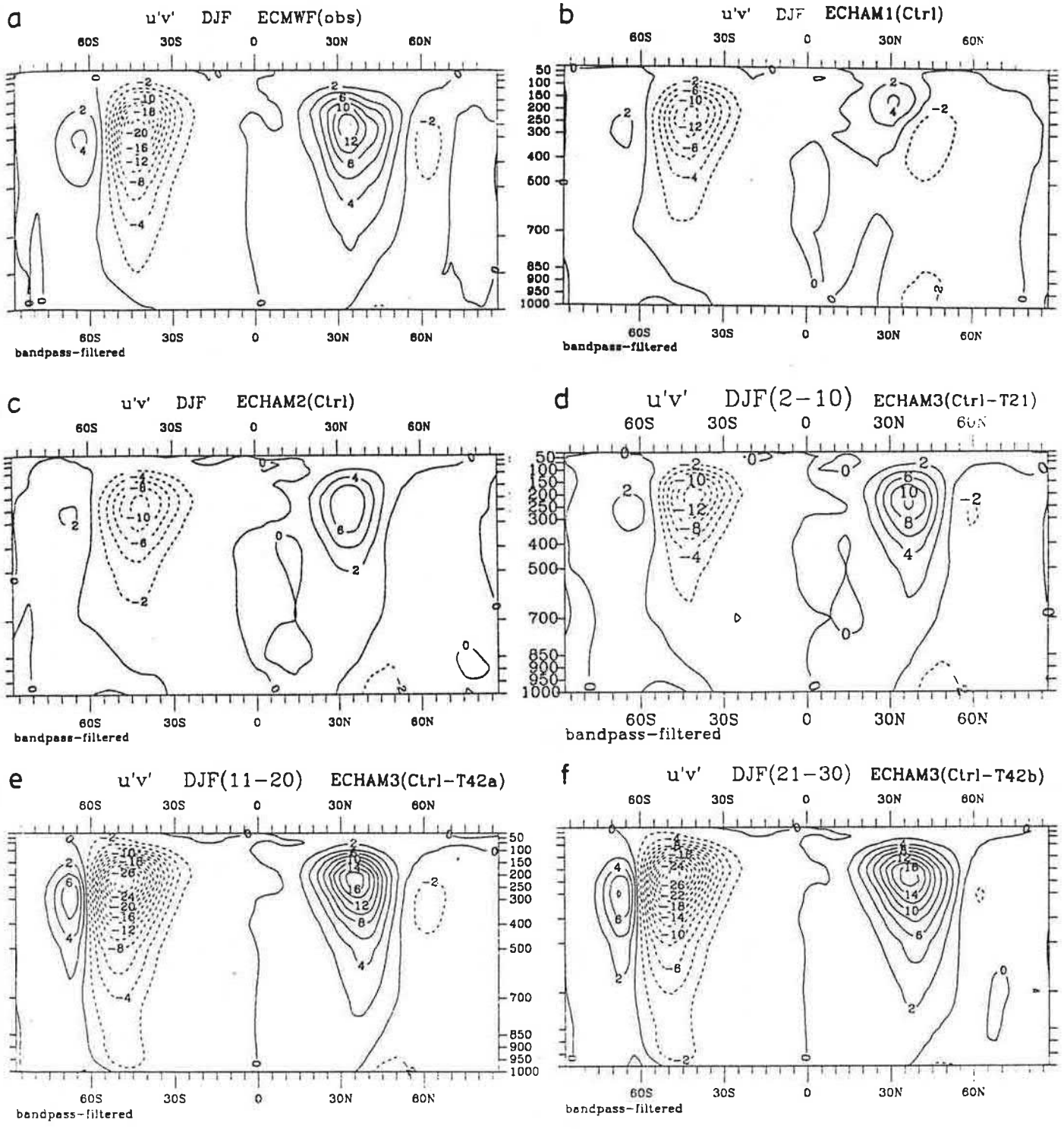

Figure 32 As in Fig. 31 except for the band-pass filtered frequency range.

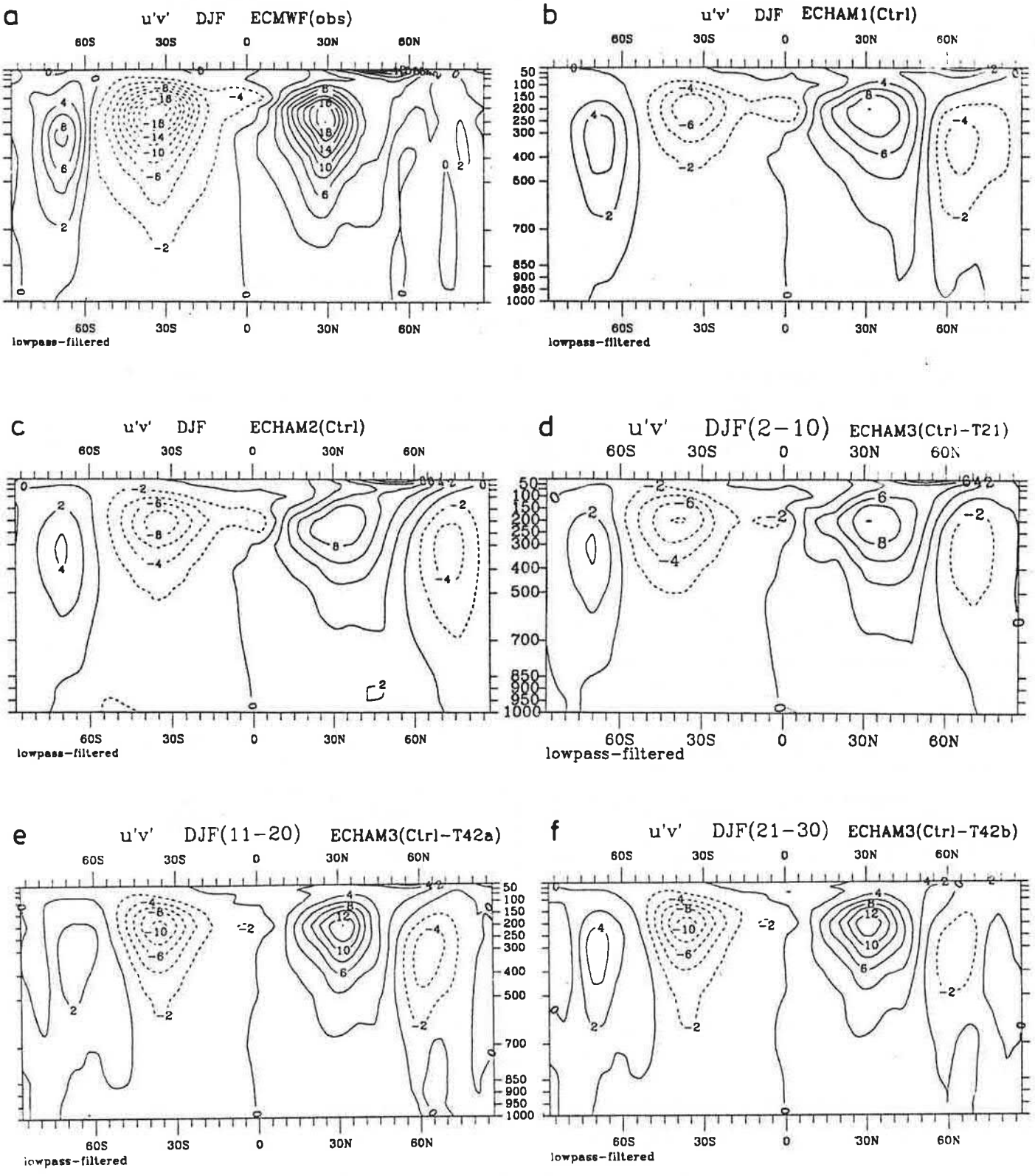

Figure 33 As in Fig. 31 except for the low-pass filtered frequency range.

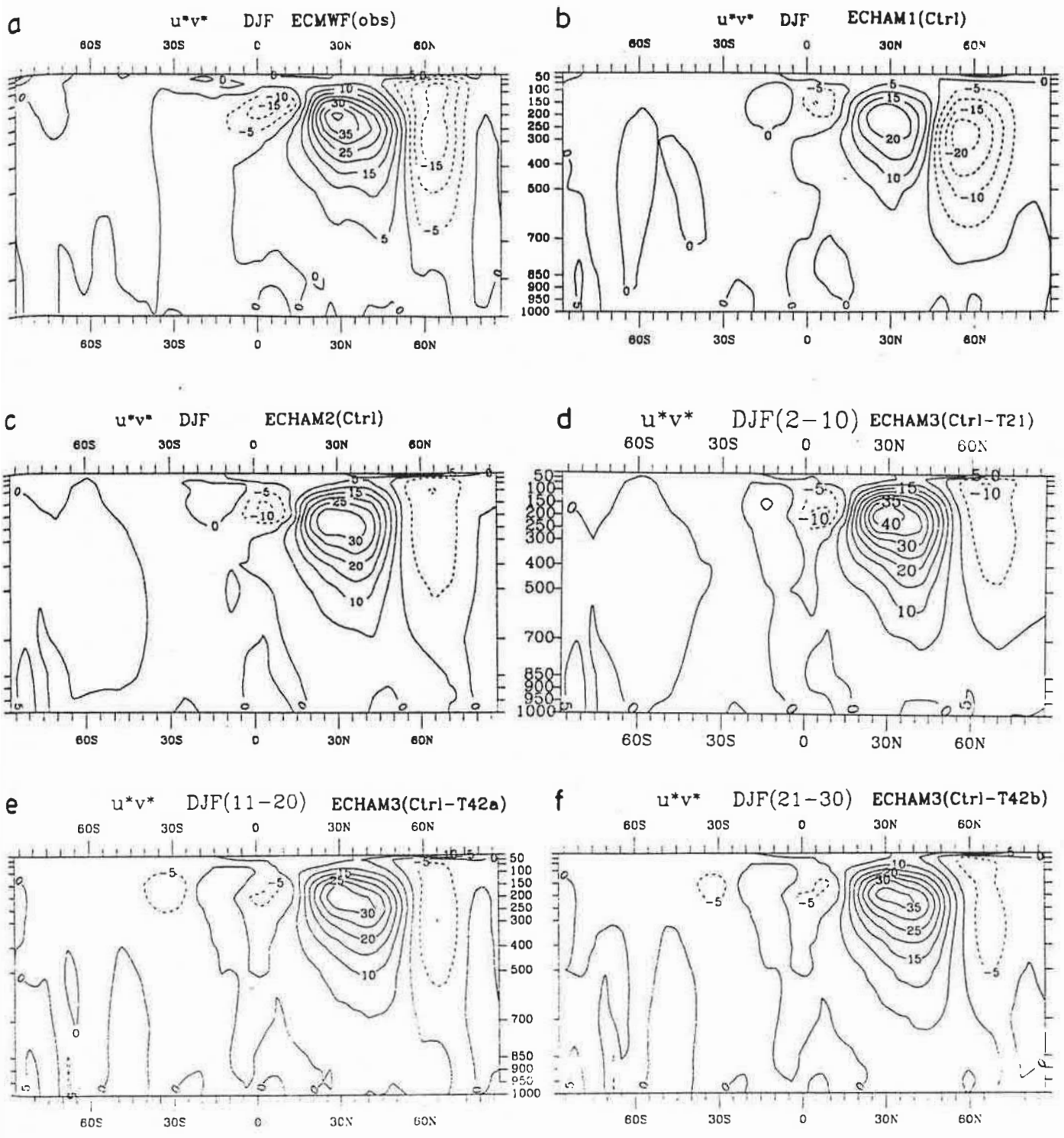

Figure 34 As in Fig. 31 except for the northward transport of westerly momentum by stationary eddies.

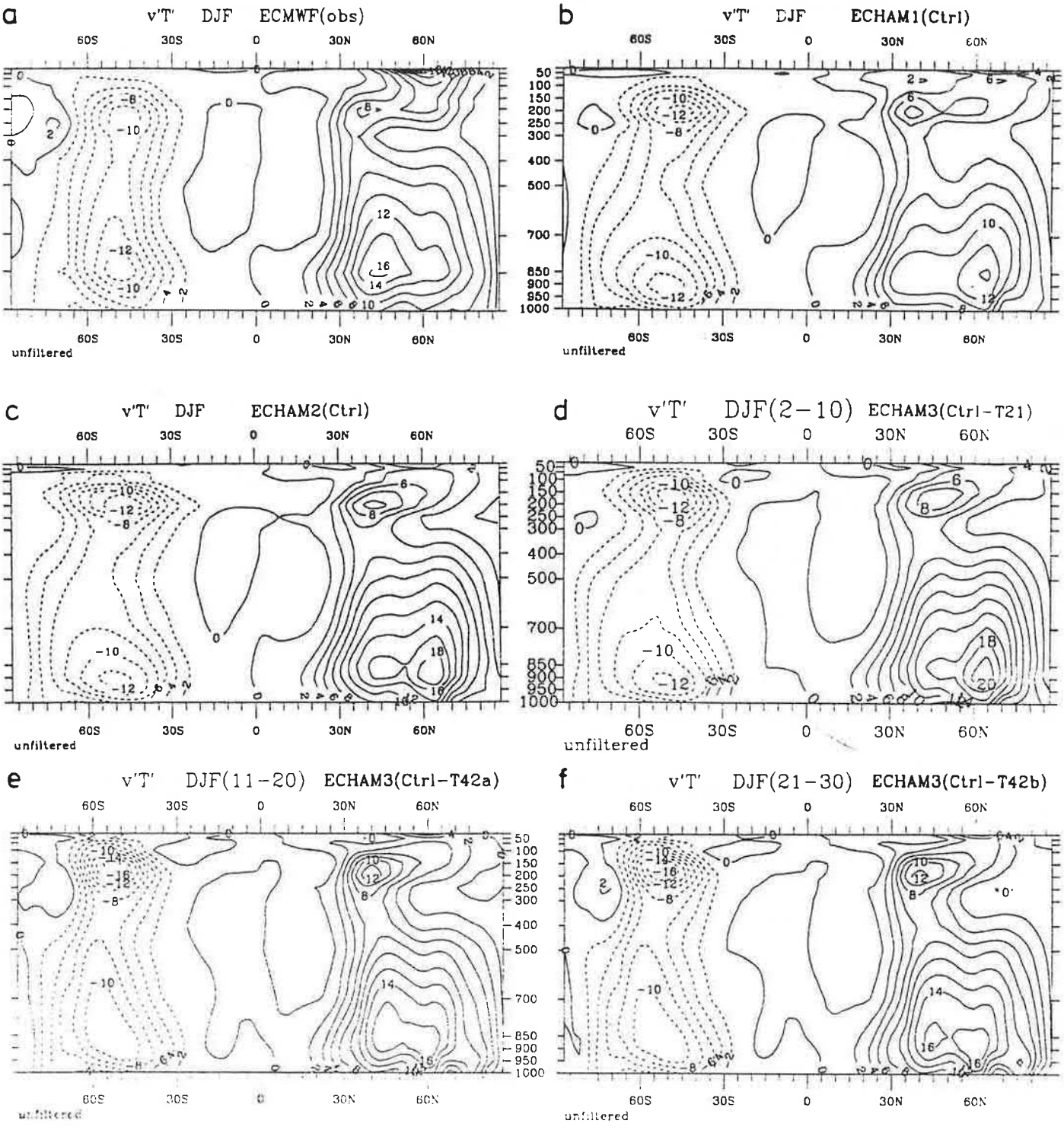

Figure 35 Latitude-pressure distributions of the zonal mean northward transport of sensible heat by transient eddies (K m/s) computed from the unfiltered time series for the DJF season. a) ECMWF analyses, (b-f) model simulations.The lower panel (e,f) shows two 10-year samples of ECHAM3/T42.

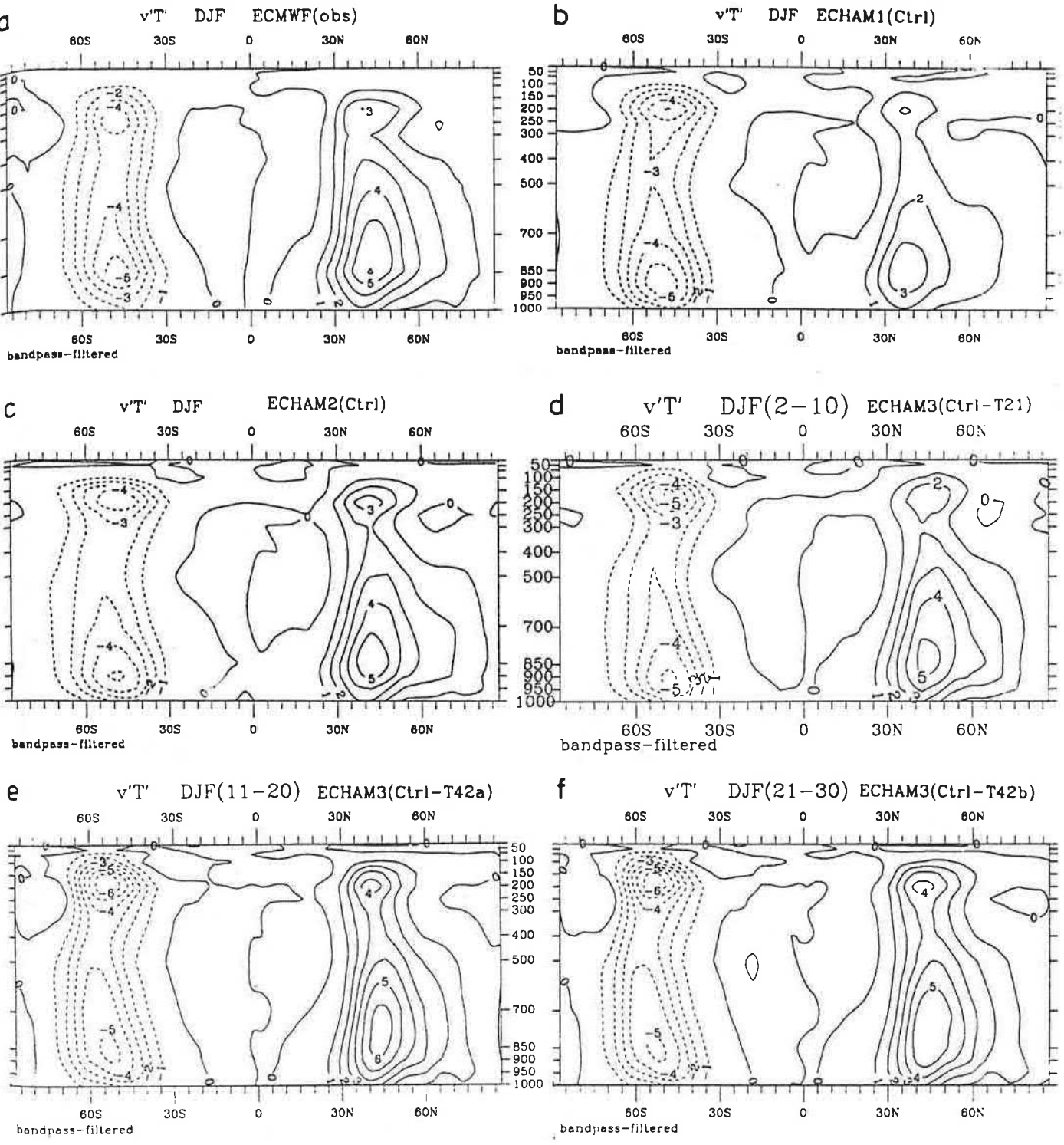

Figure 36 As in Fig. 35 except for the band-pass filtered frequency range.

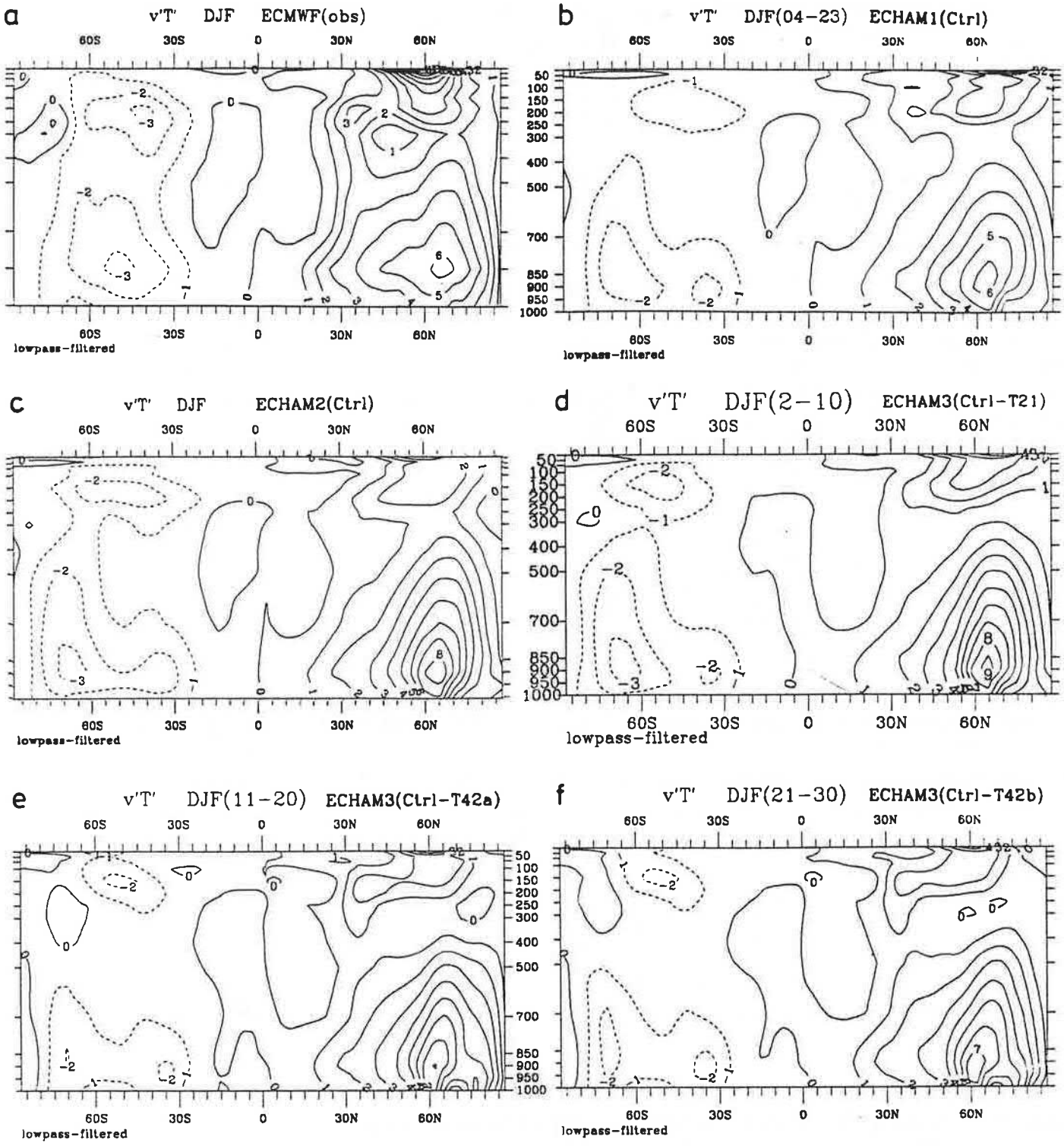

Figure 37 As in Fig. 35 except for the low-pass filtered frequency range.

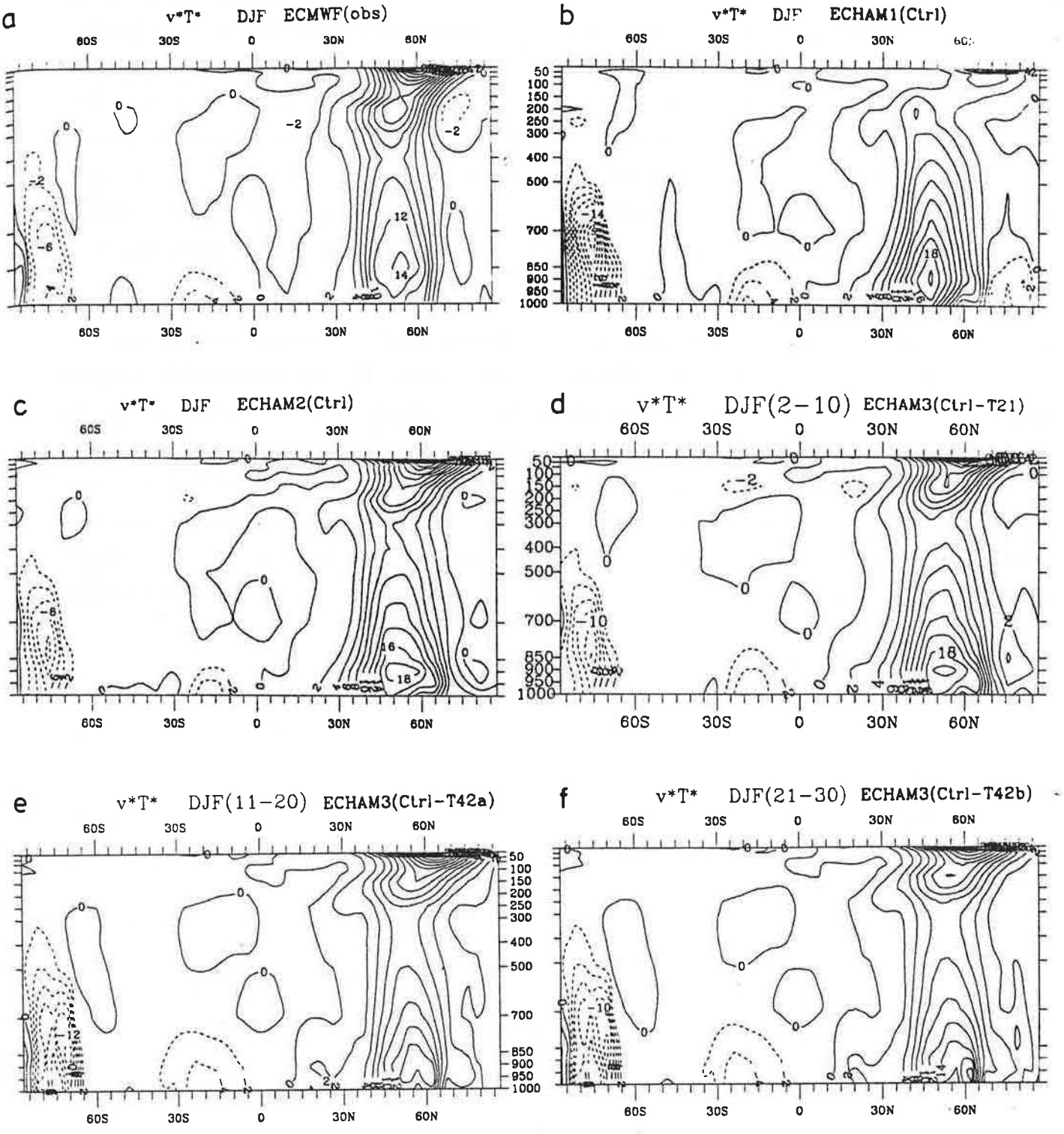

Figure 38 As in Fig. 35 except for the northward transport of sensible heat by stationary eddies.

eddies in the western parts of the oceans (Fig. A40) and low-pass fluxes with peak values over the Bering Sea and over the Norwegian Sea, associated with blocking-type regime patterns (Fig. A41). In both frequency ranges the models perform reasonably well and most of the differences between the model simulations and the ECMWF analyses are probably insignificant. In the band-pass range (Fig. A40) the T42 model shows more baroclinic activity over the Atlantic Ocean, while the ECHAM1 model is too inactive in that area. In the low-pass range, the observed peak values are reproduced by the models. The area with relatively large values is, however, more confined in the model simulations than in the analyses, and the observed secondary peak over the Black Sea, for example, is only weakly indicated in the model simulations.

At 300 hPa (Figs. A42-A44), the simulations are generally less satisfactory than at 850 hPa, however, the T42 simulation is much more realistic than the T21 simulations. The heat fluxes in the band-pass range (Fig. A43) over the East Pacific are generally too large which indicates that the eddies in that area have a spurious baroclinic component. Over the Atlantic Ocean, the simulated patterns agree better with the analyses. In particular the T42 model is able to capture the observed pattern both in shape and magnitude. The T42 model performs also slightly better than the T21 models in the low-frequency range. The observed pattern of northward heat transport over the southeastern United States, for example, is reproduced only at high resolution (Figs. A44e,f). All models fail, however, to simulate the observed dipole over the Mediterranian Sea.

6. SUMMARY AND CONCLUSIONS

The objectives of this report are (i) to study the impact on the simulated climate of changed physical parameterizations in three low-resolution (T21) versions of the ECHAM model, and (ii) to study the respective impact of increased horizontal resolution (T42) using ECHAM3.

Concerning the first objective, there is abundant evidence that the most deficient simulation of the present-day climate is provided by ECHAM1/T21 due to excessive damping by orographically excited gravity waves. In particular, the winter circulation over the North Atlantic is much too weak, and the quasi-permanent pressure systems in that area such as the Icelandic low or the Azores high are hardly detectable. Consistent with this error in the time-mean state is the underestimation of high-frequency variability due to traveling cyclones, and there is also a lack of stationary eddy variance.

The ECHAM2/T21 model, on the other hand, which does not employ a gravity wave drag (GWD) parameterization and which uses a "mean" orography instead of an "envelope" orography is able to reproduce the observed wintertime circulation over the North Atlantic with much more fidelity although it is still too weak. In the Southern Hemisphere and during the summer months in the Northern Hemisphere, the differences between ECHAM2 and ECHAM1 are less apparent. There is, however, evidence that even at low horizontal resolution a (moderate) stratospheric drag should be included: In the ECHAM2 simulation, the North Polar vortex in the winter stratosphere is too cold, the meridional temperature gradient is nearly twice as large as observed, and the polar night jet is accordingly too fast.

Although the ECHAM3 physics differs from that of ECHAM2 in more than one respect, the most important difference is supposed to be the change of the cumulus convection scheme from the Kuo-scheme in ECHAM2 to a more elaborate mass-flux scheme in ECHAM3. The resulting change of the circulation is less dramatic than between ECHAM1 and ECHAM2 noted above. There is a small but consistent reduction of the lower tropospheric temperature error, particularly over the low-latitude oceans. The tropical precipitation patterns are generally more realistic, except for a few areas where the ECHAM3 model generates clearly too much precipitation as, for example, over South Africa and Australia during summer. The impact on the the time-mean circulation is modest, but the flow is generally more intense than in ECHAM2. Similarly, the high-frequency variability and the stationary eddy variances and covariances are larger and more realistic. On the regional scale, the winter circulation (time-mean state and transient eddies) is improved over the North Atlantic - European area while over the North Pacific the ECHAM3 simulation is less realistic in the band-pass filtered frequency range indicating that the storm track region is systematically shifted to the east.

The impact of increased horizontal resolution on the time-mean climate is favourable in most cases. The most apparent improvement is found in the Southern Hemisphere where the flow is significantly enhanced as compared to all T21 models, particularly in the lower troposphere, independent of season. In the Northern Hemisphere, the winter circulation over the Atlantic Ocean is improved while the changes in

the Pacific are less significant. In summer, the high pressure cells over the North Pacific and North Atlantic are more pronounced than in the T21 models and they agree also better with the observations. The precipitation patterns are generally more realistic in the tropics and at high latitudes, especially, where the high precipitation bias seen in most of the T21 simulations is considerably reduced, if present at all. There is also a significant and consistent improvement of the transient eddy fluctuations. In particular, the band-pass filtered variances and covariances are larger than in the T21 models and also more realistic. The level of transient kinetic energy, for example, is accurately simulated and the differences between the model and the analyses are largely insignificant. The differences between the T42 model and the T21 models are less apparent in the low-frequency range, where a considerable lack of variance is still present in the T42 simulation.

Although the ECHAM3/T42 model is able to simulate most aspects of the observed time-mean circulation and its intraseasonal variabilities with remarkable skill, there are a few problem areas which deserve attention (most of these errors are even more pronounced in the T21 simulations):

* The warm bias in the tropical upper troposphere and the cold bias in the polar upper troposphere and lower stratosphere cause a spurious increase of the meridional temperature gradient and, according to the thermal wind relation, a spurious acceleration of the mean zonal flow at these levels, in particular during the respective winter season.

* Although less obvious than in the upper troposphere, the summer circulation (DJF) in the lower troposphere around Antarctica is too strong, and the circulation patterns are displaced polewards by about 5°. This result is consistent with the surface pressure distribution during Southern Hemisphere summer (DJF) showing a poleward displacement of the subtropical highs (which are too strong) and of the Antarctic trough (which is too deep).

* The mean wintertime circulation in the Northern Hemisphere is too zonal over the eastern part of the North Pacific, and the Pacific storm track region is displaced to the east. The ridge centred over the west coast of North America is poorly developed at the 500 hPa level, and the North American trough is displaced to the east.

* While the location and magnitude of the Icelandic and Aleutian lows during winter are simulated correctly, their spatial extent is too small due to a spurious northward extension of the subtropical highs. The centre of the Azores high is also displaced to the east so that the surface pressure over the Western and Southern Europe is higher than observed.

* During the respective summer season, there is too much precipitation over South Africa and Australia (DJF), and off the west coast of Central America (JJA), whereas the rainfall over India is underestimated during the summer monsoon season. There is also a lack of precipitation over the Northern Hemisphere continents during summer, for example over the United States, over Europe and over the dry regions of Asia. In these areas, the temperatures are generally too high with the largest error of about 6K at 850 hPa

over the central part of the United States.

* Although the intraseasonal variability is fairly well simulated in general, there are a few exceptions: The band-pass filtered eddy momentum fluxes during DJF are too strong in both hemispheres, and the respective heat fluxes in the upper troposphere in both hemispheres are too strong as well. The most apparent model error, however, is a significant underestimation of the low-frequency variability, and this bias can be identified in each of the statistics presented in this report.

We have to consider, however, that not all of the simulation errors noted above may result from model deficiencies but may also be related to the experimental design of artificially suppressing interannual variations of sea surface temperature and sea-ice extent, let alone the uncertainties of the observational analyses. In a parallel experiment, the sea surface temperatures and sea-ice limits have been prescribed month by month from observations for the period 1979-1988. A preliminary analysis indicates that the simulated climate is more realistic than in the case of climatological SST forcing. Although the basic error patterns are still present, their magnitude is considerably reduced: For example, the winter circulation over the North Pacific is more realistic and the level of low-frequency variability is enhanced, although still too low.

To summarize, the impact of changed model physics (here: gravity wave drag parameterization switched on and off and Kuo-convection-scheme vs. mass-flux scheme) is particularly evident in the simulated time-mean climate state. The impact of increased resolution in ECHAM3 (T42 vs. T21) can be identified not only by a generally improved time-mean circulation, particularly in the Southern Hemisphere, but most significantly by the increased level of high-frequency variability due to more vigorous cyclone-scale eddies. The often hypothesized transient eddy forcing of low-frequency variability (e.g., Metz, 1987) is not so obvious in the ECHAM simulations: Despite of a significantly improved simulation of high-frequency variability (as compared to the T21 simulations), the low- frequency variability remains at a low level.

Acknowledgements. This work was supported by Bundesminister für Forschung und Technologie (BMFT) through Grant 07 KFT 05/6 to the University of Hamburg. We gratefully acknowledge the assistance of Arno Hellbach, Kornelia Müller, Norbert Noreiks and Claudia Schröder in typing the manuscript and preparing the figures. We are grateful to the staff of ECMWF for providing us with an earlier version of the operational model. Part of the model description is based on the ECMWF model documentation.

7. REFERENCES

Alexander, R.C. and Mobley, R.L., 1976:
Monthly average sea-surface temperatures and ice-pack limits on a global grid:
Mon. Wea. Rev., 104, 143-148.

Asselin, R., 1972:
Frequency filter for time integrations;
Mon. Wea. Rev., 100, 487-490.

Baede, A.P.M., M. Jarraud and U. Cubasch, 1979:
Adiabatic formulation and organization of ECMWF's spectral model:
ECMWF Tech. Rep., 15, 40 pp.

Bakan, S., A. Chlond, U. Cubasch, J. Feichter, H. Graf, H. Graßl, K. Hasselmann, I. Kirchner, M. Latif, E. Roeckner, R. Sausen, U. Schlese, D. Schriever, I. Schult, U. Schumann, F. Sielmann and W. Welke, 1991:
Climate response to smoke from burning oil wells in Kuwait;
Nature, 351, 367-371.

Barnett, T.P., L. Dümenil, U. Schlese, E. Roeckner and M. Latif, 1989:
The effect of Eurasian snow cover on regional and global climate variations:
J. Atm. Sci., 46, 661-685.

Barnett, T.P., M. Latif, E. Kirk and E. Roeckner, 1991:
On ENSO physics;
J. Climate, 4, 487-515.

Bauer, H., E. Heise, J. Pfaendtner and V. Renner, 1985:
Development of an economical soil model for climate simulation.
In: A. Ghazi and R. Fantechi (Eds.)
Current Issues in Climate Research, Proceedings of EC Climatology Programme Symposium, Sophia Antipolis, France, 2-5 Oct. 1984, D. Reidel, Dordrecht, 219-226.

Bennetts, A., and B.J. Hoskins, 1979:
Conditional symmetric instability - a possible explanation for frontal rainbands;
Quart. J. Roy. Meteor. Soc., 105, 945-962.

Bennetts, A., and J.C. Sharp, 1982:
The relevance of conditional symmetric instability to the prediction of meso-scale frontal rainbands;
Quart. J. Roy. Meteor. Soc., 108, 595-602.

Betts, A.K., 1973:
Non-precipitating cumulus convection and its parameterization;
Quart. J. Roy. Meteor. Soc., 99, 178-196.

Blackadar, A.K., 1962:
The vertical distribution of wind and turbulent exchange in a neutral atmosphere:
J. Geophys. Res., 67, 3095-3102.

Blackmon, M.L., 1976:
A climatological study of the 500 mb geopotential height of the Northern Hemisphere;
J. Atm. Sci., 33, 1607-1623.

Blondin, C., 1989:
Research on land surface parameterization schemes at ECMWF;
Proceedings of the workshop on "Parameterization of fluxes over land surface". ECMWF, Reading, UK.

Boer, G.J., N.A. McFarlane, R. Laprise, J.D. Henderson, and J.-P. Blanchet, 1984:
The Canadian Climate Centre spectral atmospheric general circulation model:
Atmos.-Ocean, 22, 397-429.

Boer, G.J. and M. Lazare, 1988:
Some results concerning the effect of horizontal resolution and gravity-wave drag on simulated climate;
J. Climate, 8, 789-806.

Boer, G.J., K. Arpe, M. Blackburn, M. Deque, W.L. Gates, T.L. Hart, H. Le Treut, E. Roeckner, D.A. Sheinin, I. Simmonds, R.N.B. Smith, T. Tokioka, R.T. Wetherald and D. Williamson, 1991:
An intercomparison of the climate simulated by 14 atmospheric general circulation models;
CAS/JSC Working Group on Numerical Experimentation, Report No. 15, WMO/TD-No. 425.

Boville, B.A., 1985:
The thermal balance of the NCAR Community Climate Model;
J. Atm. Sci., 42, 695-709.

Boville, B.A., 1991:
Sensitivity of simulated climate to model resolution;
J. Climate, 4, 469-485.

Brinkop, S., 1991:
Inclusion of cloud processes in the ECHAM PBL parameterization;
In: R. Sausen (Ed.)
Studying Climate with the ECHAM Atmospheric Model.
Large Scale Atmospheric Modelling, Report No. 9, 5-14,
Meteorologisches Institut der Universität Hamburg.

Brinkop, S., 1992:
Parameterisierung von Grenzschichtwolken für Zirkulationsmodelle;
Berichte aus dem Zentrum für Meeres- und Klimaforschung, Reihe A: Meteorologie, Nr. 2,
Meteorologisches Institut der Universität Hamburg, 77 pp.

Browning, K.A., M.E. Hardman, T.W. Harrold and C.W. Pardoc, 1973:
The structure of rainbands within a mid-latitude depression;
Quart. J. Roy. Meteor. Soc., 99, 215-231.

Charnock, M., 1955:
Wind stress on a water surface;
Quart. J. Roy. Meteor. Soc., 81, 639-640.

Cheng, L., T.-C. Yip and H.-R. Cho, 1980:
Determination of mean cumulus cloud vorticity from GATE A/B-scale potential vorticity budget;
J. Atm. Sci., 37, 797-811.

Cubasch, U., K. Hasselmann, H. Höck, E. Maier-Reimer, U. Mikolajewicz, B.D. Santer and R. Sausen, 1992:
Time-dependent greenhouse warming computations with a coupled ocean-atmosphere model;
Climate Dyn., in press.

Deutsches Klimarechenzentrum (DKRZ), 1992:
The ECHAM3 atmospheric general circulation model;
DKRZ Technical Report, No. 6, edited by Modellbetreuungsgruppe (DKRZ).

Dorman, J.L. and P.J. Sellers, 1989:
A global climatology of albedo, roughness length and stomatal resistence for atmospheric general circulation models as represented by the Simple Biosphere Model (SiB);
J. Appl. Meteor., 28, 833-855.

Dümenil, L. and U. Schlese, 1987:
Changes to the parameterization package and their impact on perpetual January simulations;
In: G. Fischer (Ed.)
Climate Simulations with the ECMWF T21-model in Hamburg.
Large Scale Atmospheric Modelling, Report No. 1, 121-139,
Meteorologisches Institut der Universität Hamburg.

Dümenil, L. and E. Todini, 1992:
GCM parameterization of soil hydrology using a catchment scheme;
in preparation.

Eickerling, H., 1989:
Parameterisierung des infraroten Strahlungstransports für Kohlendioxid, Wasserdampf und Ozon in einem breitbandigen Strahlungstransportmodell; *Diplomarbeit*, Institut für Meteorologie und Geophysik, Univ. Köln, FRG.

Eliasen, E., B. Machenhauer and E. Rasmussen, 1970:
On a numerical method for integration of the hydrodynamical equations with a spectral representation of the horizontal fields;
Inst. of Theor. Meterol., Univ. of Copenhagen, Report No. 2.

Ellison, T.H., 1957:
Turbulent transfer of heat and momentum from an infinite rough plane;
J. Fluid. Mech., 2, 456-466.

Emanuel, K.A., 1982:
Inertial instability and mesoscale convective systems,
Part II: Symmetric CISK in a baroclinic flow;
J. Atm. Sci., 39, 1080-1097.

Foster, D.S., 1958:
Thunderstorm gusts compared with computed downdraft speeds;
Mon. Wea. Rev., 86, 91-94.

Fischer, G. (Ed.), 1987:
Climate Simulations with the ECMWF T21-model in Hamburg;
Large Scale Atmospheric Modelling, Report No. 1,
Meteorologisches Institut der Universität Hamburg.

Fischer, G. (Ed.), 1989:
Climate Simulations with the ECMWF T21-model in Hamburg ,
Part III: Diagnosis of response experiments;
Large Scale Atmospheric Modelling, Report No. 7,
Meteorologisches Institut der Universität Hamburg.

Fritsch, J. M. and C. G. Chapell, 1980:
Numerical prediction of convectively driven mesoscale pressure systems.
Part I: Convective parameterization;
J. Atm. Sci., 37, 1722-1733.

Geleyn, J.-F. and A. Hollingsworth, 1979:
An economical analytical method for the computation of the interaction between scattering and line absorption of radiation;
Beitr. Phys. Atmosph., 52, 1-16.

Geleyn, J.-F., 1981:
Some diagnostics of the cloud/radiation interaction in ECMWF forecasting model;
ECMWF Workshop on Radiation and Cloud-Radiation Interaction in Numerical Modelling, 15-17 Oct. 1980, *Workshop Report* pp. 135-162, ECMWF Reading, UK.

Geleyn, J.F. and H.J. Preuss, 1983:
A new data set of satellite-derived surface albedo values for operational use at ECMWF;
Arch. Meteor. Geophys. Bioclim., Ser. A, 32, 353-359.

Hense, A., M. Kerschgens and E. Raschke, 1982:
An economical method for computing radiative transfer in circulation models;
Quart. J. Roy. Meteor. Soc., 108, 231-252.

Herzegh, P.H. and P.V. Hobbs, 1980:
The mesoscale and microscale structure and organization of clouds and precipitation in mid-latitude cyclones, Part II: Warm frontal clouds;
J. Atm. Sci., 37, 597-611.

Heymsfield, A.J., 1977:
Precipitation development in stratiform ice clouds: A microphysical and dynamical study;
J. Atm. Sci., 34, 367-381.

Houze, R.A., J.D. Locatelli and P.V. Hobbs, 1976:
Dynamics and cloud microphysics of the rainbands in an occluded frontal system;
J. Atm. Sci., 35, 1921-1936.

ICAO, 1964:
Manual of the ICAO Standard Atmosphere;
U.S. Government Printing Office, Washington, D.C.

Jaeger, L., 1976:
Monatskarten des Niederschlages für die ganze Erde;
Berichte des Deutschen Wetterdienstes, 139, 1-38.

Johnson, R.H., 1976:
The role of convective-scale precipitation downdrafts in cumulus and synoptic scale interactions;
J. Atm. Sci., 33, 1890-1910.

Johnson, R.H., 1980:
Diagnosis of convective and mesoscale motions during Pase III of GATE;
J. Atm. Sci., 37, 733-753.

Kerschgens, M., U. Pilz, E. Raschke, 1978:
A modified two-stream approximation for computations of the solar radiation budget in a cloudy atmosphere;
Tellus, 30, 429-435.

Kessler, E., 1969:
On the distribution and continuity of water substance in atmospheric circulation;
Meteorological Monographs, 10, Americ. Meteor. Soc., Boston, MA.

Kukla, G. and D. Robinson, 1980:
Annual cycle of surface albedo;
Mon. Wea. Rev., 108, 56-58.

Kuo, H. L., 1965:
On formation and intensification of tropical cyclones through latent heat release by cumulus convection;
J. Atm. Sci., 22, 40-63.

Kuo, H. L., 1974:
Further studies of the parameterization of the influence of cumulus convection on large-scale flow;
J. Atm. Sci., 31, 1232-1240.

Latif, M., J. Biercamp, H. v. Storch, M. McPhaden and E. Kirk, 1990:
Simulation of ENSO related surface wind anomalies with an atmospheric GCM forced by observed SST;
J. Climate, 3, 509-521.

Laursen. L. and E. Eliasen, 1989:
On the effects of the damping mechanisms in an atmospheric general circulation model;
Tellus, 41A, 385-400.

Legates, D. R. and Willmott, C. J, 1990:
Mean seasonal and spatial variability in gauge corrected global precipitation:
J. Climatology, 10, 111-127.

Le Mone, M. A. and W. T. Pennell, 1976:
The relationship of trade wind cumulus distribution to subcloud layer fluxes and structure;
Mon. Wea. Rev., 104, 524-539.

Lindzen, R. S., 1981:
Some remarks on cumulus parameterization;
Rep. on NASA-GISS Workshop "Clouds in Climate": Modelling and Satellite Observational Studies, 42-51.

Louis, J. F., 1979:
A parametric model of vertical eddy fluxes in the atmosphere;
Boundary Layer Meteorology, 17, 187-202.

Louis, J. F., Tiedtke, M., Geleyn, J.-F., 1982:
A short history of the PBL parameterisation at ECMWF;
Proceedings, ECMWF workshop on planetary boundary layer parameterization, Reading, 25-27 Nov. 81, 59-80.

Lowe, P.R., 1977:
An approximating polynomial for the computation of saturation vapor pressure;
J. Appl. Meteor., 16, 100-103.

Manabe, S., 1969:
Climate and the ocean circulation
1. The atmospheric circulation and the hydrology of the earth's surface;
Mon. Wea. Rev., 97, 739-774.

Mason, B.J., 1971:
The physics of clouds
Clarendon Press, Oxford, 671 pp.

Matthews, E., 1983:
Global vegetation and land use: New high-resolution data bases for climate studies;
J. Clim. Appl. Meteor., 22, 474-487.

Matveev, L. T., 1984:
Cloud dynamics;
Atm. Sci. Library, D. Reidel Publishing Company, Dordrecht, 340 pp.

McFarlane, N.A., 1987:
The effect of orographically excited gravity-wave drag on the general circulation of the lower stratosphere and troposphere;
J. Atm. Sci., 44, 1775-1800.

Metz, W., 1987:
Transient eddy forcing of low frequency atmospheric variability;
J. Atm. Sci., 44, 2407-2417.

Metz, W. and M.-M. Lu, 1990:
Storm track eddies in the atmosphere and in an T21 climate model;
Beitr. Phys. Atmosph., 63, 25-40.

Miller, M. J., T. N. Palmer and R. Swinbank, 1989:
Parameterization and influence of sub-grid scale orography in general circulation and numerical weather prediction models;
Met. Atm. Phys., 40, 84-109.

Miller, M. J., A. Beljaars and T. N. Palmer, 1992:
The sensitivity of the ECMWF model to the parameterization of evaporation from the tropical oceans;
J. Clim., in press.

Nitta, T., 1975:
Observational determination of cloud mass flux distributions;
J. Atm. Sci., 32, 73-91.

Orszag, S.A., 1970:
Transform method for calculation of vector coupled sums;
J. Atm. Sci., 27, 890-895.

Palmer, T. N., G. J. Shutts and R. Swinbank, 1986:
Alleviation of a systematic westerly bias in general circulation and numerical weather prediction models through an orographic gravity wave drag parameterization;
Quart. J. Roy. Meteor. Soc., 112, 1001-1031.

Pandolfo, J.P., 1967:
Wind and temperature profiles for constant-flux boundary layer in lapse rate conditions with a variable eddy conductivity to eddy viscosity ratio;
J. Atm. Sci., 23, 495-502.

Peltier, W.R. and T.L. Clark, 1987:
Nonlinear mountain waves and wave-mean flow interaction: elements of a drag parameterization;
ECMWF Seminar/Workshop on Observation, Theory and Modelling of Orographic Effects, ECMWF, Reading, 15-20 Sep. 1986, Vol 1, 223-249.

Ponater, M., E. Kirk and U. Schlese, 1990:
GCM-simulated transient variability in the Northern Hemisphere extratropics and its sensitivity to sea surface temperature variation;
Beitr. Phys. Atmosph., 63, 189-204.

Reynolds, R. W., 1988:
A real-time global sea surface temperature analysis;
J. Climate, 1, 75-86.

Robertson, A.W. and W. Metz, 1990:
An investigation of the storm-track eddies in a low-resolution climate model using linear theory;
Beitr. Phys. Atmosph., 63, 177-188.

Robock, A., 1980:
The seasonal cycle of snow cover, sea-ice and surface albedo;
Mon. Wea. Rev., 108, 267-285.

Rockel, B., E. Raschke and B. Weyres, 1991:
A parameterization of broad band radiative transfer properties of water, ice and mixed clouds;
Beitr. Phys. Atmosph., 64, 1-12.

Roeckner, E. and U. Schlese, 1985:
January simulation of clouds with a prognostic cloud cover scheme;
ECMWF Workshop on "Cloud cover in numerical models", 26-28 Nov. 1984, 87-108, ECMWF, Reading, UK.

Roeckner, E., U. Schlese and B. Rockel, 1989:
The impact of cloud and radiation parameterization changes in January and July simulations with the ECMWF T21-model;
In: G. Fischer (Ed.)
Climate Simulations with the ECMWF T21-model in Hamburg.
Large Scale Atmospheric Modelling, Report No. 7, 139-186,
Meteorologisches Institut der Universität Hamburg.

Roeckner, E., L. Dümenil, E. Kirk, F. Lunkeit, M. Ponater, B. Rockel, R. Sausen and U. Schlese, 1989:
The Hamburg version of the ECMWF model (ECHAM);
In: G.J. Boer (Ed.)
Research Actvities in Atmospheric and Oceanic Modelling.
CAS/JSC Working Group on Numerical Experimentation,
Report No. 13, WMO/TD-No. 332, 7.1-7.4.

Roeckner, E., M. Rieland and E. Keup, 1991:
Modelling of cloud and radiation in the ECHAM model;
ECMWF/WCRP Workshop on "clouds, radiative transfer and the hydrological cycle", 12-15 Nov. 1990, 199-222, ECMWF, Reading, UK.

Sasamori, T., 1975:
A statistical model for stationary atmospheric cloudiness, liquid water content and rate of precipitation;
Mon. Wea. Rev., 103, 1037-1049.

Schneider, E.K. and R.S. Lindzen, 1976:
A discussion of the parameterization of momentum exchange of cumulus convection;
J. Geophys. Res., 81, 3158-3160.

Sellers, P.J., Y. Mintz, Y.C. Sud and A. Dalcher, 1986:
A simple biosphere model (Sib) for use within general circulation models;
J. Atm. Sci., 43, 505-531.

Shettle, E.P. and R. Fenn, 1976:
Models of the atmospheric aerosols and their optical properties;
AGARD Conference Proceedings, No. 183, AGARD-CP-183.

Simmons, A.J., D.M. Burridge, M. Jarraud, C. Girard and W. Wergen, 1989:
The ECMWF medium-range prediction models, development of the numerical formulations and the impact of increased resolution;
Meteorol. Atmos. Phys., 40, 28-60.

Simmons, A.J. and J. Chen, 1991:
The calculation of geopotential and pressure-gradient in the ECMWF atmospheric model: Influence on the simulation of the polar atmosphere and on temperature analyses;
Quart. J. Roy. Meteor. Soc., 117, 29-58.

Simpson, J., 1971:
On cumulus entrainment and one-dimensional models;
J. Atm. Sci., 28, 449-455.

Simpson, J. and V. Wiggert, 1969:
Models of precipitating cumulus towers;
Mon. Wea. Rev., 97, 471-489.

Smith, R.N.B., 1990:
A scheme for predicting layer clouds and their water content in a general circulation model;
Quart. J. Roy. Meteor. Soc., 116, 435-460.

Sperber, K.R. and T.N. Palmer, 1992:
The effect of horizontal resolution on Indian summer monsoon precipitation in the ECMWF model; WCRP Workshop on Simulation of Interannual and Intraseasonal Monsoon Variability, 21-24 Oct. 1991, Boulder, Colorado, USA. *Report of Workshop*, 2.159-2.160, WCRP-68, WMO/TD-No. 470.

Stephens, G.L., 1978:
Radiation profiles in extended water clouds: 2. parameterization schemes;
J. Atm. Sci., 35, 2123-2132.

Sundquist, H., 1978:
A parameterization scheme for non-convective condensation including prediction of cloud water content;
Quart. J. Roy. Meteor. Soc., 104, 677-690.

v. Storch, H. (Ed.), 1988:
Climate Simulations with the ECMWF T21-model in Hamburg,
Part II: Climatology and Sensitivity Experiments;
Large Scale Atmospheric Modelling, Report No. 4,
Meteorologisches Institut der Universität Hamburg.

Tiedtke, M., 1989:
A comprehensive mass flux scheme for cumulus parameterization in large-scale models;
Mon. Wea. Rev., 117, 1779-1800.

Tiedtke, M., W.A. Heckley, and J. Slingo, 1988:
Tropical forecasting at ECMWF: On the influence of physical parameterization on the mean structure of forecasts and analyses;
Quart. J. Roy. Meteor. Soc., 114, 639-664.

Warrilow, D.A., A.B. Sangster and A. Slingo, 1986:
Modelling of land surface processes and their influence on European climate;
Meteorological Office, Met O 20 Tech. Note DCTN 38, Bracknell, U.K.

Wexler, R., and D. Atlas, 1959:
Precipitation generating cells;
J. Meteor., 16, *327-332*.

Wigley, T.M.L. and B.D. Santer, 1990:
Statistical comparison of spatial fields in model validation, perturbation and predictability experiments;
J. Geophys. Res., 95, D1, 851-865.

Xu, K.M., and S.K. Krueger, 1991:
Evaluation of cloudiness parameterizations using a cumulus ensemble model;
Mon. Wea. Rev., 119, 342-367.

Yanai, M., S. Esbensen and J.-H. Chu, 1973:
Determination of bulk properties of tropical cloud clusters from large-scale heat and moisture budgets;
J. Atm. Sci., 30, 611-627.

Zdunkowski, W.G., R.M. Welch, G. Korb, 1980:
An investigation of the structure of typical two-stream methods for the calculation of solar fluxes and heating rates in clouds;
Beitr. Phys. Atm., 53, 147-166.

Appendix A

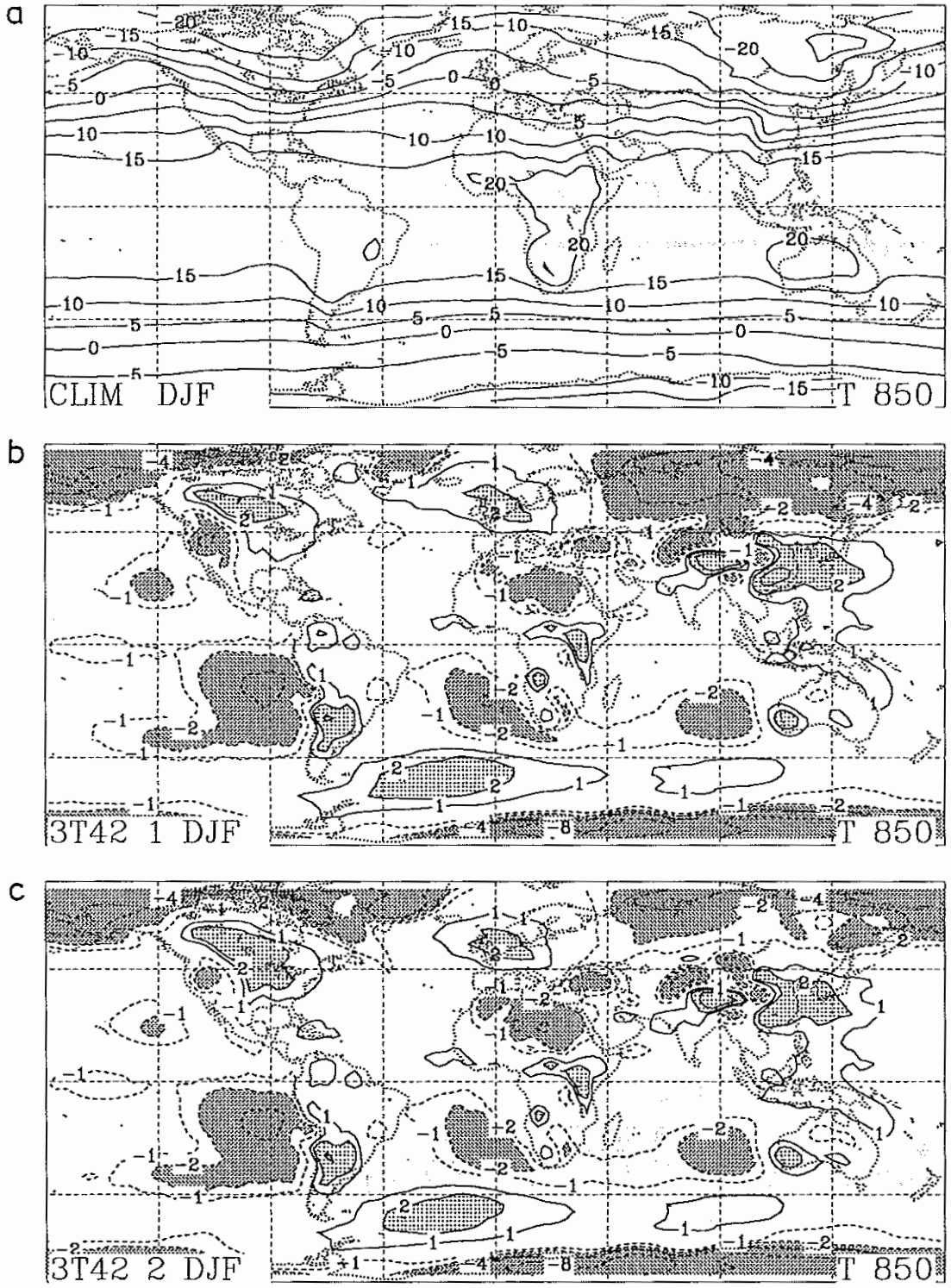

Figure A 1 a) Climatological distribution of temperature at 850 hPa (°C) for the DJF season based on ECMWF analyses. b)-f) Simulation errors of different versions of the ECHAM model. Contour spacing: +/- 1,2,4,8°C. Light (dark) stippling indicates errors of more (less) than +2°C (-2°C), respectively. nTxx denotes ECHAMn at Txx resolution. The panels b) and c) show the respective errors of two 10-year samples of ECHAM3/T42.

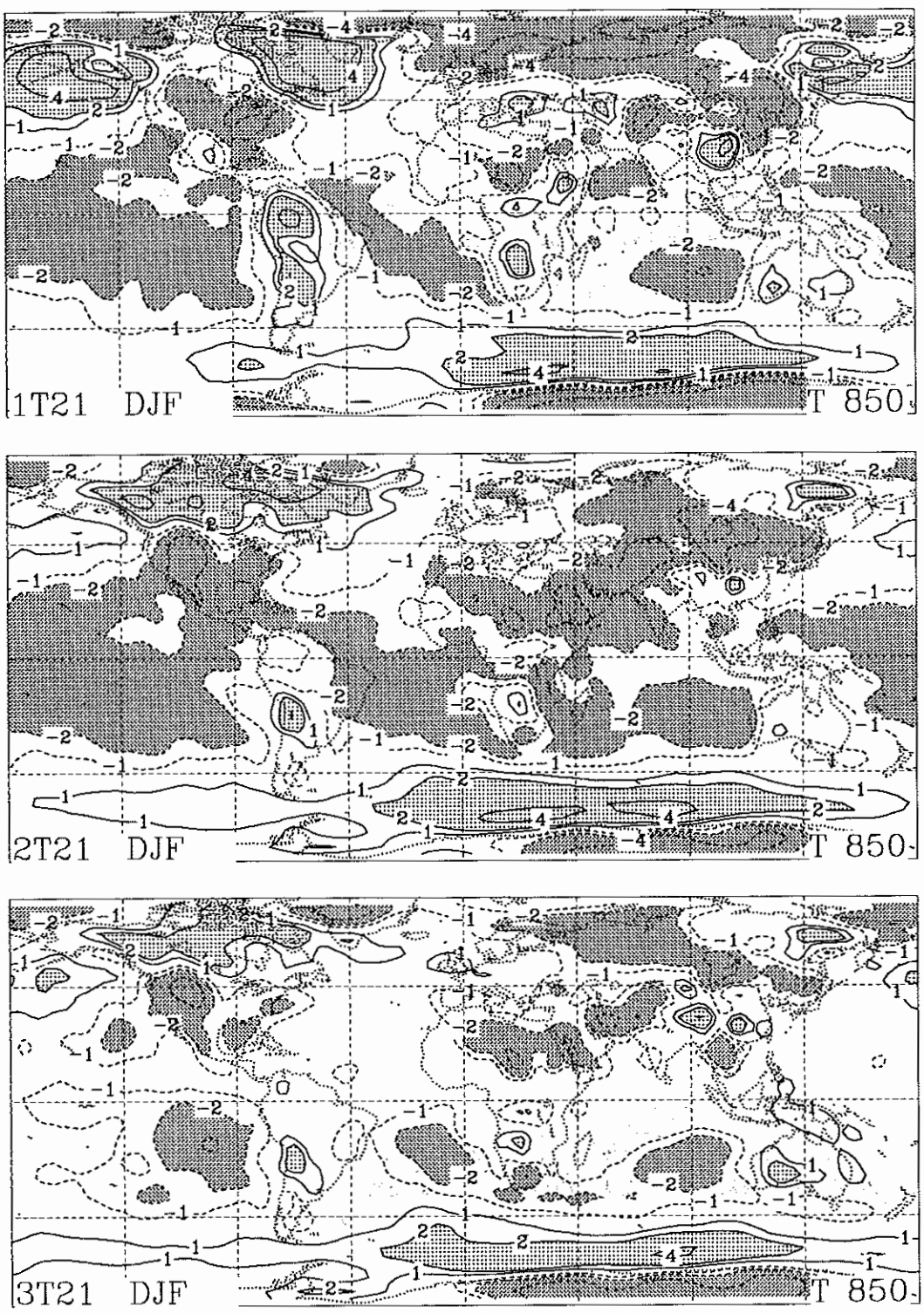

Figure A 1 (cont.)

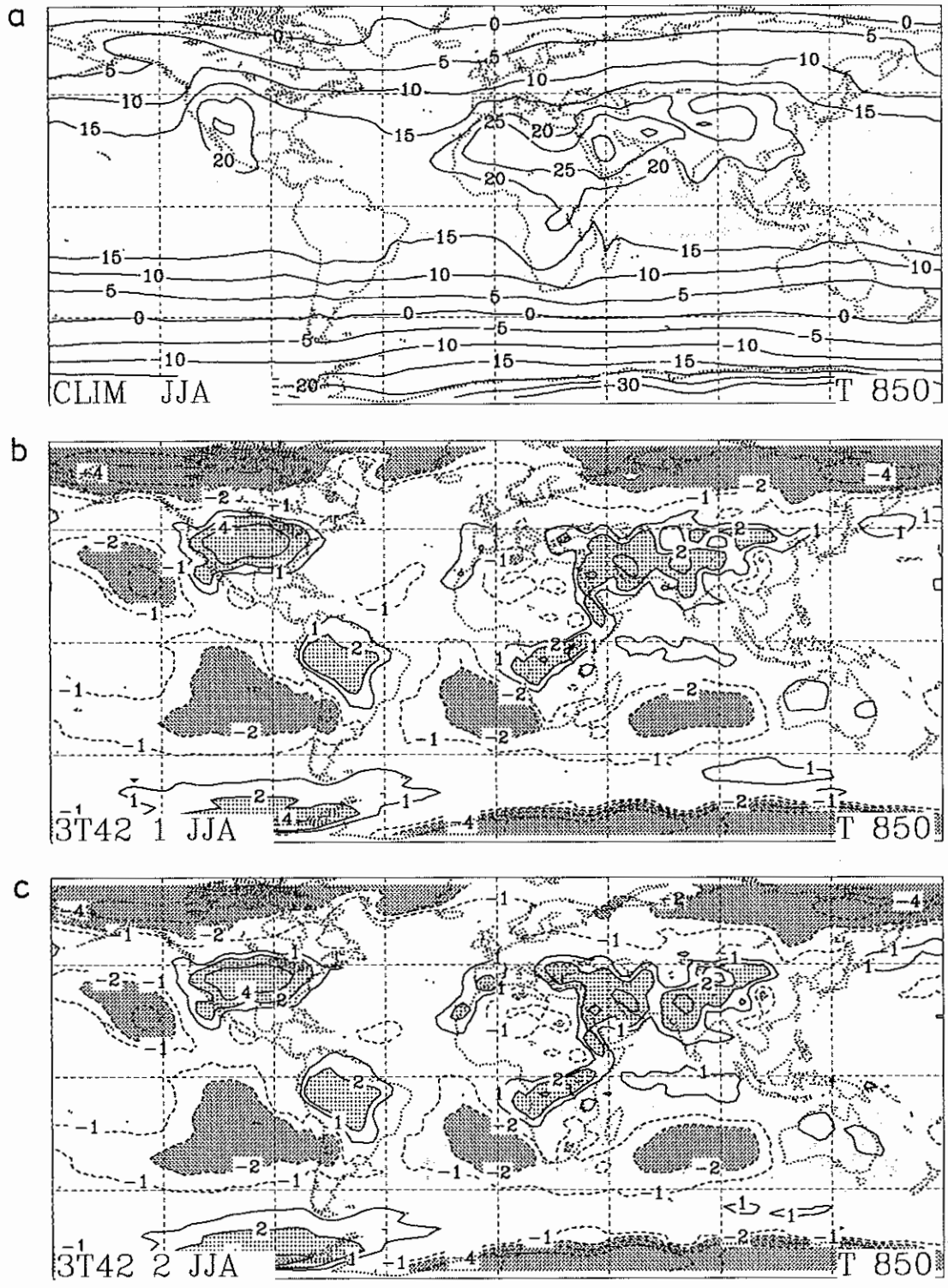

Figure A 2 As in Fig. A1 except for the JJA season.

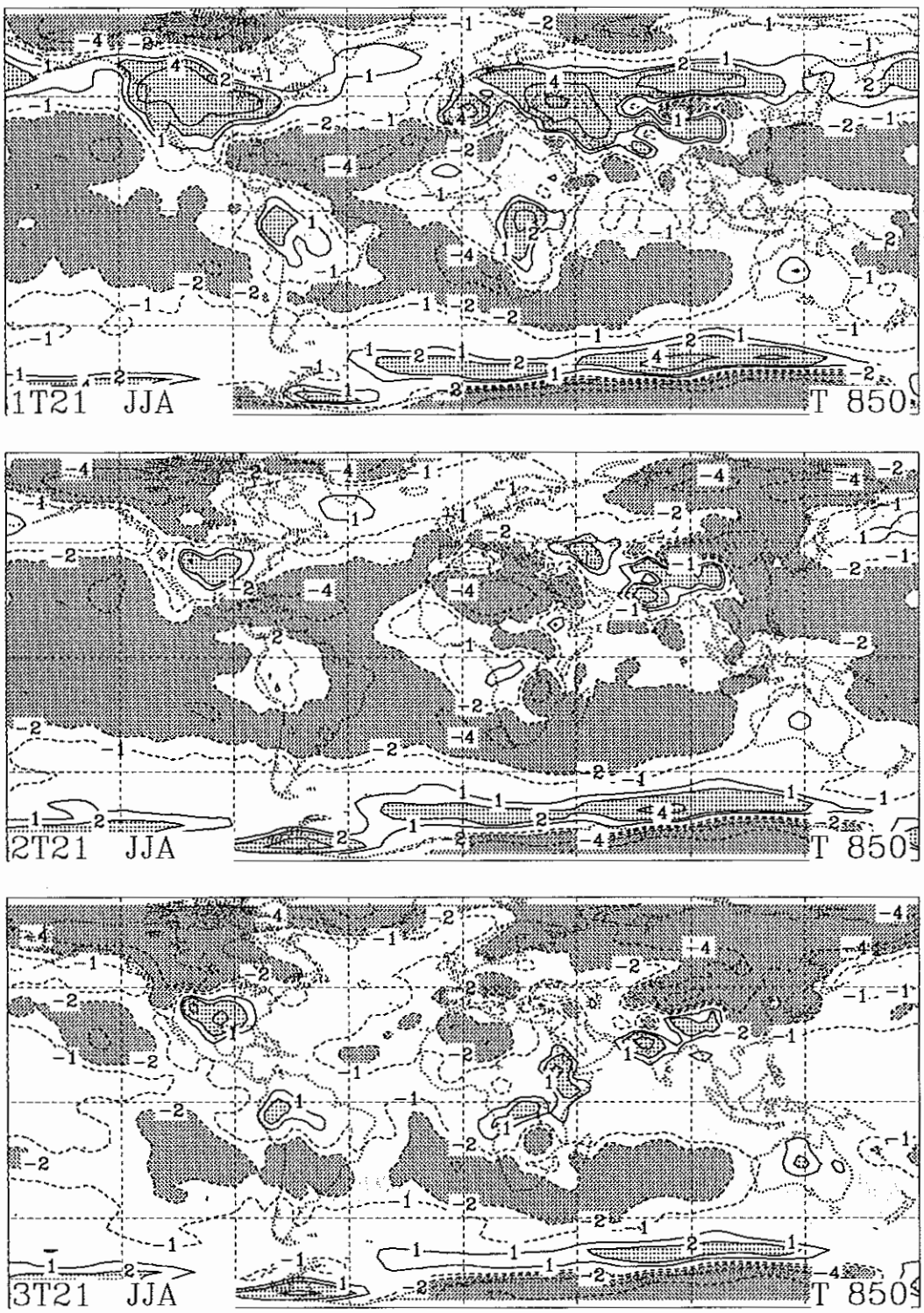

Figure A 2 (cont.)

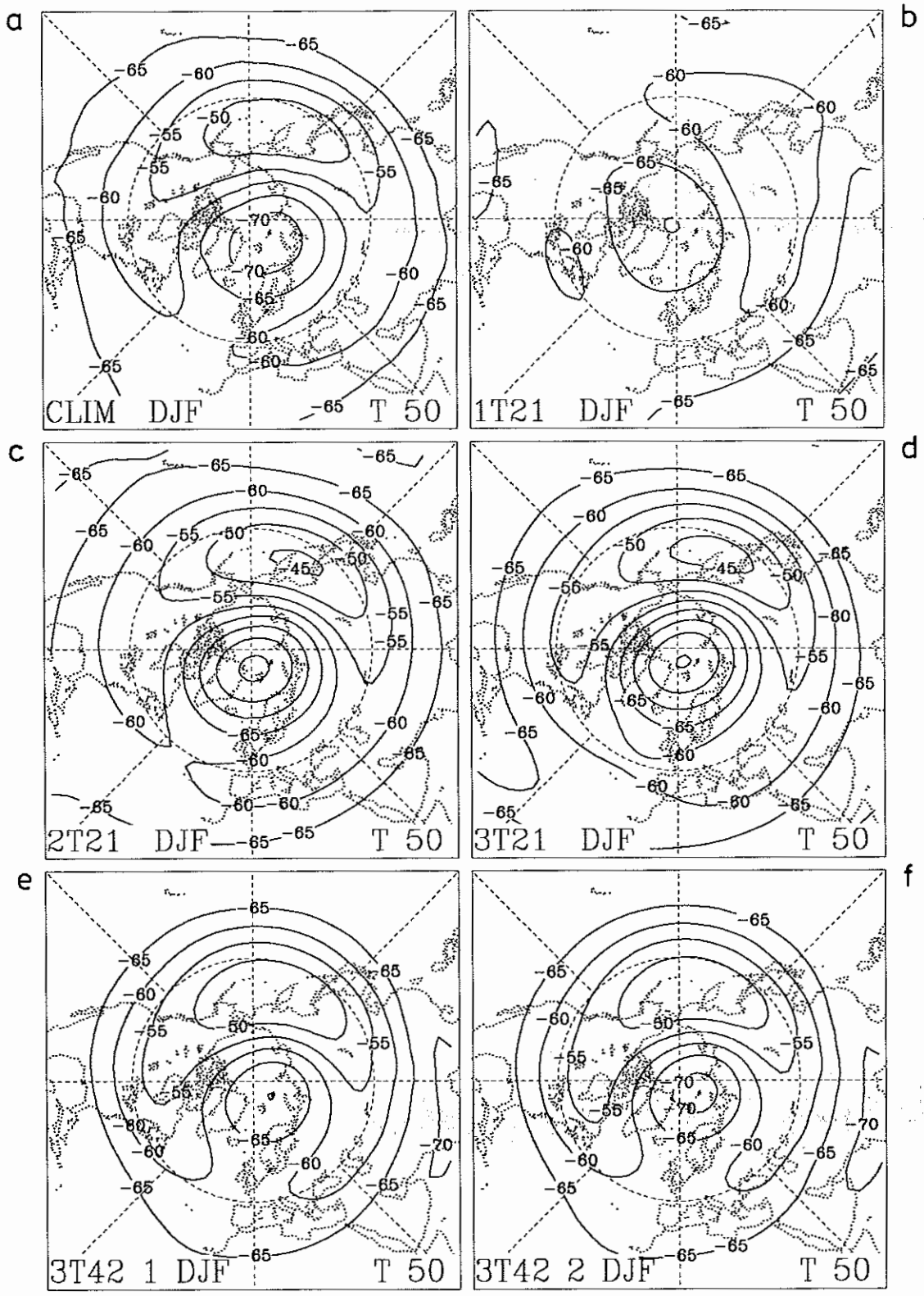

Figure A 3 a) Climatological distribution of temperature (°C) at 50 hPa in the Northern Hemisphere for the DJF season based on ECMWF analyses. b)-f) Simulated distributions obtained with different versions of the ECHAM model. For model notations see Fig. A1.

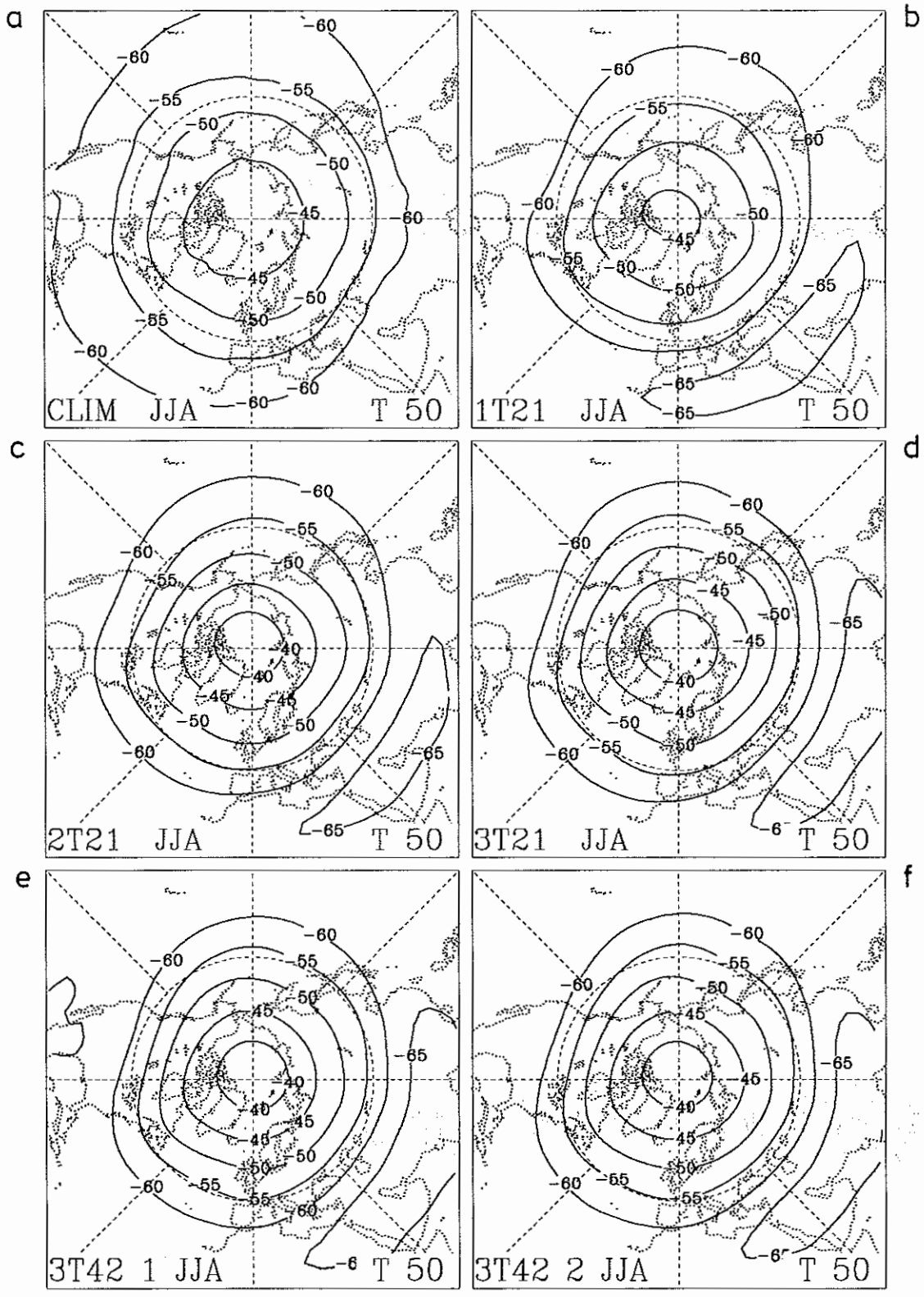

Figure A 4 As in Fig. A3 except for the JJA season.

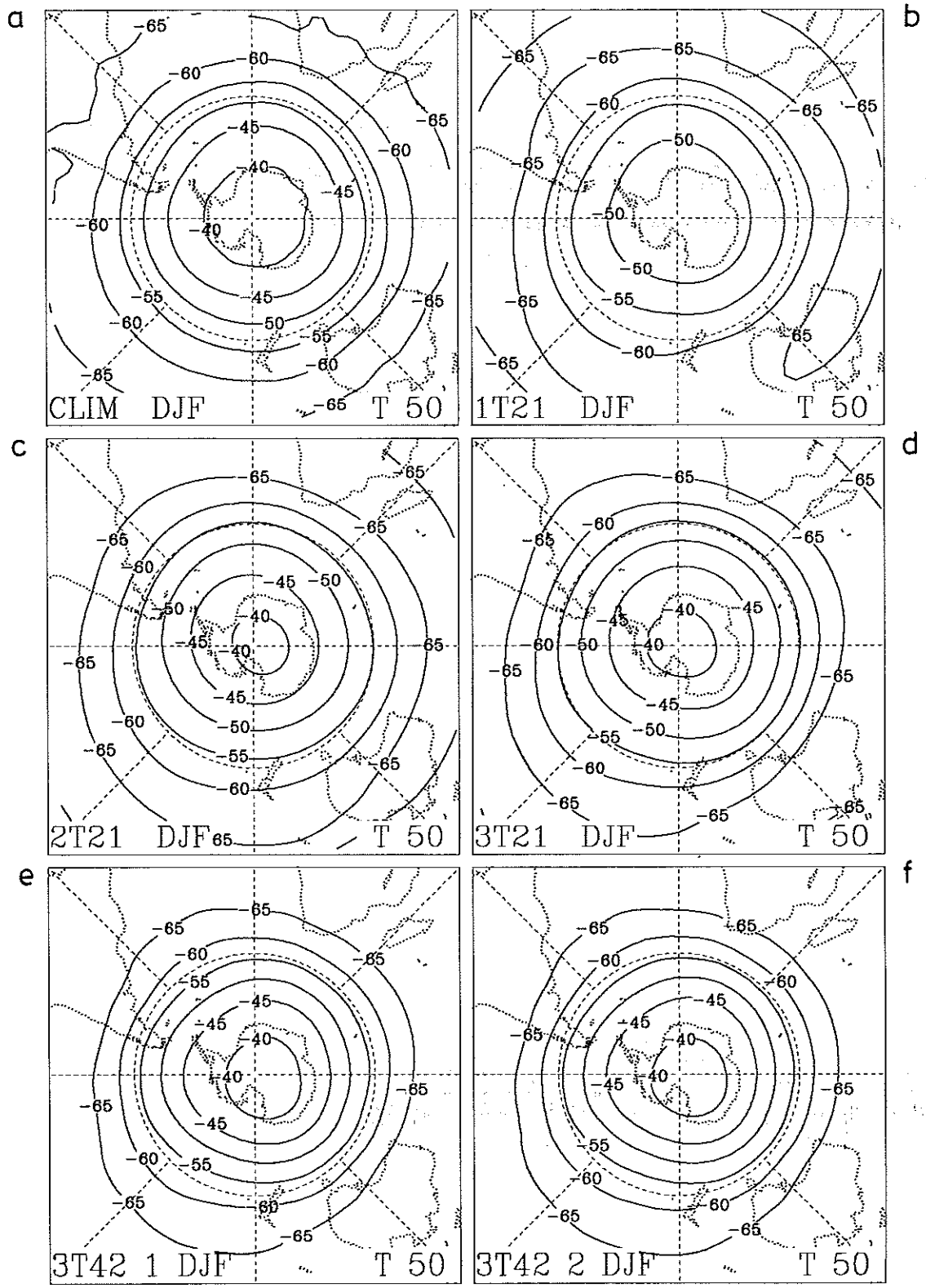

Figure A 5 As in Fig. A3 except for the Southern Hemisphere.

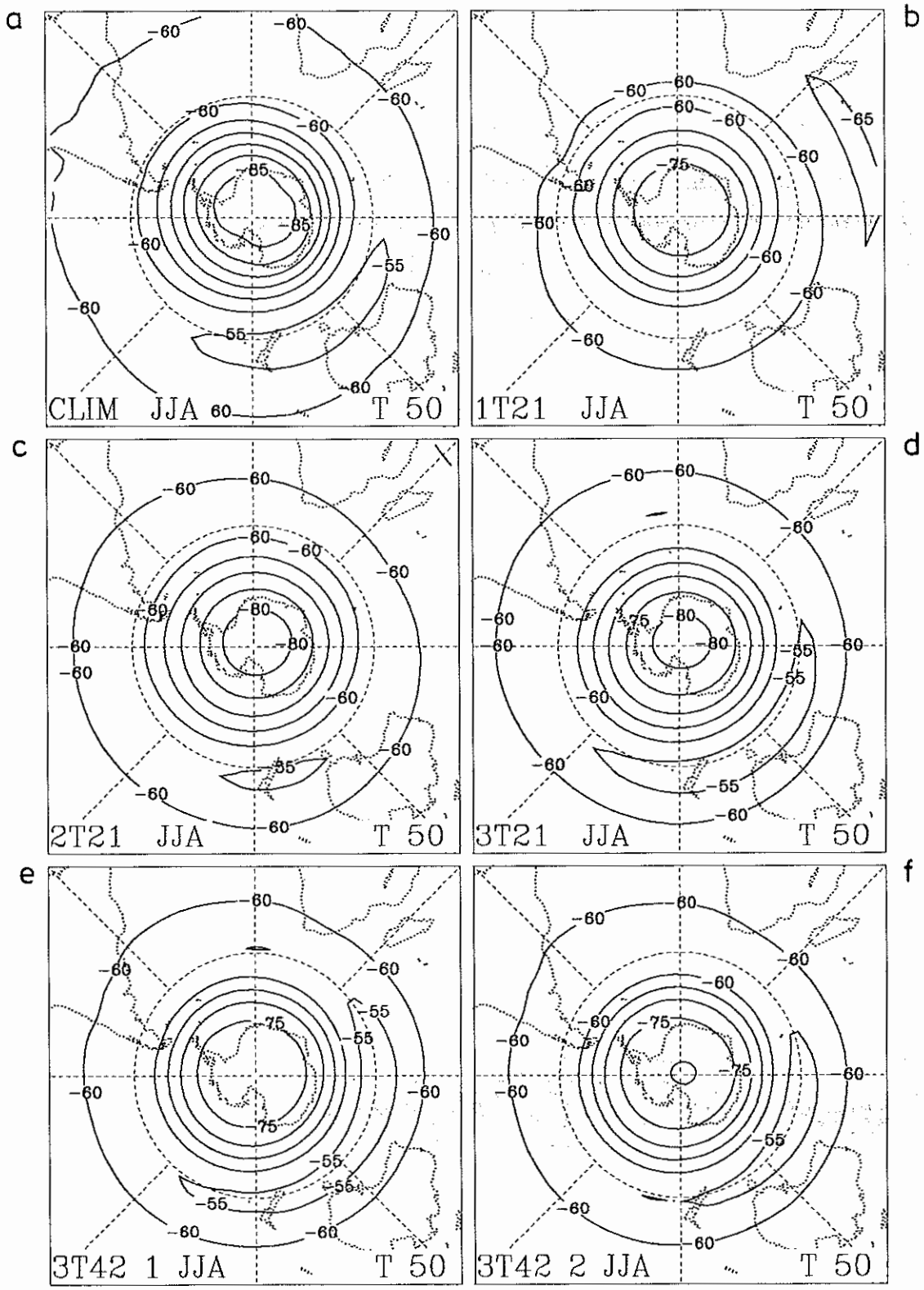

Figure A 6 As in Fig. A4 except for the Southern Hemisphere.

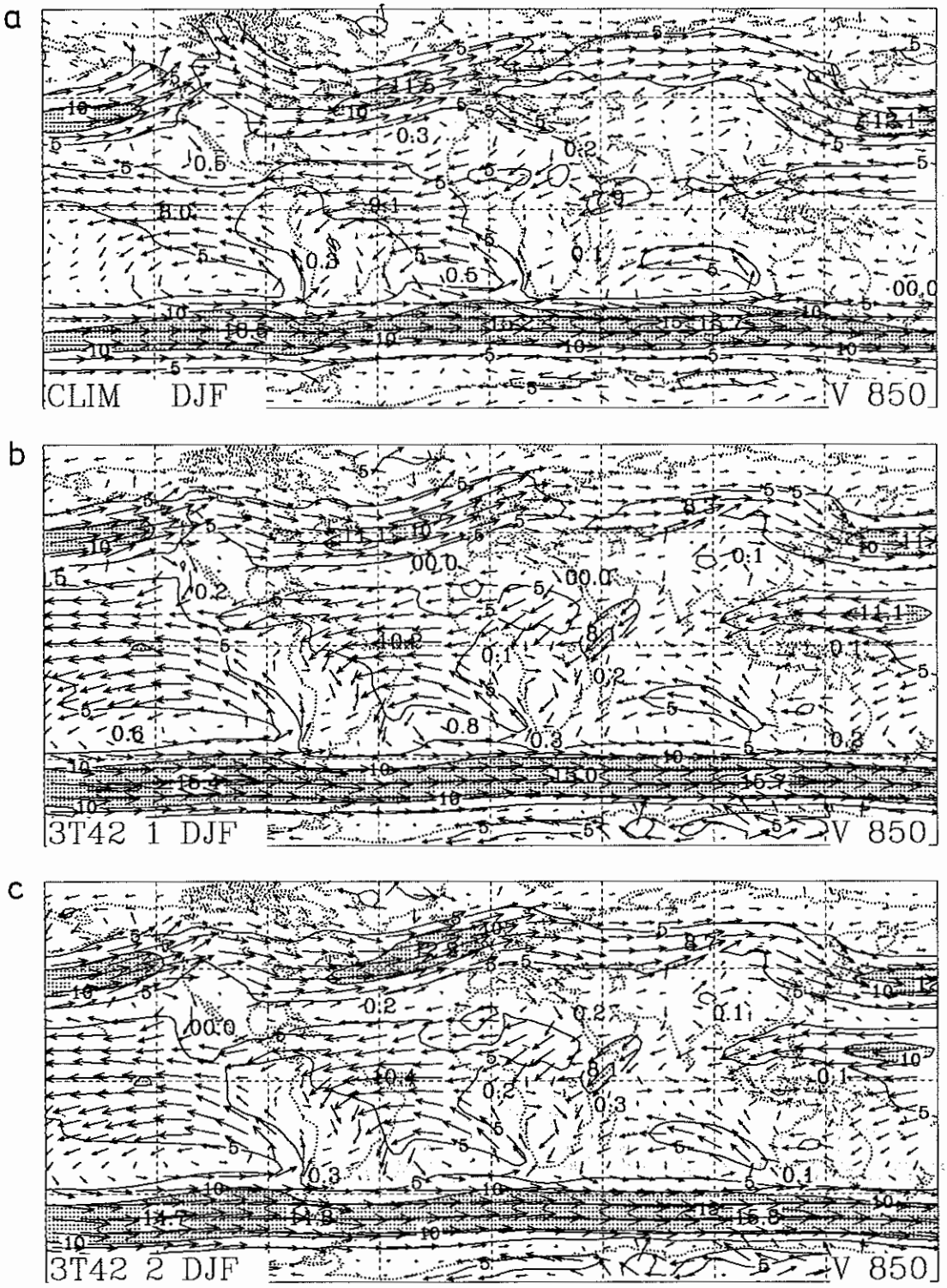

Figure A 7 a) Climatological distribution of wind (m/s) at 850 hPa for theDJF season based on ECMWF analyses. b)-f) Simulated distributions obtained with different versions of the ECHAM model. For model notations see Fig. A1. Contour spacing: 5 m/s. Stippling indicates areas with V > 10 m/s.

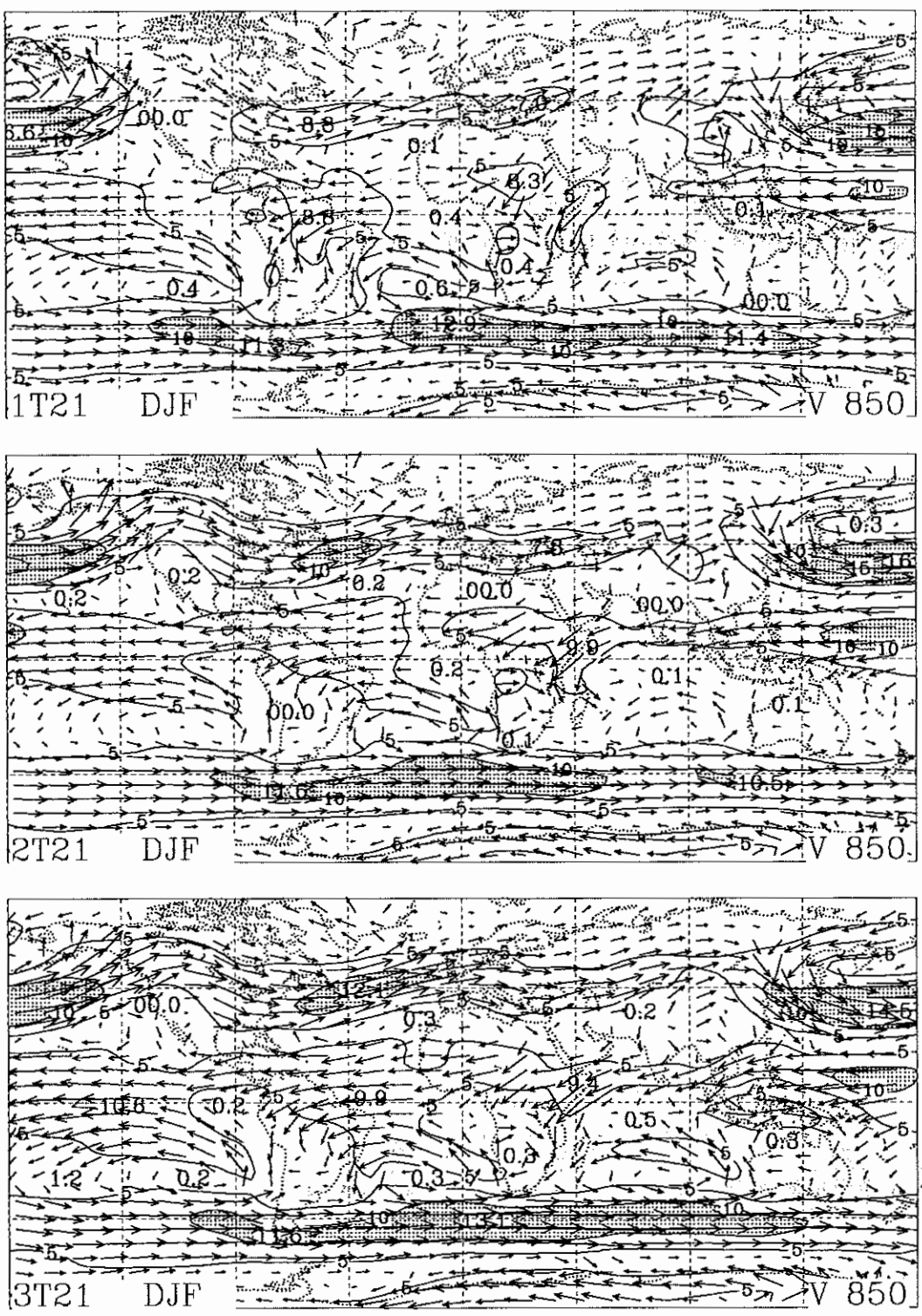

Figure A 7 (cont.)

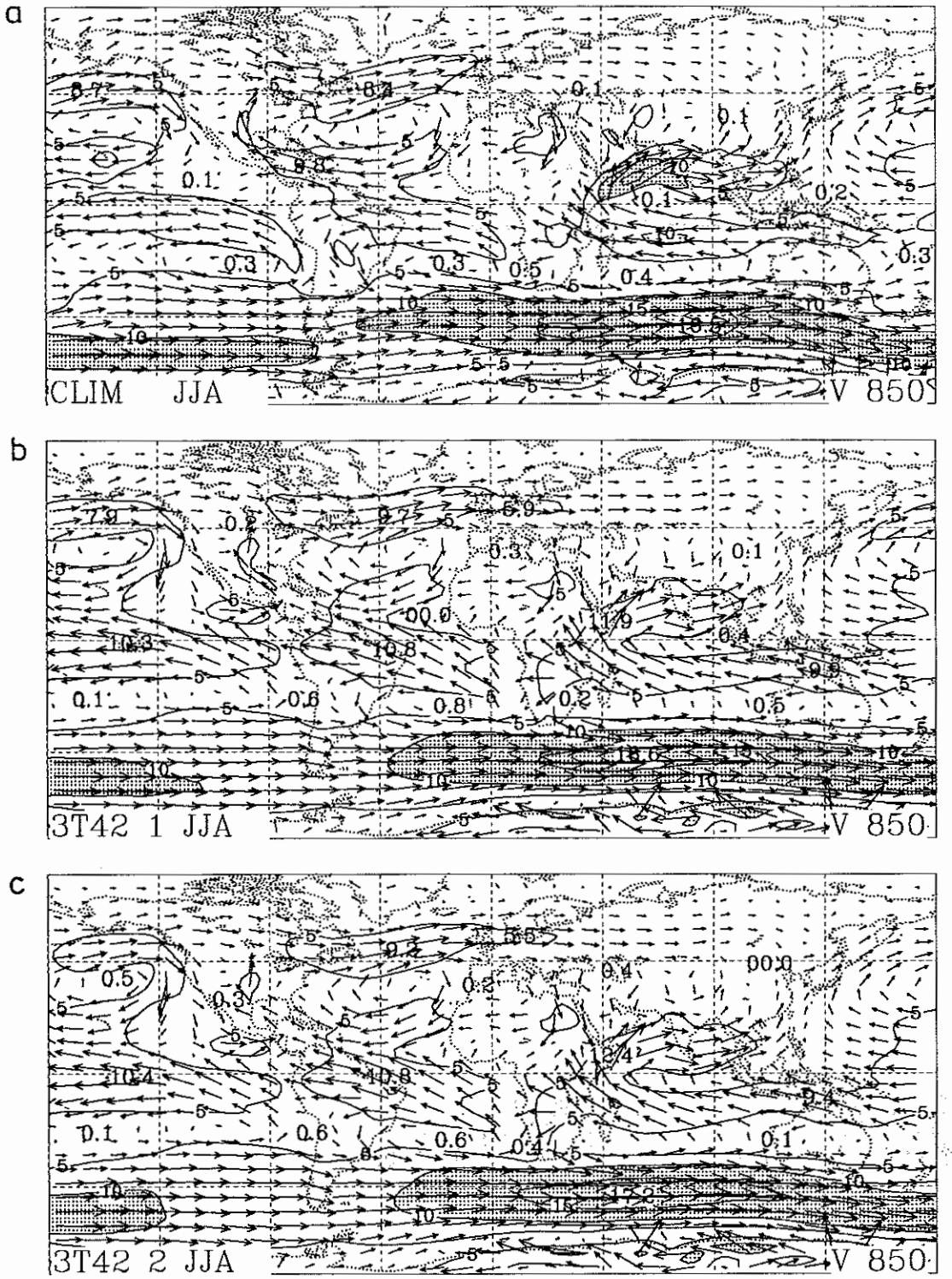

Figure A 8 As in Fig. A7 except for the JJA season.

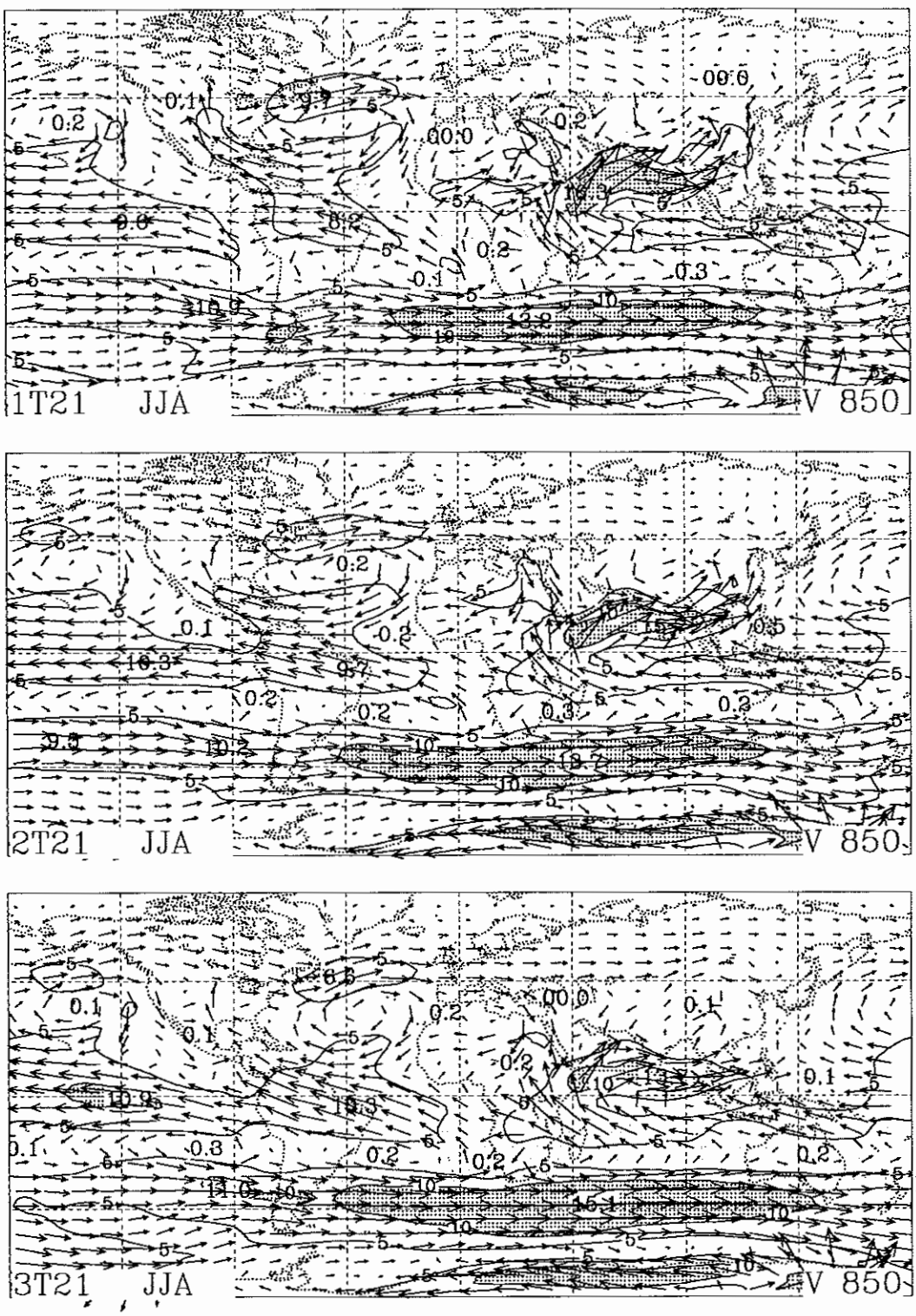

Figure A 8 (cont.)

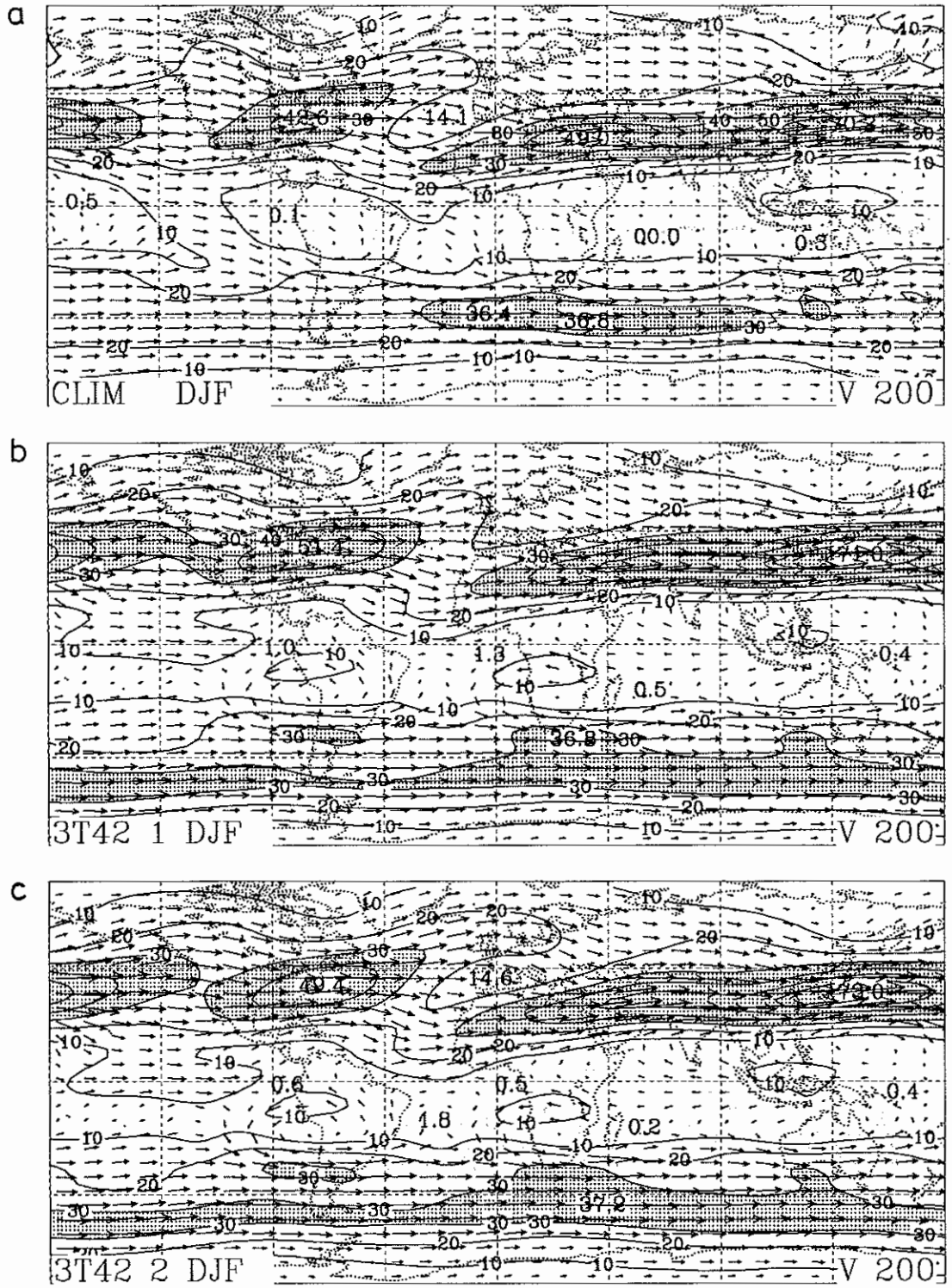

Figure A 9 a) Climatological distribution of wind (m/s) at 200 hPa for the DJF season based on ECMWF analyses. b)-f) Simulated distributions obtained with different versions of the ECHAM model. For model notations see Fig. A1. Contour spacing: 5 m/s. Stippling indicates areas with V > 30 m/s.

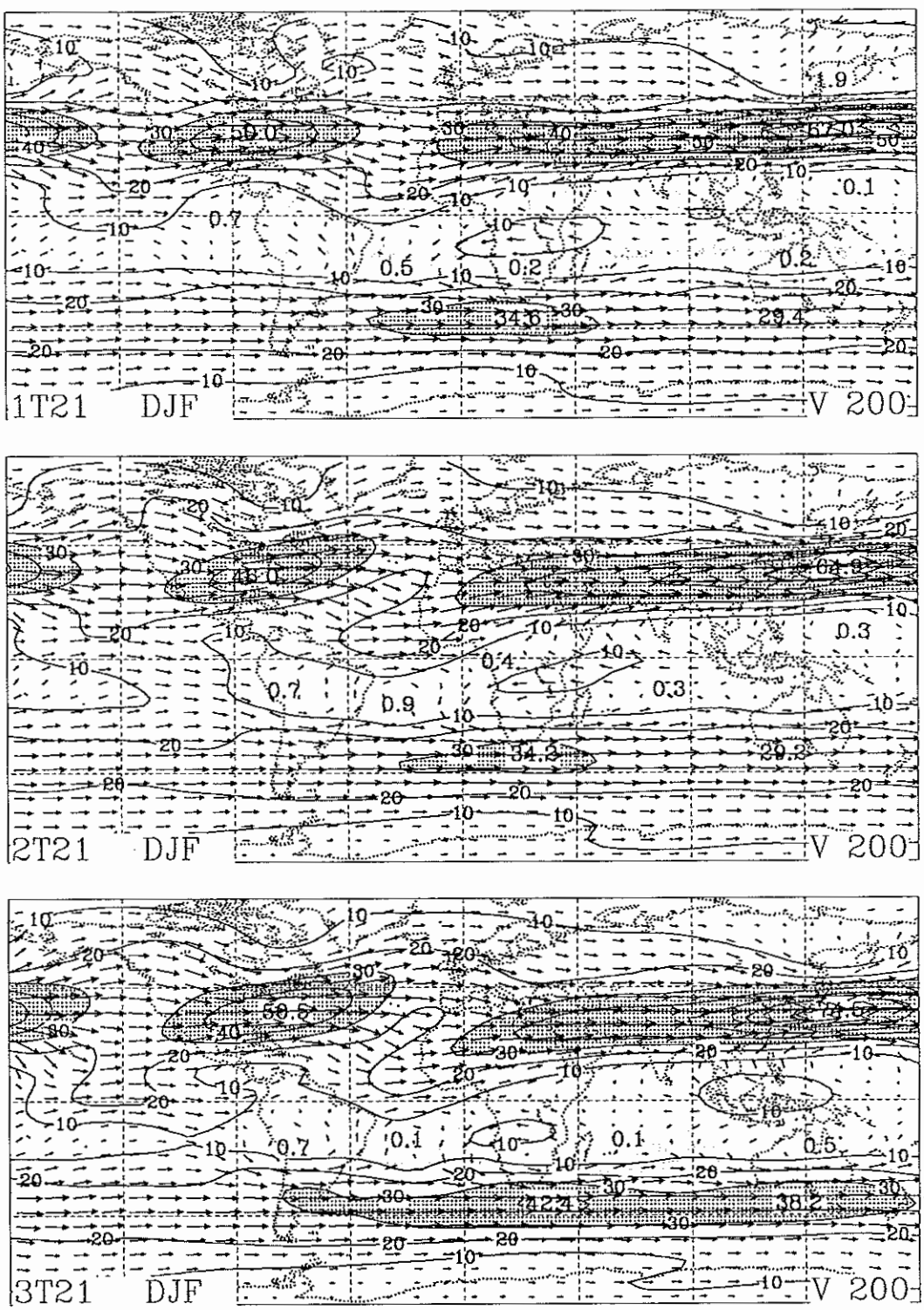

Figure A 9 (cont.)

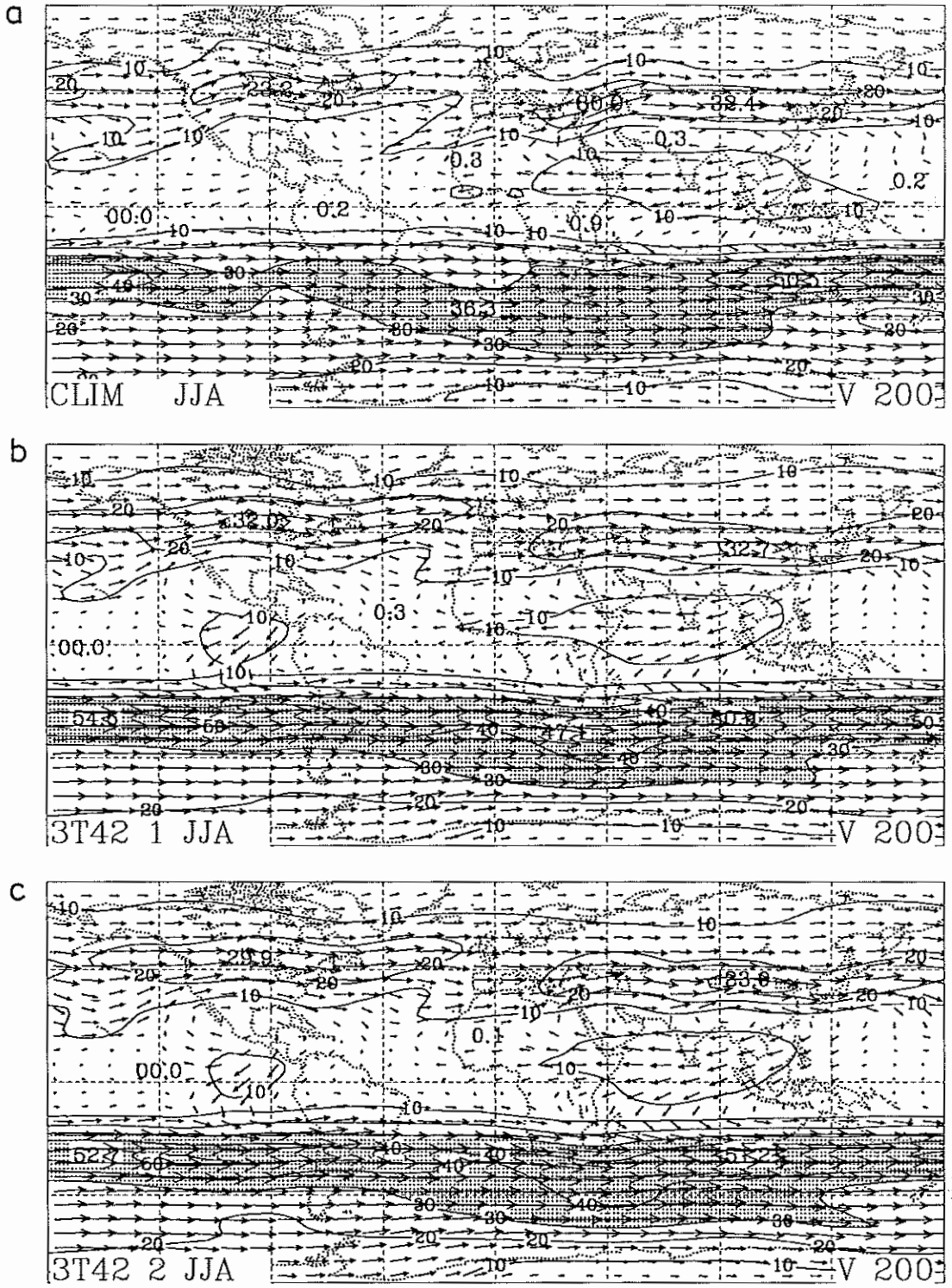

Figure A 10 As in Fig. A9 except for the JJA season.

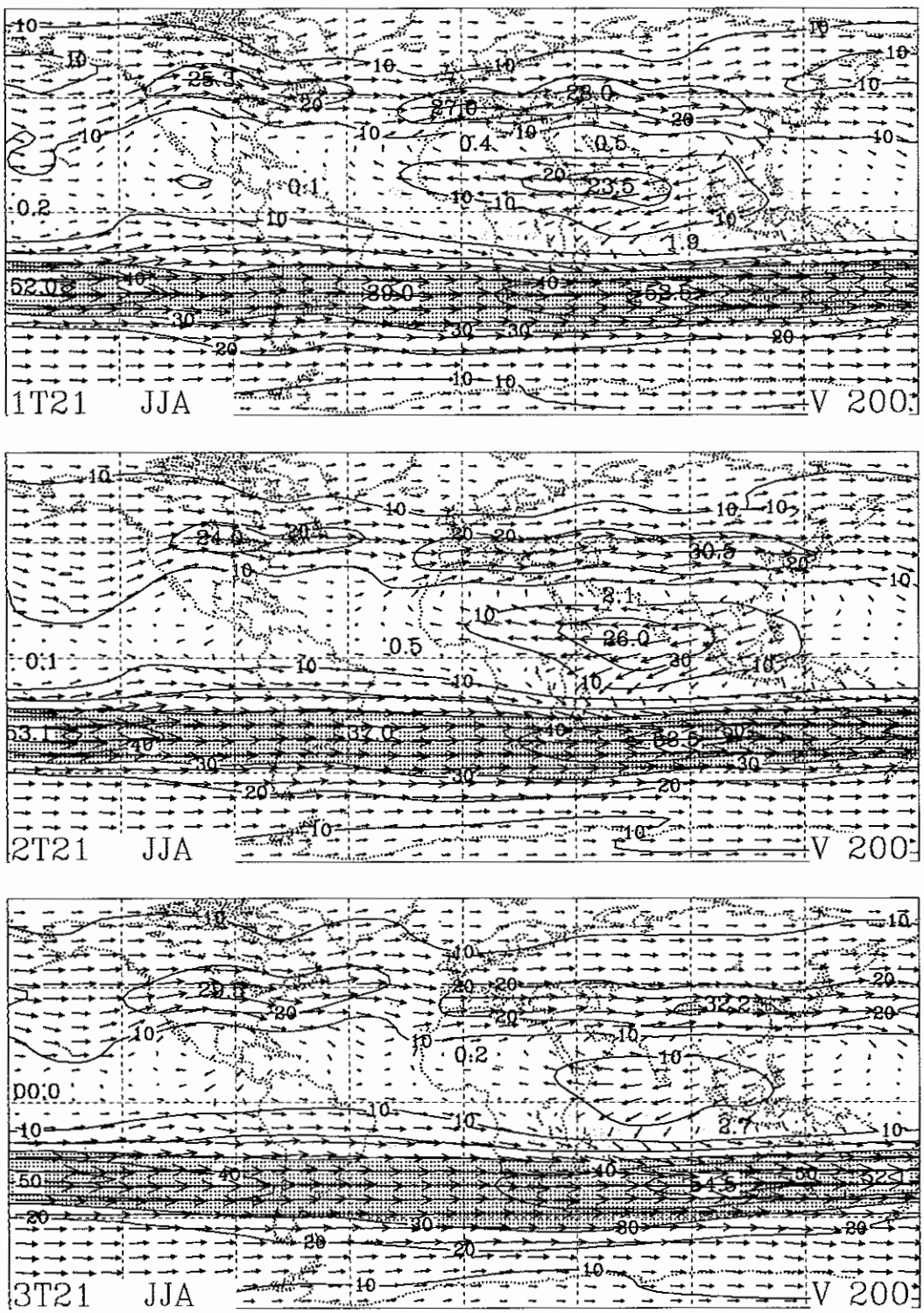

Figure A 10 (cont.)

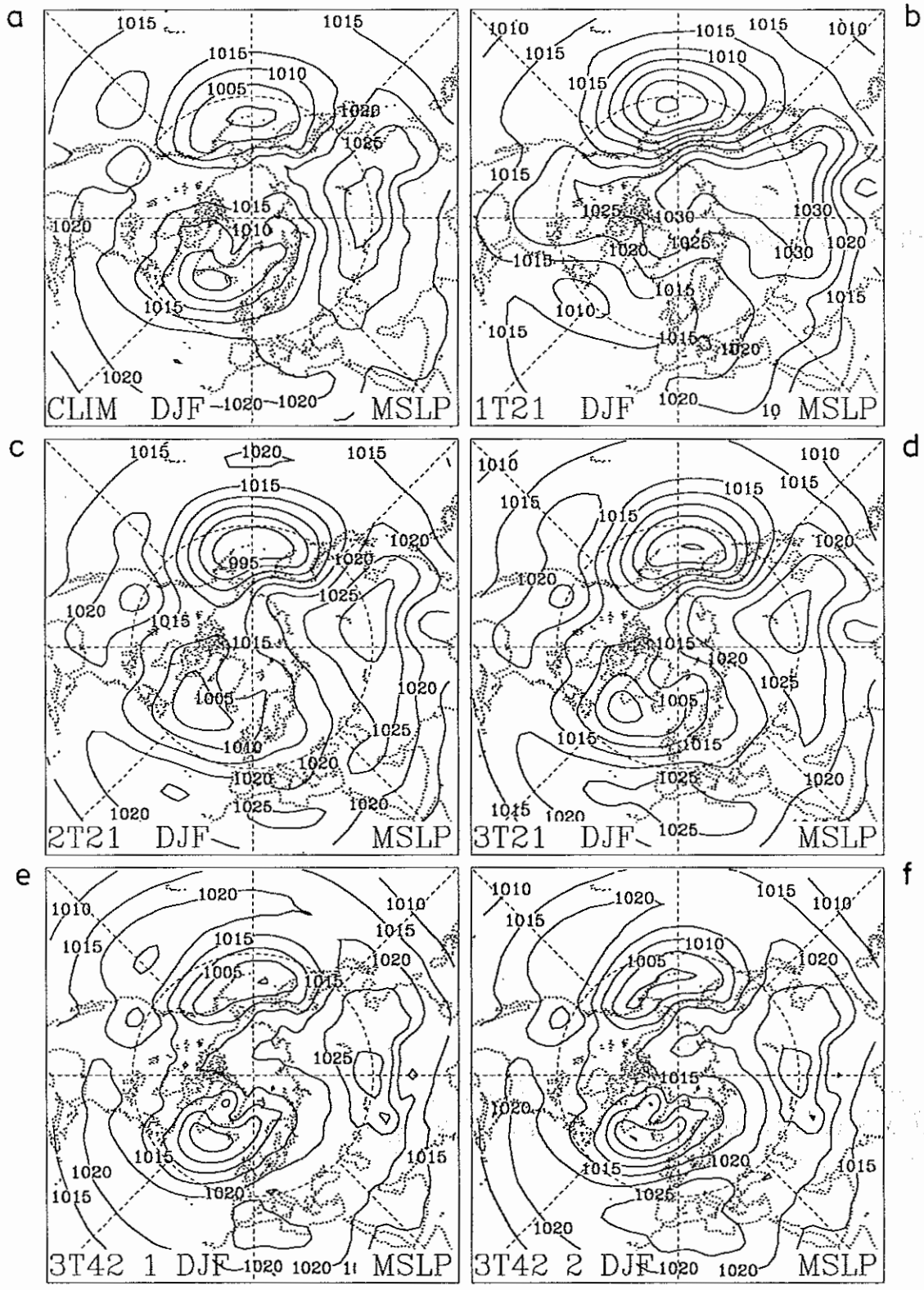

Figure A 11 a) Climatological distribution of mean sea level pressure (hPa) in the Northern Hemisphere for the DJF season based on ECMWF analyses. b)-f) Simulated distributions obtained with different versions of the ECHAM model. For model notations see Fig. A1.

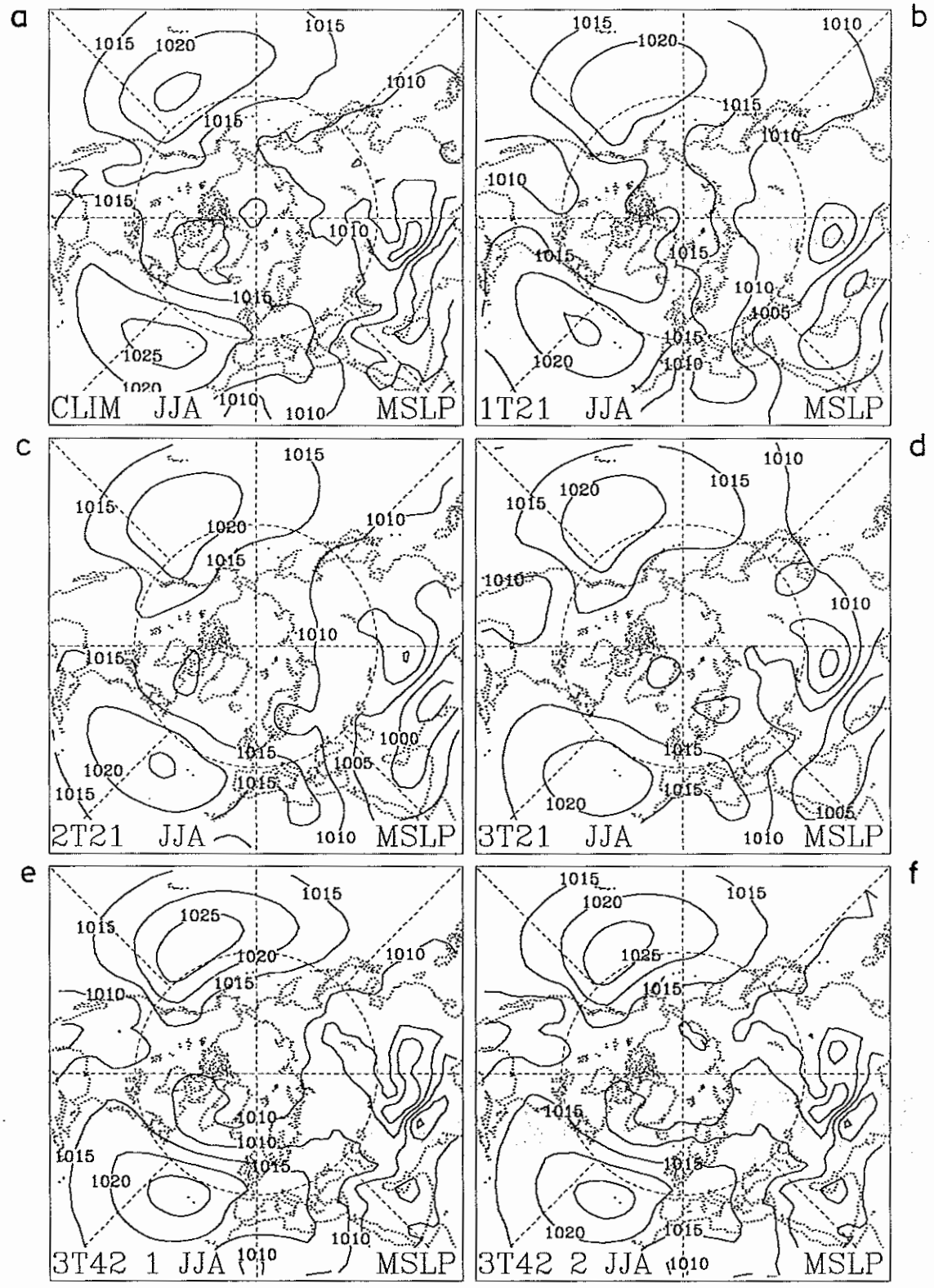

Figure A 12 As in Fig. A11 except for the JJA season.

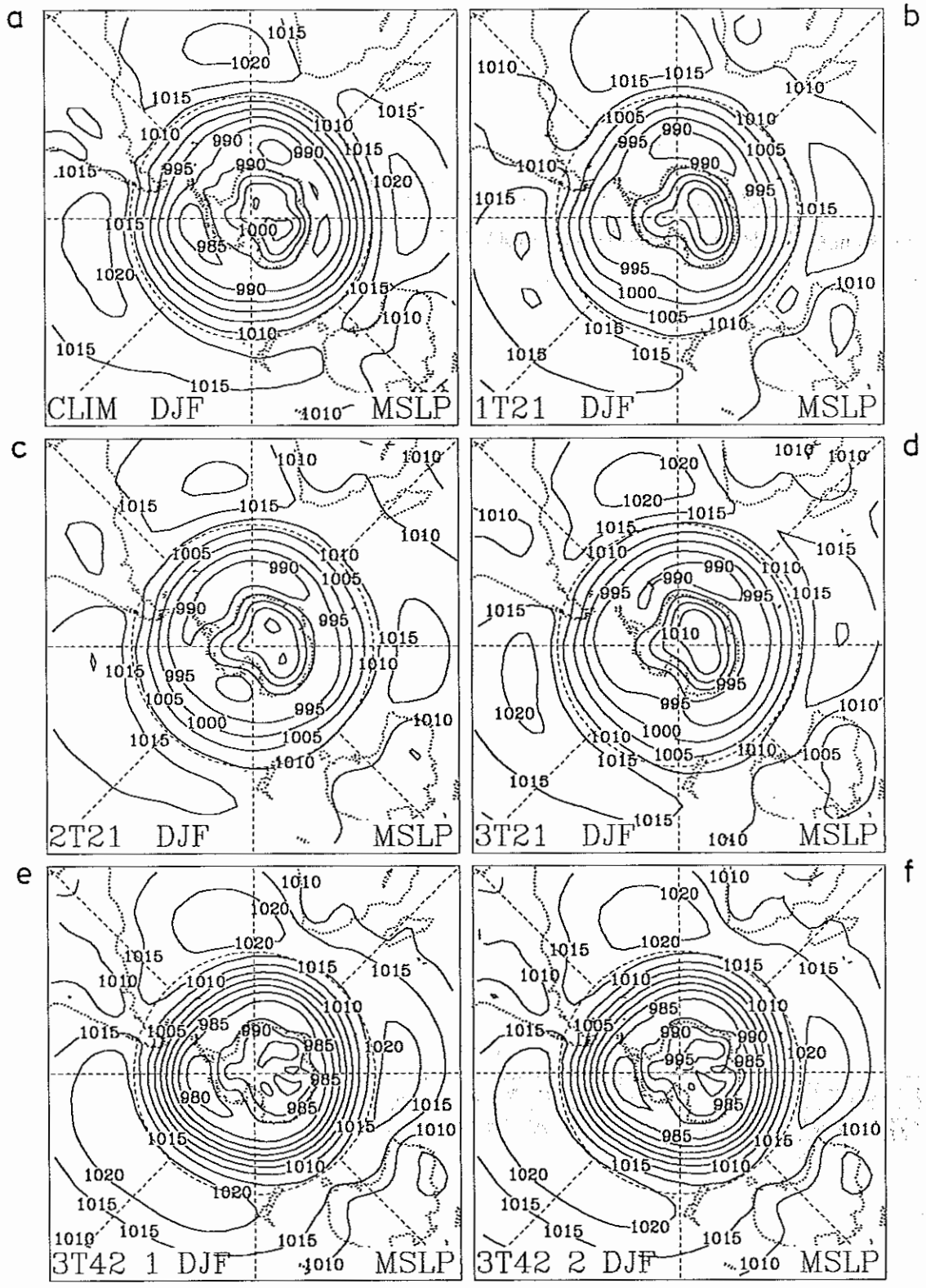

Figure A 13 As in Fig. A11 except for the Southern Hemisphere.

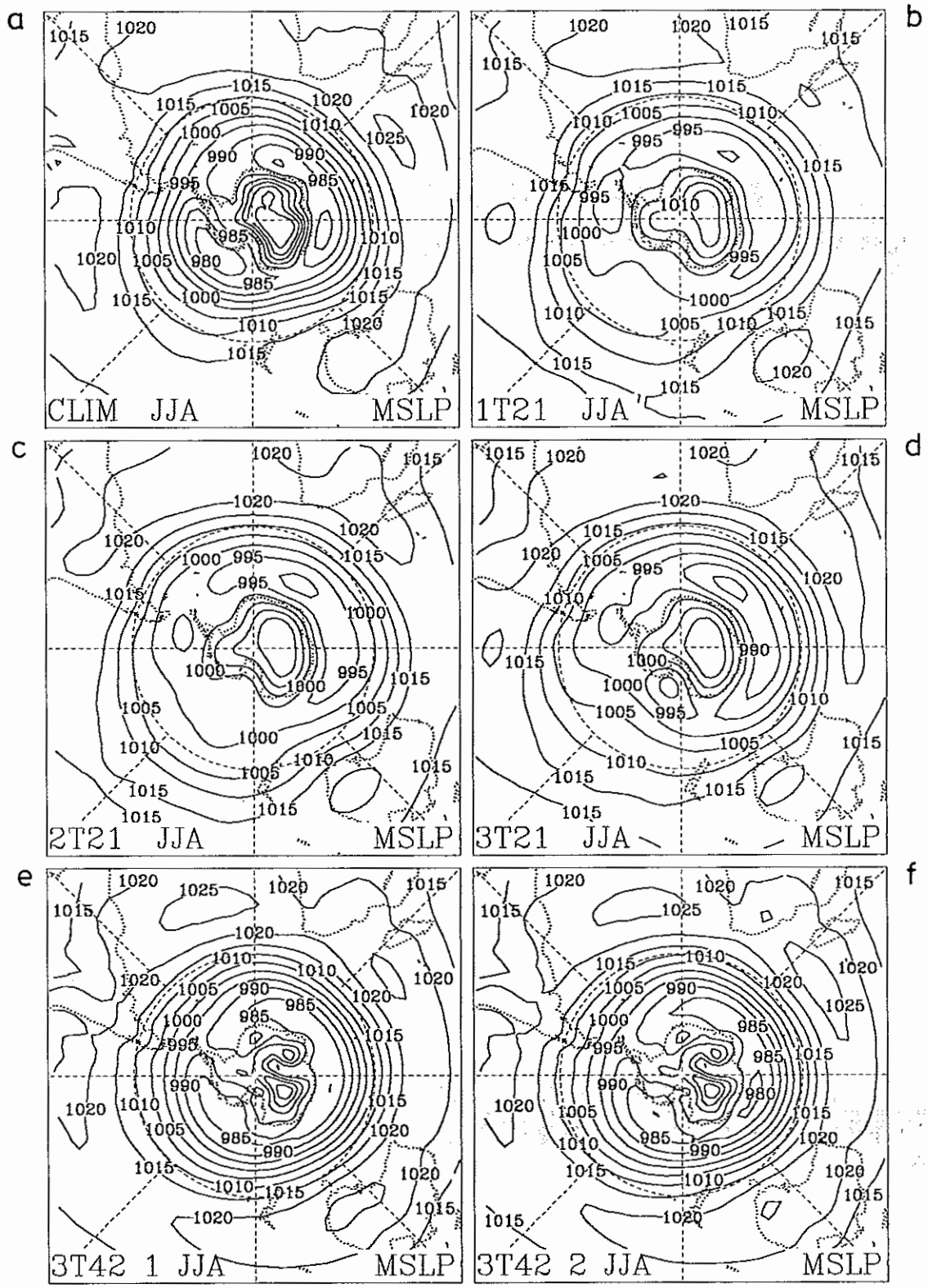

Figure A 14 As in Fig. A12 except for the Southern Hemisphere.

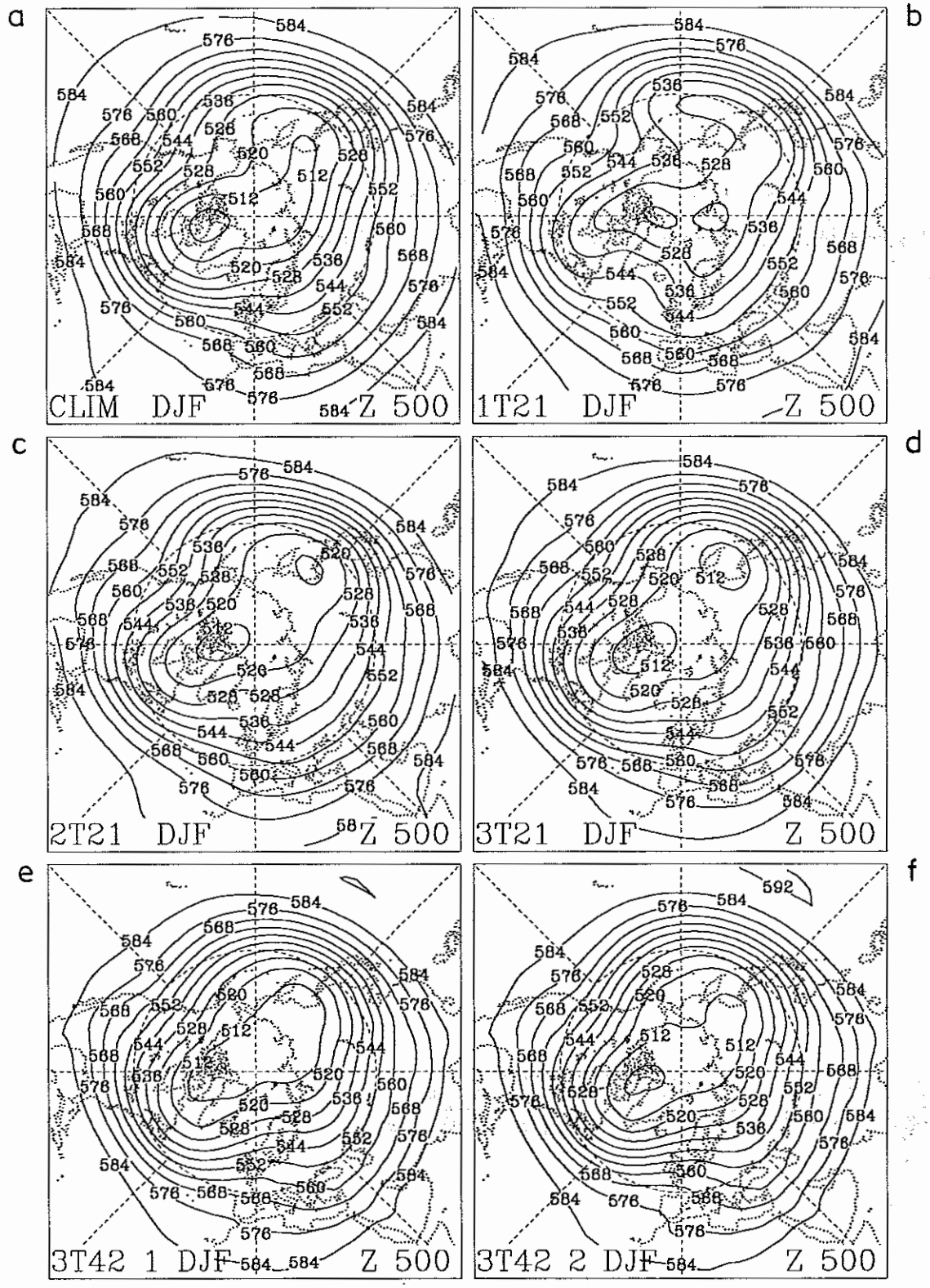

Figure A 15 a) Climatological distribution of 500 hPa geopotential height (dm) in the Northern Hemisphere for DJF based on ECMWF analyses. b)-f) Simulated distributions obtained with different versions of the ECHAM model. For model notations see Fig. A1.

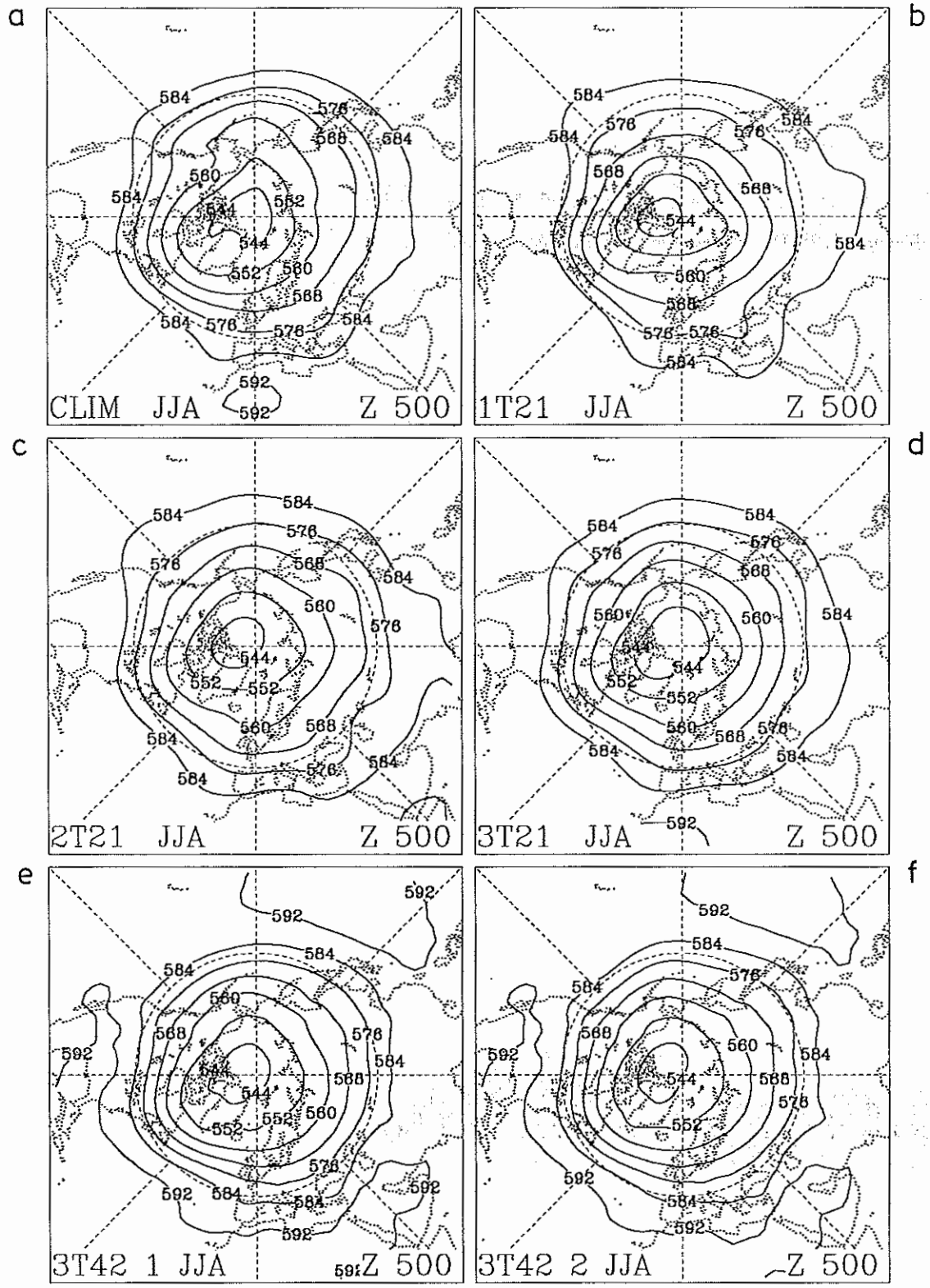

Figure A 16 As in Fig. A15 except for the JJA season.

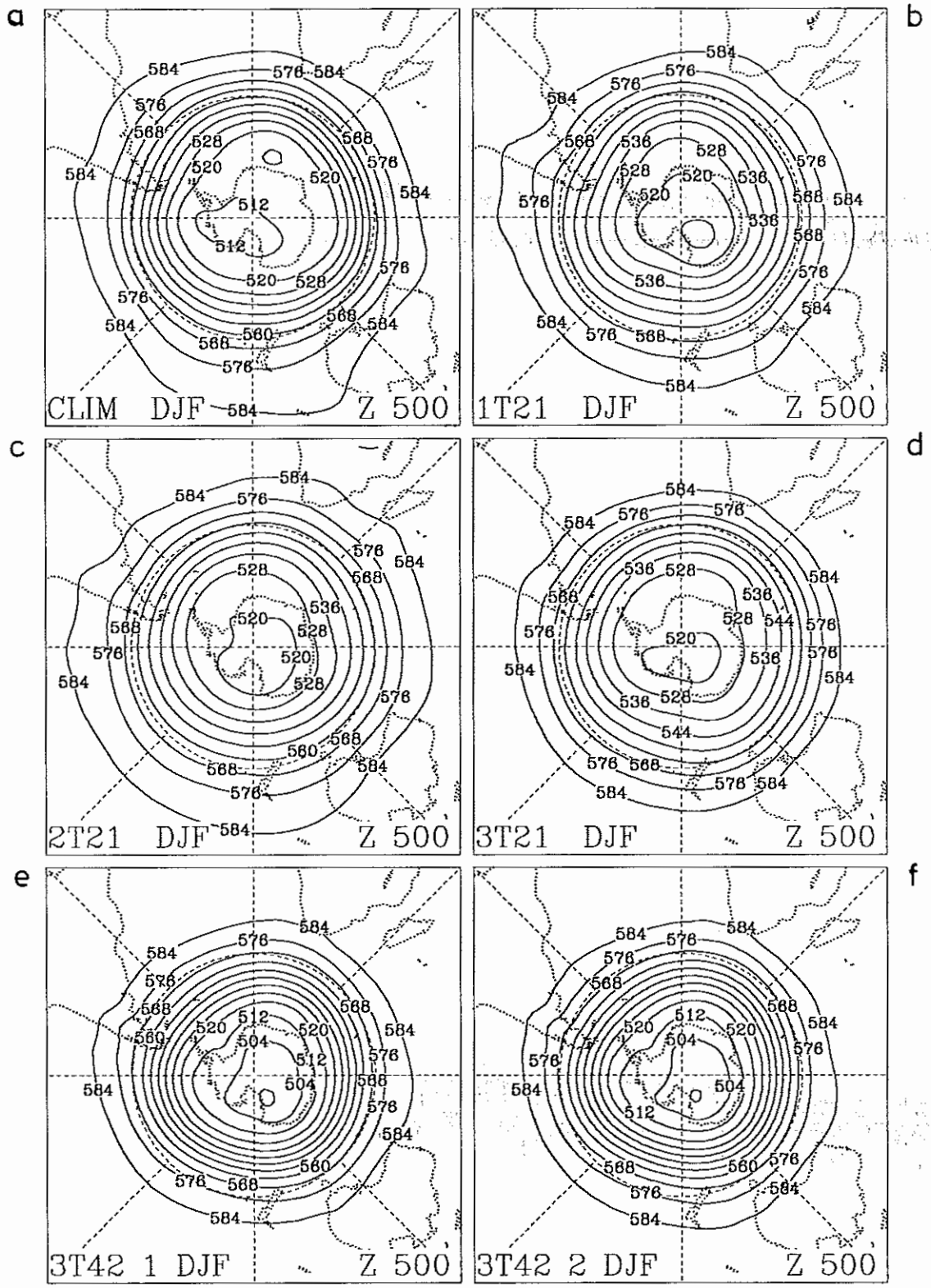

Figure A 17 As in Fig. A15 except for the Southern Hemisphere.

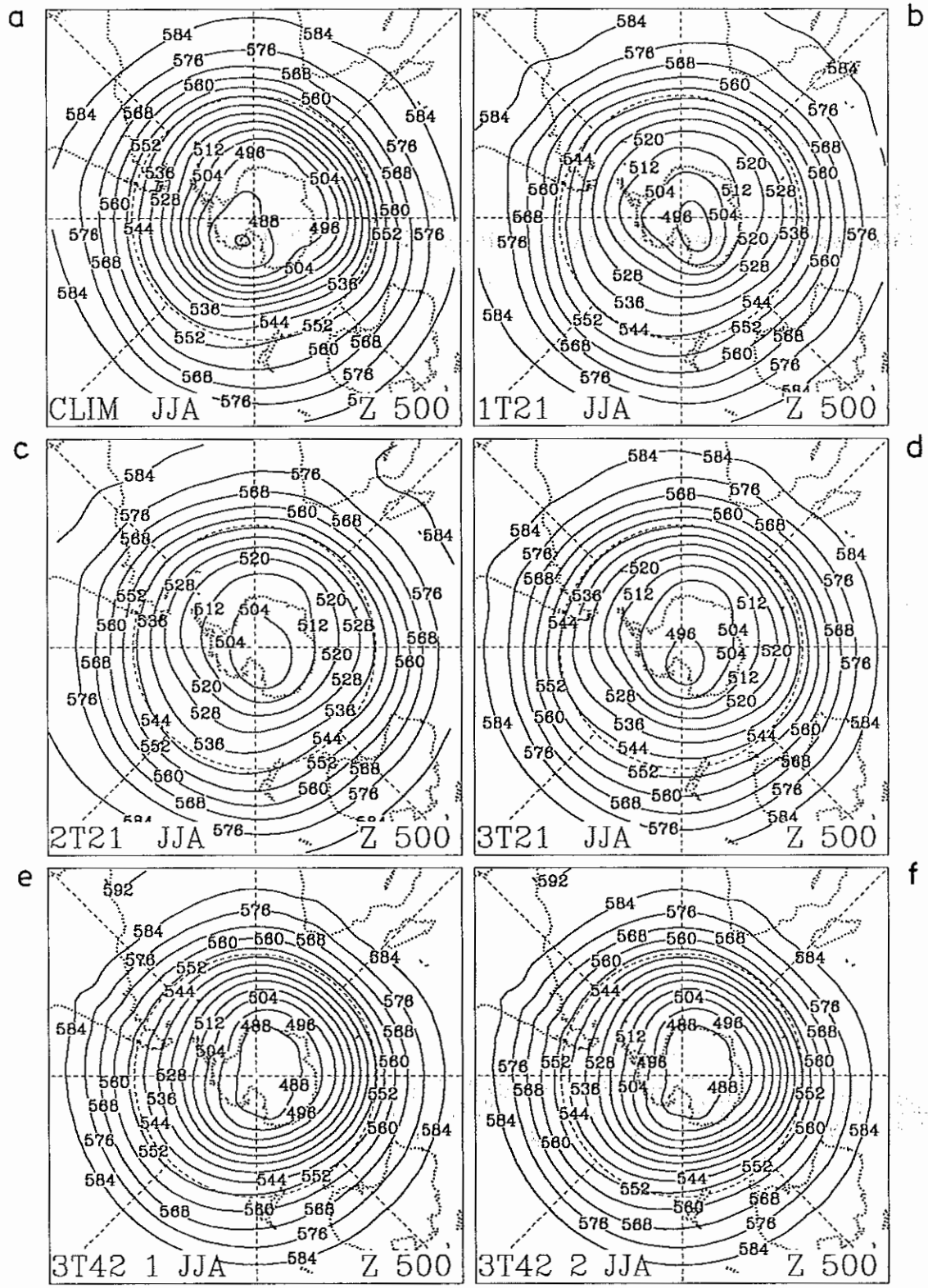

Figure A 18 As in Fig. A16 except for the Southern Hemisphere.

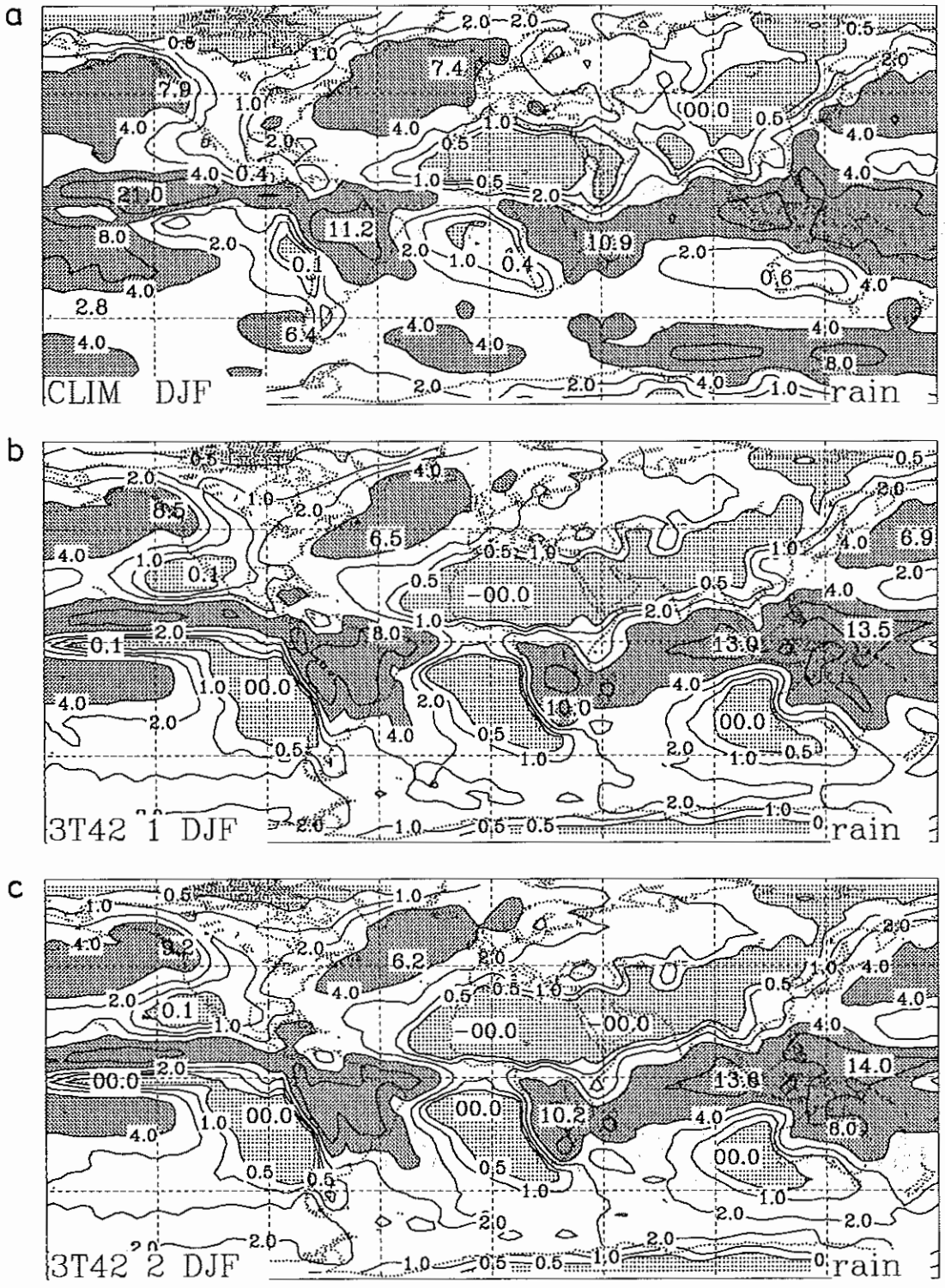

Figure A 19 a) Climatological distribution of precipitation (mm/d) for the DJF season based on the analysis of Legates and Willmott (1990). b)-f) Simulated distributions obtained with different versions of the ECHAM model. For model notations see Fig. A1. Contour spacings: .5, 1., 2., 4., 8., ... mm/d. Light (dark) stippling indicates areas with P<0.5 (P>4) mm/d, respectively.

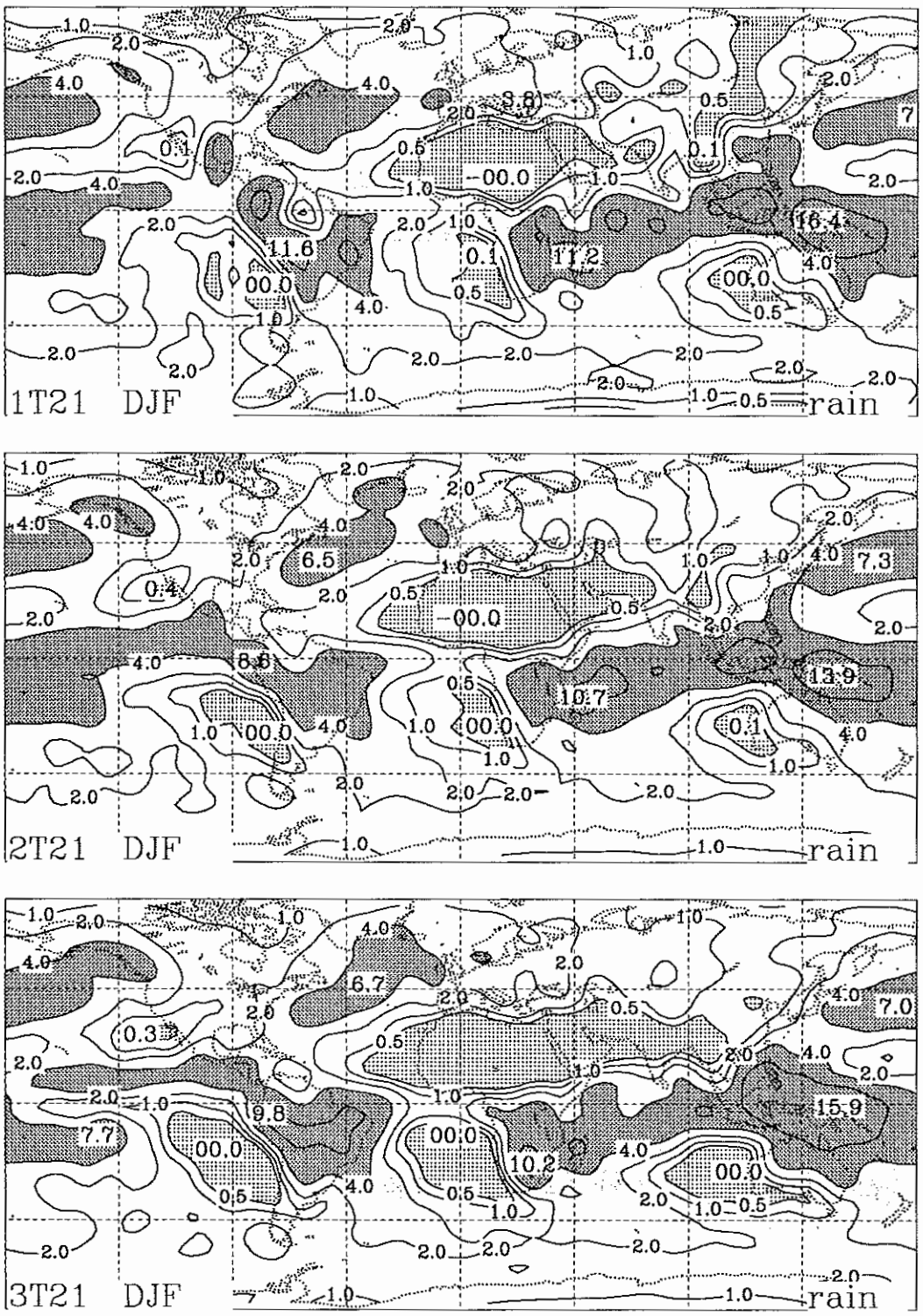

Figure A 19 (cont.)

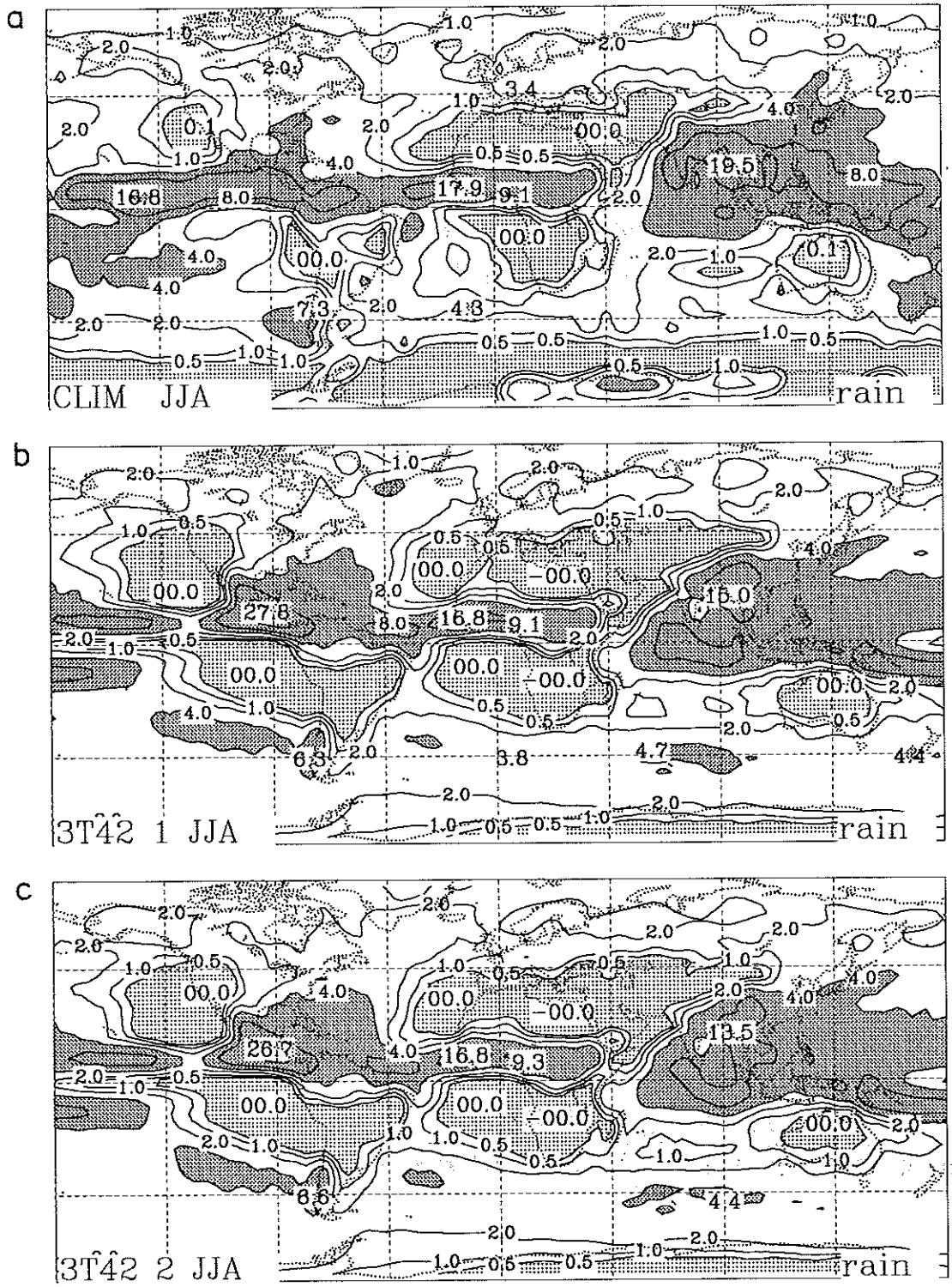

Figure A 20 As in Fig. A19 except for the JJA season.

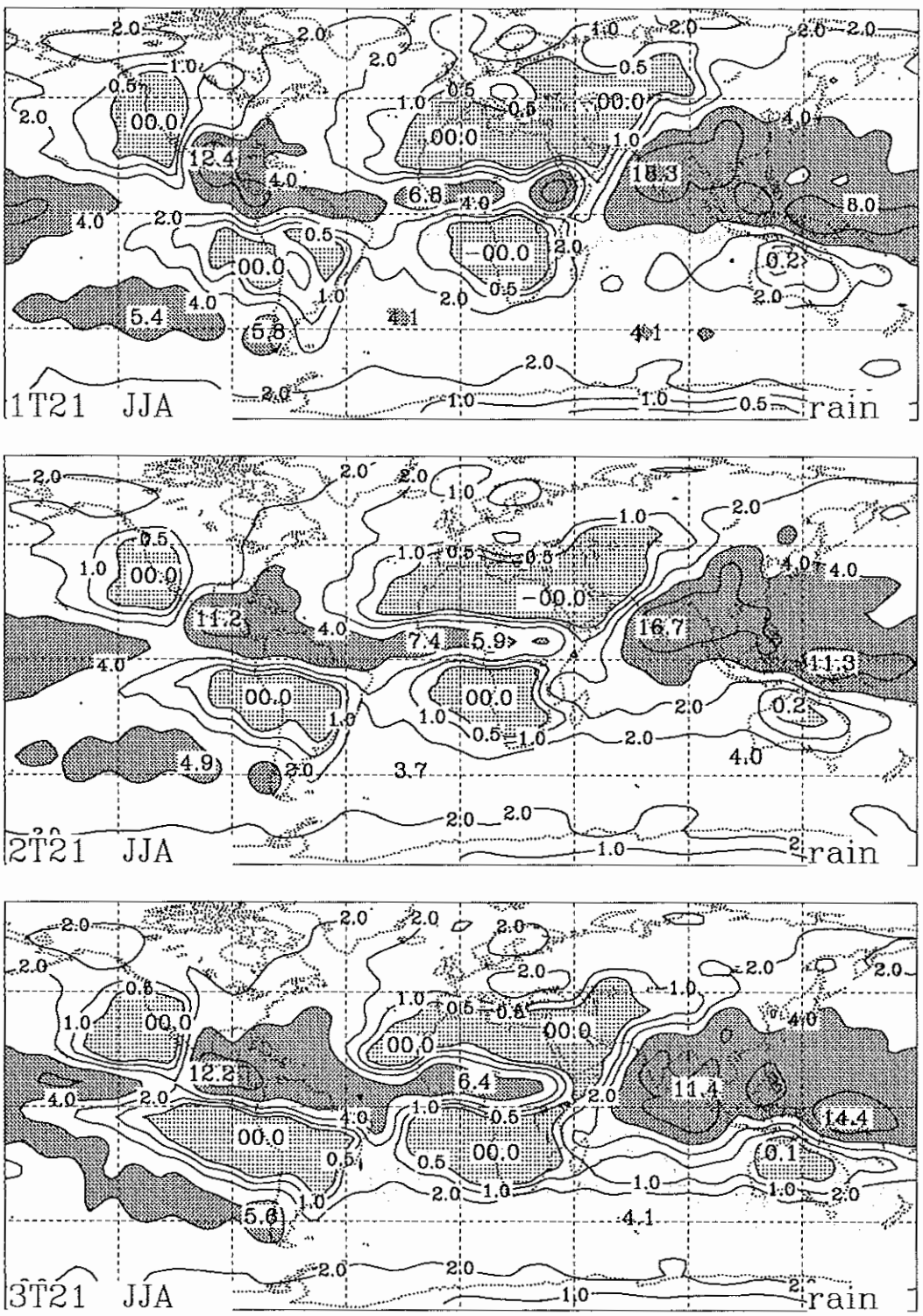

Figure A 20 (cont.)

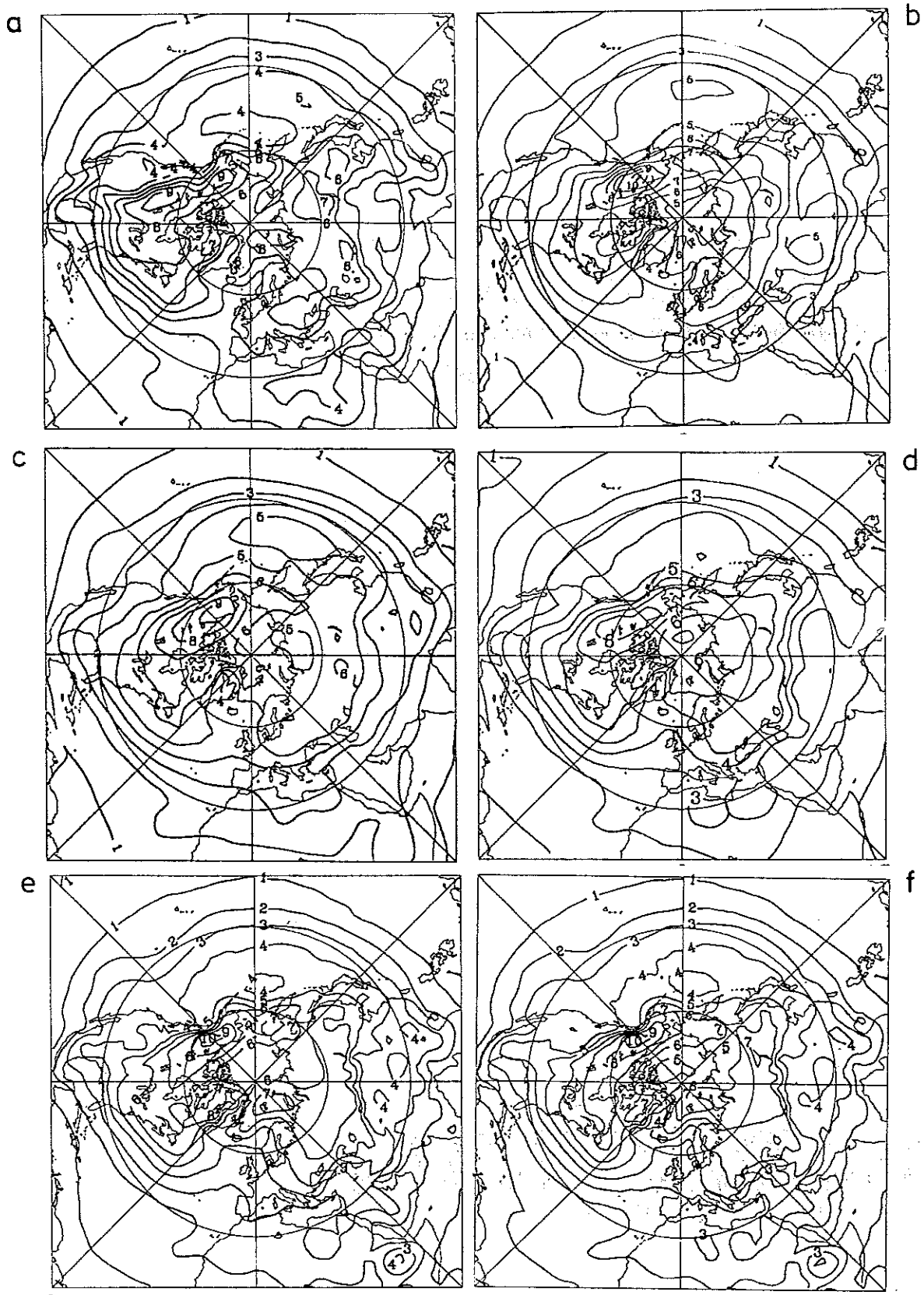

Figure A 21 Standard deviation of 850 hPa temperature (K) due to transient eddies computed from the unfiltered time series for the DJF season. a) ECMWF analyses, b) ECHAM1, c) ECHAM2, d) ECHAM3/T21, e) ECHAM3/T42 (1. decade), f) ECHAM3/T42 (2. decade).

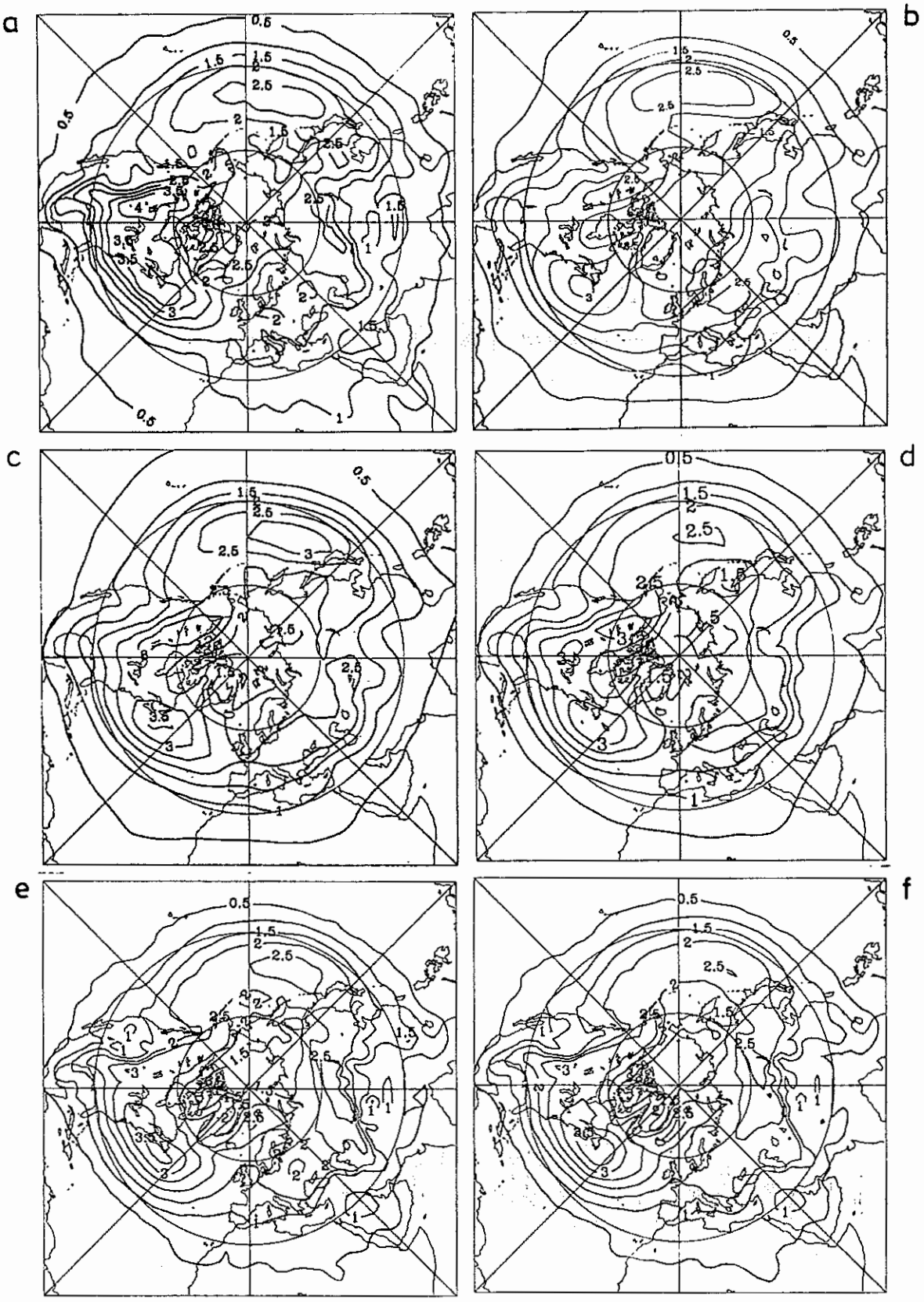

Figure A 22 As in Fig. A21 except for the band-pass filtered frequency range.

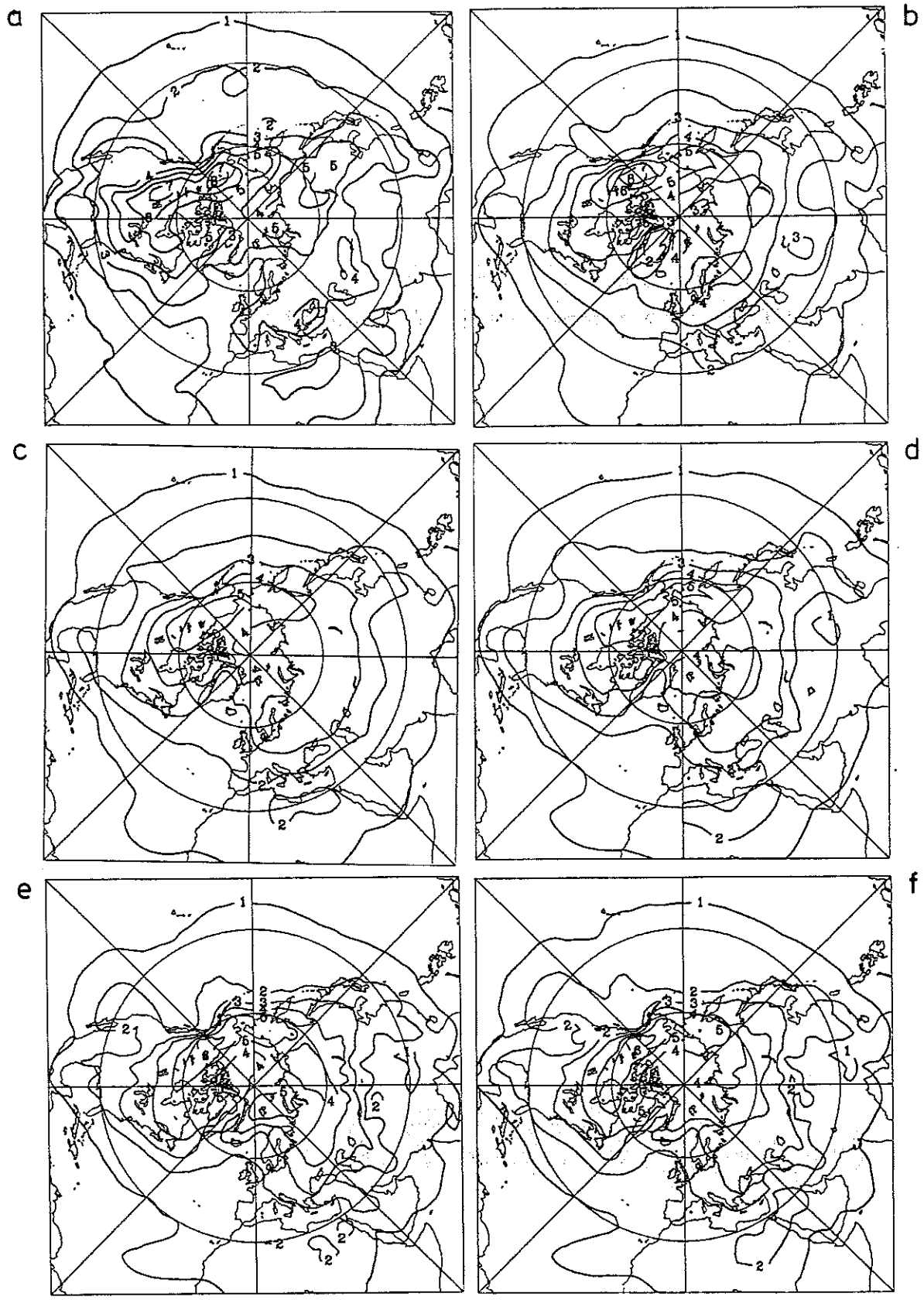

Figure A 23 As in Fig. A21 except for the low-pass filtered frequency range.

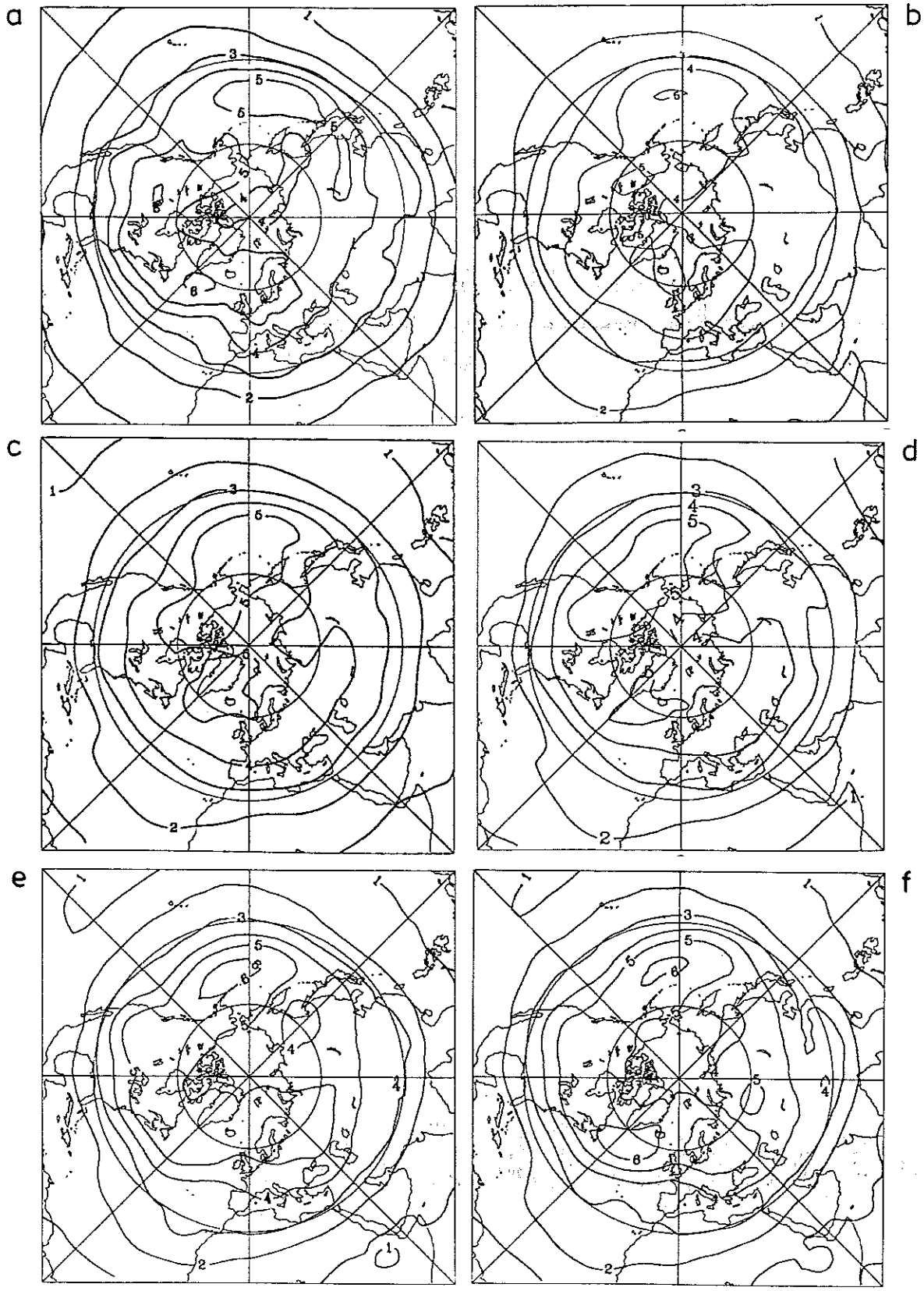

Figure A 24 Standard deviation of 500 hPa temperature (K) due to transient eddies computed from the unfiltered time series for the DJF season. a) ECMWF analyses, b) ECHAM1, c) ECHAM2, d) ECHAM3/T21, e) ECHAM3/T42 (1. decade), f) ECHAM3/T42 (2. decade).

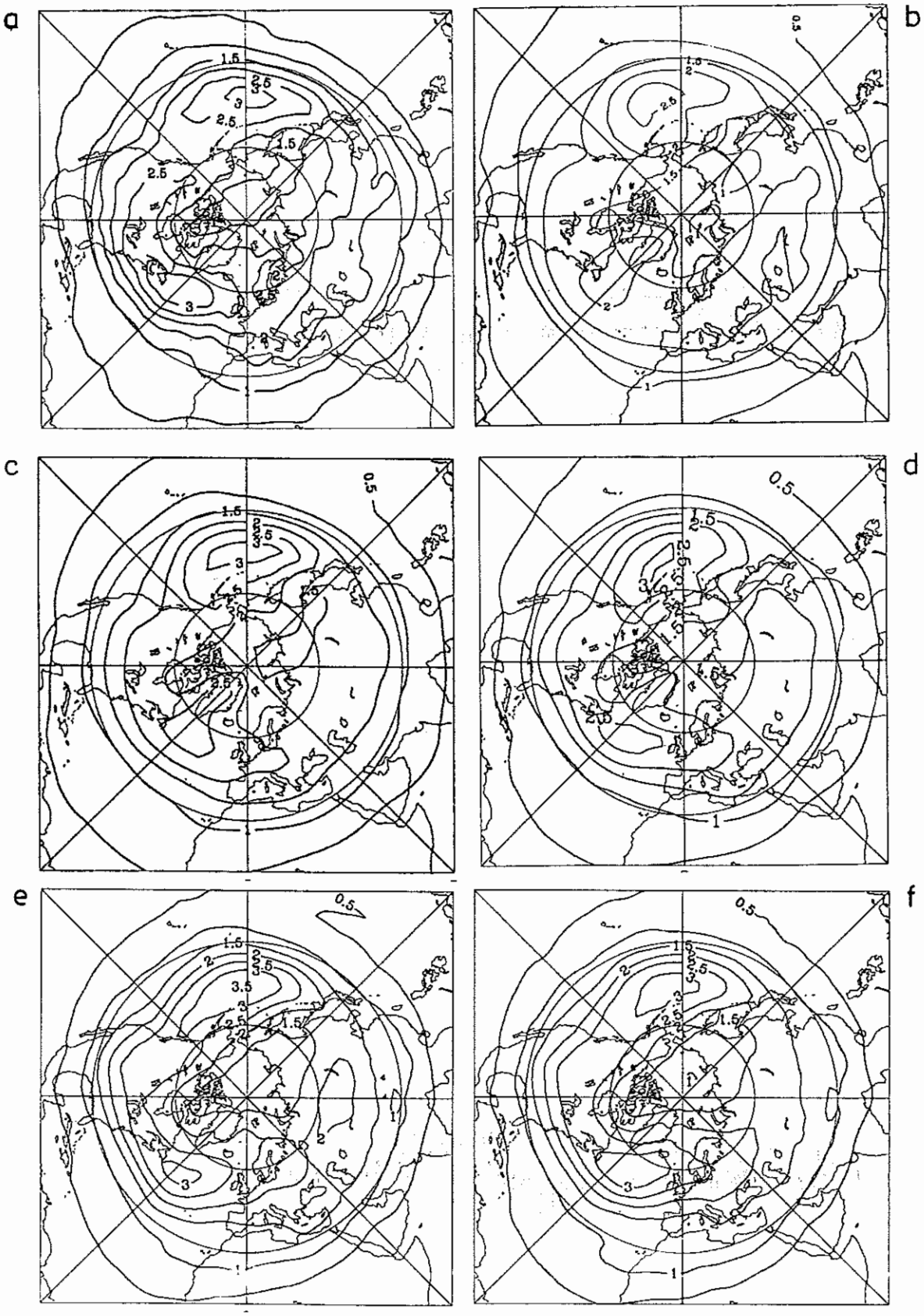

Figure A 25 As in Fig. A24 except for the band-pass filtered frequency range.

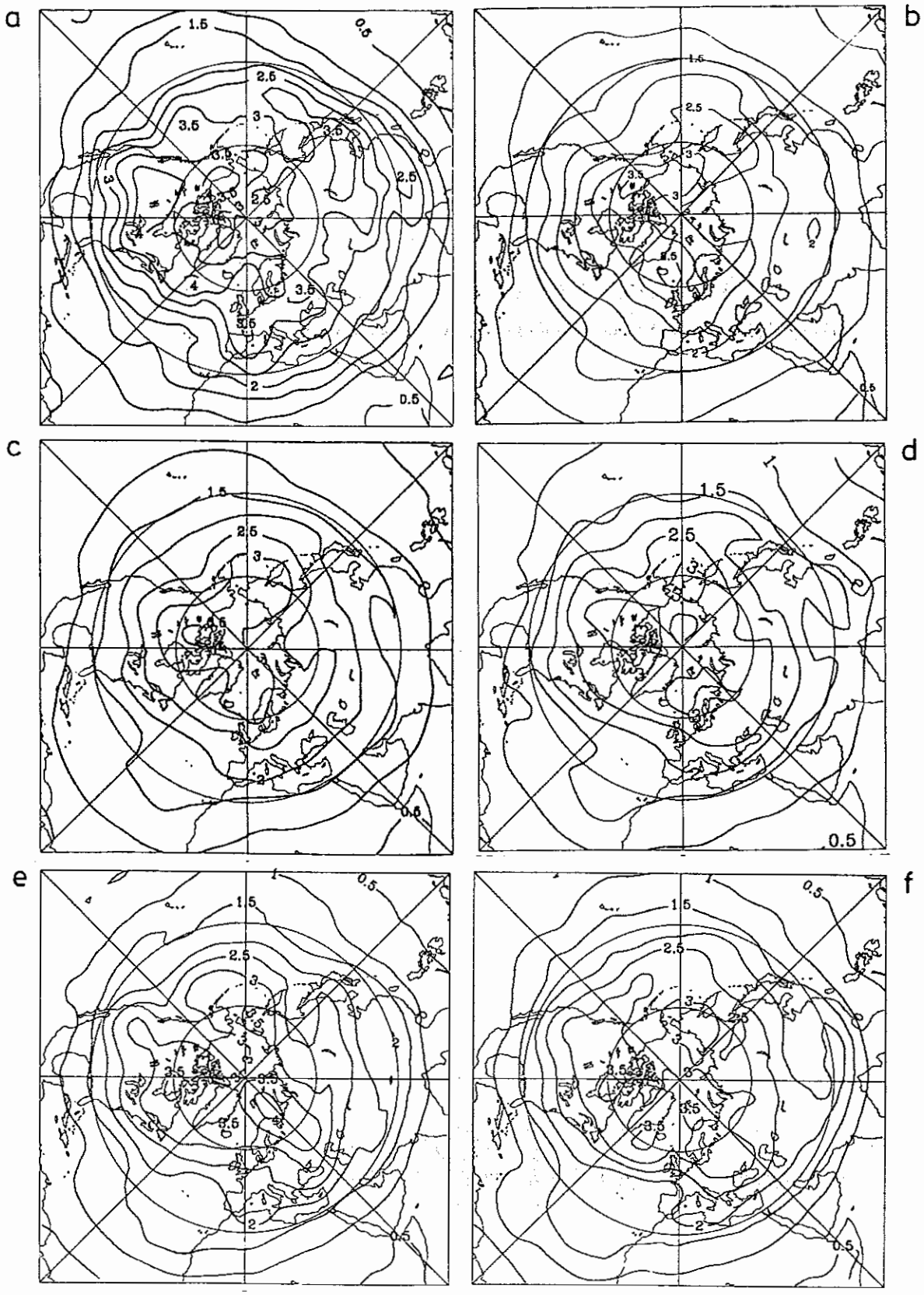

Figure A 26 As in Fig. A24 except for the low-pass filtered frequency range.

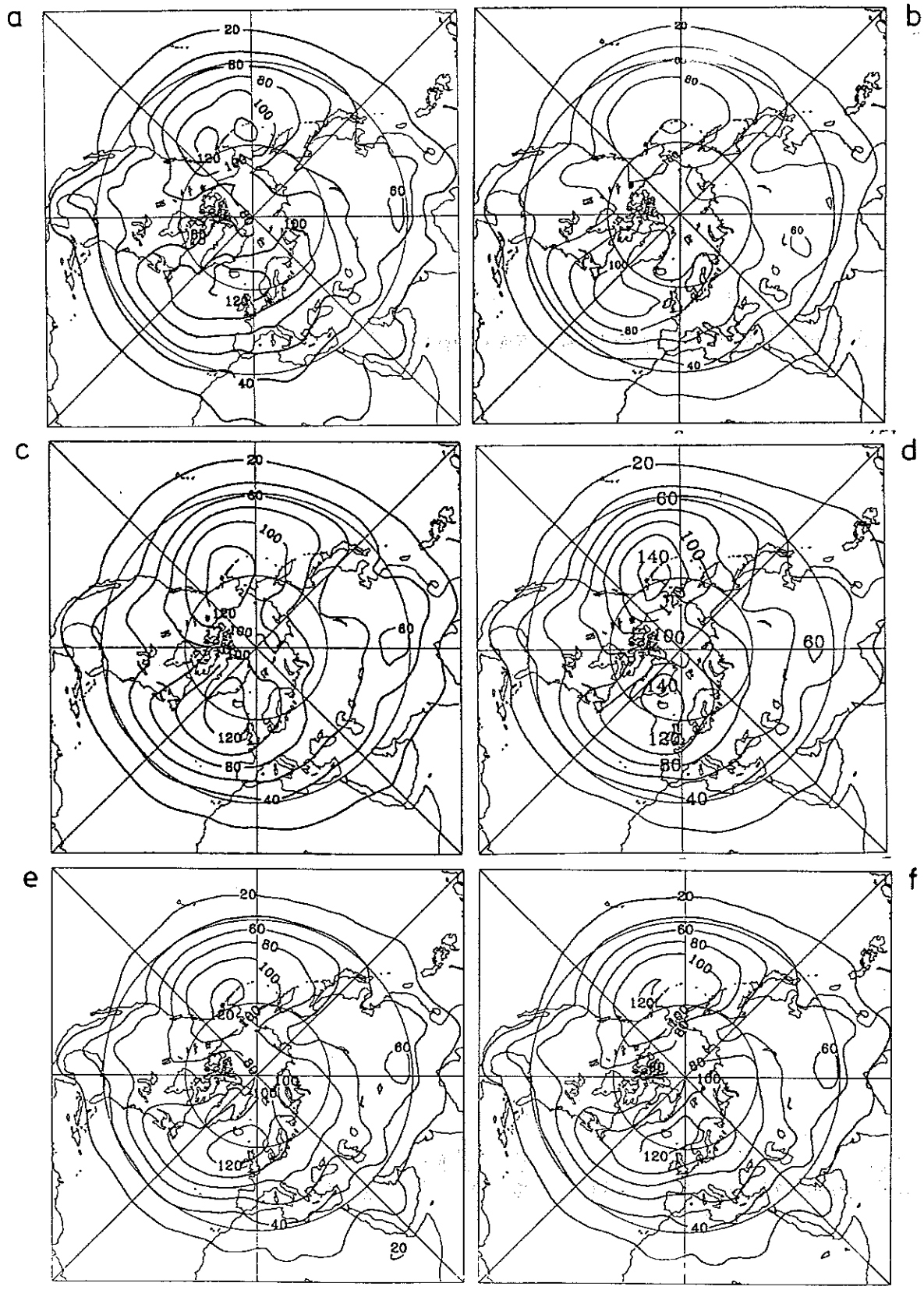

Figure A 27 Standard deviation of 1000 hPa geopotential height (m) due to transient eddies computed from the unfiltered time series for the DJF season. a) ECMWF analyses, b) ECHAM1, c) ECHAM2, d) ECHAM3/T21, e) ECHAM3/T42 (1. decade), f) ECHAM3/T42 (2. decade).

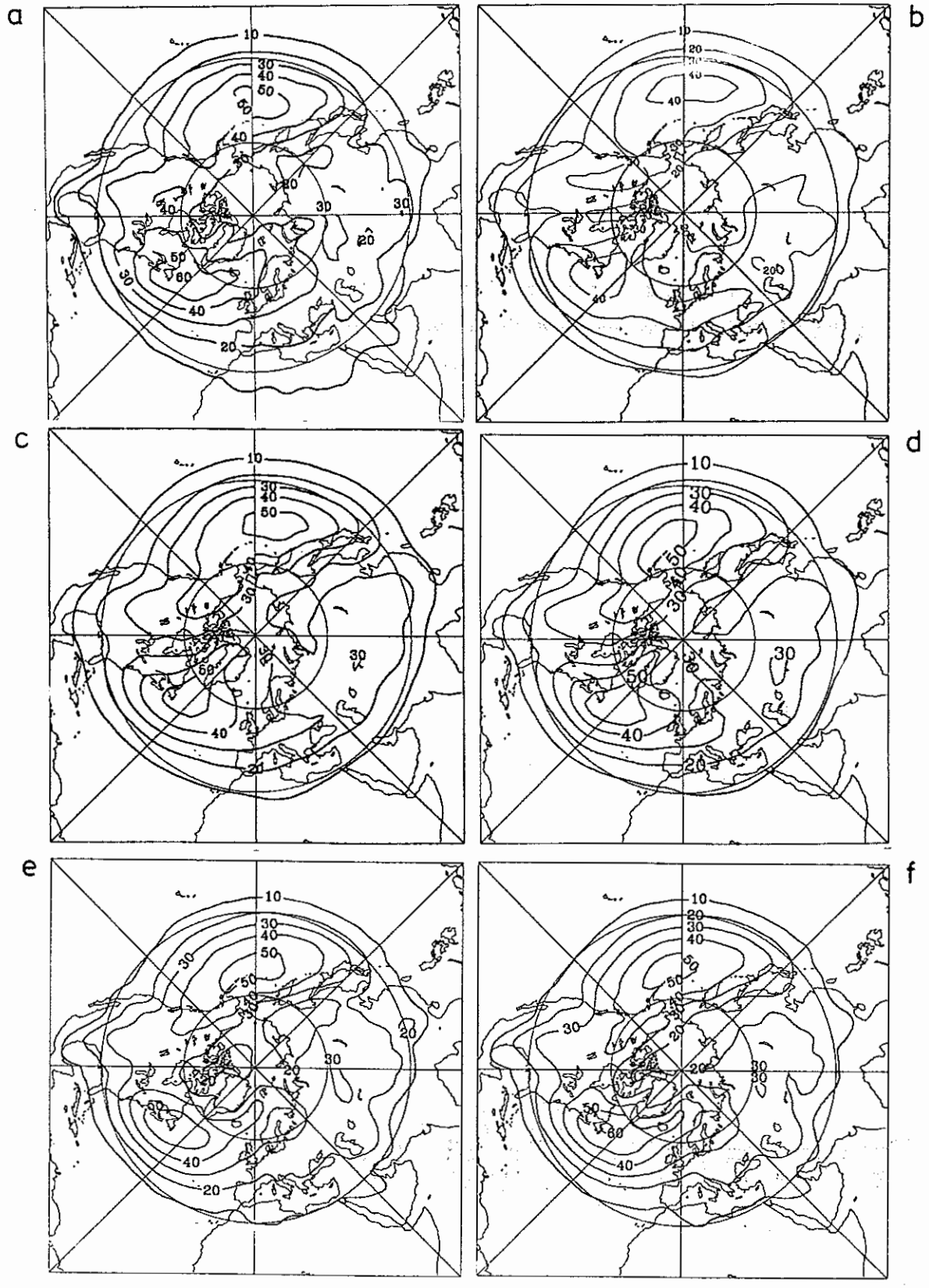

Figure A 28 As in Fig. A27 except for the band-pass filtered frequency range.

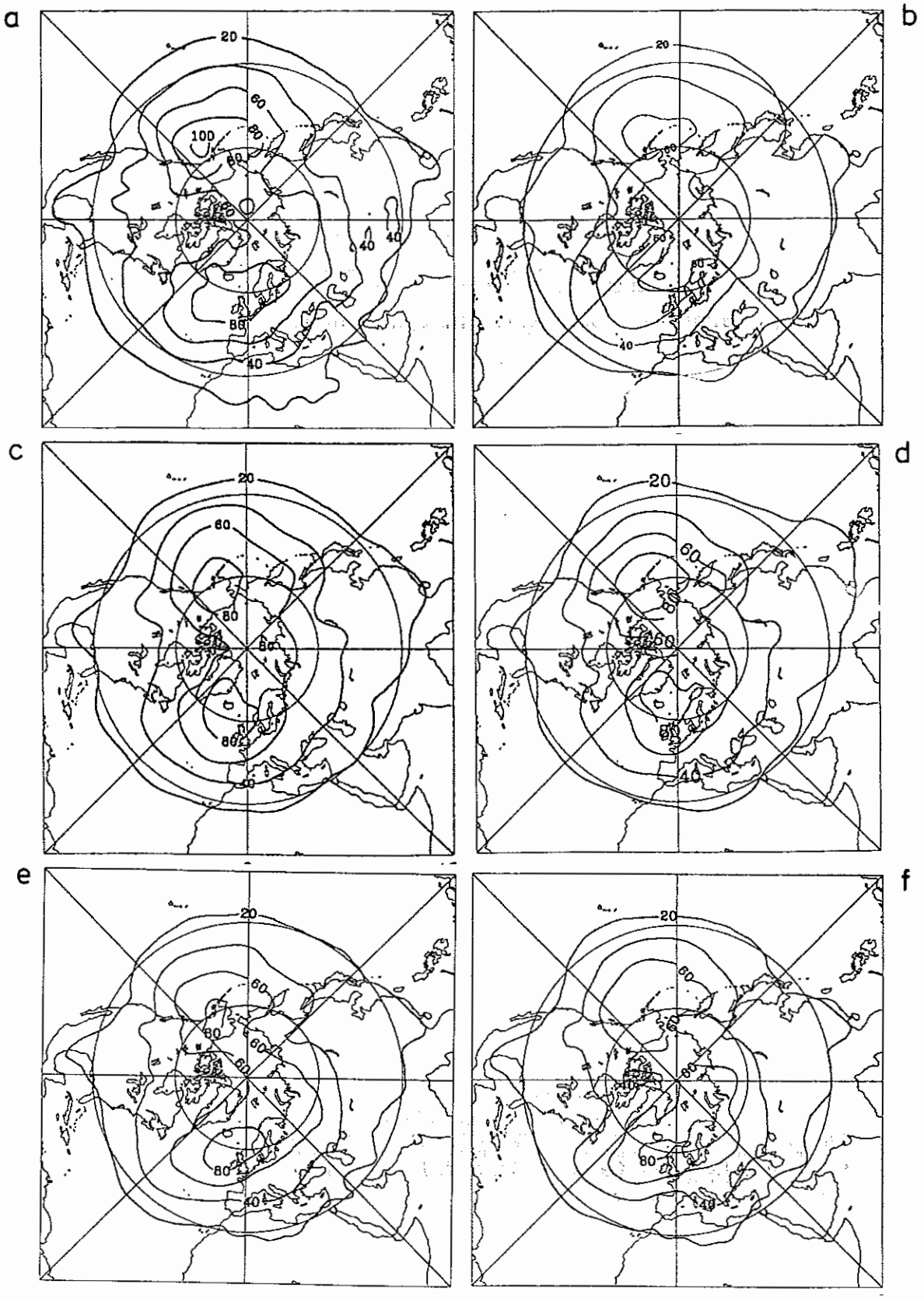

Figure A 29 As in Fig. A27 except for the low-pass filtered frequency range.

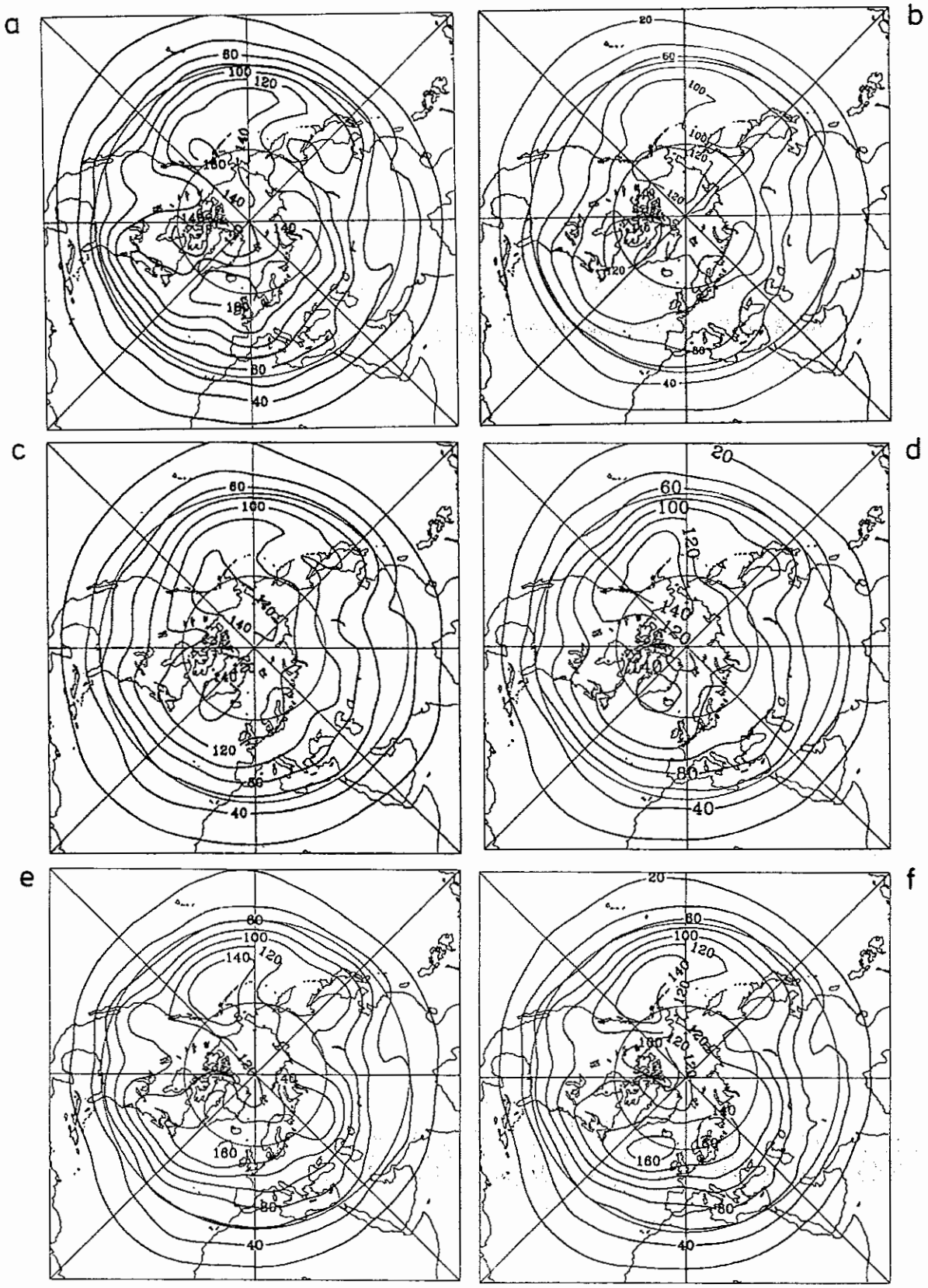

Figure A 30 Standard deviation of 500 hPa geopotential height (m) due to transient eddies computed from the unfiltered time series for the DJF season. a) ECMWF analyses, b) ECHAM1, c) ECHAM2, d) ECHAM3/T21, e) ECHAM3/T42 (1. decade), ECHAM3/ T42 (2. decade).

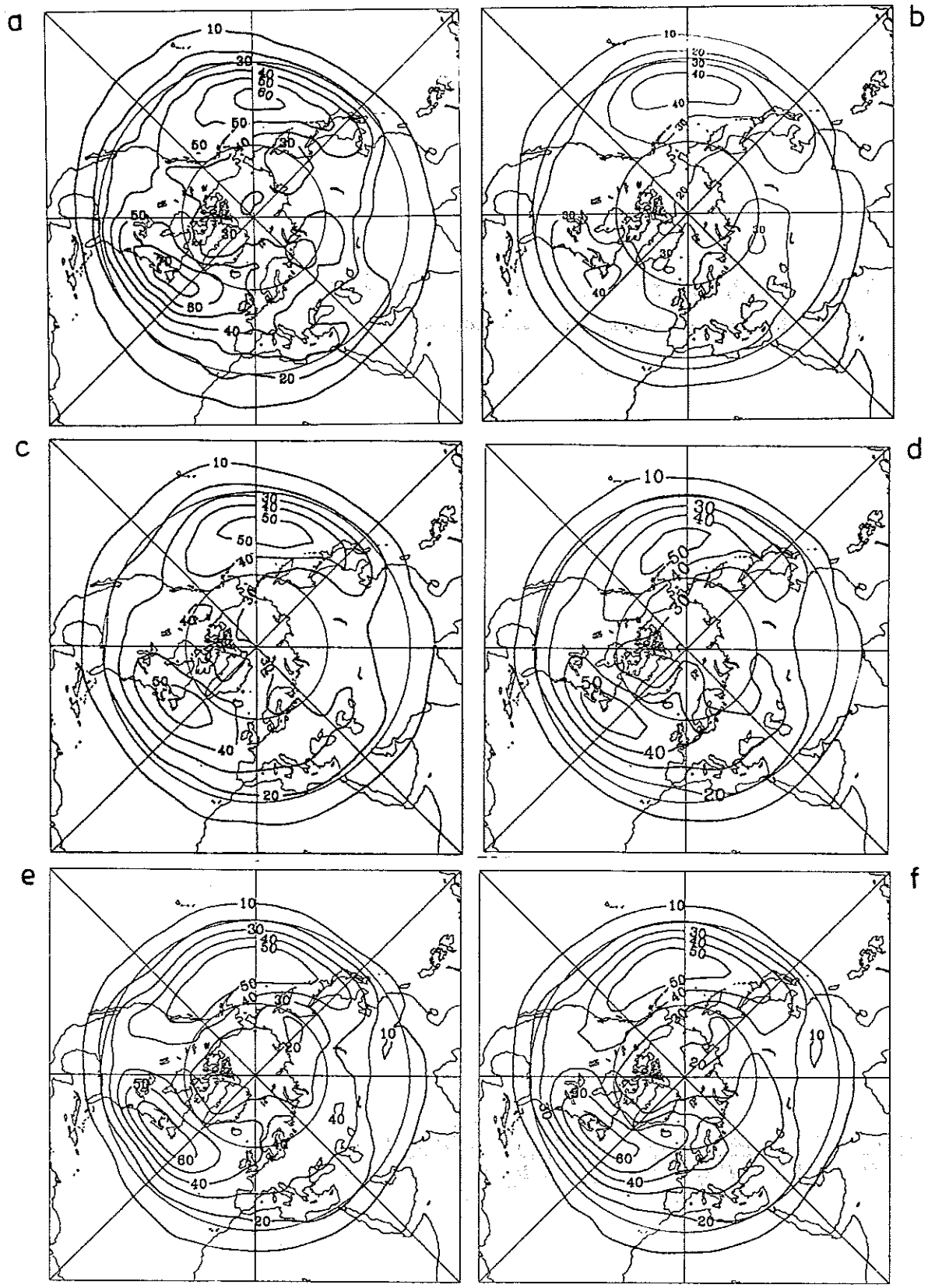

Figure A 31 As in Fig. 30 except for the band-pass filtered frequency range.

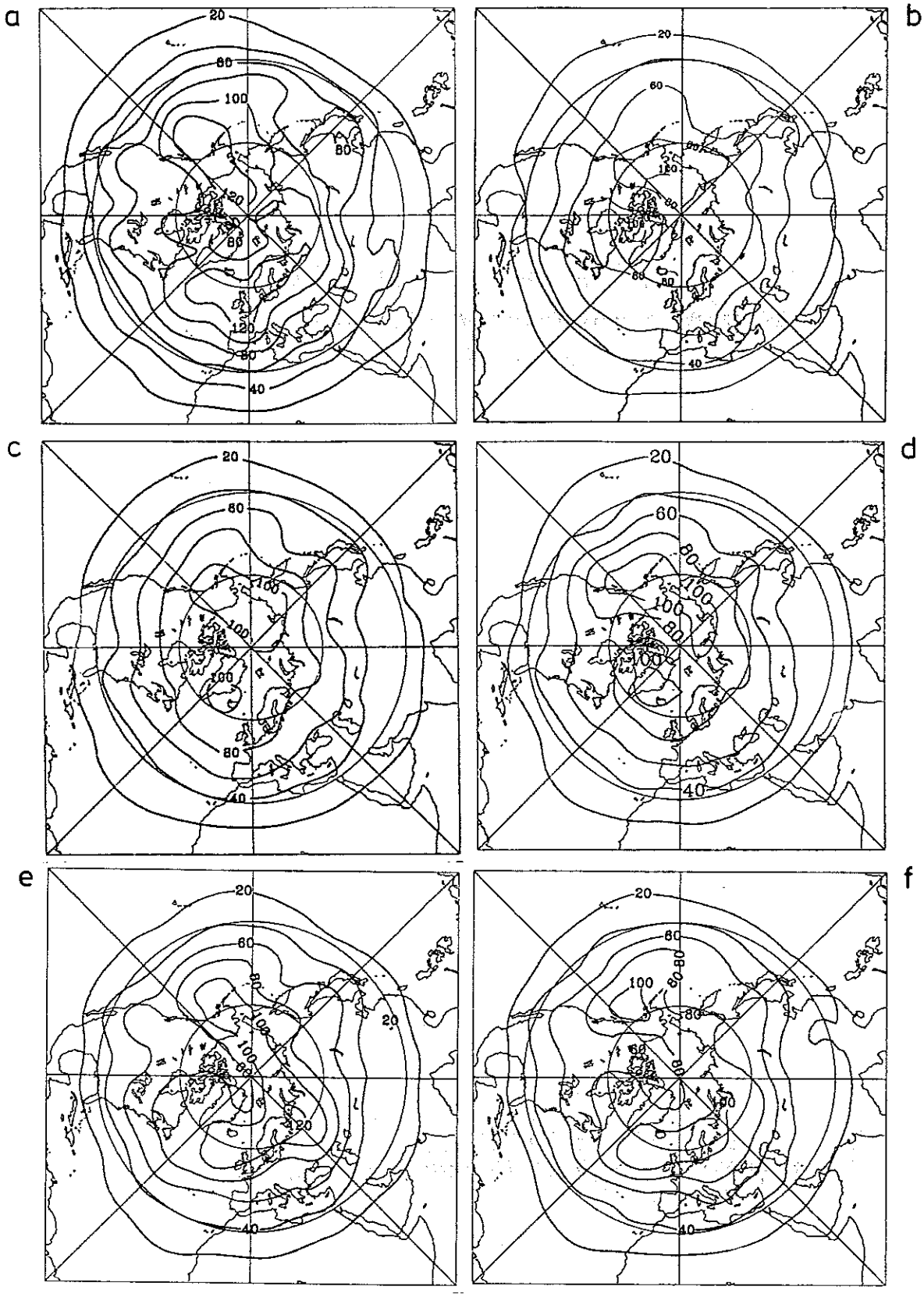

Figure A 32 As in Fig. 30 except for the low-pass filtered frequency range.

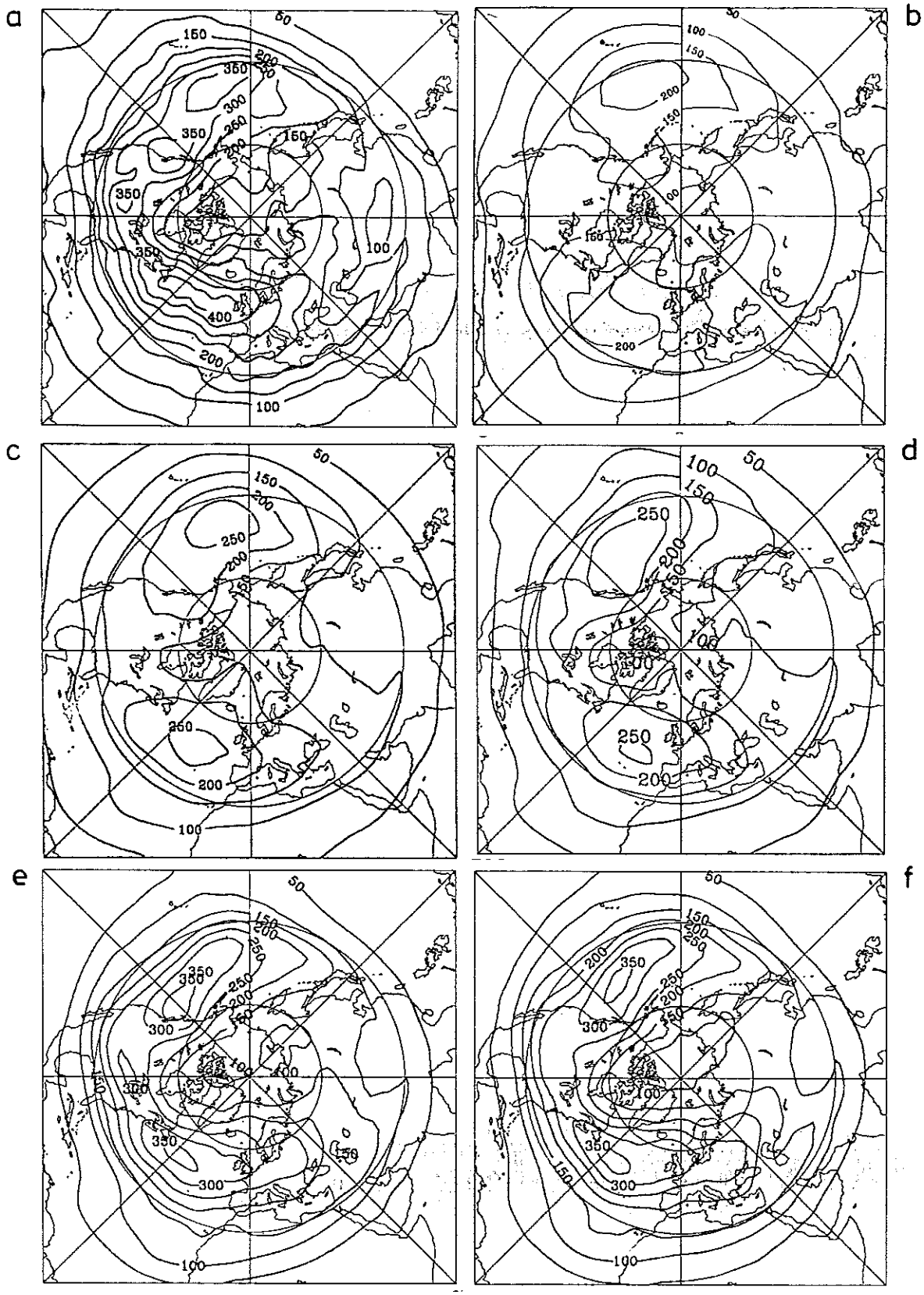

Figure A 33 Transient eddy kinetic energy (m^2/s^2) at 300 hPa computed from the unfiltered time series for the DJF season. a) ECMWF analyses, b) ECHAM1, c) ECHAM2, d) ECHAM3/T21, e) ECHAM3/T42 (1. decade), f) ECHAM3/T42 (2. decade).

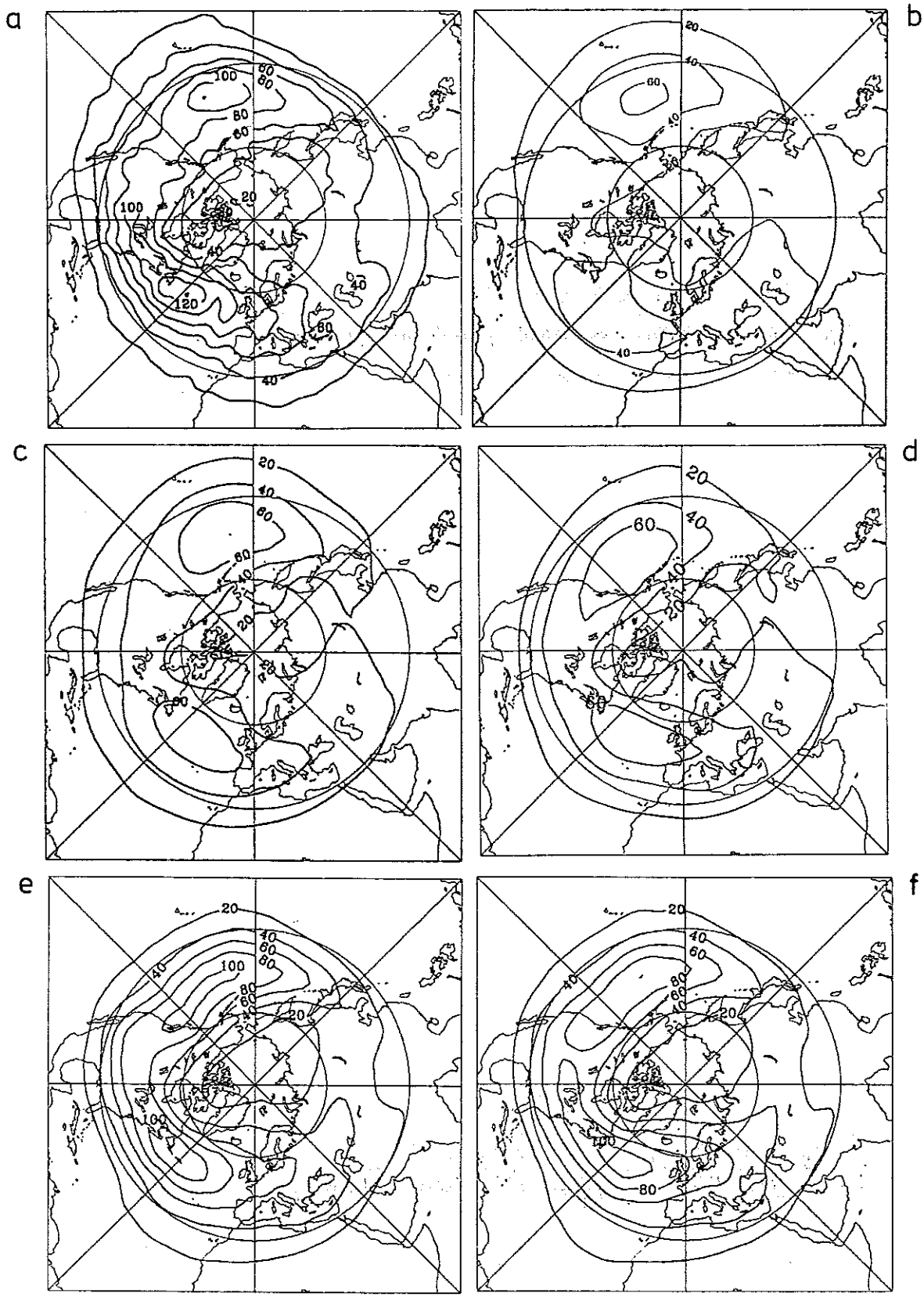

Figure A 34 As in Fig. A33 except for the band-pass filtered frequency range.

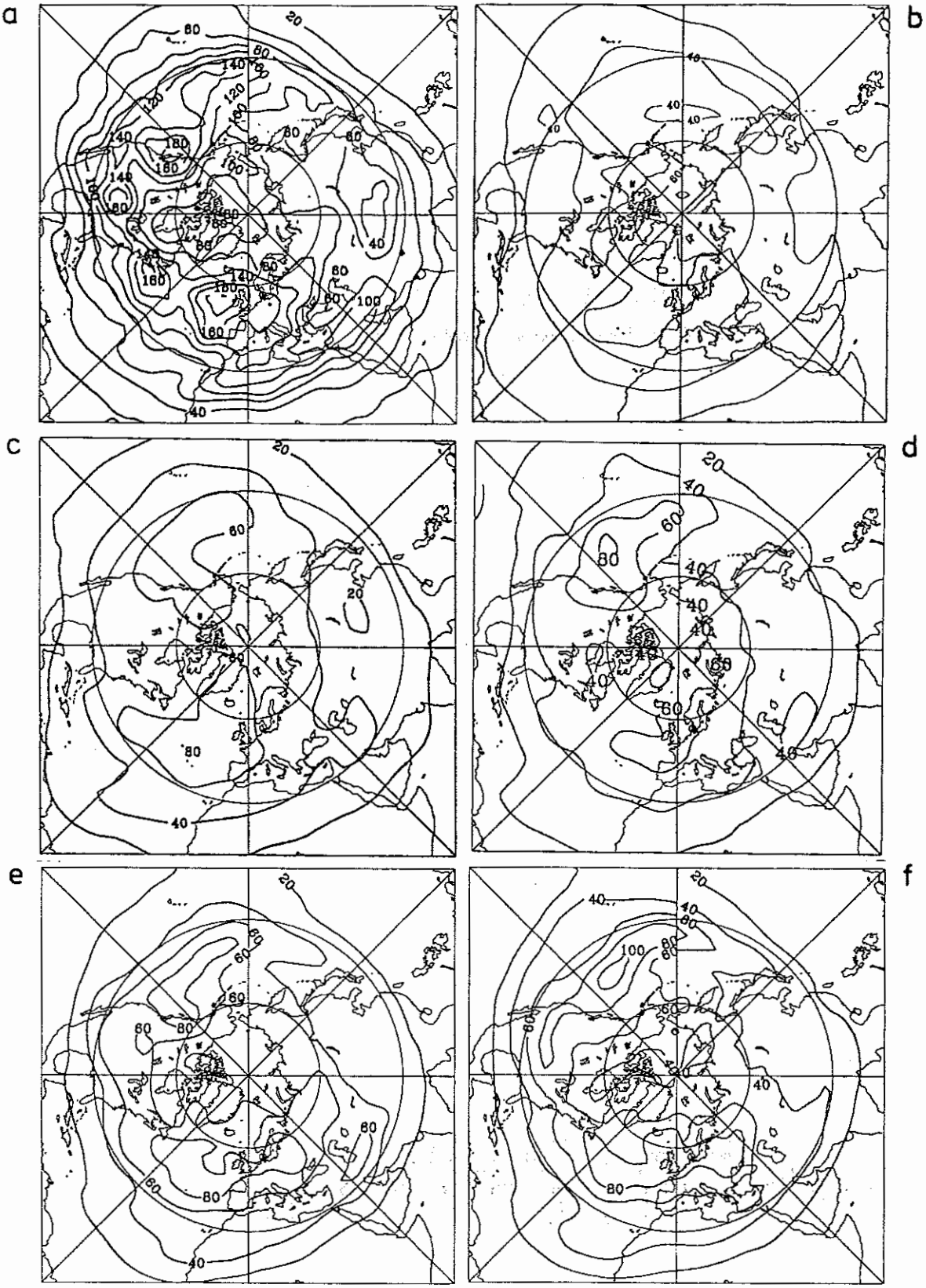

Figure A 35 As in Fig. A33 except for the low-pass filtered frequency range.

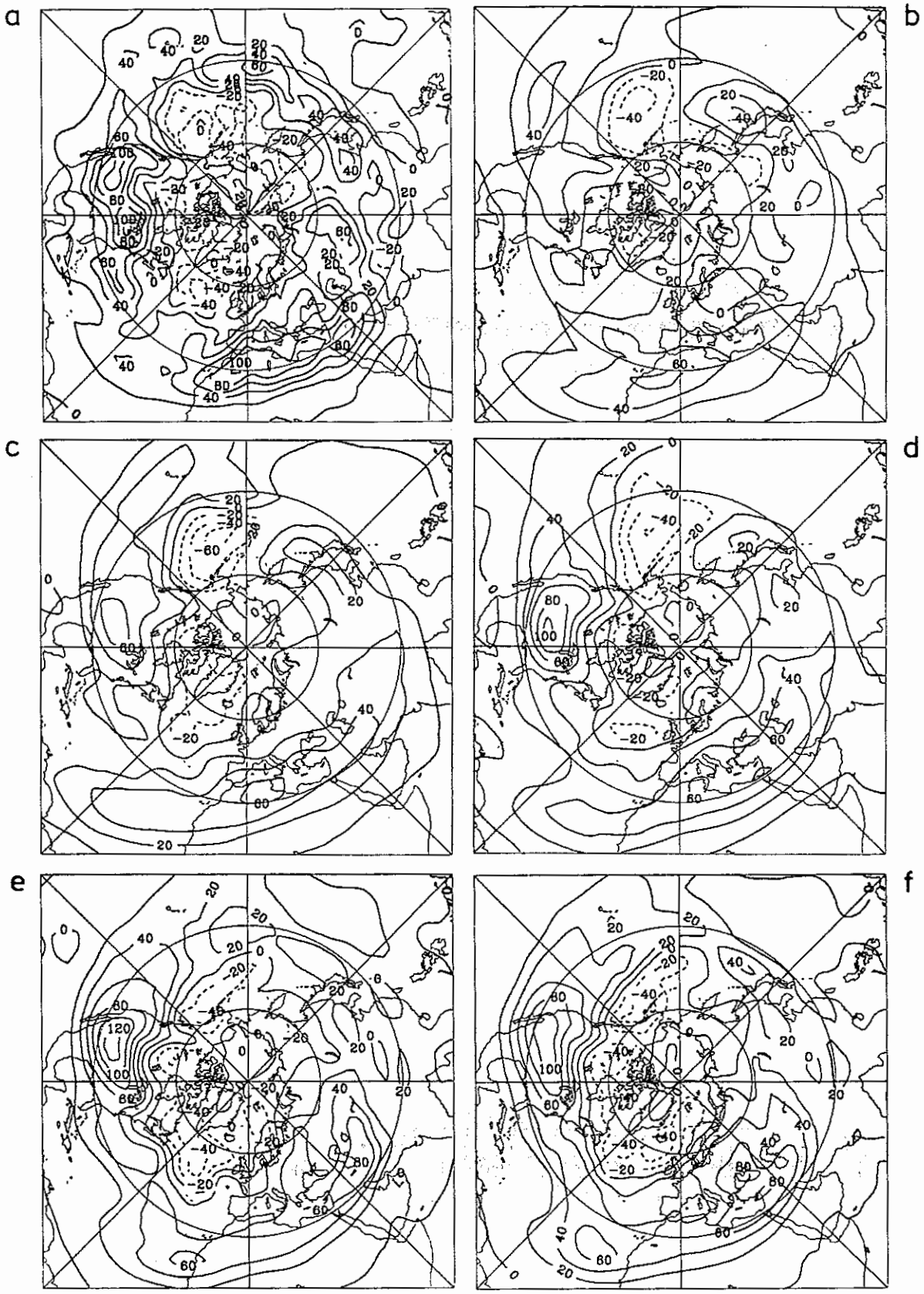

Figure A 36 Northward transport of westerly momentum (m^2/s^2) by transient eddies at 300 hPa computed from the unfiltered time series for DJF. a) ECMWF analyses, b) ECHAM1, c) ECHAM2, d) ECHAM3/T21, e) ECHAM3/T42 (1. decade), f) ECHAM3/T42 (2. decade).

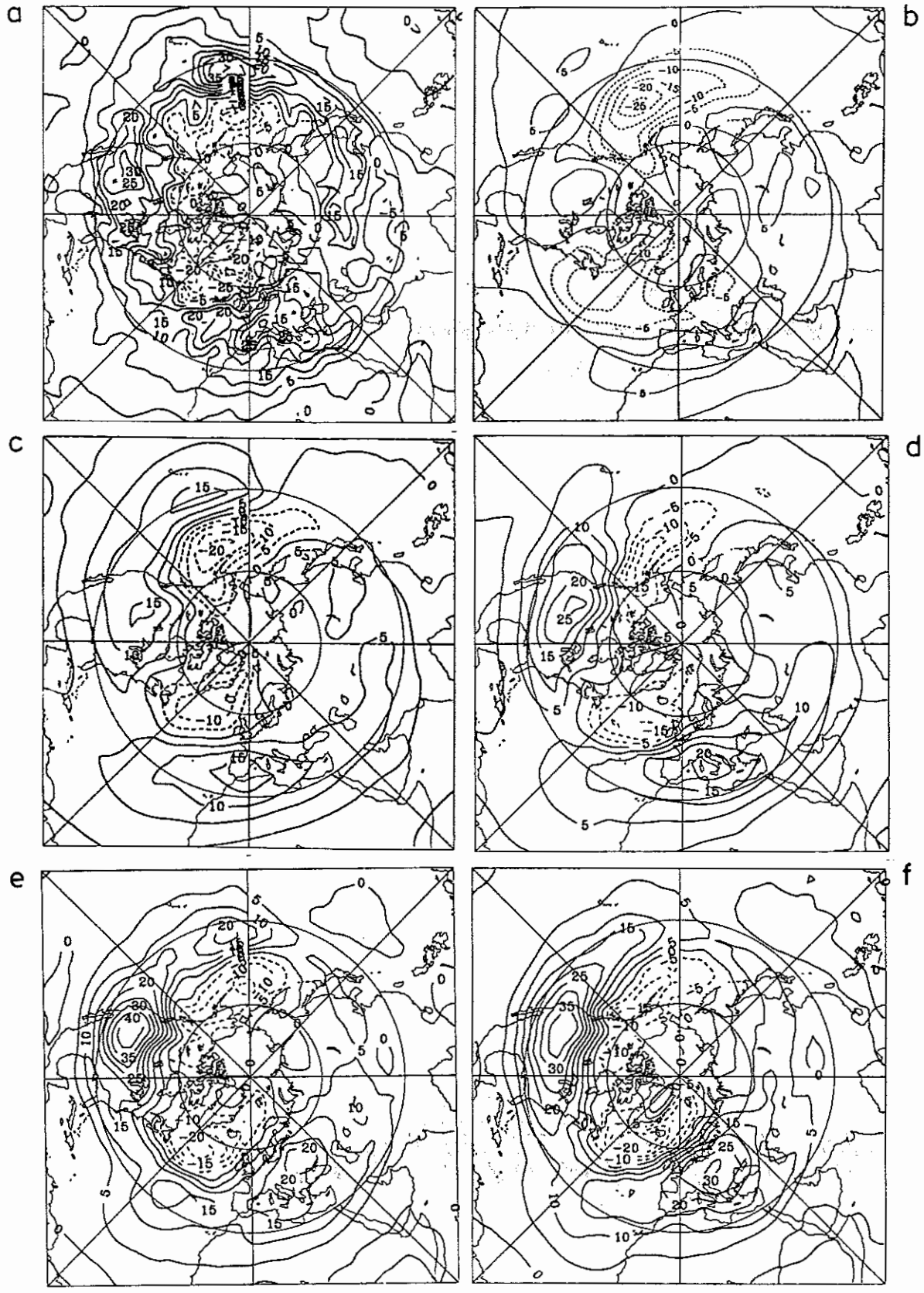

Figure A 37 As in Fig. A36 except for the band-pass filtered frequency range.

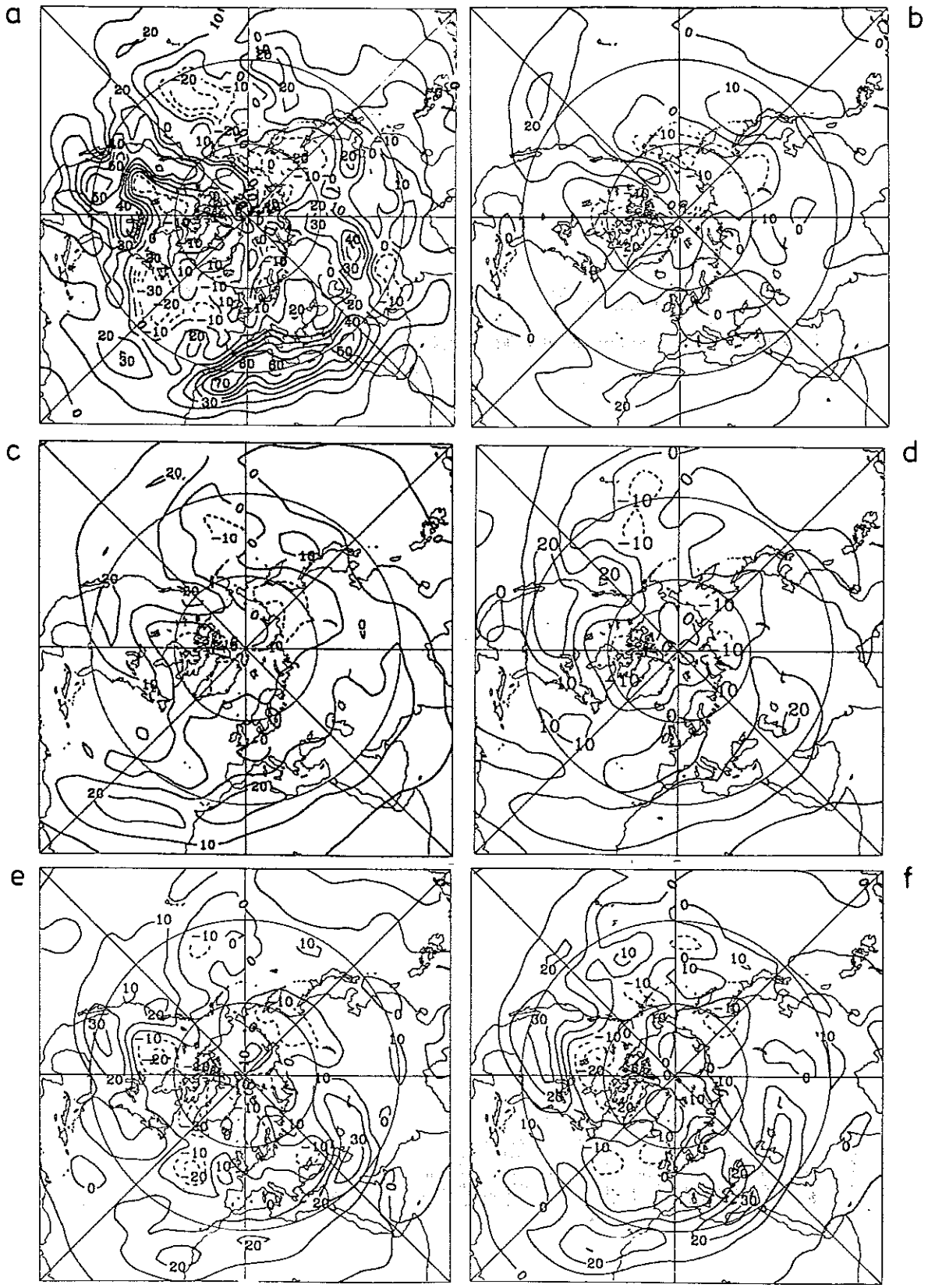

Figure A 38 As in Fig. A36 except for the low-pass filtered frequency range.

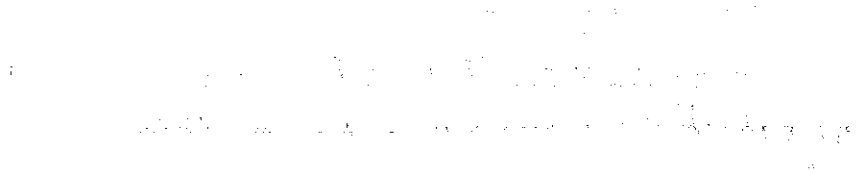

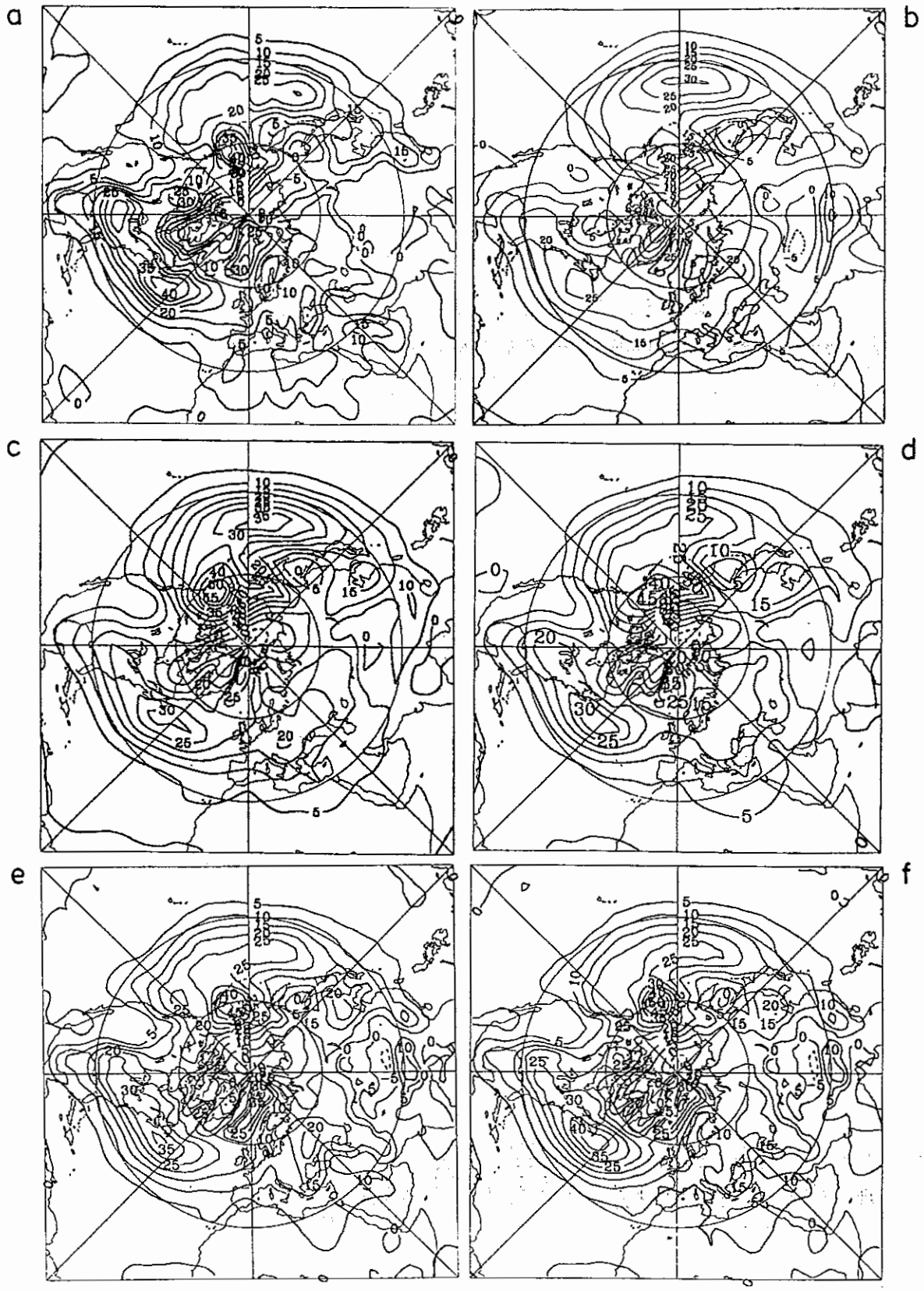

Figure A 39 Northward transport of sensible heat (Km/s) by transient eddies at 850 hPa computed from the unfiltered time series for the DJF season. a) ECMWF analyses, b) ECHAM1, c) ECHAM2, d) ECHAM3/T21, e) ECHAM3/T42 (1. decade), f) ECHAM3/T42 (2. decade).

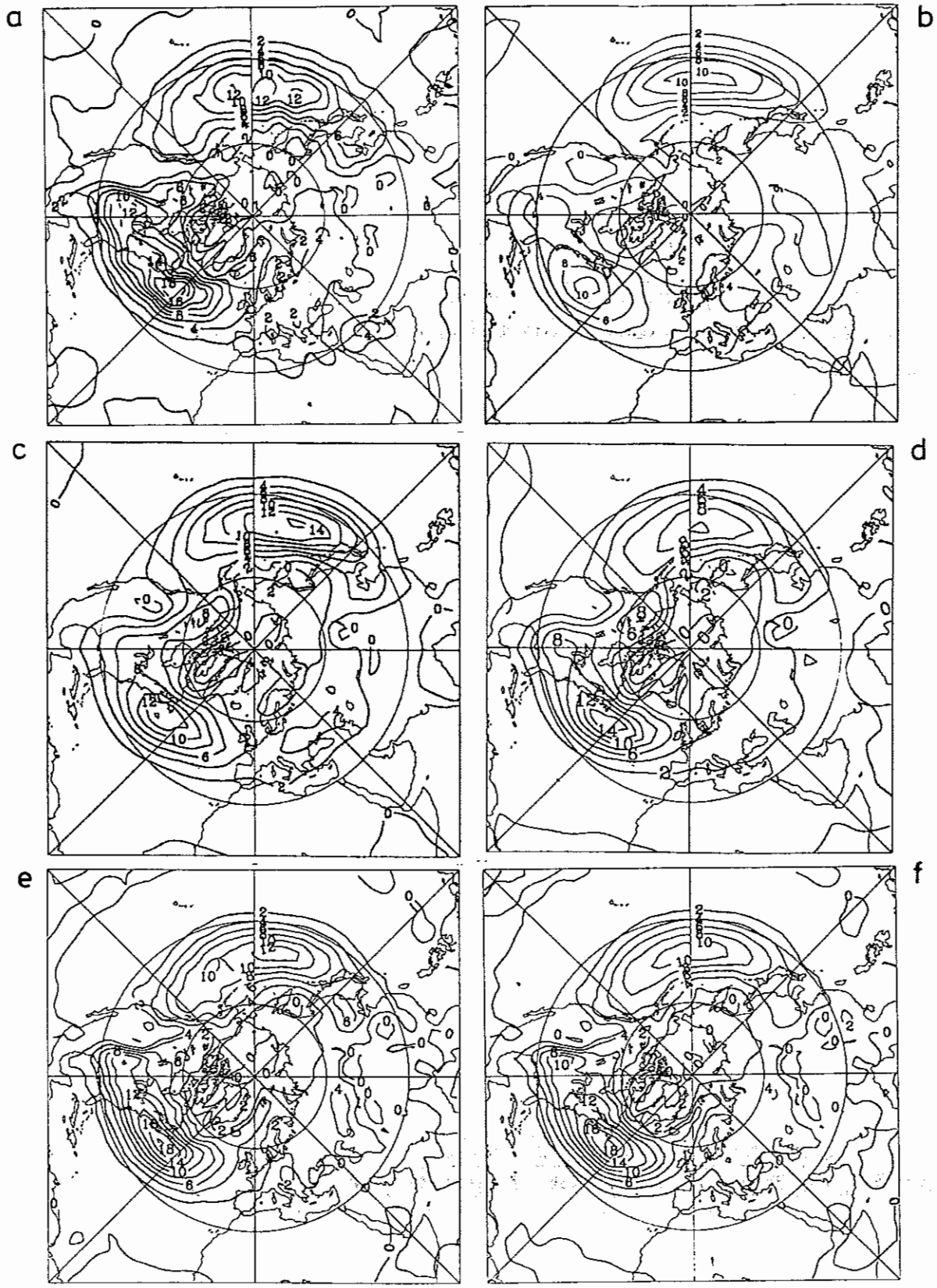

Figure A 40 As in Fig. A39 except for the band-pass filtered frequency range.

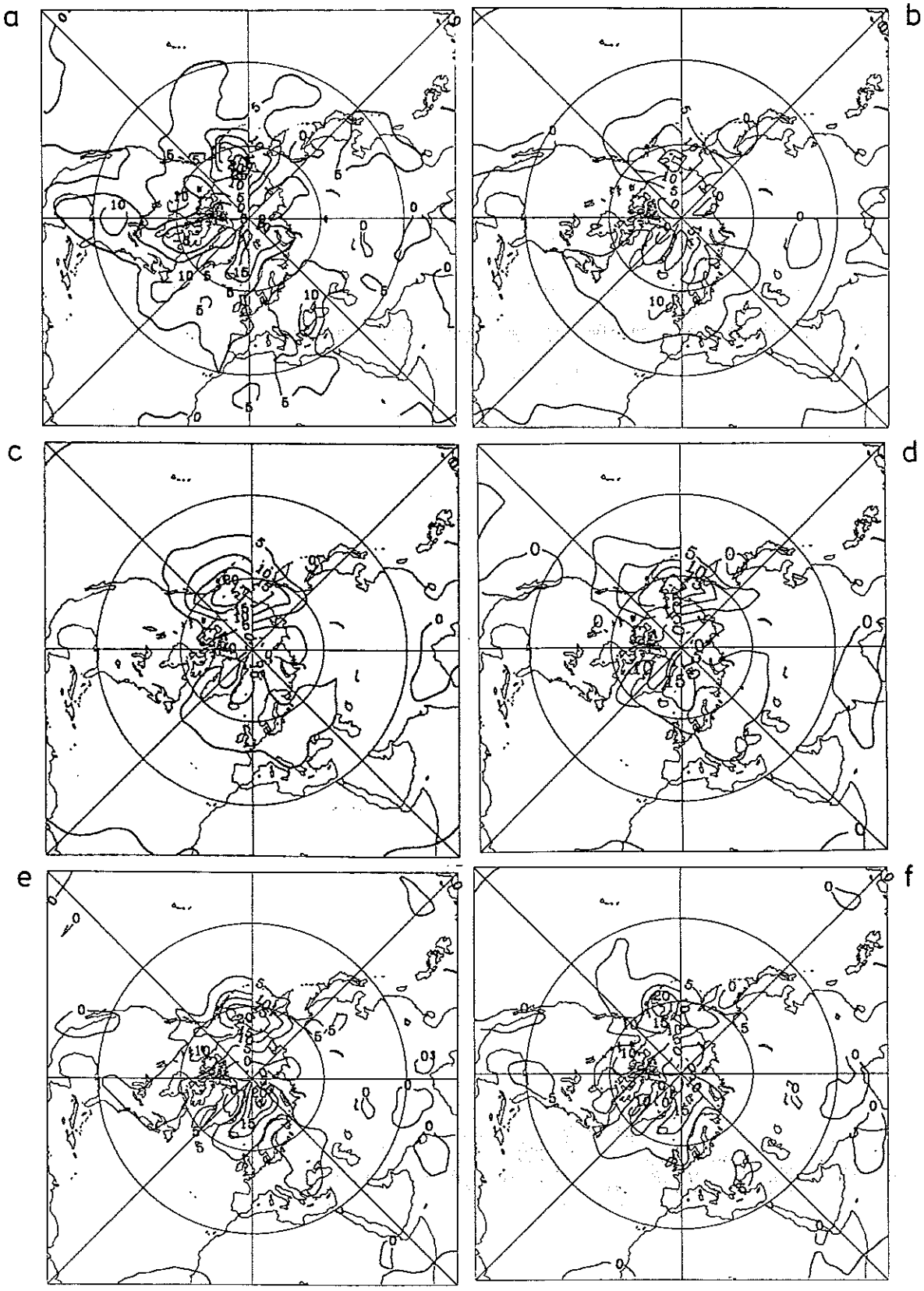

Figure A 41 As in Fig. A39 except for the low-pass filtered frequency range.

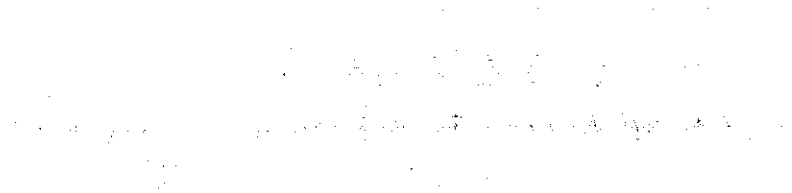

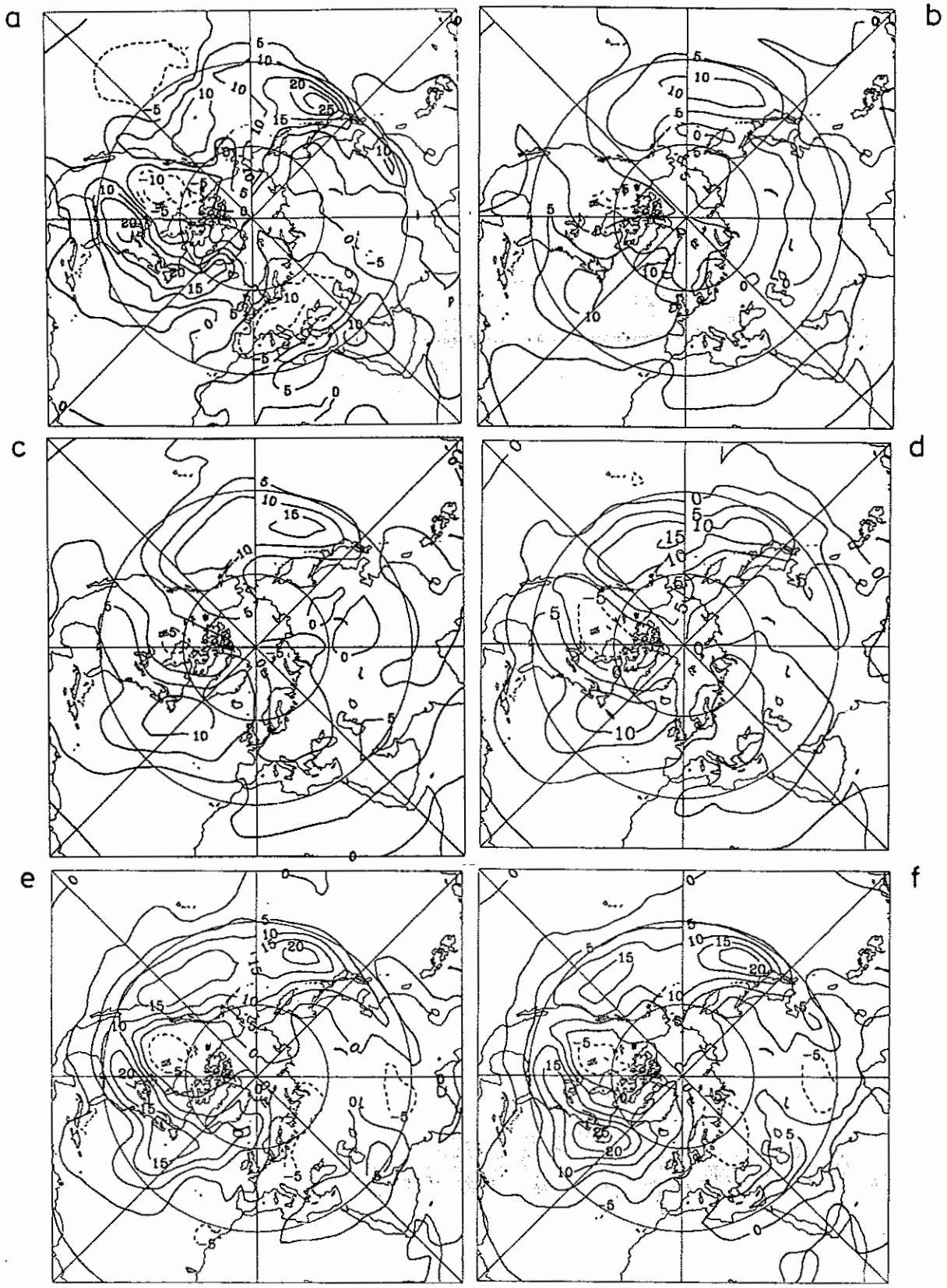

Figure A 42 Northward transport of sensible heat (Km/s) by transient eddies at 300 hPa computed from the unfiltered time series for the DJF season. a) ECMWF analyses, b) ECHAM1, c) ECHAM2, d) ECHAM3/T21, e) ECHAM3/T42 (1. decade) f) ECHAM3/T42 (2. decade).

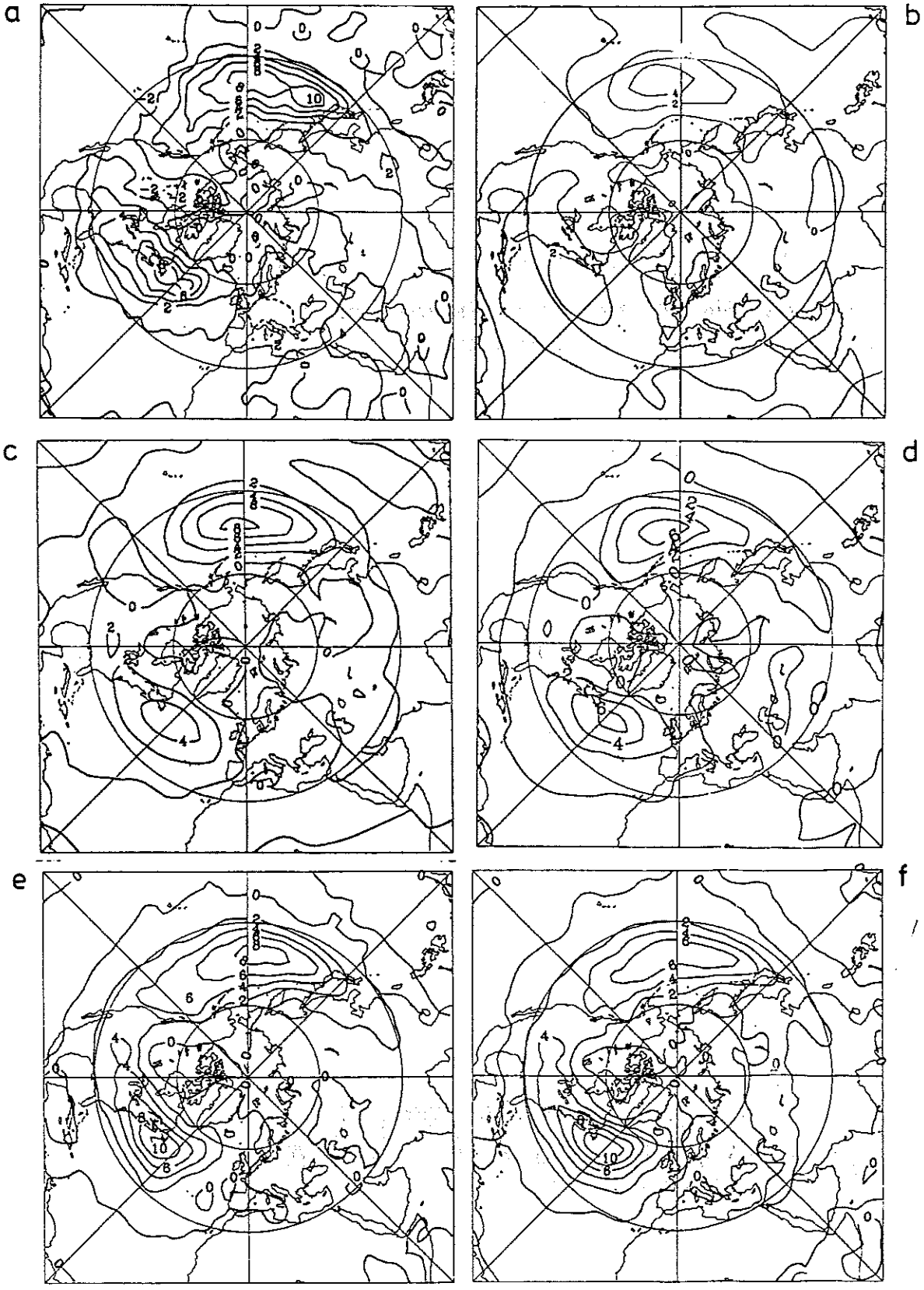

Figure A 43 As in Fig. A42 except for the band-pass filtered frequency range.

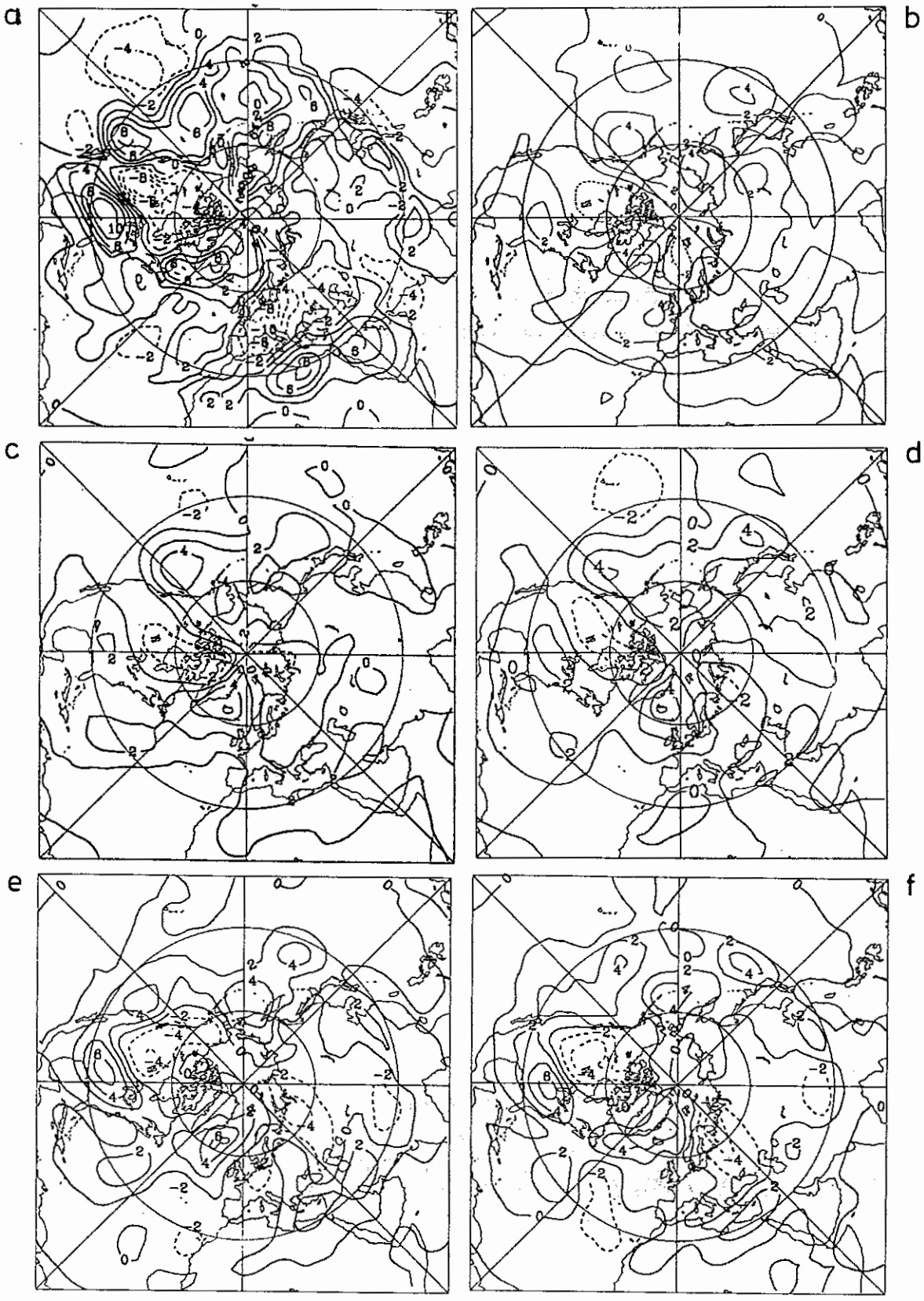

Figure A 44 As in Fig. A42 except for the low-pass filtered frequency range.